Hydrogen Production by Aqueous Phase Reforming of Biomass-derived Glycerol over Cobalt-based Catalysts

Alberto J. Reynoso E.

Universidad del País Vasco Euskal Herriko Unibertsitatea

eman ta zabal zazu

Universidad
del País Vasco

Euskal Herriko
Unibertsitatea

Departamento de Ingeniería Química
Ingeniaritza Kimikoa Saila

HYDROGEN PRODUCTION BY AQUEOUS-PHASE REFORMING OF BIOMASS-DERIVED GLYCEROL OVER COBALT-BASED CATALYSTS.

Obtención de Hidrógeno por Reformado Catalítico en Fase Líquida (APR) de Glicerol derivado de la Biomasa sobre Catalizadores de Cobalto.

MEMORIA

Para optar al grado de
Doctor en Ingeniería Química

Presentada por

ALBERTO JOSÉ REYNOSO ESTÉVEZ

Directores: Jose Luis Ayastuy Arizti
               Miguel Ángel Gutiérrez Ortiz

Leioa, Enero de 2021

A mi abuela Juana (mamá)

A mis padres

Llegar a este punto ha sido un trayecto laborioso, pero a la vez entretenido y gratificante, y aunque el tiempo impacta cual kamikaze, citando a John F. Kennedy: "Siempre hay que encontrar el tiempo para agradecer a las personas que hacen una diferencia en nuestras vidas".

Agradecer a mis directores Dres. Jose Luis Ayastuy Arizti y Miguel Ángel Gutiérrez Ortiz por su apoyo, confianza y efectiva orientación en todo este proceso. Definitivamente este trabajo no habría sido posible sin la dedicación y el ahínco manifestado por ustedes. Igualmente, he de agradecer la cercanía, afabilidad y empatía que siempre han mostrado.

Quiero expresar mi agradecimiento especial al Dr. Jose Ignacio Gutiérrez Ortiz bastón fundamental en la dinámica diaria de nuestros laboratorios. Gracias por siempre estar disponible, y no solo para cuestiones técnicas.

Deseo extender mi agradecimiento a todo el personal del grupo de investigación TQSA, por hacer de estos años una experiencia intelectual y personal inigualable. Al personal docente e investigador por su disponibilidad, consejos y cordialidad y a todos los compañeros de laboratorio por el agradable ambiente de trabajo, su ayuda y los buenos momentos compartidos. Menciones especiales para Adriana MM, que iniciamos juntos este proyecto y con quien he compartido alegrías y frustraciones típicas de un día de laboratorio; Juani MM y Adrián QR, por las tertulias y los ratos a modo de válvula de escape. Y por último en este mismo ámbito, a Mikel Arrese-Igor y Borja Molinuevo quienes directa o indirectamente han contribuido con sus trabajos de grado a este proyecto.

Expresar también mis más sinceros agradecimientos a los investigadores y técnicos del Servicios Generales de Investigación (SGiker) de la Universidad del País Vasco UPV/EHU por su colaboración, y en particular, a los doctores Francisco Javier Sangüesa y María Belén Sánchez por sus interesantes comentarios y su dedicada labor.

J´exprime toute ma reconnaissance et ma gratitude aux Mesdames Catherine Especel et Laurence Vivier pour m'avoir donné l'opportunité de travailler dans les laboratoires de l'équipe du Site Actif au Matériau Catalytique (SAMCat) à l'Institut de Chimie des Milieux et des Matériaux de l'Université de Poitiers

(IC2MP, UMR 7285) et pour votre soutien continu pendant mes jours à Poitiers. Mes remerciements s´adressent également à tous les membres de l`équipe SAMCat pour m'avoir bien accueillie au sein de l'institut. Je remercie à tous les doctorants pour la bonne ambiance et les soirées dans la patinoire. Je souhaite particulièrement remercier Aurélien Fouquet pour avoir partagé son expérience et savoir-faire avec bienveillance et gentillesse

Durante estos años de este lado del charco he conocido a tanta gente que han contribuido, de una manera u otra, a hacer mi estancia especial que resulta complicado expresar en unas cuantas líneas el agradecimiento hacia ellos. A mis amigos de La Cuadripanda, y en especial a Pau y Yoshi, por todos los momentos vividos, por todos los pueblos recorridos. A los Gaubeka, Agur, Arkaitz, por la acogida, el apoyo y el cariño. A mi familia boliviana, Leny, Pablo, Jhadir, Inés, que desde el primer momento me han hecho sentir uno más de los Delgadillo Arteaga.

No puedo olvidarme de los amigos en República Dominicana, esos que a pesar de la distancia y la diferencia horaria siempre se han mantenido en contacto. Y por supuesto a mi extensa familia, hermanos/as, tíos/as, primos/as, sobrinos/as, por el apoyo, porque son parte fundamental de mi vida y me siento dichoso de la familia que tengo.

A mi padre, a mi madre y en especial a mamá, todo lo que soy se lo debo a ustedes. Gracias, por tanto.

A todos, y a los demás que se han quedado en el tintero,

Muchisimas gracias!

Oui, mes amis, je crois que l'eau sera un jour employée comme combustible, que l'hydrogène et l'oxygène, qui la constituent, utilisés isolément ou simultanément, fourniront une source de chaleur et de lumière inépuisables et d'une intensité que la houille ne saurait avoir. Un jour, les soutes des steamers et les tenders des locomotives, au lieu de charbon, seront chargés de ces deux gaz comprimés, qui brûleront dans les foyers avec une énorme puissance calorifique. Ainsi donc, rien à craindre. Tant que cette terre sera habitée, elle fournira aux besoins de ses habitants, et ils ne manqueront jamais ni de lumière ni de chaleur, pas plus qu'ils ne manqueront des productions des règnes végétal, minéral ou animal. Je crois donc que lorsque les gisements de houille seront épuisés, on chauffera et on se chauffera avec de l'eau. L'eau est le charbon de l'avenir.

Cyrus Smith, fictional character

L'Île mystérieuse, Jules Verne

ABSTRACT

Aqueous-phase reforming (APR) is a suitable and efficient alternative process for production of hydrogen and other high value-added chemicals. APR of oxygenated compounds from biomass presents several advantages in comparison to the benchmark steam reforming, such as: (i) lower energy demand, since it is not necessary to evaporate the reagents, and (ii) the favourable operating conditions (low temperature and moderate pressure) for obtaining hydrogen with low CO content that would facilitate its purification in other stages. The use of hydrogen produced from biomass as an energy vector would drastically reduce CO_2 emissions, contribute to reducing the current dependence on fossil fuels and, due to its greater availability, would improve the economic situation of many countries that are still facing energy poverty.

Due to regulations to promote the use of biofuels and other renewable fuels for transportation purposes, in recent years, there has been a large increase in the production of biodiesel, with the consequent increase in glycerol stock, its major by-product. This Doctoral Thesis has addressed the glycerol valorisation by APR for obtaining hydrogen over cobalt aluminate-based catalysts, seeking to enhance the economic viability of biorefinery systems.

For the catalytic studies, three groups of cobalt aluminate-based catalysts were synthesized. First, cobalt aluminate catalysts at varying Co/Al ratios, by coprecipitation. Then, based on the most active catalyst of the previous series and with the aim of improving its hydrothermal stability, two other groups were synthesized: one, incorporating cerium (at 0.3, 0.7 and 2.1 wt.%) by coprecipitation, and the other, incorporating platinum (at 0.3, 1 and 3 wt.%) by impregnation.

Catalysts (in fresh, reduced and used samples) have been thoroughly characterized by several analytical techniques. Techniques have been grouped on the basis of: (i) bulk chemical composition and textural properties (ICP-OES/MS, N_2 physisorption); (ii) reducibility of the solids (H_2-TPR); (iii) nature and morphology of the phases (XRD, STEM); (iv) metallic function (H_2 chemisorption, cyclohexane dehydrogenation); (v) structure and coordination state (FTIR, UV-Vis-NIR-DRS, NMR, XPS); (vi) acid-base sites on

the catalyst surface (NH$_3$-TPD, isomerization of 33DM1B, CO$_2$-TPD); carbonaceous material deposition (Raman spectroscopy, TPH).

The APR tests have been performed in a fixed-bed up-flow reactor and the products analysed by various chromatographic techniques: μGC and GC-MS, for on-line analysis of the gas phase; and high-pressure liquid chromatography (HPLC) and GC-FID for the identification and quantification of liquid products. In addition, Total Organic Carbon (TOC) analyser was used to quantify carbon conversion to gas.

Cobalt aluminate catalysts, with different Co/Al ratios, were tested in glycerol APR at WHSV = 24.5 h^{-1} and under two temperature/pressure conditions (235 °C/35 bar and 260 °C/50 bar). Among these catalysts, 0.625CoAl exhibited the highest conversion of glycerol and H$_2$ yield.

Under the same reaction conditions mentioned above, the promoting effect of cerium was studied. The catalytic results, however, showed a negative effect of Ce-addition on both glycerol conversion and H$_2$ yield. Furthermore, a greater deactivation due to phenomena such as carbonaceous deposition, re-oxidation and leaching, already observed in bare cobalt aluminate samples, enhanced in Ce-containing samples.

On the other hand, Pt-impregnation improved catalytic activity in glycerol APR. In addition, these bimetallic catalysts proved to be very stable for more than 100 h TOS at 0.68 h^{-1} and 260 °C/50 bar. Further investigations led to the conclusion that bimetallic catalysts were more selective towards liquid-phase Water-Gas Shift (WGS) reaction than CO hydrogenation, regardless of the availability of hydrogen in the reaction medium.

The study of the effect of operating conditions was carried out with the stable 0.3Pt/CoAl catalyst. Generally speaking, H$_2$ production is favoured at a higher reaction temperature/pressure, at lower WHSV and/or a lower glycerol content in the feed. It was also found that reforming short chain compounds produces a higher H$_2$ yield.

Due to the high concentration of organic and inorganic impurities present in the crude bioglycerol, it was subjected to a physico-chemical treatment before its

catalytic study. The catalytic tests carried out with both 0.625CoAl and 0.3Pt/CoAl catalysts showed very encouraging results (high glycerol conversion and carbon conversion to gas) and a positive effect of the remaining organic compounds in the production of hydrogen.

Last but not least, sorbitol transformation was studied in a batch reactor at 240 °C and 60 bar, under H_2 and N_2 atmosphere. Under both conditions, Pt-Co bimetallic catalysts were the ones that presented the best results. Regardless of the reaction atmosphere, all catalysts initially favoured retro-aldol condensation pathway. Nevertheless, sorbitol conversion was lower under N_2 pressurisation.

LABURPENA

Erregai fosilen erabilerak dakarren ingurumenaren kutsadura dela eta, garapen iraunkorra bermatzeko iturri berriztagarriak erabiltzea ezinbestekoa bihurtu da. Ildo honetan, garapen iraunkorra bermatzeko hidrogenoa da aukera nagusia, berarengandik energia lortzean negutegi efektua sortzen duten gasik igortzen ez delako. Garraiorako bioerregaien eta bestelako erregai berriztagarrien erabilera sustatzeko araudiekin, azken urteotan biodieselaren ekoizpena nabarmen handitu da eta, ondorioz, bere ekoizpen-prozesuan azpiproduktu nagusi den glizerolaren izakina. Glizeroletik abiatuz hidrogenoa lortzea da Doktorego Tesi honen helburu nagusia. Horretarako, fase urtsuko erreformatze erreakzioa arakatu da kobalto aluminatoan oinarritutako katalizatzaileak erabiliz, biofindegiaren bideragarritasun ekonomikoa hobetzeko helburuarekin.

Fase urtsuko erreformatzea (APR) aukera egokia eta eraginkorra da hidrogenoa eta balio erantsi handiko beste produktu kimiko batzuk ekoizteko. Biomasatik eratorritako konposatu oxigenatuen APRak abantaila ugari ditu beste erreformatze-moten aldean, hala nola: (i) energia eskari txikiagoa, erreaktiboak lurruntzeko beharrik ez baitago; (ii) CO eduki txikiagoa duen hidrogeno korrontea lortzen da eragiketa tenperatura txikian eta presio ertainean burutzen delako, sasi-erreakzioak murriztuz. Biomasatik sortutako hidrogenoa erabiltzeak, CO_2-aren isurketak izugarri murriztuko lituzke, erregai fosilekiko egungo mendekotasuna murrizten lagunduko luke eta, pobrezia energetikoari aurre egiten dioten herrialde askoren egoera ekonomikoa hobetuko luke.

Kobalto aluminatoan oinarritutako hiru katalizatzaile-talde sintetizatu dira. Abiapuntu bezala, Co/Al erlazio desberdinak arakatu dira, koprezipitazioz sintetizatuz. Ondoren, aurreko taldeko katalizatzaile eraginkorrena aukeratu da egonkortasun hidrotermala hobetzeko helburuarekin formulazioa aldatzeko. Horrela, beste bi talde sintetizatu dira: bata, koprezipitazio prozesuan zerioa gehituz, (pisuan %0,3, %0,7 eta %2,1 edukiekin); bestea, platinoa inpregnatuz (pistutan % 0,3, %1 eta %3 edukiekin). Prestatutako katalizatzaileen konposizioa, egitura, ehundura eta azidotasun/basikotasun propietateak ezagutzeko, teknika espektroskopikoak, mikroskopikoak, tenperatura programatukoak eta eredu-erreakzioak erabili dira, bai prestatu berritan, baita erreduzitu eta erreaktorean erabili ondoren. APRan duten eraginkortasuna

aztertzeko, ohantze finkoko goranzko fluxudun erreaktorea erabili da. Sortutako produktuak hainbat kromatografia teknika erabiliz aztertu dira: μGC eta GC-MS, gas fasea aztertzeko; presio handiko likido kromatografia (HPLC) eta GC-FID, produktu likidoak identifikatu eta kuantifikatzeko. Gainera, Karbono Organikoa (TOC) analizatzailea erabili da likidoan dagoen karbonoa kuantifikatzeko.

Co/Al erlazio desberdineko kobalto aluminato katalizatzaileak glizerolaren APRan aztertzeko, bi tenperatura/presio baldintza (235 °C/35 bar eta 260 °C/50 bar) erabili dira, 24,5 h^{-1} WHSVan jardunez. Talde horretako katalizatzaileen artean, 0.625CoAl izan da glizerola gehien bihurtu eta H$_2$ etekin handiena eman duena.

Arestian aipatutako erreakzio-baldintza berean, zerioaren efektu sustatzailea aztertu da. Emaitzak aztertuz, zerioak ez du ez glizerolaren bihurtze-maila ezta H$_2$ etekina hobetu, txikitu baizik. Gainera, zeriodun katalizatzaileek desaktibazio handiagoa izan dute, kokearen aitzindari den karbono metaketa, kobaltoaren bir-oxidazioa eta metalen lixibiazioa areagotu baitira.

Bestalde, kobalto aluminioaren gainean Pt inpregnatzean, glizerolaren APRan jarduera katalitikoa hobetu da. Gainera, katalizatzaile bimetaliko hauek oso egonkorrak direla ikusi da, 0,68 h^{-1} eta 260 °C/50 bar baldintzan burututako 100 h^{-1} TOS iraupeneko erreakzioan ikusi den bezala. Likido fasean egindako ondorengo ikerketek ondorioztatu dute katalizatzaile bimetalikoak WGS erreakziorako COren hidrogenaziorako baino hautakorragoak direla, edozein izanda ere hidrogenoaren eskuragarritasuna erreakzio inguruan.

Eragiketa baldintzek APRaren errendimenduan duten eragina 0.3Pt/CoAl katalizatzaile egonkorra erabiliz aztertu da. Oro har, erreakzio tenperatura/presio handiagoan, WHSV txikiagoan eta glizerol eduki txikiagoko elikadurarekin H$_2$ ekoizpena handitzen da. Kate laburreko konposatu oxigenatuen erreformatzean H$_2$ etekin handiagoa ematen duela ere ikusi da.

Bioglizerol gordinaren ezpurutasun organiko eta ezorganikoen eduki handia dela eta, azterketa katalitikoa egin aurretik haren tratamendu fisiko-kimikoa egin da. 0.625CoAl eta 0.3Pt/CoAl katalizatzaileekin egindako glizerol gordinaren APR erreakzioek oso emaitza onak erakutsi dituzte (bai glizerol

bihurtze-maila eta bai karbonoa gas bihurtze-maila handiak), izan ere tratatutako glizerolean dauden konposatu organikoek ere erreformatu egiten baitira, hidrogenoaren ekoizpenean ekarpen positiboa eginez.

Bukatzeko, glizerolaren APRrako optimizatutako katalizatzaileek sorbitolaren eraldaketarako duten moldakortasuna aztertu da. Erreakzio hauek erreaktore ez jarraituan burutu dira, 240 °C eta 60 bar presioan, H_2 zein N_2 atmosferan (HDO eta APR aztertzeko). Bi baldintzetan, Pt-Co katalizatzaile bimetalikoek izan dituzte emaitzarik onenak. Erreakzioa burutu den giroa edozein dela ere, kondentsazio retro-aldolikoa izan da sorbitolaren eraldaketarako lehen urratsa, katalizatzaile guztiekin. Hala ere, sorbitol gutxiago bihurtu da N_2 erabili denean presioa mantentzeko.

RESUMEN

El hidrógeno es un vector energético limpio y técnicamente viable tanto para la producción y exportación de energía a gran escala (producción centralizada) como para el suministro de energía a pequeña escala (generación distribuida de energía). Como en condiciones normales el hidrógeno no se encuentra de forma aislada, hay que producirlo. Por ejemplo, para su utilización en procesos industriales, como el refinado de petróleo y síntesis de fertilizantes, se obtiene mediante la gasificación o el reformado de combustibles fósiles.

El uso como vector energético del hidrógeno, producido a partir de biomasa, reduciría drásticamente las emisiones de CO_2, contribuiría a reducir la dependencia actual de los combustibles fósiles y, por su mayor disponibilidad, mejoraría la situación económica de muchos países que aún se enfrentan a la pobreza energética.

En los últimos años, varios países, incluyendo a la UE, han legislado para promover el uso de biocombustibles y otros combustibles renovables con fines de transporte. Esto ha generado un importante aumento en la producción de biodiesel, generando un elevado abastecimiento de glicerol, su principal subproducto. Como consecuencia, el precio del glicerol, un producto químico esencial y extremadamente versátil dentro de la biorrefinería, ha disminuido. La utilización del glicerol, derivado del proceso del biodiésel, agrega valor a la cadena productiva de esta industria, contribuyendo a su competitividad.

El reformado en fase acuosa (APR) es una tecnología prometedora para la producción de hidrógeno y otros productos químicos de alto valor añadido. El APR de compuestos oxigenados derivados de la biomasa ofrece varias ventajas en comparación con el más extendido reformado con vapor de hidrocarburos, como son: (i) menor demanda de energética, ya que no es necesario evaporar los reactivos; (ii) los compuestos oxigenados de interés no son inflamables ni tóxicos, lo que permite almacenarlos y manipularlos de forma segura; (iii) las condiciones de operación (baja temperatura y presión moderada) son favorables para la reacción de WGS, siendo posible obtener hidrógeno con bajo contenido en CO que facilitaría su depuración en etapas posteriores.

Esta Tesis Doctoral se ha centrado en la valorización de glicerol por APR enfocado a la obtención de hidrógeno, utilizando catalizadores basados en aluminatos de cobalto, buscando potenciar la viabilidad económica de la biorefinería.

Con este objetivo, se han preparado y caracterizado con una amplia gama de técnicas tres series de catalizadores basados en aluminato de cobalto. Las técnicas empleadas incluyen: (i) análisis ICP, para determinar la composición química; (ii) fisisorción de nitrógeno, para medir las propiedades texturales (área superficial, volumen y diámetro de poros); (iii) reducción a temperatura programada (TPR), para evaluar la reducibilidad de las muestras; (iv) difracción de rayos X (XRD), para identificar y evaluar las estructuras cristalinas; (v) microscopía electrónica de transmisión (STEM), para visualizar su morfología y obtener la distribución del tamaño de partículas; (vi) quimisorción isoterma de hidrógeno y reacción modelo de deshidrogenación de ciclohexano, para evaluar la superficie metálica; (vii) varias técnicas espectroscópicas (FTIR, Uv-Vis-NIR-DRS, NMR y XPS), para estudiar el estado de coordinación de los metales y cuantificar la composición elemental superficial de los catalizadores; (viii) desorción de amoniaco a temperatura programada, para cuantificar la acidez total; (ix) reacción modelo de isomerización de 3,3-dimetilbut-1-eno, utilizada para evaluar la acidez tipo Brønsted; (x) desorción de CO_2 a temperatura programada, para cuantificar la basicidad total; (xi) espectroscopía Raman e hidrogenación a temperatura programada, para obtener información cualitativa y cuantitativa del material carbonoso en las muestras usadas.

Los ensayos catalíticos se han realizado en un reactor de lecho fijo de flujo ascendente, y los productos de reacción se han enfriado a 5 °C y separado en fase líquida y gaseosa. Ambas fases han sido analizadas por diversas técnicas cromatográficas: μGC and GC-MS, para el análisis *online* de la fase gaseosa y cromatografía líquida de alta presión (HPLC) y GC-FID para la identificación y cuantificación de productos líquidos. El analizador de carbono orgánico total (TOC) se ha utilizado para cuantificar la conversión de carbono a gas.

Primeramente, se han sintetizado catalizadores de espinela de aluminato de cobalto con diferentes ratios molares Co/Al y oxido de cobalto (Co_3O_4). Se ha elegido este tipo de estructura ya que presenta una alta estabilidad térmica y de

pH, moderada acidez superficial y elevada reactividad química, lo que la convierte en una alternativa prometedora como precursor de catalizadores de cobalto, que conjugan las ventajas catalíticas de un metal altamente activo soportado sobre una estructura estable.

El análisis de textural ha determinado que los sólidos presentan una estructura mesoporosa con una superficie específica moderada, que ha disminuido levemente por reducción a 600 °C. La fuerte interacción Co-O-Al en las espinelas mixtas aumenta la temperatura necesaria para la reducción completa de todas las especies de cobalto. La formación de estructura de espinela en la serie xCoAl se ha confirmado mediante las técnicas de XRD, UV-vis-NIR DRS y FTIR. Además, por ^{27}Al NMR, se ha evidenciado una estructura de espinela parcialmente invertida.

La incorporación de aluminio ha dificultado la cristalización del Co_3O_4, que ha repercutido en que se han obtenido tamaños de cristal más pequeños. En consecuencia, se logra una mejor dispersión de Co en los catalizadores basados en espinela de aluminato de cobalto. Los resultados obtenidos mediante la desorción programada a temperatura de CO_2 y NH_3 sugieren que los catalizadores xCoAl han mantenido la basicidad superficial del cobalto metálico, mientras que la fuerte acidez de la alúmina se ha visto atenuada. Los sitios ácidos resultantes fueron principalmente de fuerza débil y media, y su baja actividad en la isomerización de 33DM1B ha confirmado que presentan una acidez de tipo Lewis, lo que podría inhibir la deshidratación de glicerol no deseada y otras reacciones secundarias.

Los ensayos de desorción de glicerol a temperatura programada nos han avanzado los posibles productos en el reformado acuoso de glicerol y la viabilidad de estos catalizadores para la producción de H_2. Los ensayos catalíticos han sido realizados inicialmente a 24,5 h^{-1} y a dos condiciones de temperatura/presión (235 °C/35 bar y 260 °C/50 bar). A ambas condiciones, el catalizador 0.625CoAl (mayor relación atómica Co/Al) ha mostrado los resultados más destacados en conversión de glicerol, en conversión a gas y en la producción de H_2. Este catalizador ha estado operando durante 30 h y ha mostrado una marcada desactivación atribuida a la re-oxidación del cobalto que actúa como fase activa y su posterior lixiviación, favorecida por el medio de

reacción y, en menor medida, a la deposición de material carbonoso en la superficie del catalizador.

Con el objetivo de mejorar la actividad catalítica se ha procedido a incorporar cerio como promotor, por coprecipitación. Se ha elegido este elemento del grupo de los lantánidos por su conocido rendimiento en la reacción de WGS. La modificación con cerio del catalizador 0.625CoAl ha aumentado la S_{BET}, de aproximadamente 16-30%, y otros parámetros texturales. Por medio de XRD, también se ha verificado un aumento del tamaño del cristal de la espinela. Además de las especies de aluminato de cobalto y cobalto metálico, en las muestras reducidas, se ha identificado una fase estructural Ce_5Co_{19}. Con respecto a los sitios de ácidez-basicidad, la adición de cerio ha aumentado tanto la acidez total como la basicidad y la conversión obtenida por isomerización de 33DM1B ha indicado una alta densidad de centros Brønsted para muestras que contienen cerio, excepto para el catalizador 0.7CeCoAl.

Los resultados globales de estos catalizadores modificados han sido inferiores a los mostrados por el catalizador de partida. Los catalizadores xCeCoAl han mostrado una mayor selectividad a hidrógeno; sin embargo, también han presentado una alta selectividad a alcanos, por lo que el rendimiento de hidrógeno se ha visto claramente disminuido. La baja actividad catalítica de las muestras xCeCoAl puede atribuirse a una menor área metálica superficial y a la formación de la fase tipo estructura Ce_5Co_{19}. Además, los catalizadores con cerio han presentado una mayor desactivación.

Los catalizadores xCeCoAl también han experimentado un aumento de S_{BET} y un cambio en la distribución del tamaño de poro que se puede atribuir a la hidratación de la alúmina y la deposición de material carbonoso en la superficie de los catalizadores. Asimismo, en las condiciones hidrotermales en las que se realizaron las reacciones se ha formado $Ce(CO_3)OH$. A pesar de la adición de cerio, los catalizadores continuaron presentando fenómenos de re-oxidación y lixiviación, lo que explica la notable desactivación presentada durante las 3 h de cada reacción.

Se ha demostrado que los sistemas catalíticos basados en metales del grupo del platino son efectivos para la producción de hidrógeno mediante el reformado en

fase acuosa de hidrocarburos oxigenados gracias a su capacidad para escindir enlaces C-C y aumentar la actividad de la reacción de WGS. Considerando estas cualidades, la impregnación de platino se ha realizado sobre el soporte 0.625CoAl.

La caracterización de las muestras bimetálicas Pt-Co ha revelado que la carga de Pt estabilizó las propiedades estructurales y texturales de los catalizadores basados en espinela de cobalto. Además, la fuerte interacción Pt-Co ha promovido la reducibilidad y aumentado la disponibilidad metálica, tanto del Co como del Pt. La caracterización de los sitios ácidos y básicos, por su parte, ha determinado que estos presentan, principalmente, fortaleza débil y media.

Los catalizadores bimetálicos de Pt-Co han mostrado una actividad superior a los demás catalizadores, siendo estables por más de 100 h de reacción. Se ha investigado, además, el rendimiento catalítico de estos catalizadores bimetálicos en las reacciones en fase líquida de Water-Gas Shift (WGS) e hidrogenación de CO en fase líquida (260 °C/50 bar), ambas de crucial importancia para definir la distribución de productos en el APR.

Entre los catalizadores bimetálicos, se ha elegido el catalizador 0.3Pt/CoAl para estudiar el efecto de varios parámetros de operación (concentración de glicerol, temperatura/presión, tiempo de contacto, tipo de compuesto alimentado) sobre el rendimiento de APR. Los mejores resultados se han logrado alimentando concentraciones diluidas de glicerol, operando a altas temperaturas/presiones y/o a tiempos de contactos prolongados. Además, se ha comprobado que el reformado de compuestos de cadenas cortas (etilenglicol) presentan mayores rendimientos a hidrógeno comparado con los sustratos de cadena larga (glicerol y sorbitol).

Se ha estudiado el rendimiento APR alimentando glicerol procedente de una biorefinería. La caracterización del bioglicerol crudo recibido de la industria ha indicado una alta concentración de impurezas orgánicas e inorgánicas, por lo que se ha procedido a realizar un tratamiento físico-químico antes de ser alimentado al reactor y evitar problemas de operatividad. Las pruebas catalíticas realizadas con los catalizadores 0.625CoAl y 0.3Pt/CoAl han mostrado altas

conversiones de glicerol y a gas, mientras que las impurezas orgánicas residuales muestran un efecto positivo en la producción de hidrógeno.

Finalmente, se ha estudiado el reformado en fase acuosa de sorbitol en un reactor discontinuo a 240 °C y 60 bar, tanto en atmosfera de H_2 como de N_2. En ambas condiciones, los catalizadores bimetálicos de Pt-Co han sido los que presentan mejores resultados. Independientemente de la atmósfera de reacción, todos los catalizadores inicialmente han favorecido la ruta de reacción retro-aldólica. Sin embargo, la conversión de sorbitol ha sido menor bajo presión de N_2. Consecuentemente, la ausencia de una fuente externa de hidrógeno ha limitado las reacciones de deshidratación/hidrogenación.

TABLE OF CONTENTS

TABLE OF CONTENTS

Chapter 1

INTRODUCTION

1.   CONTEXT FOR THE RESEARCH

The current energy model, strongly based on fossil fuels, is not economically nor environmentally sustainable. Regardless of whether these fossil energy resources are finite or if the peak oil has already been exceeded, two compelling reasons have arisen, environmental protection and social progress, make a change towards a more sustainable model based on renewable sources imperative.

Fluctuations in the price of oil directly affect the economies of all countries. Consumer prices, wage determination and business margins are disturbed by changes in the crude oil market [1], these fluctuations condition citizen welfare. The other negative side of oil, as regards the social issue, is the multiple conflicts that have arisen from the control of oil wells [2].
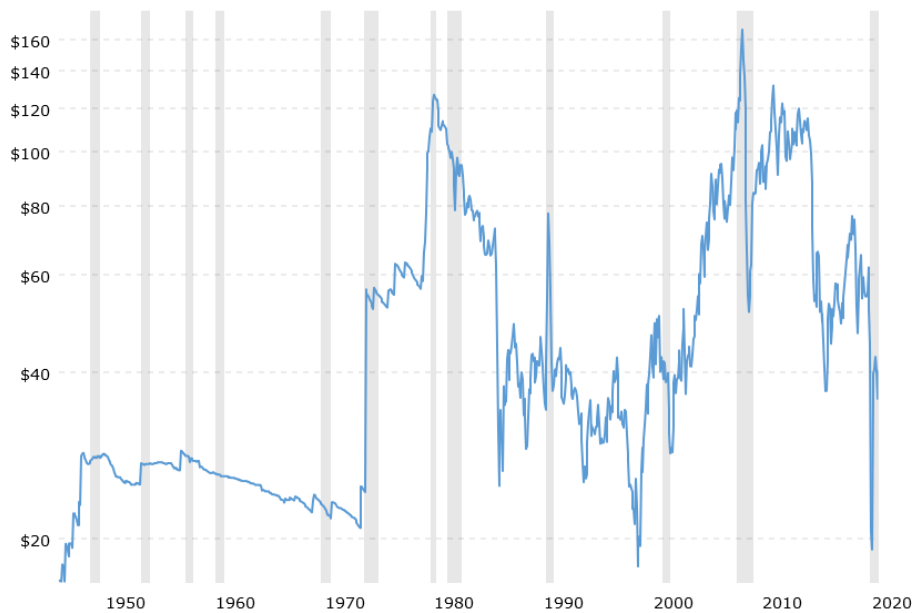
Figure 1.1. Historical chart of crude oil prices (inflation-adjusted, recessions periods shows in grey scale) (source: macrotrends.net [3]).

Fossil fuel consumption accounts for the majority of global anthropogenic greenhouse gas (GHG) emissions. These gases are primarily responsible for the increase in the global average temperature since the mid-20th century. Despite

the multiple options to reduce GHG emissions such as energy conservation and efficiency, nuclear energy and carbon capture and storage (CCS), replacing fossil fuels by renewable energy alternatives not only guarantees the energy access and a secure energy supply but also contributes to social and economic development and other important environmental benefits [4].

Consequently, the development of renewable energy, including biomass, solar, hydropower, wind, ocean, geothermal energy, etc. respects and favours the goals set in the 2030 Agenda for Sustainable Development adopted by the United Nations [5]. In this agenda, in addition to specifying a goal on climate change (goal 13), targets within other goals related to pollution control, reduction and prevention are included. The agenda demonstrates the influence of climate in sustainable development and how all sectors, social, economic and environmental, are interrelated amongst each other [6].

Figure 1.2. Blueprint of the 2030 Agenda for Sustainable Development adopted by all United Nations Member States in 2015.

To cope with the climate crisis, the production chain needs to be diversified, with a quest for new synthesis routes for chemicals and use renewable energy resources to reduce GHG emissions. It is widely agreed that there is no single fuel or energy source that is the panacea, nor a single solution to these problems, for which combined actions are needed. Some of which include changes in

behaviour, changes in vehicle technologies, expansion of public transport and introduction of innovative fuels and technologies [7,8]

1.1 BIOMASS AS ALTERNATIVE TO FOSSIL FUELS

Biomass is organic material that comes from plants and animals, and it is a renewable source. Biomass is, probably, our oldest source of energy after the sun. People have burned wood to heat their homes and cook their food since ancient times [9]. Biomass is a widely distributed, abundant and low-cost renewable organic carbon source [10]. A huge range of products can be derived from biomass using different types of conversion technologies, such as pyrolysis, gasification, torrefaction, anaerobic digestion and hydrothermal processing (Figure 1.3).
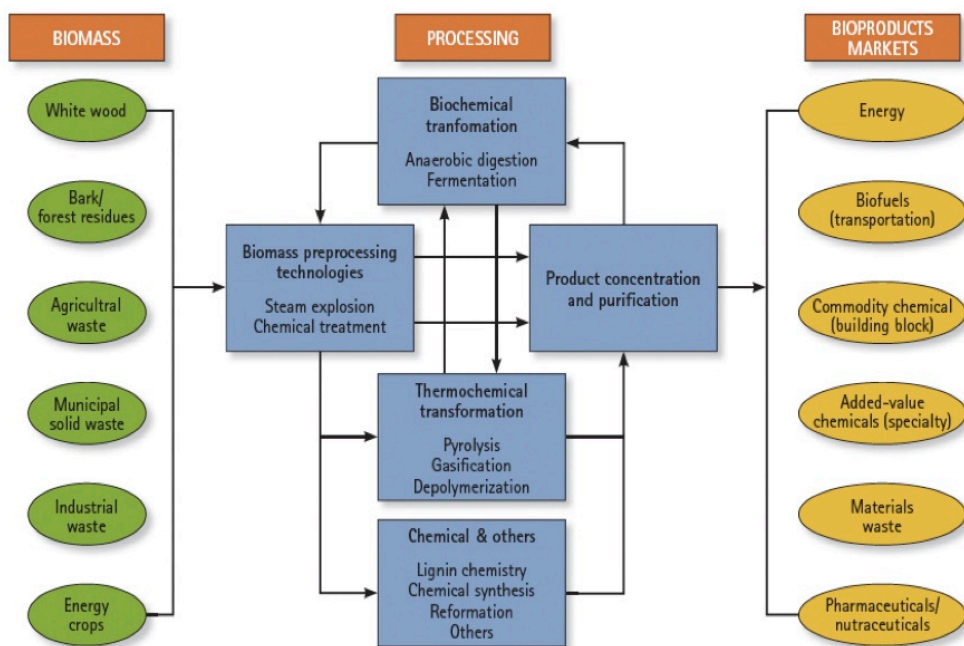
Figure 1.3. Biomass processing diagram (source: USDA National Institute of Food and Agriculture [11]).

A new industry concept has emerged with the growth of biomass as raw material. The International Energy Agency (IEA) Bioenergy Task 42 "Biorefineries" [12] defines Biorefining as a sustainable processing of biomass into a portfolio of marketable bio-based products (food and feed ingredients,

chemicals, materials, fuels, energy, minerals, CO_2) and bioenergy (fuels, power, heat). Biorefinery process technologies include thermochemical, biochemical, mechanical or chemical pathways. The products of biorefinery systems can be grouped into two broad categories: material products and energy products [13].

Within the range of chemicals that can be produced from biomass, we have fine chemicals, building blocks, bulk chemicals, organic acids, polymers and resins, food and animal feed, fertilizers and biomaterials such as wood panels, pulp, paper and cellulose [7]. Energy products, grouped under the label of bioenergy, include power, heat, and biofuels. Biofuel refers to solid, liquid, and gas fuels. Solid fuels are typically used for space heating via combustion, while liquid and gas fuels are mainly used for transportation and industrial processes [14].

Some examples of biomass and their uses for energy [9]:

- × Wood and wood processing wastes: burned to heat buildings, to produce and process heat in industry, and to generate electricity.

- × Agricultural crops and waste materials: burned as a fuel or converted to liquid biofuels.

- × Food, yard, and wood waste in garbage: burned to generate electricity in power plants or converted to biogas in landfills.

- × Animal manure and human sewage: converted to biogas, which can be burned as a fuel.

Bioethanol and biodiesel are major forms of biofuel [15]. Biodiesel is a fuel usually made by transesterification of short chain alcohols with vegetable oils, animal fats, or recycled greases. Biodiesel is most often produced from oil-based crops such as rapeseed, sunflower, and soybean but also from palm oil and edible waste oils [16].

Thanks to its physico-chemical characteristics and being a clean, biodegradable, non-toxic, renewable, sulfur-free and usable in unmodified diesel engines with the existing fuelling infrastructure, biodiesel is presented as an attractive substitute for petroleum-distilled diesel [17].
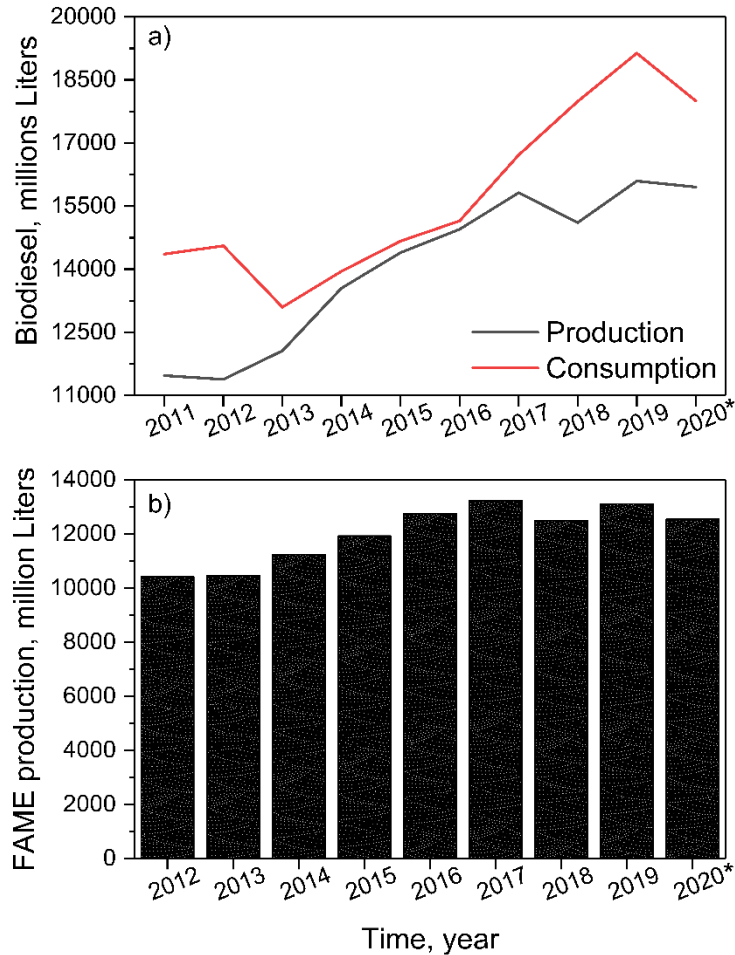
Figure 1.4. Evolution of consumption and/or production in the EU of (a) biodiesel and renewable diesel, and (b) FAME (From the USDA National Institute of Food and Agriculture [18]) *forecast data.

In the last two decades, global biodiesel production has experienced a boom spurred by the various regulations established worldwide to mitigate the climate crisis. The countries of the European Union (EU) were among the first to bet on biofuels, considering them more sustainable than gasoline and diesel. The Directive 2003/30/EC on the promotion of the use of biofuels and other renewable fuels for transport established minimum required volumes of biofuels in all fossil transport fuels and originated the tax incentives that led to the biodiesel upswing [19]. This and other subsequent regulations [20] created a favourable climate that led to biodiesel consumption increasing tenfold between

2003 and 2012. Although the most recent regulations [21-24] have limited the contribution of conventional biofuels due to the impact on deforestation and changes in the use of land when produced from certain raw materials such as palm oil [25], consumption of biodiesel in the EU continues to increase. Currently, 188 biodiesel plants are operational in Europe with a production capacity of over 21,441 million litres. In terms of reported production, in 2019, the EU reached 16,099 million litres. By 2020, despite the impact of COVID-19 pandemic, according to the latest annual biofuels report filed with the USDA Foreign Agricultural Service's Global Agricultural Information Network, the total EU biodiesel and renewable diesel production is forecast to remain relatively stable compared to 2019, at around 15,955 million litres, and the total consumption is expected to reach approximately 18,000 million litres [18].

In the Americas, biofuels have also been committed to reducing GHG and as an economically viable and available alternative. In the case of the United States, the most produced biofuel is bioethanol [26]. However, biodiesel production has been on the rise in recent years [27]. Argentina, Brazil and Colombia are the largest Latin American producers of biodiesel, being even, as in the case of Argentina, one of the main exporters to Europe. [28-29]. Other countries in the region such as Peru and small countries in Central America and the Caribbean, such as El Salvador, Guatemala, Dominican Republic and Jamaica, are currently developing infrastructures and regulations for the production and consumption of biodiesel and other biofuels [30].
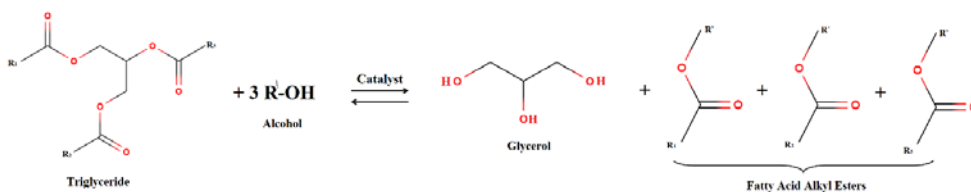
Scheme 1.1. Transesterification of a triglyceride with alcohol.

Returning to its production method, in the most used process, one mole of vegetable oil (triglycerides) reacts with three moles of alcohol in the presence of a base or acid catalyst and undergoes three sequential reactions to yield one mole of glycerol and three moles of biodiesel (fatty acid alkyl esters). Therefore,

about 10 wt.% of the total product is glycerol, which has led to a surplus of glycerol in the world market. [31].

Bioglycerol (glycerol from biodiesel process) contains many impurities and other chemicals, for instance, alcohols, organic and inorganic salts, water, vegetable colours, mono- and diglyceride traces and soap. The high cost of refining bioglycerol makes its use unfeasible in industries where high levels of purity are required, such as pharmaceutical or personal care [31,32].

Considering the high viscosity of this bioglycerol, its direct burning is not a practical alternative. In addition, its high ignition temperature reduces combustion efficiency, resulting in the formation of toxic compounds such as acrolein, and its high concentration of residual salts can clog the entire system [33]. Fortunately, bioglycerol can be transformed using biorefinery processes into important commodity chemicals, fuel additives, methanol generation and hydrogen production [34]. As glycerol can serve as a substrate for the production of various other higher value-added products in biorefineries, it has been included as one of the 12 platform molecules by the Department of Energy (DOE) [35].

1.2   GLYCEROL
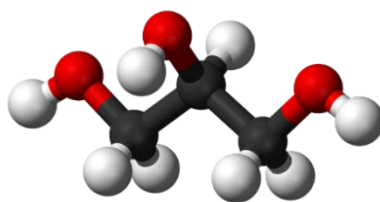
Figure 1.5. 3D structure of the glycerol molecule.

Glycerol, also called glycerin or glycerine[1], is a highly functionalized and simple polyol compound. Glycerol is a triol with a structure of propane substituted at positions 1, 2 and 3 by hydroxyl groups, which are responsible for its miscibility

---

[1] Regardless of the slight difference between these terms, "glycerol" is used in this text without distinction.

in water and hygroscopic nature. It is a colourless, odourless, viscous liquid that is sweet-tasting and non-toxic [36].

Table 1.1. Selected glycerol properties.

Properties	Values
Molecular formula	$C_3H_5(OH)_3$
Molecular weight, g	92
Melting point, °C	17.8
Boiling point, °C	290
Viscosity, Pa·s^{-1}	1.5
Vapour pressure at 20 °C, mmHg	<1
Density at 20 °C, g·cm^{-3}	1.261
Flash point, °C	160 (closed cup)
Residue on ignition, wt%	<0.01
Heat of fusion at 18.07 °C, cal·g^{-1}	47.49
Auto-ignition temperature, °C	400
Critical temperature, °C	492.2
Critical pressure, atm	42.5
Surface tension, N·m^{-1}	64,000
Specific heat, cal·g^{-1}·°C^{-1}	0.579
Heat of combustion, kcal·mol^{-1}	397

Currently, more than 1,500 uses of glycerol are known, including many applications in the cosmetic, paint, automotive, food, tobacco, pharmaceutical, pulp and paper, leather and textile industries. The glycerol backbone is found in those lipids known as glycerides. Due to its antimicrobial and antiviral properties it is widely used in wound and burn treatments. It is also widely used as a sweetener in the food industry and as a humectant in pharmaceutical formulations. Glycerol is also used as a solvent, sweetener and preservative in the food and beverages industry. In personal care products it works as an emollient, humectant, solvent and lubricant in a wide variety of products [37].

All these traditional glycerol applications are well regulated and a high level of purity is required for use as a raw material in these processes.

As aforementioned, glycerol availability has increased due to the boom in biodiesel production, but the cost of refining makes its use in traditional applications unfeasible. That is the reason why new valorisation routes have been researched and developed, mainly, in the last two decades.

1.3   VALORISATION ROUTES FOR GLYCEROL

The valorisation of glycerol meets the objective of reducing glycerol surplus in the market and, at the same time, reducing the price of biodiesel production through the generation of basic chemical products, fuels and fuel additives through clean and sustainable routes. The valorisation of glycerol became into an opportunity to promote the concept of circular economy.

There are several biological, chemical and catalytic processes to which glycerol can be subjected. Glycerol can be used as the carbon source for a growth medium, and be fermented to produce alcohol, hydrogen, and other products via bacteria and/or yeast [38-40]. Waste glycerol also can produce biogas via decomposition along with sewage sludge or other biomass by a microbial community [41]. Some research has also focused on the use of glycerol as a carbon source for the removal of nitrate and phosphorus in wastewater treatment [42,43]. Glycerol has also been investigated as a raw material to obtain glycerol carbonate and glycidol via carboxylation [44] or transesterification [45]. Valuable building blocks and fuel additives can also be synthesized by glycerol acetalization/ketalization [46,47], through the acetylation with acetic acid [48] and via etherification, oligomerisation or polymerization, for example, to obtain ether derivatives, glycerol esters and polyglycerols after subsequent esterification [49-52].
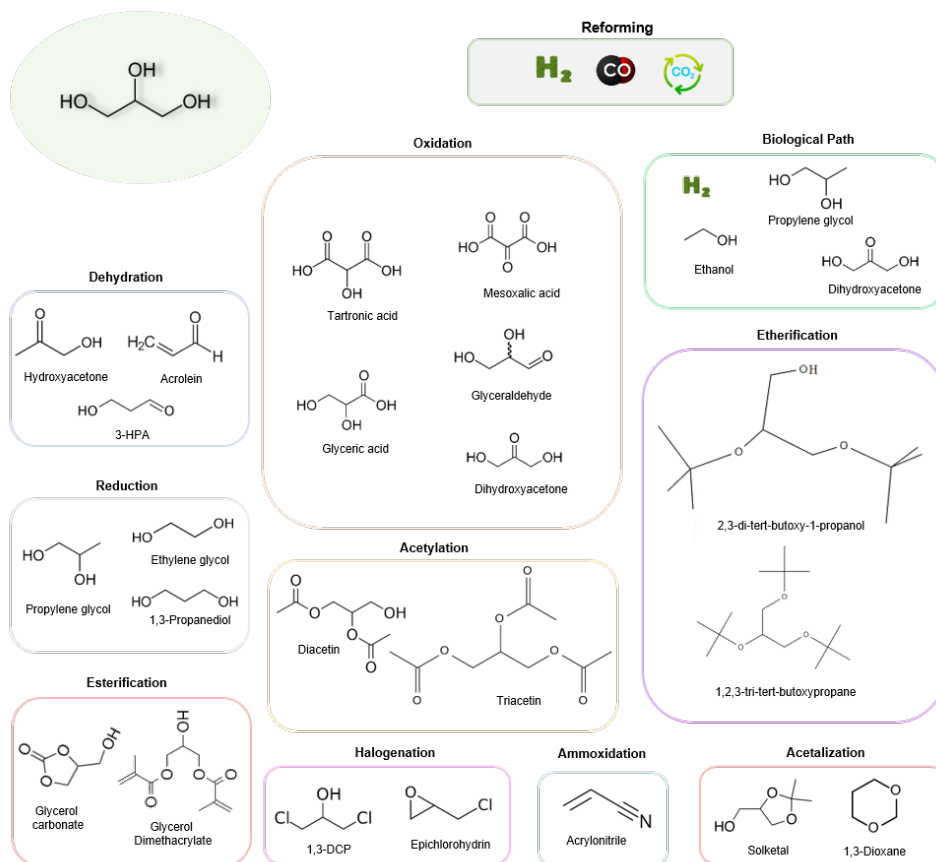
Scheme 1.2. Roadmap of glycerol valorisation (source: Len & Luque (2014) [53]).

The development of new catalysts and processing methods for the catalytic conversion of glycerol, focused on the production of chemicals and renewable energy, continues to increase. Recent advances have been made in processes as varied as oxidation to obtain valuable oxygenates [54], dehydration to obtain acrolein [55], ammoxidation for the direct production of acrylonitrile [54] and chlorination (halogenation) to synthesize epoxy resins [56]. In addition, catalytic reduction of glycerol can generate important chemicals such as 1,2-ethanediol, 1,2-propanediol, 1,3-propanediol, lactic acid, hydroxyacetone, propanol, or 2-propenal (acrolein) [54,57]. Bioglycerol is also used as an additive in the gasification of biomass to improve hydrogen yield [58,59]. Other widely used thermochemical processes are pyrolysis and liquefaction, both focused on the

production of bio-oil [60-62]. Other interesting routes for energy solutions from glycerol are the different reforming processes: steam reforming (SR) [63-66], aqueous-phase reforming (APR) [67-69], supercritical water reforming (SCW) [70,71], and autothermal reforming (ATR) [72,73].

Some of above mentioned processes have proven technologically and economically viable to be scaled to the industry. Such is the case of epichlorohydrin (ECH) manufacturing, an organochlorine compound previously used for glycerol production and that can currently be produced from glycerol. In 2007, Solvay company opened a 10,000 t/year ECH plant from rapeseed oil biodiesel glycerol supplied from Diester Industries in Tavaux, France. This project has provided satisfactory results and in 2012, the company started the largest biobased ECH in the world in Ma Ta Phut, Thailand [74].

The construction industry increasingly employs raw glycerol by-product of biodiesel as a performance enhancer of cement, since this bioglycerol upgrades the strength of hardened concrete and eases the clinker grinding process [75]. Another field of great advances in the use of glycerol in industrial processes is the production of esters, ethers, polyglycerols, polyesters and epoxy resins [76]. This proves that glycerol has a promising future in the chemical industry. Nevertheless, more research should be focused on new processes and catalysts to make biorefinery a leading industry for our environmental and economic benefit.

Among all these interesting processes for glycerol valorisation, we briefly develop in more detail, due to the affinity with our target process, the following routes:

1.3.1   Selective Oxidation

Oxygenated derivatives from glycerol are products of valuable commercial interest due to their use as intermediaries towards fine chemicals and new polymer products [77]. Platinum, palladium and gold catalysts have proven effective for glycerol oxidation to glyceric acid [78,79]. This compound is formed through the oxidation of the primary hydroxyl group initially obtaining glyceraldehyde, which due to its great reactivity, quickly becomes glyceric acid. Prolonging the oxidation, glyceric acid is further oxidized to tartronic acid that

is a high value-added chemical that is widely used as a pharmaceutical and anti-corrosive agent. Another possible route is the oxidation of the secondary hydroxyl group to form dihydroxyacetone that can subsequently generate hydroxypyruvic acid and mesoxalic acid [80].

In summary, the main products that can be obtained from glycerol oxidation are dihydroxyacetone, glyceric acid, glycolic acid, glyceraldehyde, hydroxypyruvic acid, mesoxalic acid and tartronic acid, all of which are chemicals of high value.

1.3.2   Dehydration

Acrolein, hydroxyacetone (acetol) or 3-hydroxypropionaldehyde (3-HPA) can be obtained through glycerol dehydration depending on the catalyst used and the process conditions. Dehydration to acrolein is carried out at high temperature and under acidic conditions, generally using zeolites and aluminas as catalysts [81]. Acrolein is produced via the dehydration of 3-hydroxypropanal that had, previously, been formed through dehydration of the secondary hydroxyl group present in glycerol. Acrolein is an important industrial intermediate that can be oxidized to acrylic acid and further polymerized to give acrylic resin [55].

Hydroxyacetone is also an organic intermediate widely use in the industry for the production of 1,2 and 1,3-propanediol, propionaldehyde, acetone and furan derivatives. It is, likewise, use in textile industry and in food industry as an aromatic [82]. Hydroxyacetone is formed via dehydration of the primary hydroxyl. To obtain hydroxyacetone, the transition metal catalysts have been the most used, obtaining the best results with copper-based catalysts and with copper-chromium alloy [83,84].

1.3.3   Hydrodeoxygenation

Hydrodeoxygenation (HDO) is an effective alternative in transforming biomass-derived feedstock into liquid fuels. HDO reaction removes oxygen atoms from oxygenated hydrocarbons in the presence of hydrogen.

The aqueous-phase hydrodeoxygenation process is typically carried out at moderate temperature (180-250 °C), high pressure (20-60 bar) and required an

external H_2 supply or source. However, the latest research has used hydrogen generated *in situ* by aqueous-phase reforming to promote glycerol hydrodeoxygenation [85,86]. The main product obtained via glycerol HDO is 1,2-propanediol, commonly named propylene glycol. Propylene glycol is a value-added chemical with a wide range of applications in pharmaceuticals, food, cosmetics, paints, tobacco industry, as an anti-freeze agent and as a monomer for polyester resins.

In literature, three proposed mechanisms can be found depending on the type of catalyst used and the operating conditions. The first one, dehydrogenation-dehydration-hydrogenation [87] takes place under alkaline conditions and leads to the formation of glyceraldehyde that can either undergo dehydration or retro-aldol reactions followed by hydrogenation for obtaining the target product. The route via dehydration-hydrogenation reactions, the most commonly accepted, proposes the formation of hydroxyacetone after glycerol dehydration by the acidic sites of the catalyst. Hydroxyacetone is subsequently hydrogenated to form propylene glycol promoted by the metal [86,88]. Other proposed mechanism suggests a direct glycerol hydrogenolysis with the formation of 2,3-dihydroxypropoxide and 1,3-dihydroxyisopropoxide in the surface of the metal and then, obtaining 1,3-propanediol or propylene glycol depending on whether the hydride attack is in 2- or 3-position [89]. It should be noted that this last mechanism has occurred especially in rhodium-rhenium and iridium-rhenium catalysts in the presence of H_2 [90,91]. Therefore, the widespread use of the term hydrogenolysis for all dehydration-hydrogenation processes is not entirely correct [92].

1.3.4   Reforming

The main objective of the reforming process is to obtain synthesis gas (syngas), consisting mainly of CO and H_2, and used in the synthesis of ammonia, methanol, hydroformylations, in the Fischer-Tropsch synthesis to produce hydrocarbons and to generate electric power via fuel cells [93]. When the objective is to produce energy using the Proton Exchange Membrane fuel cell (PEMFC), a later stage is required to reduce the concentration of CO due to the sensitivity of the platinum catalyst of the anode to CO poisoning.

As we have already mentioned, there are several types of reforming processes depending on the operating conditions and the co-feeding used. In some of them, glycerol reforming produces mainly H_2, CO_2 and traces of CO.

Steam reforming (SR) is a process widely used in the petrochemistry industry for the production of H_2. Glycerol steam reforming is a bio-alternative route for syngas production. This process involves the rupture of the hydrocarbon in the presence of water vapour and the Water-Gas Shift reaction (WGS). SR is an endothermic process (for glycerol SR: ΔH^0 = 411 kJ·mol^{-1}), which is usually carried out at high temperatures (400-850 °C) and ambient pressure. Therefore, this process requires a considerable heat input to vaporize the reagents, which increases operating costs and a high initial investment for the construction of reactors and appliances [65]. Moreover, many side reactions such as methanation and carbon formation may occur [94].

Catalytic partial oxidation (POx) consists of reacting organic feedstock with sub-stoichiometric oxygen. It is an exothermic process, therefore, it requires less energy consumption and shorter residence time in relation to the SR, which has an impact on the size and price of the reactor used [95]. When water vapour is co-fed into the partial oxidation process, the result can be heat-balanced reaction because the water vapour absorbs part of the heat generated by the oxidation reaction. This type of reforming, named autothermal reforming (ATR), does not require an additional/external heat supply and catalyst deactivation by sintering or carbon deposition is minimized [73]. However, both ATR and POx have lower H_2 yield than SR.

Another interesting reforming which has attracted great attention recently is glycerol dry reforming (DR). This process utilises CO_2, a greenhouse gas, as a feedstock together with glycerol to produce syngas. The thermodynamics of DR is similar to SR, and thus, it is also performed at high temperatures and ambient pressure. Its main drawback is its tendency for coking, aggravated by the lack of steam to remove carbon [96].

Reforming in supercritical water (SCW) of glycerol is a reforming carried out at conditions above the critical water temperature (374 °C) and pressure (221 bar). Under these conditions, water has hybrid properties between liquid and steam,

which favours the reforming process due to its high diffusivity, low viscosity, greater miscibility of organic compounds and greater oxidizing power [70]. Usually, the operating temperature is between 600-650 °C and around 300 bar of pressure. A short residence time (9-165 s) to achieve a complete conversion of glycerol and the ease of separating the gases obtained from the water phase by cooling to ambient temperature are the main advantages of this process. On the other hand, among the disadvantages are low selectivity at temperatures below 600 °C, high initial investment and operational costs and safety problems associated with the process [97].

In order to avoid feedstock vaporization and degradation and therefore, reduce the energy demand, Aqueous-Phase Reforming (APR) process was developed at the University of Wisconsin-Madison by Dumesic et al. [98]. This process allows obtaining hydrogen from oxygenated compounds that can be found in wastewater biomass-derived processing. APR reaction is performed under moderate temperatures (180-280 °C) and pressures (20-50 bar), remaining the feedstock in liquid state. Another of its main advantages is to obtain H_2 with low CO concentration in the outflow because the operating conditions are favourable for the WGS reaction [94].

1.4   HYDROGEN AS AN ENERGY CARRIER

Hydrogen is the simplest, lightest, and most abundant element in the universe. It is a flammable, colourless, odourless, non-metallic gas that is insoluble in water. Hydrogen is naturally found in the earth in a compound form with other elements. Thus, more commonly, it can be found bound to oxygen in the form of water or combined with carbon in different hydrocarbons found in natural gas, coal, petroleum, alcohols and biomass. Therefore, hydrogen must be obtained through a primary energy source making it an energy storage medium.

This energy vector has a very high specific energy content, is non-polluting and greenhouse gasses emission free, since its combustion generates mostly water as its only by-product [99]. Its peculiar physical-chemical characteristics (Table 1.2) make it an environmentally safe gas due to its low toxicity and being more diffusive than air and gasoline, it presents less danger of explosion and fire.

However, due to its low density, its handling, storage, transport and distribution represent a big challenge.

Table 1.2. Physical properties of hydrogen (source: IEA [100]).

Property	Hydrogen	Comparison
Density (gaseous)	0.089 kg·m^{-3} (0 °C, 1 bar)	1/10 of natural gas
Density (liquid)	70.79 kg·m^{-3} (-253 °C, 1 bar)	1/6 of natural gas
Boiling point	-252.76 °C (1 bar)	90 °C below LNG
Energy per unit of mass (LHV)	120.1 MJ·kg^{-1}	3x that of gasoline
Energy density (ambient cond., LHV)	0.01 MJ·L^{-1}	1/3 of natural gas
Specific energy (liquefied, LHV)	8.5 MJ·L^{-1}	1/3 of LNG
Flame velocity	346 cm·s^{-1}	8x methane
Ignition range	4-77% in air by volume	6x wider than methane
Autoignition temperature	585 °C	220 °C for gasoline
Ignition energy	0.02 MJ	1/10 of methane

LNG: Liquefied Natural Gas; LHV: lower heating value.

Hydrogen economy is a concept that was first proposed by J. B. S. Haldane in 1923, that was resumed and coined by Prof. John Bockris in 1970 [101]. Hydrogen economy is an economic model integrated in the low-carbon economy. This model is based on the use of hydrogen as a commercial fuel that would provide a substantial fraction of the energy in the world, especially within the transportation sector. For this vision to become a reality, hydrogen must be produced from domestic energy sources in an economical and ecological way [102]. This model proposes the creation of a decentralized energy network through many small generation sources, installed near the consumer.
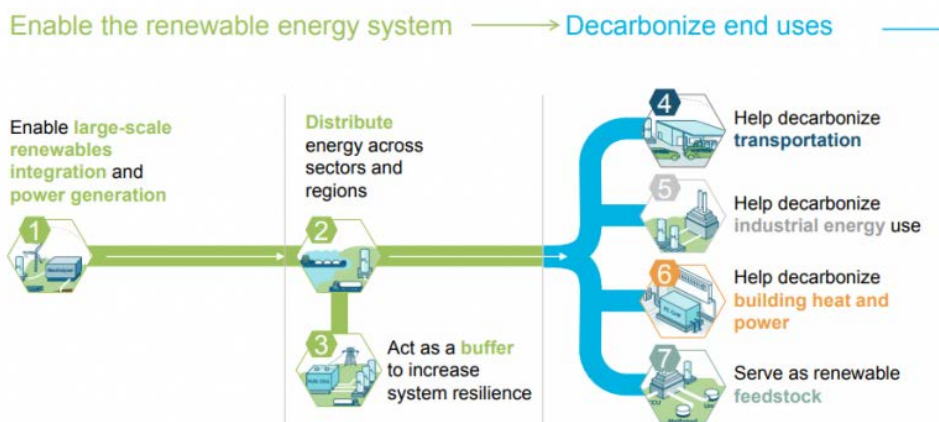
Figure 1.6. Roles of hydrogen in the energy transition (from Hydrogen council).

According to the Hydrogen Council, hydrogen could meet 18% of the global energy demand, create 30 million jobs and generate $2.5 trillion in sales, all while helping to abate 6 Gt of CO_2 annually. These benefits will help us achieve the 2 °C scenario by mid-century [103]. Countries like Australia, Canada, China, France, Germany, Japan, Norway, South Korea, the United Kingdom and the United States are moving toward a green hydrogen economy with far-reaching projects in the use of H_2.

The current use of hydrogen is concentrated in the petrochemical industry to remove impurities from crude oil and upgrade heavier crude and in the production of ammonia and methanol (Figure 1.7). Hydrogen is also used in food processing, metal refining, electronics manufacturing and in several other smaller-scale chemical processes [104,105]. From an energy-environmental point of view, the most important use of hydrogen is in internal combustion engines, for example as a hythane, and in fuel cells [106]. Fuel cells create electricity via an electrochemical process combining hydrogen and oxygen. Unlike batteries, in the fuel cell the reagents are supplied as a continuous flow from the outside, which allows uninterrupted power generation [107]. These devices have high efficiency thanks to their direct generation of electrical energy, produce clean energy, can be manufactured in different sizes and for different applications, are noiseless and have low maintenance cost [102]. Despite the advantages of fuel cells, these technologies should be further developed so that fuel cells and fuel cell vehicles are economically attractive.
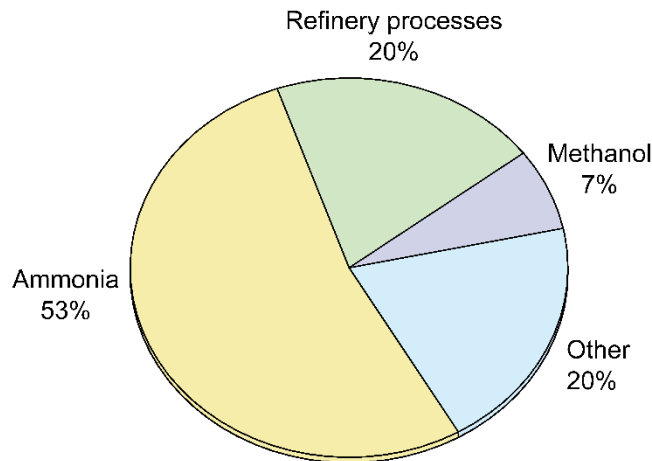
Figure 1.7. Uses of hydrogen.

It is especially important to keep in mind that the use of hydrogen as an energy vector can help decarbonisation of the biosphere, provided it is obtained from renewable sources or nuclear energy input. Nonetheless, currently the most developed and industrially consolidated processes are based on fossil fuels. Currently, about 275 Mtoe of energy is consumed in hydrogen production and around 830 Mt of CO_2 is generated per year due to the use of natural gas and coal as raw material [100].

Currently, most hydrogen produced is via methane steam reforming (SMR) and coal gasification (Figure 1.8). SMR is a mature and widely used technology where natural gas is used as a primary source. Other raw materials are also used, to a lesser extent, to obtain hydrogen by reforming as liquefied petroleum gas and naphtha. On the other hand, coal gasification is extensively used for hydrogen production mainly in China, which has large reserves of this combustible. Both processes, SMR and coal gasification, need to employ carbon capture and storage (CCS) technologies, increasing the process cost [108].
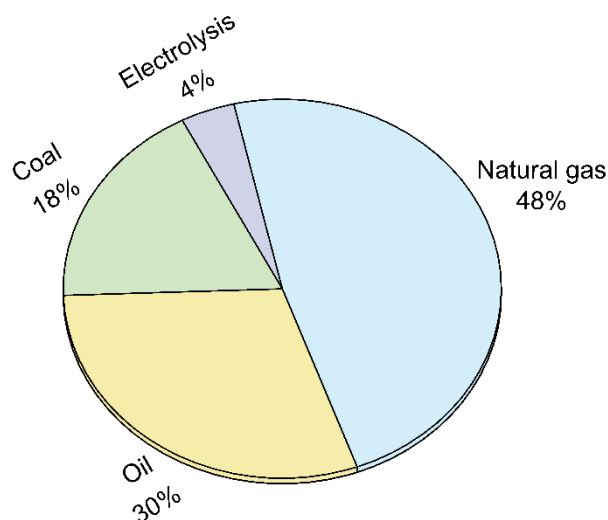
Figure 1.8. Current hydrogen production sources.

Electrolysis is the process of using electricity to split water into hydrogen and oxygen. It is the simplest of all the water-splitting techniques and depending on the source of electricity may result in zero GHG emissions. The production of hydrogen by water electrolysis is limited to markets where high purity hydrogen is required and as a by-product in the production of chlorine and caustic soda. The electrolytic reaction takes place in a unit called electrolyser and, usually, in an alkaline medium as this increases electrical conductivity [109]. Other water-splitting processes, which must be developed technologically, are thermolysis or thermochemical water splitting and photocatalytic water splitting. Thermolysis consists of the decomposition of water at very high temperatures (1000-2000 °C) [110], while photocatalytic water splitting is an artificial photosynthesis process using either artificial or natural light, in a photoelectrochemical cell, for the dissociation of water promoted by catalyst [111]. The provision of heat to carry out these processes can be supplied by wind, geothermal, nuclear or solar energy.

Biological processes are an interesting pathway for long-term hydrogen production. The main biological processes to obtain hydrogen are direct and indirect biophotolysis [112], photo and dark fermentations, and multi-stage or sequential dark and photofermentation [113]. Biophotolysis is the

decomposition of water into hydrogen and oxygen through the combined action of sunlight and the photosynthetic capacity of green plants, certain microalgae, cyanobacteria and bacteria. Fermentative processes can convert carbohydrate containing materials, obtained from biomass or waste stream, into organic compounds and then to hydrogen gas by using bioprocessing technologies [111,114]. In spite of the intense laboratory-scale research that has been carried out in recent years, the energy efficiency of these biochemical processes is notably low (less than 10%). This fact, together with the low H_2 yield and rate of production, are the main drawbacks of these processes to scale-up to the industry [115].
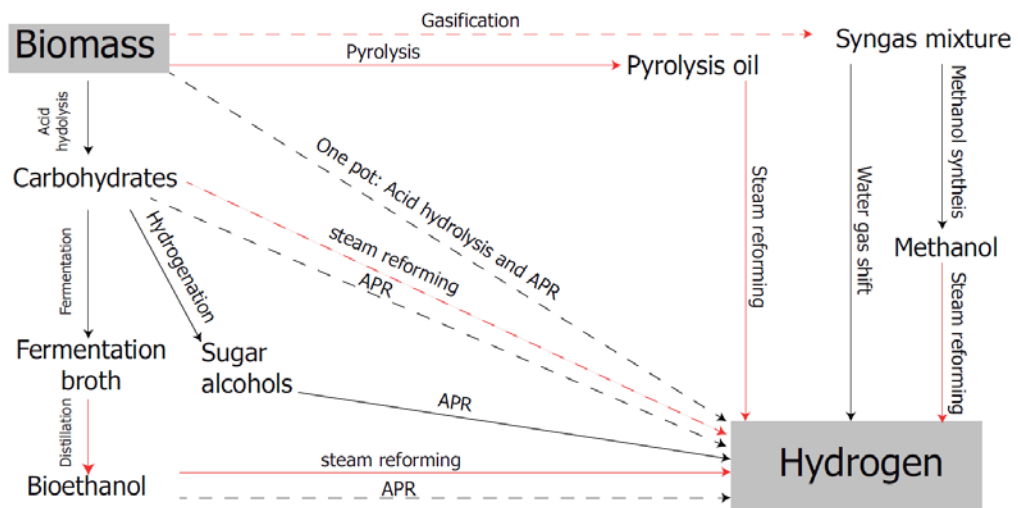
Scheme 1.3. Summary of routes for hydrogen production from biomass (adapted from d'Angelo (2014) [116]). The type and colour of lines indicate the selectivity and the energy requirements of the process, respectively: Dashed lines, low selectivity; Solid lines, high selectivity; Red line, high-energy consumption; and black line, low energy consumption.

In addition to the biological process, hydrogen can be produced from biomass through a number of methods (Scheme 1.3). Most of them have been discussed previously in this chapter, concluding that the high-energy requirement and, consequently, the high operating and maintenance costs are the bottlenecks of these technologies. However, among all these processes, APR attracts great interest as it allows obtaining high selectivity and low energy requirement. This thesis focuses on this process, which is further discussed in the following section.

1.5   AQUEOUS-PHASE REFORMING (APR)

Aqueous-phase reforming (APR) process is an innovative process developed at the University of Wisconsin-Madison in 2002 [98]. The main advantage of this process lies in the possibility of reforming the biomass derived liquid without vaporization, thus reducing energy requirements. The APR of the oxygenated hydrocarbons compounds proceeds through a complex reaction network, in a single-pass reactor, resulting in a mixture of H_2 and CO_2 and in other high value-added chemicals depending on the catalyst used. Suitable starting materials for APR include sugars, polyols, wood and paper waste [117,118], Fisher-Tropsch residuals [119], and wastewater from various industrial processes such as the food [120,121] and brewery industries [122].
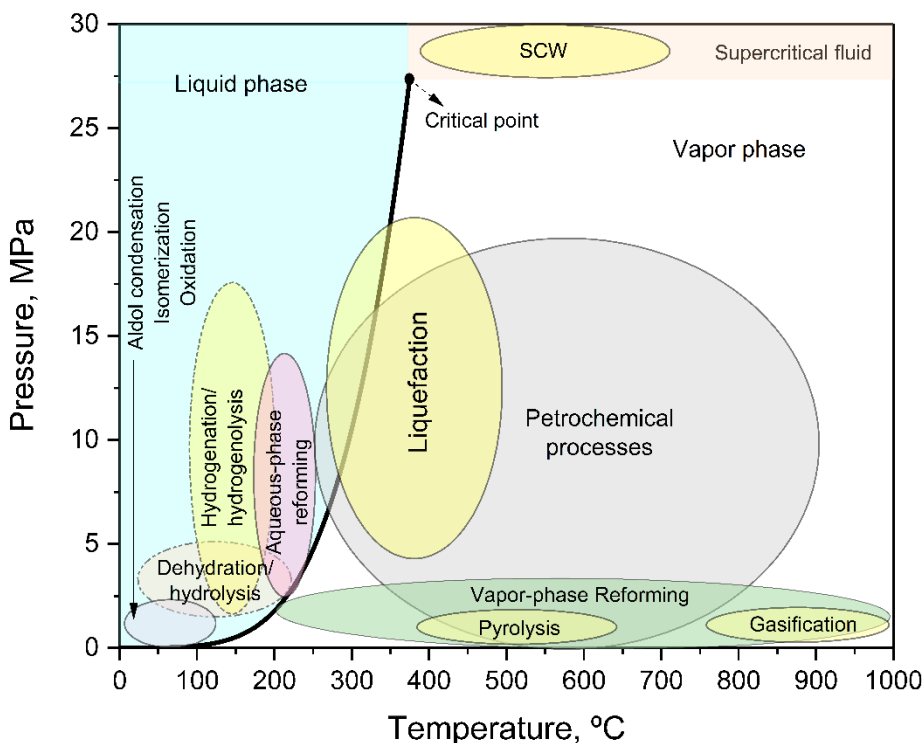
Figure 1.9. Phase diagram for water indicating the temperature and pressure regimes for reactions of interest in the conversion of biomass-derived molecules (adapted from Chheda et al. (2007) [123]).

Compared to other reforming methods (Figure 1.9), APR is performed at moderate pressures where the CO_2 can be separated for subsequent use and the H_2 stream can be purified using membrane technologies or other separation techniques. In addition, undesired decomposition reactions of the substrates are minimized at the temperature conditions that the APR proceeds. Both, temperature and pressure favour the equilibrium of WGS reaction, which modulates H_2/CO ratio obtained in the reforming [124].
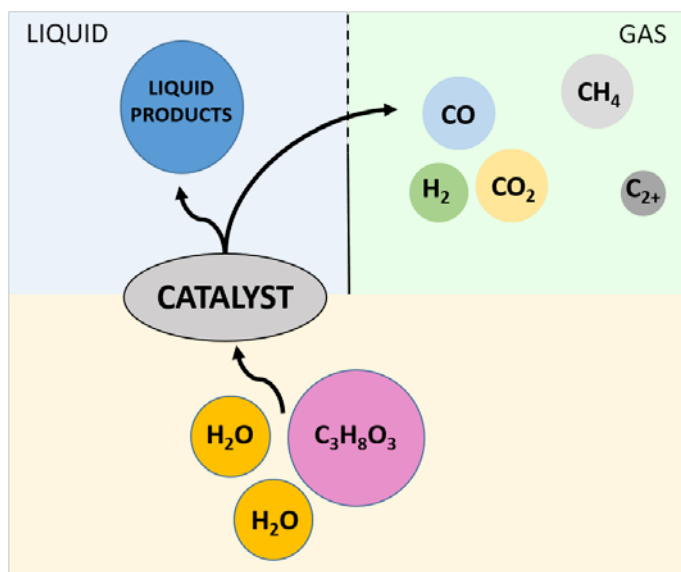
Scheme 1.4. Schematic representation of the APR reaction.

APR constitutes a three-phase system where liquid reactants are converted to gaseous products on the surface of a solid catalyst (Scheme 1.4). Ideally, dehydrogenation of the substrate occurs on the metal to give H_2 and adsorbed organic species on metal site. This results in C-C bond cleavage and formation of CH-OH group adsorbed on metal, undergoing dehydrogenation to CO and H_2. Then, CO reacts through the WGS reaction to give CO_2 and H_2 [125]. This process involves the following two main reactions:

C–C cleavage leading to CO and H_2,

$$C_nH_xO_y(l) \rightarrow (2n-y)CO + \frac{x}{2}H_2 \qquad\qquad \Delta H^0 > 0 \qquad (1.1)$$

Water-Gas Shift (WGS) reaction,

$$CO + H_2O(l) \leftrightarrow CO_2 + H_2 \qquad\qquad \Delta H^0 = +3.38 \text{ kJ·mol}^{-1} \qquad (1.2)$$

The resulting overall APR reaction,

$$C_nH_xO_y(l) + (2n-y)H_2O(l) \rightarrow nCO_2 + (2n + \frac{x}{2} - y)H_2 \quad \Delta H^0 > 0 \quad (1.3)$$
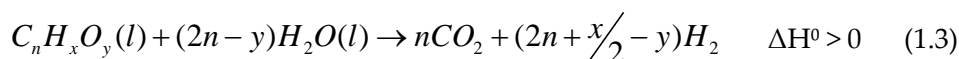
As can be seen, WGS reaction plays a key role in hydrogen production from APR. WGS in the liquid phase is a slightly endothermic reaction that, therefore, is thermodynamically favoured at high temperatures [126]. WGS reaction in the gas phase has been extensively studied [127], but there are few studies in the liquid phase.

Side reaction also can occur, such as methane production by reacting H_2 with CO or CO_2. Both reactions are thermodynamically favoured at low temperatures. Moreover, the formation of other alkanes can take place via the Fischer-Tropsch reaction. Apart from these reactions, in the process of obtaining hydrogen, the substrate can undergo dehydration, hydrogenation/dehydrogenation thus, obtaining liquid products [128].

Hence, efficient catalysts for the APR must present high catalytic activity for C-C and C-H scission and promote WGS reaction, while inhibit C-O bond cleavage, Fisher-Tropsch and methanation reactions [124].

1.6   LITERATURE REVIEW ON APR CATALYSTS

APR involves C-C, C-H and O-H bonds cleavage. These bonds are easily cleaved on the surface of several catalysts, mainly based on metals with hydrogenating activity. Typically, the most used catalysts in this process are transition metals

such as Ni, Pd, Pt, Ru, Rh, Ir and Co. Well-dispersed nanoparticles of these metals usually are deposited on high surface area solid supports such as alumina, silica or activated carbon [129]. In the APR reaction, the catalyst support influences the reaction pathways depending on its acid-base properties. Basic/neutral supports favour the H_2 production and low selectivity toward alkanes. In addition, as is well known, a suitable support improves the metal dispersion of a supported catalyst and increases the utilization rate of the active sites enhancing activity and stability. The interfacial sites have special properties, which provides evidence of synergy between the active metal and the support [130].

Among active metals for APR, platinum has been one of the most scrutinized metals. Shabaker et al. [131] have studied the Pt catalyst on different supports for the 10 wt.% ethylene glycol APR. These authors observed that Pt/Al_2O_3 and Pt/ZrO_2 were more selective for H_2, while Pt/C, Pt/TiO_2, Pt $/SiO_2$-Al_2O_3 and Pt-black were active in the production of alkanes and other liquid by-products. The effects of different metal particle sizes and support material have been studied by Lehnert and Claus [132], concluding that these catalytic properties strongly influence the catalytic activity. The surface acidity of the support has also been correlated with the low activity of supported catalysts, with the low selectivity towards hydrogen, and with the catalyst deactivation [124]. Continuing with the noble metals, Luo et al. [133] have studied different operating conditions and the effect of metal loading on the Pt/Al_2O_3 catalyst. Iridium supported on different metal oxides has also been investigated as a catalyst in the APR of different biomass-derived compounds [134,135]. Other noble metals that have been studied for the APR process are rhodium and rhenium [136,137].

Due to the high cost associated with the use of noble metals, numerous studies have been performed to seek more cost-effective metals with adequate catalytic characteristics for the APR process. Several investigations have focused on nickel as an alternative to noble metal catalysts, obtaining high conversions of the reagent [138] although the yield and the selectivity towards hydrogen must be improved [139,140]. However, cobalt has been poorly researched metal as monometallic catalysts in this process [141]. As Cu is deficient in actively catalysing C-C scission and the intrinsic ability to catalyse C-O scission, its use

as the only active metal for the APR application has been discarded [142] although it works as a promoter.

The incorporation of other active metals as promoters offers the potential of increased activity and selectivity combined with enhanced stability compared to their monometallic counterparts. Several families of bimetallic catalysts have been studied for the production of hydrogen through APR [143]. Iriondo et al. [64] have studied the addition of Ce, La Mg and Zr to Ni/Al$_2$O$_3$ for the APR of glycerol and have observed an increase of the initial glycerol conversions obtained over the bare Ni/Al$_2$O$_3$, except for Mg. This same group of authors [144] have studied the synergy Pt-Ni alloy in the glycerol APR. Coronado et al. [145] have studied the promoting effect of ceria and copper on nickel-based catalysts. The effect of the Cu loading in the Ni-Cu catalysts derived from hydrotalcite-like compounds on the catalytic activity for glycerol reforming reaction was studied and a decrease in methane formation was observed when incorporating copper [128]. Dumesic group has also studied various combinations of metals, such as the addition of Sn to Raney-Ni catalysts [146], as well as the synergy between noble and base metals like Pt-Ni, Pt-Co, Pt-Fe and Pd-Fe [147].

Regarding catalyst deactivation, El Doukkali et al. [148] have studied the deactivation phenomena in catalysts supported on alumina. These researchers showed that γ-alumina under APR hydrothermal conditions is transformed into boehmite, leading to catalyst deactivation. Other possible causes of deactivation that have been detected are due to metal oxidation and coking [149]. Coke tends to occur due to the formation of unsaturated hydrocarbons and other strongly adsorbed intermediates. On the other hand, after oxidation the metal can be leached more easily. Van Haasterecht et al. [150] correlated the stability of the catalyst with the reaction conditions evidencing a loss of metallic surface area due to leaching of the nickel because of the acidic APR conditions.

1.6.1   Cobalt-based catalysts

Cobalt (Co) is a chemical element of atomic number 27 that belongs to the group of transition metals in the periodic table of the elements. Cobalt was initially coveted for its colour. Cobalt is mostly mined as a by-product of either copper or nickel. Democratic Republic of the Congo accounts for more than 60% of the

global cobalt production, but is also extracted in mines located in Russia, Cuba, Australia, The Philippines, Canada, Madagascar, Papua New Guinea, China and Morocco [151]. Accusations of child exploitation in cobalt mining of African artisanal mines has caused unease [152]. Nevertheless, the problem is not exclusive to mining and cobalt extraction [153]. Therefore, instead of punishing the element, mining policies should be reformulated, and legislation to eradicate child labour in this and in all countries of the world must be adopted.

Cobalt has low oxidation states. The most frequent oxidation states are Co^{2+} and Co^{3+}, although there are also important complexes where oxidation state is Co^{1+}. Less commonly, it is found in compounds with oxidation status of Co^{4+} or Co^{5+}. The metallic cobalt (Co^0) is usually constituted by a mixture of two allotropic forms with hexagonal close packed (*hcp*) and face centred cubic (*fcc*) crystalline structures.

Cobalt is a ferromagnetic metal used in lithium-ion batteries, and in the manufacture of magnetic, wear-resistant and high-strength alloys. Cobalt, cobalt isotopes and cobalt-based alloys have several biomedical applications. ^{60}CO is used in radiotherapy and sterilization of medical equipment, ^{57}Co calculates the amount of vitamin B12 present in the body and sundry of its alloy have orthopaedic applications [154]. In addition, Cobalt is used as a catalyst in many processes and applications, such as the Fischer-Tropsch synthesis process [155,156], air purification and control of gaseous emissions. Cobalt-based catalysts are used to remove sulphur moieties from natural gas and refined petroleum products [157], to synthesis polyester precursors, in the production of aldehydes from alkenes in the OXO reaction [158] and WGS reaction [159,160]. Cobalt-based catalysts, side by side with nickel and iron, could one day replace precious metals in industry.

Among cobalt-based compounds, cobalt aluminate ($CoAl_2O_4$) possesses interesting optical, magnetic and physico-chemical properties for technological and catalytic applications. $CoAl_2O_4$, commonly known as Thenard's blue, is widely used in the production of ceramics, plastics, paint, rubber and glass [161-163]. It is characterized by a spinel-type structure (AB_2O_4), a complex structure where oxygen anions are tightly packed in a face-centred cubic (*fcc*) arrangement and cations occupy the space between them. According to their cationic

occupations, spinels are divided into two types. The normal spinel structure has 8 bivalent cations (A^{2+}) located in the tetrahedral interstices and its 16 trivalent cations (B^{3+}) in the allowed octahedron voids of the unit cell. The second arrangement is more complex, the A^{2+} cations occupy half of the allowed octahedral interstices, while the B^{3+} cations are distributed evenly between the octahedral and tetrahedral interstices allowed in the unit cell, this structure is known as the inverse spinel. There are also mixed spinels, which are intermediate between the normal and inverse spinel structure. The degree of inversion is determined by the method of synthesis and/or the thermal history of the material [164].
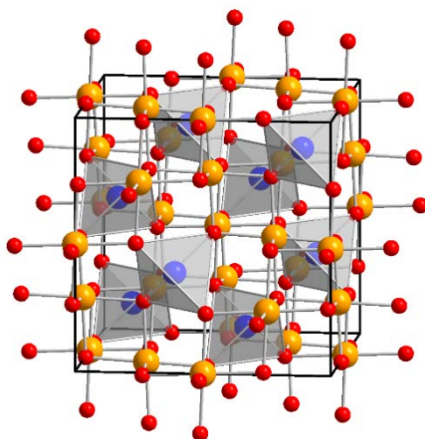
Figure 1.10. Crystal structure of spinel. A^{2+} are yellow, B^{3+} are blue and oxygen sites are red.

Cobalt aluminate spinel exhibits high thermal and pH stability, low surface acidity and chemical reactivity [165], making it a promising alternative as a precursor to cobalt-based catalysts conjugating the catalytic advantages of a highly active metal supported on a stable structure. $CoAl_2O_4$ has been employed in catalytic reactions such as soot combustion with NOx/O_2 [166], oxidation of CO, carbon monoxide hydrogenation and methane dry reforming [167].

1.6.2   Ceria promoters and catalysts

Cerium oxide (CeO_2) is an oxide of the rare-earth metal cerium. It is known for its redox properties, presenting strong catalytic activity in oxidation and

reforming reactions [168]. The redox properties of CeO_2 are related to its fluorite-type crystalline structure. Fluorite structure is a *fcc* array of cations (Ce^{4+}) in which all the tetrahedrally coordinated interstices are filled with anions (O^{2-}) and the octahedrally coordinated ones are empty. Octahedral voids are larger than tetrahedral ones occupied by oxygen anions. Therefore, oxygen anions tend to move in the octahedral interstices and oxygen mobility within the structure is favoured. This property gives CeO_2 excellent characteristics to be used in the WGS and reforming reactions [169].

In recent years, cerium oxide and CeO_2-containing catalysts have been intensively studied as catalysts and as structural promoters of heterogeneous catalytic reactions, thanks not only to its redox properties but also to its versatile acid-base properties. Ceria is an appropriate and cheap alternative for fuel cell application [170,171].

Catalytic applications of CeO_2-containing materials can be divided into three large blocs. On the one hand, there are the reactions preferentially catalysed on acid-base sites, such as dehydration of alcohols or diols [172,173], ketonization by acid condensation [174], ketonization, of aliphatic or aromatic esters [175], and dimerization of alcohols [176]. Redox properties are the most studied characteristics of ceria. Several reactions are preferentially catalysed by redox centres. Important reactions for the production of value-added chemicals are possible thanks to this mechanism [177]. CeO_2-containing catalysts have proven their effectiveness in the total oxidation process, being widely used in the hydrocarbon combustion, volatile organic compound elimination [178], wet-air oxidation of organics compounds desulfurization and NO_X abatement processes [179]. Other reactions such as alkylation and nitration of aromatic compounds, oxidative esterification, aldolic condensations, isomerization or ethylbenzene dehydrogenation to produce styrene require both acid-base and redox sites [177].

As aforementioned, due to its redox properties, ceria-based catalysts are competent for the WGS and CO-PrOx reaction [180]. Taking advantage of its proper performance in the WGS reaction, these catalysts have been studied for reforming reactions. Ceria support is used in several formulations of Ni catalysts for SR because it increases catalytic stability by promoting carbon removal from

the metallic surface [181]. Manfro et al. [168] demonstrated that the Ni supported on ceria have a lower methane formation than their counterparts on alumina. CeO_2 has also been researched as a promoter in the ethanol APR, concluding that its high oxygen mobility improves WGS reaction, enhances selectivity to H_2 and reduces carbon deposition [182].

1.6.3   Platinum-containing catalysts

Platinum (Pt) is a chemical element of atomic number 78. Platinum is a noble metal used in catalytic converters, laboratory equipment, electrical contacts, dentistry equipment, and jewellery. Pt have been widely used as a catalysts in hydrogenation of various functional groups, dehydrogenation, reforming, and oxidation reactions [183]. Platinum is also used for Polymer Electrolyte Fuel Cell (PEMFC), Direct Methanol Fuel Cell (DMFC), Microbial Fuel Cell (MFC), and Phosphoric Acid Fuel Cell (PAFC) applications as the cathode catalyst or anode catalyst [184,185].

We have already written about the large amount of research done with platinum as a catalyst for the production of hydrogen by aqueous-phase reforming [133,141]. This coveted metal have shown improved activity in WGS, C-C and C-H cleavage obtaining high activity and selectivity to hydrogen [186]. Combinations of platinum with other metals have been applied to enhance the catalyst performance in APR [187-189].

1.7   SCOPE AND OBJECTIVE

In view of the current increase in the demand for energy and the imperative need to decarbonize the global energy system and further avoid the worst of a climate change that has become a crisis, hydrogen is a promising energy alternative. Hydrogen can supply energy demand in the transportation sector, in addition to generating electricity and heat for industries and housing. The energy generated from hydrogen is beneficial for our planet when hydrogen is produced from renewable and carbon neutral sources such as solar energy and biomass. Biomass and biomass-derived are also important and promising sources for the sustainable production of energy and other chemicals. Among biomass-derived feedstock, glycerol constitutes a highly appealing and easily available raw material due to the large surplus currently existing as a by-product

in the production of biodiesel in biorefineries. In this framework, the research and development of catalytic technologies for glycerol Aqueous-Phase Reforming (APR) is an innovative challenge that can contribute to the generation of energy according to energy efficiency standards and current emission regulations.

Suitable catalysts for APR process should be active to C-C and C-H bonds cleavage and to WGS reaction. Cobalt-based catalysts could provide similar activity to noble metal catalysts in the C-C bond cleavage, even at low operating temperatures being economically attractive to carry through hydrogen rich gas. However, conventional supports such as γ-alumina show low stability under APR hydrothermal conditions. Thus, this Doctoral Thesis proposes the development of new cobalt catalysts with improved performance, based on the use of spinel catalytic precursors (cobalt aluminate), with metal crystallite sizes of high intrinsic activity. Cobalt aluminate, in addition, has low surface acidity, high thermal-mechanical and pH stability improving cobalt catalytic attributes.

Given this background, the main objective of this project is the glycerol valorisation by aqueous-phase reforming process for obtaining H_2-rich output on improved cobalt-based catalysts. To achieve this principal aim, several strategies and specific objectives have been proposed:

- $\times$ Synthesis of cobalt-based catalysts from cobalt aluminate spinel prepared by coprecipitation.

- $\times$ Extensive characterisation of the catalysts dealing with the textural, structural, surface and chemical properties, by means of a wide number of analytical techniques.

- $\times$ Evaluation of the catalytic activity in glycerol aqueous-phase reforming. Determination of the key catalytic properties responsible for the observed catalytic behaviour. Determination of the optimal reforming conditions. Determination of the reaction pathway.

- $\times$ Improvement of catalytic properties (increased gas yield and hydrogen selectivity) with the addition of promoters.

× Analysis of catalytic behaviour during long periods of operation. Determination of the main deactivation phenomena. Definition of strategies for minimizing deactivation.

× Analysis of the versatility of catalysts for the transformation of other oxygenated organic compounds.

× Valorisation of bioglycerol and analysis of the impact of impurities present in the feed on catalytic performance.

At the beginning of this chapter (Chapter 1), the current environmental and energy situation of the planet has been put into context. The role of biomass and its derivatives has been emphatically treated as promising alternatives for the production of energy and other value-added chemicals within an ecological system. Additionally, the advantages of hydrogen as an energy carrier have been exposed, highlighting, among the various processes that can be used to obtain it, the aqueous-phase reforming process. To close this chapter, an overview of the different catalysts used for this process is realized, to finally address the strategies that have been carried out throughout the Doctoral Thesis.

Chapter 2 lists the chemicals used in the different processes and analysis performed and describes the different analytical techniques applied for the characterization of the catalytic precursors, the reduced and used catalysts. In addition, the reaction units used for the catalytic tests are detailed, as well as the experimental system used for the analysis of the reaction products. Finally, the equations chosen for the calculations made are based.

Chapters 3, 4 and 5 present the results obtained with the different catalysts prepared and their respective modifications. This triad of chapters include the synthesis route of the catalysts, the main results obtained after the characterization of both calcined and reduced samples, the catalytic behaviour results in glycerol transformation and the characterization results of the spent catalysts after aqueous-phase reforming reactions.

Maintaining the aforementioned structure, Chapter 3 develops the data obtained with spinel-type cobalt catalysts. In that chapter, in addition to analysing the glycerol aqueous-phase reforming, dehydration/dehydrogenation of said

molecule is also treated. In view of the results previously achieved, Chapter 4 focuses on the modification with cerium of the cobalt aluminate catalyst that had presented the best catalytic performance, seeking to improve selectivity to hydrogen. Likewise, with the aim of improving the catalytic behaviour of the base sample, Chapter 5 proposes the incorporation of platinum into the well-known spinel structure in order to anchor metallic cobalt and therefore improve stability.

Chapter 6 studies several operating variables and their influence, mainly, on glycerol APR. The glycerol content in the feed, the changes in temperature/pressure conditions and the modification of the space velocity is investigated using one of the catalysts that presented greater activity and stability. In addition, ethylene glycol and sorbitol APR has been carried out in order to assess the effect of the complexity of the molecule to be transformed.

Chapter 7 focuses on the complexity of bioglycerol reforming. First of all, the characterization results of the bioglycerol to be used are presented. Then, the procedure for adjusting this bioglycerol in order to be used in the reactor is detailed. Finally, the most relevant results of the aqueous reforming of this compound are analysed.

Chapter 8 shows part of the results obtained during the doctoral stay at the *Université de Poitiers*. For this reason, this section is structured in a self-contained way. The reaction system and products characterization techniques and equipment are described. The results obtained in the aqueous-phase transformation of sorbitol are also analysed. These experiments were performed both under hydrogen atmosphere and with inert gas to take advantage of the hydrogen-generated *in situ*.

Although a summary is made at the end of each chapter, Chapter 9 outline the global vision of this Doctoral Thesis and encapsulates the most relevant conclusions of this research work. In addition, an outlook of the process is presented, its issues and challenges. As a final point, Chapters 10, 11 and 12 indicate the nomenclature, references employed throughout this report and addendum, respectively.

Chapter 2

EXPERIMENTAL PROCEDURE

2. EXPERIMENTAL PROCEDURE

Materials, equipment and experimental methods used for the development of this work are explained in this chapter. Firstly, reagents utilized in catalysts preparation are listed and the methodology and theoretical basis for carrying out the experimental work are specified. Subsequently, the equipment used for catalytic activity evaluation is described, detailing the operating conditions employed. Finally, the analysis system for determining effectively and accurately the composition and quantification of the reaction products is described. This chapter does not describe the catalyst preparation steps, as they are detailed in their corresponding chapters (Chapters 3, 4 and 5).

2.1 MATERIALS

The chemicals used in this work for the synthesis and characterization of catalysts and to carry out the catalytic reactions are displayed as follows: Table 2.1 listed the reactants used for the synthesis of catalysts and for the catalytic tests, while Table 2.2 summarized the gases utilized for characterization and catalytic activity.

Table 2.1. Reactants used in catalysts preparation and catalytic reactions.

Name	Chemical formulae	Purity wt.%	Supplier
Cobalt(II) nitrate hexahydrate	$Co(NO_3)_2 \cdot 6H_2O$	≥ 98	Sigma-Aldrich
Aluminium nitrate nonahydrate	$Al(NO_3)_3 \cdot 9H_2O$	≥ 98	Fluka
Cerium(III) nitrate hexahydrate	$Ce(NO_3)_3 \cdot 6H_2O$		
Tetraammineplatinum(II) nitrate	$Pt(NO_3)_2(NH_3)_4$		
Cobalt(II) oxide	CoO	99.995	Alfa Aesar
Sodium carbonate	Na_2CO_3	≥ 99.8	Riedel-de Haën
Sodium hydroxide	$NaOH$	≥ 98	Panreac

Continuation Table 2.1

Glycerol	$C_3H_8O_3$		Panreac
Sorbitol	$C_6H_{14}O_6$	99	Sigma-Aldrich
Ethylene glycol	$C_2H_6O_2$		
Cyclohexane anhydrous	C_6H_{12}	99.5	Sigma Aldrich
3,3-Dimethylbut-1-ene	C_6H_{12}	95	Alfa Aesar

Table 2.2. Gases used in experimental work.

Gas (gas-mixture)		Purity, % vol.	Supplier
Synthetic Air		≥ 99.999	Air Liquide
Hydrogen	H_2	≥ 99.999	Air Liquide
Argon	Ar	≥ 99.999	Air Liquide
Helium	He	≥ 99.999	Praxair
Nitrogen	N_2	≥ 99.999	Praxair
Hydrogen/Argon	H_2-Ar	5.0 (H_2)	Praxair
Ammonia/Helium	NH_3-He	10.0 (NH_3)	Praxair
Oxygen/Helium	O_2-He	5.0 (O_2)	Praxair
Oxygen	O_2	≥ 99.999	Praxair
Carbon dioxide/Helium	CO_2-He	5.0 (CO_2)	Praxair

2.2   CATALYSTS CHARACTERIZATION TECHNIQUES

Several characterization techniques were used in order to gain knowledge on the physico-chemical properties of the catalysts, both for fresh and spent catalysts. This way, the catalyst structure-activity relationship can be stablished. The principles of the techniques and the equipment and protocols used are described in this section.

2.2.1 Inductively Coupled Plasma-Based Systems (ICP-OES and ICP-MS)

Inductively Coupled plasma-based systems, ICP-OES and ICP-MS, are cost-effective techniques that allow the simultaneous analysis of several elements with low detection limits, generally depending on the element to be analysed. This technique was used to determine both the bulk chemical composition of the catalysts and the leached elements in the liquid stream of the reactor effluent.

Both ICP-OES and ICP-MS use an argon plasma as the excitation source. A very high temperature plasma is generated by subjecting a flow of argon gas to the action of an oscillating magnetic field induced by a high frequency current. In ICP-OES, plasma is used to generate photons by exciting electrons from a ground state atom to a higher energy level. Upon returning to their ground state, these excited ions or atoms emit radiation of a wavelength characteristic of each element and their content is determined as a function of the radiation intensity [190].

ICP-MS combines the plasma coupling technology with mass spectrometry, since positively charged ions are detected thanks to a mass analyser according to their mass and their charges. The mass analyser most commonly used is the quadrupole filter, in which the ions pass by four hyperbolic magnetic poles created by a radio frequency field. The magnetic poles separate the ions by their mass/charge ratio, successively focusing ions with increasing mass onto a detector for counting. ICP-MS is capable of detecting concentrations at milligram to nanogram levels per litre.

× Experimental Procedure

The bulk chemical composition of the synthesized cobalt oxide, cobalt aluminate and Ce-containing catalysts were determined by ICP-OES on Perkin Elmer, model Optima 8300 equipment. Analysis was carried out at the General Research Services of the UPV/EHU (SGIker in advance). The samples were processed by alkaline fusion using $LiBO_2$ as a fluxing agent on Pt-Au crucibles and pouring the melted glass on a diluted HNO_3 solution, suitable for quantification [191].

The chemical analysis of Pt-containing catalysts and the outgoing liquid stream were carried out by ICP-MS on Thermo XSERIES-II quadrupole Thermo Fisher Scientific brand equipment, with Peltier cooled impact bead spray chamber and concentric glass nebulizer. The ICP-MS was configured with the Xt interface, a screened torch, an autosampler Cetac ASX-510. The Pt-containing samples were not treated with the fusion-dissolution procedure to avoid interference with the Pt-Au crucibles. Instead, they were treated in an aqueous medium with a mixture of concentrated HNO_3:HCl in closed containers at 100 °C for 24 h. The liquid effluent of the reactor was analysed with the objective of quantifying the leached metals. As this analyte contains high organic loading, it was first diluted with ultrapure water (Milli-Q quality) and then treated with HNO_3 0.32N in order to ensure total disintegration of solids content.

2.2.2   Nitrogen Physisorption

Nitrogen physisorption is the most widely used method to study the textural properties of solids. N_2 adsorption-desorption isotherms provide information on surface area and pore structure. Physisorption occurs whenever an adsorbable gas (the adsorbate) is brought into contact with the surface of a solid (the adsorbent). This phenomenon is characterized by low energy forces (Van der Waals forces), independently of the solid material that is treated. It is a static method in which the solid sample subjected to an adsorbate pressure reaches equilibrium [192].

At low temperature, adsorbate gas molecules tend to form a monolayer on the solid surface, which depends exclusively on the size of the molecule, since they are grouped as close as their size allows. In this way, by measuring (either by volumetric or gravimetric methods) the number of adsorbed gas molecules necessary to form a monolayer, the surface area of the solid can be calculated. N_2 is the most frequently used adsorbate for the determination of areas, and at 77 K (operation temperature) its cross-sectional area is 0.162 nm^2.

The adsorption of a gas on a solid is normally characterized by an isotherm, which represents at a given temperature, the amount of adsorbed gas at equilibrium as a function of pressure. Plotting the total adsorbed and desorbed volume at different equilibrium pressures, the corresponding adsorption and

desorption curves are obtained. The form of the isotherm and the hysteresis (if present) provides information about the solid porosity.

× Experimental Procedure

Textural properties of the solids were obtained from the nitrogen adsorption-desorption isotherms at 77 K, carried out in a fully automated Micromeritics TRISTAR II 3020 equipment. For each experiment, about 0.1-0.2 g of catalyst was used. Prior to the adsorption, the samples were outgassed at atmospheric pressure and 300 °C for 10 h to remove moisture, adsorbed molecules and possible condensates that may interfere with the measurement. The adsorption branch was obtained by adding successive volumes of N_2 to the solid sample and recording the equilibrium pressure, from the lowest pressure (< $1 \cdot 10^{-3}$ kPa) up to the saturation pressure of N_2 (≈ 101.3 kPa). Subsequent desorption branch was obtained by removing successive known volumes of N_2 and registering values of equilibrium pressure until the closing hysteresis is reached.

The specific surface area of the catalysts (S_{BET}) was calculated using the method proposed by Brunauer, Emmet and Teller (BET) [193], in the 0.05 and 0.21 relative pressure range:

$$S_{BET} = \frac{V_m \cdot N_A}{V_{mol}} \cdot A_m \qquad (2.1)$$

where V_m is the adsorbate volume for monolayer; V_{mol} is the molar volume of adsorbate (34.65 $cm^3 \cdot mol^{-1}$); A_m is the adsorbate cross sectional area (16.2 $Å^2$); N_A is Avogadro´s number.

The pore size distribution was determined according to the Barrett-Joyner-Halenda (BJH) method, considering the entire desorption branch from 0.99 to 0.40 partial pressure range [194]:

$$d_P = \frac{4 \cdot \sigma \cdot V_{ads} \cdot \cos \theta}{RT \ln \left(P/P_0 \right)} + 2t_l \qquad (2.2)$$

where d_P is the pore diameter; σ is the surface tension of adsorbate (8.9 mN·m^{-1}); θ is the contact angle between condensed phase and the solid walls; R is the gas constant; T is temperature; and t_l is the adsorbed layer depth.

2.2.3   X-Ray Power Diffraction (XRD)

X-ray powder diffraction (XRD) is a rapid analytical technique primarily used for phase identification of a crystalline material and can provide information on unit cell dimensions. The analysed material must be finely ground, homogenized, and average bulk composition is determined.

XRD is based on constructive interference of monochromatic X-rays and a crystalline sample. X-rays are generated by a cathode ray tube, filtered to produce monochromatic radiation, collimated to concentrate, and directed toward the sample [195]. The interaction of the incident rays with the sample produces constructive interference (and a diffracted ray) when conditions satisfy Bragg's Law:

$$n\lambda = 2d \cdot sen\theta \qquad (2.3)$$

where n is an integer determined by the order given; λ is the wavelength of X-ray; d is the spacing between the planes in the atomic lattice; and θ is the angle between the incident ray and the scattering planes.

When the samples to be analysed are in powder form, all possible orientations are represented on their surface, and therefore exposed to the X-ray beam. As the sample rotates, the incidence angle θ varies and the detector rotates a double angle (2θ), picking up a continuous radiation background with a series of maxima corresponding to the diffracted X rays. As a result, a spectrum called diffractogram is obtained, whose positions 2θ and intensities are characteristic of each crystalline phase. The identification of the crystalline phases is done by

comparing the experimental diffractogram with those of each phase collected in a database called PDF (PDF, Powder Diffraction File) established by the ICDD (International Center for Diffraction Data).

Through XRD technique and applying the Scherrer equation (2.4) it is possible to determine the size of the crystallites [196].

$$d_{crystallite} = \frac{k\lambda}{\beta \cdot \cos\theta} \qquad (2.4)$$

where $d_{crystallite}$ is the mean diameter of the crystalline domain in Å; θ is the Bragg angle in °; K is a dimensionless shape factor (0.9 for spheres); and β is the line broadening at half the maximum intensity (FWHM), in radians, calculated as follows:

$$\beta^2 = \beta_{exp}^2 - \beta_i^2 \qquad (2.5)$$

where β_{exp} is the experimental width; and β_i is a correction due to the device. The determination of the FWHM has been obtained by processing the diffractograms with the interface WinPLOTR from Fullprof suite software.

Another interesting parameter that can be calculated from the XRD data and using the Bragg equation is the lattice parameter (a), which refers to the physical dimension of unit cell in a crystal lattice. For cubic system, the equation is as follows:

$$a = \frac{\lambda}{2\sin\theta}\sqrt{h^2 + k^2 + l^2} \qquad (2.6)$$

where h, k, and l are the Miller indices that indicates the orientation of a plane or set of parallel planes of atoms in a crystal.

× Experimental Procedure

Measurements were carried out in a PANalytical Xpert PRO model diffractometer with graphite secondary monochromator and PixCel detector, vertical goniometer (Bragg-Brentano geometry), operating with Cu_{K_α} (1.541874 Å). Each sample was scanned from 10 to 80° (2θ), with a step size of 0.026° (2θ) and a counting time of 2 s. The equipment was controlled with the PANalytical Xpert HighScore Data Collector software. Analysis and identification of phases were carried out at SGIker.

2.2.4   Wavelength Dispersive X-Ray Fluorescence (WDXRF)

Wavelength Dispersive X-Ray Fluorescence (WDXRF) is an analytical technique used to obtain bulk elemental information from solid samples. This technique uses the X-rays generated in a sample subjected to electron bombardment to identify the elements present and establish their concentration. The wavelength dispersive detection system detects by analyzing crystals, which separate X-rays based on their wavelength, or conversely their energies. The analysis can be performed sequentially, measuring the intensity of X-rays at different wavelengths one after another, or simultaneously, when at fixed positions the intensities of X-rays at different wavelengths are measured at the same time.

× Experimental Procedure

This technique was used to determine the composition of the bioglycerol ash. The chemical analyses were carried out in a PANalytical AXIOS model sequential WDXRF spectrometer equipped with a rhodium tube, three detectors (gas flow, scintillation and Xe sealing) and a maximum power of 4 kW. The crystal bead was prepared by melting a mixture of the flux in an induction micro-furnace, Spectromelt A12 (from Merck, chemical composition: 66% dilithium tetraborate, 34% lithium metaborate), with the sample dried and ground in proportions of approximately 20:1. Well-characterized international rock and mineral standards were used for calibration.

2.2.5   Temperature   Programmed   Reduction   (H₂-TPR)   and Temperature Programmed Hydrogenation (TPH)

Temperature Programmed Reduction (TPR) is a technique widely used in catalysis, when the type of solid material to characterize is susceptible to being reduced by a diluted gas. An oxidized solid is submitted to a programmed temperature increase while a reducing gas mixture is flowed over it. This way, as the temperature increases, the solid is reduced. During the TPR analysis, the concentration of the reducing gas in the exhaust stream must be continuously measured by a proper detector, usually by TCD (thermal conductivity), or by MS (mass spectroscopy). Also, the process can be followed by thermogravimetry, measuring the weight loss.

H_2 is the most used reducing agent due to its simplicity and its high reducing power. The water released in the reduction of an oxide may disturb the TCD detector performance and must be trapped before. The integration of released H_2 flow versus time reveals the capacity of reduction of the solid and the temperature at which the reduction takes place reflects the ability to reduce the sample (reducibility) [197]. The reduction profile also reveals deeper surface chemical information, such as number of metal species, metal distribution, and information on metal/support interactions in the case of supported catalysts.

When this technique is used to analyse carbonaceous material, hydrogenation of the C-containing material may occur with a release of methane, that can be easily measured by MS. In this case, the technique is named Temperature Programmed Hydrogenation (TPH).

×   Experimental Procedures

The reducibility of the fresh and spent catalysts was evaluated by H_2-TPR, while the quantification of carbonaceous materials deposited on spent catalysts was performed by TPH. Both H_2-TPR and TPH assays were carried out in a Micromeritics AutoChem 2920 apparatus. About 50 mg of sample was placed in an U-shape quartz reactor and was initially flushed in He stream at 550 °C for 1 h (heating rate 10 °C·min⁻¹). The sample was then cooled to room temperature in Ar. At that time, a freezing mixture (liquid nitrogen/isopropanol) was placed to trap the H_2O molecules that would be generated. Then, a 5% H_2-Ar flow was

passed through the sample while temperature was increased up to 950 °C (heating rate 10 °C·min^{-1}) and held for 1 h. The H_2 consumption rate was monitored in a thermal conductivity detector (TCD) (H_2-TPR) and m/z = 15 (CH_4) signal was recorded in a Pffeifer Vacuum OmniStar mass spectrometer (TPH).

2.2.6   Temperature   Programmed   Desorption   (NH_3-TPD   and CO_2-TPD)

Temperature programmed Desorption (TPD) is a powerful technique with wide ranging applications for determining site densities and understanding surface-catalysed reactions on typical oxide catalysts. TPD is based on the chemisorption of a gas on a solid and its subsequent desorption by a progressive temperature increase [198]. The amount of desorbed species at each temperature can be determined with different types of detectors. The peak temperature and peak area provide information about the strength and amount of the chemisorption, respectively.

NH_3-TPD is a typical method to determine total acidity and acid strength distribution of a solid surface. Ammonia is a thermally stable basic molecule (pKa = 9.27) with a kinetic diameter of 0.26 nm, which makes it virtually accessible to all acid sites, from weak to strong. However, the TPD experiment does not offer information concerning the nature (Lewis or Brønsted) of the acid centres.

CO_2-TPD is a widely used method in the determination of the basicity of solid surface. CO_2 is an ideal acidic molecule (pKa = 6.1) because of its high stability and accessibility to all basic centres (kinetic diameter 0.33 nm).

×   Experimental Procedure

The total acidity/basicity of the reduced samples was evaluated by means of pulse NH_3/CO_2 adsorption followed by subsequent TPD of NH_3/CO_2, respectively. Experiments were carried out in a Micromeritics AutoChem 2920 equipment coupled to Mass Spectroscopy (MKS, Cirrus 3000). Each sample (approximately 50 mg) was initially pre-treated in a He stream at 550 °C for 1 h (heating rate 10 °C·min^{-1}) and cooled down to room temperature.

For acidity measurements, the samples were reduced at 600 °C in 5% H_2-Ar flow (heating rate 10 °C·min^{-1}), held for 2 h, and then cooled down into He flow. Then, a series of 10% NH_3-He pulses were introduced at 90 °C. Subsequently, the sample was exposed to He flow for 60 min at the corresponding temperature of adsorption stage in order to remove reversibly and physically bound NH_3 from the solid surface. Finally, the temperature was raised up to 950 °C (heating rate 5 °C·min^{-1}) and the resultant signal was followed by MS (m/z = 17). The total acidity of the samples was calculated from the integration of the pulses, and the strength of the acid sites was evaluated from the corresponding TPD curves.

In order to measure the basicity, the same procedure described above was performed. For this experiment, a series of 5% CO_2-He pulses were introduced at 40 °C and the m/z = 44 signal was monitorized by MS.

2.2.7   Isothermal Hydrogen Chemisorption

Selective gas chemisorption is the most widely used technique for characterizing metal sites in heterogeneous catalysts, as the determination of the metallic surface and its dispersion. H_2 is a particularly suitable gas for characterizing metal surfaces, since its physical adsorption on the metal is negligible, and has a well-defined stoichiometric factor. Chemisorption of hydrogen on metal surfaces requires the dissociation of the H_2 molecule [199]. The spillover and hydride formation should be avoided in order to assure correct metal surface estimation. The analysis can be performed by both static volumetric and dynamic techniques. Pulse chemisorption is a dynamic technique, where small quantities of reactant are injected until the sample is saturated, and the quantity of reactant molecules taken up by active sites is measured by means of calibrated TCD detector.

×   Experimental Procedure

Isothermal H_2 chemisorption measurements were carried out in a Micromeritics AutoChem 2920 apparatus in dynamic mode (pulses), at 40 °C, which is low enough to avoid the H_2 spillover. Two protocols were performed depending on whether the catalyst was monometallic or bimetallic. At the outset, a preliminary surface cleaning by treatment in He at 550 °C was carried out for 1 h.

For monometallic Co catalysts, the sample was previously reduced at 600 °C for 30 min under 5% H_2-Ar flow, and then cooled down to 40 °C under Ar flow. Afterward, 5% H_2-Ar pulses were injected until the eluted peak had equal area.

For bimetallic Pt-Co catalysts, two consecutive pulse chemisorption analysis were performed in order to discriminate between Pt and Co metallic sites. First, catalysts was reduced at 250 °C into 5% H_2-Ar flow (heating rate 10 °C·min⁻¹, hold 1 h), then cooled down to 40 °C in He flow. Straightway, pulses of 5% H_2-Ar were injected until the eluted peak area of consecutive pulses remained constant. Then, the sample was heated into 5% H_2-Ar flow at 600 °C (heating rate 10 °C·min⁻¹, hold 1 h), and then evacuated in He flow for 15 min. Then, sample temperature was cooled down to 40 °C in He flow and the second pulse chemisorption analysis was completed. Hydrogen uptake by the sample reduced at 250 °C corresponded to Pt^0 sites, while uptake by the sample reduced at 600 °C corresponded to both Pt^0 and Co^0 sites.

The volume of chemisorbed H_2 (V_{H2}) was determined as follows:

$$V_{H_2} = V_{H_2,pulse}\left(n - \sum_i^n \frac{A_i}{A_0}\right)$$ (2.7)

where n is the number of the pulses injected; $V_{H2,pulse}$ is the H_2 volume in a loop (0.5312 cm³, calibrated loop); A_i is the peak area for each pulse; and A_0 is the peak area for non-adsorbed pulses.

The number of exposed metal atoms was calculated from the volume of H_2 chemisorbed by assuming a H/Me (Me = Pt, Co) stoichiometry of 1/1 [200], a cross-sectional area of 0.0662 nm² per Co atom [201] and 0.084 nm² in the case of Pt.

2.2.8   Thermogravimetric Analysis (TGA)

Thermogravimetric analysis (TGA) measures in a thermobalance the weight change of a sample that occurs when the sample is heated at a constant rate in a controlled atmosphere. This versatile technique provides information about

physical and chemical phenomena, such as absorption, adsorption, desorption, chemisorptions, thermal stability, oxidation, reduction, etc. [202].

TG analysis can be coupled with Temperature Programmed Desorption (TG-TPD). The method involves monitoring the mass variation of the sample during the desorption of a previously impregnated reagent, and online MS analysis for the determination of the formation of different products. The TGA-TPD tests are usually complemented with the analysis of the exhaust gases by means of a mass spectrometer.

×   Experimental Procedure

Temperature Programmed Desorption of glycerol (Glycerol-TPD) experiments were carried out in a Setaram Setsys Evolution thermobalance equipped with cylindrical graphite furnace and PID integrated temperature control. This system was coupled to a mass spectrometer (Pffeifer Vacuum DUO 2.5) to monitorize the gaseous products exhausted. The samples were reduced *ex situ* at 600 °C for 2 h (heating rate 5 °C·min^{-1}) in a 50% H_2-He flow and cooled down to room temperature in inert flow. Then, about 50 mg of catalyst was wet with 10 wt.% glycerol in water solution and left for 12 h at room temperature, and then dried in a static air oven at 110 °C, all night long. Each impregnated sample was placed in a corundum crucible. Subsequently, the sample assays were performed with a constant heating rate of 10 °C·min^{-1} from room temperature up to 900 °C in He flow (50 cm^3·min^{-1}). Selected m/z of characteristic products of glycerol dehydration and dehydrogenation were online monitored in MS (MKS, Cirrus 300).

2.2.9   Scanning Transmission Electron Microscopy (STEM)

Transmission electron miscroscopy (TEM) is based on irradiating a sample layer with a beam of high energy electrons (100-400 keV), emitted from a filament and accelerated by a potential difference, and focus through a condensing lens to form a parallel beam incident on the sample. The experiment results in a number of different phenomena such as: Auger electrons, secondary electrons, backscattered electrons, X-rays, and transmitted electrons [203]. Electrons transmitted are focused with an objective lens and amplified with a lens to form the image. Scanning electron microscopy (SEM) is based on the same concept of

TEM, but the signal is analysed from secondary and backscattered electrons to create images of the sample.

TEM provides information regarding the textural and structural properties and the chemical constitution of the materials. The main advantage is the possibility of focusing the electron beam in very small sample areas. The 2D images obtained by TEM allow the direct visualization of the catalyst metal particles. On the other hand, SEM focuses on the surface of the sample and its composition and can provide 3D or 2D images.

Scanning Transmission Electron Microscopy (STEM) is a combination of TEM and SEM, where the beam is finely focused and scans the sample area, while the image is generated by the transmitted electrons. STEM mode take advantage of the capabilities of both techniques, being able to look at the inner structure of samples with very high resolving power, but also using other signals like X-rays spectroscopy (EDX) and electron energy loss (EELS).

This technique was also used to estimate the average size of the nanoparticles by measuring at least 200 particles using ImageJ software:

$$< d >= \frac{\Sigma n_i d_i^3}{\Sigma n_i d_i^2} \tag{2.8}$$

being d_i the diameter of n_i particles.

× Experimental Procedure

TEM measurements were carried out at FEI Titan Cubed G2 60-300 electron microscope at 200 kV equipped with a high-brightness X-FEG Schottky field emission electron gun, a monochromator, CEOS GmbH spherical aberration (Cs) corrector on the image side and a Super-X EDX system under high annular dark field (HAADF) detector for Z contrast imaging in STEM conditions (camera length of 185 mm) (SGIker). The nominal size of the electron probe used for STEM and EDX maps was 0.5 nm and the probe current 170 pA and the semiconvergence angle was 14 mrad. High-angle annular dark-field HAADF STEM images were collected with an inner detector radius of 63.5 mrad. The

samples for the TEM were prepared by dispersion into ethanol solvent and keeping the suspension in an ultrasonic bath for 15 min, after a drop of suspension was spread onto a TEM copper grid (300 Mesh) covered by a holey carbon film followed by drying under vacuum.

2.2.10 Fourier Transform Infrared (FTIR)

Fourier Transform-Infrared Spectroscopy (FTIR) is an analytical technique used to study the interaction between matter and infrared radiation (wavelengths between 0.7 and 1000 μm). The usefulness of FTIR spectroscopy arises because different chemical structures produce different spectral fingerprints.

When a material is irradiated with infrared radiation, absorbed IR radiation usually excites molecules into a higher vibrational state. The wavelength of light absorbed by a particular molecule is a function of the energy difference between the at-rest and excited vibrational states. The wavelengths that are absorbed by the sample are characteristic of its molecular structure.

The FTIR spectrometer uses an interferometer to modulate the wavelength from a broadband infrared source. A detector measures the intensity of transmitted or reflected light as a function of its wavelength. The signal obtained from the detector is an interferogram, which must be analysed with a computer using Fourier transforms to obtain a single-beam infrared spectrum.

× Experimental Procedure

FTIR transmittance spectra were recorded averaging 100 measurements with a resolution of 4 cm^{-1} in the 400-4000 cm^{-1} range in Agilent Cary 600 Series spectrometer by employing KBr pellet technique. KBr pellet method exploits the property that alkali halides become plastic when subjected to pressure and form a sheet that is transparent in the infrared region.

2.2.11 UV-vis-NIR   Diffuse   Reflectance   Spectroscopy (UV-vis-NIR DRS)

Ultraviolet-Visible-Near   InfraRed   Diffuse   Reflectance   Spectroscopy (UV-vis-NIR DRS) is a suitable spectroscopic technique for qualitative (and sometimes quantitative) analysis, structural determination and detection of the

coordination of metallic or organic species, provided that they present transitions between molecular levels separated by energies of the order of the UV region and/or visible and/or near infrared of electromagnetic radiation.

UV-vis-NIR DRS is based on the property of the ions and complexes of transition metals to absorb certain wavelengths of the electromagnetic spectrum. In reflectance spectroscopy a beam of radiation is incident on a rough surface, producing a diffuse reflectance, in which the radiation penetrates through the surface of the particle layer, excites the vibration modes of the sample molecules and then it disperses in all directions. This reflected radiation is detected through a photosensitive cell and, by comparing this intensity with that of a reference standard, the percentage of reflectance is established. In UV-vis-NIR spectra, the Kubelka-Munk function is plotted against the wavelength, which depends on the value of the diffuse reflectance and whose meaning is related to the transformation of the diffuse reflectance spectrum to its equivalent in absorbance units.

Changes in the lattice parameter and phase structural parameters affect the optical band gap of solids. It was estimated by Tauc plot using the formula [204]:

$$\alpha hv = A\left(hv - E_g\right)^{\eta} \tag{2.9}$$

where α is the absorption coefficient, hv is the incident photon energy, A is a constant, E_g is the band gap, and η is a constant relating to a mode of transition ($\eta = 1/2$ for direct allowed transition, $\eta = 2$ for indirect transition). The direct band transitions were obtained from extrapolating the plot of $(\alpha hv)^2$ vs hv at $\alpha=0$.

× Experimental Procedure

The experiments were carried out on powder in a UV-vis-NIR spectrophotometer model Cary 5000 (version 1.12) coupled to an integrating sphere of diffuse reflectance (Varian) (SGIker). It was operated in a range between 200 and 2500 nm, with a measurement time of 0.1 s and a speed of 600 nm·min^{-1} keeping the beam energy constant in both UV-vis range as in NIR interval. The spectra were recorded in reflectance mode, then mathematically

transformed to absorbance by applying the Kubelka-Munk model and smoothed to eliminate residual noise.

2.2.12   Solid-State Nuclear Magnetic Resonance Spectroscopy (NMR)

Nuclear magnetic resonance spectroscopy (NMR) is a suitable tool for investigate molecular structure, dynamics and reactions on catalysts. The principle behind NMR is that many nuclei have spin and all nuclei are electrically charged. In NMR, the nuclei of atoms are irradiated with radio waves, and the corresponding resonance frequency of the nuclei is observed. The primary information available from the NMR spectrum is the chemical shift, which depends on the local electronic environment. As the chemical shift is highly sensitive to changes in molecular conformation, it is useful for identifying different crystalline forms. The NMR line width provides information about the crystallinity of the sample and the relaxation times can provide information about dynamics of the system. Depending on the states of the matter studied, NMR spectroscopy can be mainly classified into two categories: solution and solid-state NMR (SSNMR) [205]. Solid state NMR was used to provide information of aluminium coordination (^{27}Al NMR).

×   <u>Experimental Procedure</u>

Solid State ^{27}Al NMR measurements were performed on a 9.4 T Bruker AVANCE III 400 spectrometer (SGIker) operating at resonance frequencies of 104.26 MHz for ^{27}Al. Chemical shifts (δ) were referenced externally to the $AlCl_3$ aqueous solution at 0.0 ppm. The spectra were acquired at a spinning frequency of 60 kHz employing a pH MASDVT400W BL 1.3 mm ultrafast probehead. A single pulse of 0.3 μs duration was applied and a recycle delay of 0.2 s and 36,000 scans were used.

2.2.13   X-Ray Photoelectron Spectroscopy (XPS)

X-ray photoelectron spectroscopy (XPS) was used to detect the electronic state of the elements in the synthesized solids. XPS is a technique based on a photoelectronic effect that allows the surface of the sample to be analysed at a depth between 1 to 10 nm. The X-ray radiation interacts with the atoms of substance with enough energy to allow the valence electrons to leave their

ground state and reach the surface [206]. The electrons are expelled and collected according to their kinetic energy (KE). The energy of an X-ray with a particular wavelength is known, and by measuring the KE of the emitted electrons, the electron binding energy (BE) of the emitted electrons can be determined by using 2.6 equation:

$$KE = hv - BE - \phi \qquad (2.10)$$

where hv is the energy of the X-ray photons used; KE is the kinetic energy of the photoelectron emitted; BE is the binding energy, characteristics of each element; and ϕ is the work function dependent on both the spectrometer and the material. The surface concentration and the oxidation state of the atoms can be obtained by measuring the BE and the photoemission peak intensities.

×   Experimental Procedure

The spectra were measured using a SPECS spectrometer with Phoibos 150 1D-DLD analyser and monochromatized Al Kα (1486.7 eV) X-ray radiation in ultrahigh vacuum (SGIker). The powder samples, previously degassed, were introduced to the ultra-high vacuum analysis chamber (10^{-6} Pa) where an initial analysis of the present elements was carried out (time 0.1 seconds and energy of passage 80 eV) and then detailed analyses of the present elements were performed (time 0.1 seconds and step energy 30 eV) with an exit angle of 90°. Samples were reduced *in situ*, when required. The spectrometer was previously calibrated with Ag (Ag 3d$_{5/2}$, 368.26 eV). The BE were calibrated by taking C 1s peak (284.6 eV) of adventitious carbon as reference. The peaks were deconvoluted after Shirley background subtraction, using a mixed Gaussian-Lorentzian function by employing the CASA XPS software.

2.2.14 Raman Spectroscopy

Raman spectroscopy was implemented to investigate the deposition of carbonaceous materials onto spent catalyst surface. This spectroscopy is a high-resolution photonic technique that provides chemical and structural information of most organic or inorganic materials or compounds relatively quickly, allowing for their identification. Raman spectroscopy relies on inelastic

scattering (Raman scattering) of monochromatic light. The laser light interacts with molecular vibrations, phonons or other excitations in the system, and as a result, the energy of the laser photons is shifted. Most of the scattered light is at the same wavelength as the laser source and does not provide useful information (Rayleigh scatter). However a small amount of light is scattered at different wavelengths (Raman scatter), which depend on the chemical structure of the analyte [207]. A Raman spectrum represents the scattered optical intensity as a function of the normalized wavenumber (in cm^{-1}) at which it is produced.

×   Experimental Procedure

The measurements were conducted by using a Renishaw InVia Raman spectrometer, joined to a Leica DMLM microscope (SGIker). The spectra were acquired with the Leica 50x N Plan (0.75 aperture) objective. Conjointly, for the visualization and focusing, another Leica 5x N Plan (0.12 aperture) and a 20x N Plan EPI (0.40 aperture) objectives were used. The spatial resolution for the 50x objectives is 1-2 microns. For the focusing and searching of the points of interest, the microscope implements a Prior scientific motorised stage (XYZ) with a joystick. In all the measurements, the power of the laser was reduced in order to avoid the photodecomposition of the samples (burning) by using neutral density filters, being the maximum power at the sample of 20 mW and a holographic net of 1,800 lines/mm. With the aim of improving the signal to noise ratio, for each spectrum 40 s were employed and 10 scans were accumulated with 10% of the maximum power of the 514 nm (ion-argon laser, Modu-Laser) laser in the spectral window from 100 to 800 cm^{-1}. The data processing was carried out by an adjustment of the spectra using a Lorentzian function model.

2.2.15   Skeletal isomerization of 3,3-dimethylbut-1-ene

The model reaction of 3,3-dimethylbut-1-ene (33DM1B) skeletal isomerization is a well-adapted reaction for characterizing the acid centres with a medium strength [208]. This reaction involves a purely protonic mechanism (Figure 2.1), being Lewis acidic sites merely spectators [209]. Therefore, it is suitable for the characterization of Brønsted centres. The slowest step of the reaction is the isomerization of the secondary carbenium ions through a methyl group migration.

It is a relatively simple reaction with only two main products: 2,3-dimethylbut-1-ene (23DM1B) and 2,3-dimethylbut-2-ene (23DM2B). Other weaker products (methylpentenes) could appear at temperatures above 300 °C.
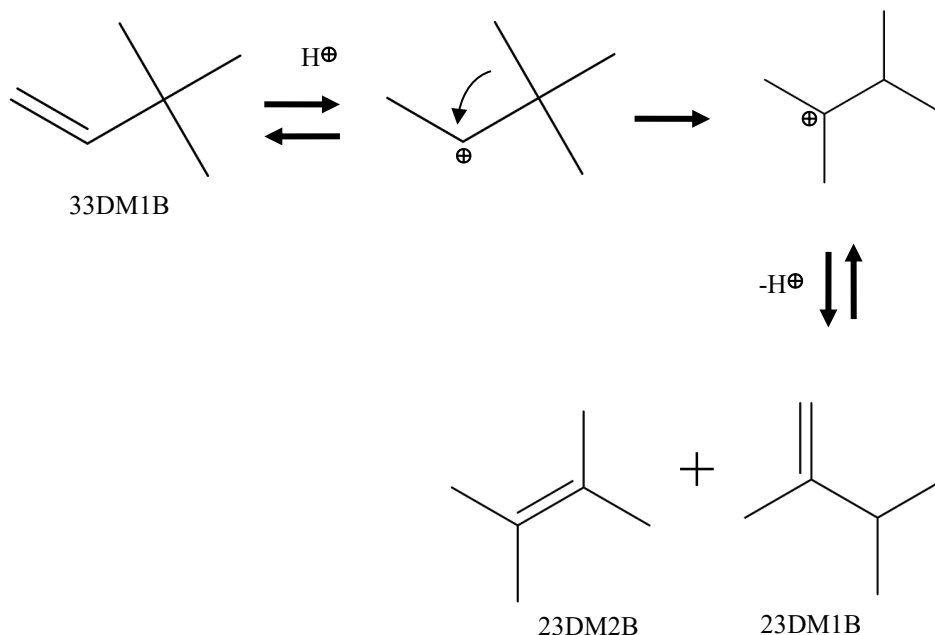
Figure 2.1. Mechanism of isomerization of 3,3-dimethylbut-1-ene (33DM1B).

×   Experimental Procedure

The 33DM1B skeletal isomerization test was carried out in the laboratories of the group "*Du Site Actif au Matériau catalytique*" (SAMCat) of the *Université de Poitiers*, in a setup shown in Figure 2.2. Tipically, 100 mg of sample was loaded in a tubular glass reactor and reduced at 600 °C for 30 min in a H_2 flow (60 cm³·min⁻¹). Then, the sample was cooled down to reaction temperature (300 °C) under N_2 flow (30 cm³·min⁻¹). The reaction was performed under atmospheric pressure with a reactant flow rate of 15.2 mmol₃₃DM1B·h⁻¹ and a reactant partial pressure of 20 kPa. Analysis of the reaction products was performed online by gas chromatography (AlphaMos PR2100) with a flame ionization detector (FID) on a RTx-1 (Restek) column (105 m × 0.53 mm × 3.00 μm). The detected products were 2,3-dimethylbut-1-ene and 2,3-dimethylbut-2-ene.
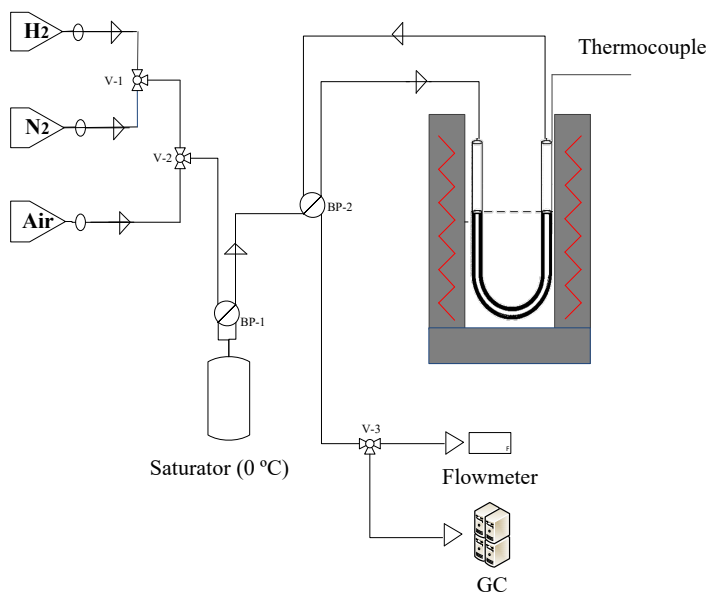
Figure 2.2. Diagram of skeletal isomerization of 3,3-dimethylbut-1-ene reaction setup.

The conversion of 33DM1B (X_{isom}) was calculated as follow:

$$X_{isom} = 100 \times \frac{\sum products}{feedstock + \sum products} \qquad (2.11)$$

The initial 33DM1B conversion ($X_{isom,0}$) was obtained by extrapolation at zero time.

The initial activity of isomerization ($A_{isom,0}$, in mmol·h^{-1}·m^{-2}) is given by the following equation:

$$A_{isom,0} = \frac{F_{33DM1B} \times X_{isom,0}}{m \times S_{BET} \times 100} \qquad (2.12)$$

where, F_{33DM1B} is the reactant flow (mmol$_{33DM1B}$·h^{-1}); m is the catalyst mass (g); and S_{BET} is the specific surface area of the catalyst (m^2·g^{-1}).

2.2.16   Cyclohexane Dehydrogenation

Cyclohexane dehydrogenation to benzene (Figure 2.3) is an endothermic reaction catalysed exclusively by the metallic function of the catalysts. This reaction is insensitive to the nature of the crystal structure and the size of the metal particles. In other words, it is a function of the metal used and the reaction rate depends only on the number of accessible active metal atoms [210,211]. Therefore, this model reaction can be employed as an indirect method for characterising the metal sites in a catalyst [212].
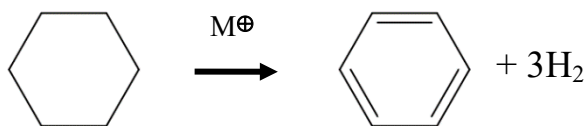
Figure 2.3. Cyclohexane dehydrogenation reaction. $M^{\oplus}$ represents metal site.

×   Experimental Procedure

The catalyst (about 20 mg) was diluted with silicon carbide (SiC), introduced in a dynamic fixed-bed reactor preceded by a preheating spiral, and placed in a tube furnace. The sample was reduced at 600 °C in H_2 flow, for 1 h. Then, the sample was cooled down in N_2 flow to reaction temperature (250 °C). During the test H_2 flow rate was set up at 100 $cm^3 \cdot min^{-1}$ by needle valves. Liquid anhydrous cyclohexane was injected upstream of the reactor at 2 $cm^3 \cdot h^{-1}$ using a syringe and a Dosimat pump 725. The gaseous effluents at the outlet of the reactor (mainly cyclohexane and benzene) were analysed online in an Agilent 7820A GC with FID detector on a HP-PLOT Al_2O_3 KCl megabore column. Oven, injector and detector temperatures were set at 160, 250 and 250 °C, respectively. Specific activity of dehydrogenation (A_{dehyd}) as well as Turnover Frequency (TOF) of the catalyst were determined analysing the chromatograms obtained after 10 successive injections. This model reaction was carried out in the laboratories of SAMCat group of the *Univesité de Poitiers*.
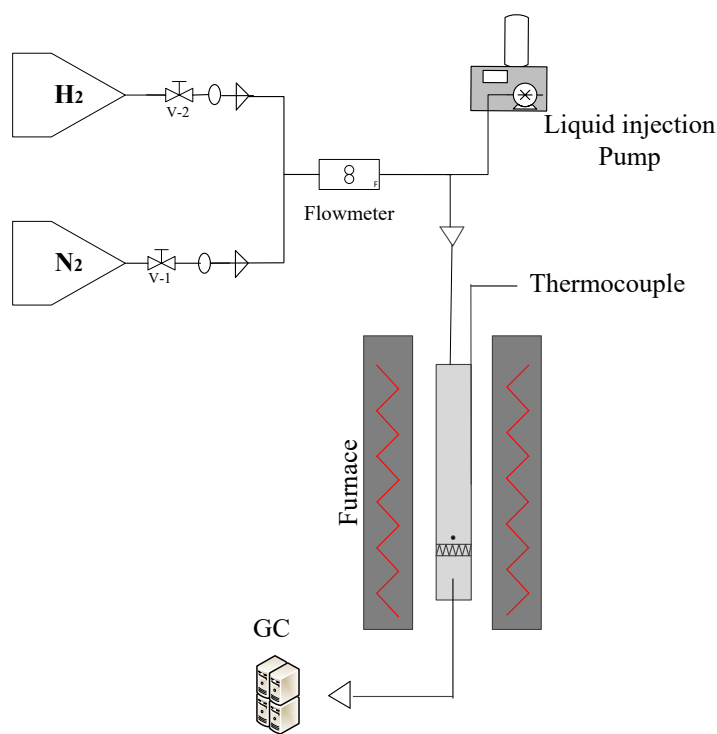
Figure 2.4. Diagram of cyclohexane dehydrogenation reaction setup.

The specific activity of dehydrogenation (A_{dehyd}) was calculated from the initial conversion of cyclohexane, as follows:

$$A_{dehyd} = X_{cycloh,0} \times \frac{F_{cycloh}}{m \times Q} \qquad (2.13)$$

where A_{dehyd} is in mol·h^{-1}·g$_{metal}$$^{-1}$; $X_{cycloh,0}$ is the cyclohexane conversion at zero time, calculated by extrapolation; F_{cycloh} is the molar flow of cyclohexane (mol·h^{-1}); m is the catalyst mass (g); and Q is the metal content of catalyst (wt.%).

Turnover Frequency for cyclohexane dehydrogenation (TOF_{dehyd}, s^{-1}) is determined from specific activity of dehydrogenation by the following equation:

$$TOF_{dehyd} = 100 \times \frac{A_{dehyd} \times M_{Me}}{D_{Me} \times 3600}$$ (2.14)

where, M_{Me} is the molar mass of metal (g·mol^{-1}); and D_{Me} is the dispersion of the metal (%).

2.3   REACTION SYSTEM

In this section, the reaction system and the operating conditions used for the glycerol APR are described. All the equipment described here and in Section 2.4 is available in the laboratories of the research group "Chemical Technologies for Environmental Sustainability" (TQSA), at the Dept. of Chemical Engineering, Faculty of Science and Technology, UPV/EHU.

2.3.1   Reaction Equipment

The activity measurements for the liquid-phase reforming and WGS reactions were performed in a bench-scale fixed-bed up-flow tubular reactor. The reaction system model is a Microactivity Effi, PID Eng &Tech, controlled by Process@ software. The process diagram of the experimental setup is shown in Figure 2.5. The reactor was placed into a furnace, and has an internal diameter of 5.1 mm, a height of 305 mm and a stainless steel frit. It was made in Hastelloy X, and can operate at a temperature of up to 1200 °C at atmospheric pressure, and 800 °C at up to 100 bar pressures. The temperature of the catalyst bed inside the reactor was controlled by a K-type thermocouple inserted through the upper part of the reactor. A PID controller receives the signal measured by the thermocouple and sends another signal in order to regulate the resistance that provides the necessary heat to reach the desired reaction temperature.

The reaction system also includes a feeding zone with a gas feed section and a liquid feed section. The gas inlet lines (H$_2$, O$_2$ and He) have a cut-off valve and an EL Flow flowmeter (Bronkhorst High-Tech) for the flow regulation. For pumping the liquid reagent two piston pumps were available: a GILSON 307 (able to pump flows from 0.02 to 5 cm^3·min^{-1}) and a Eldex 5985 optos 1LMP (for flow rates between 0.002 to 2.5 cm^3·min^{-1}). Both, gas and liquid lines were mixed

and pre-heated inside the reaction zone at a temperature of 100 °C in order to avoid possible condensation in the lines and elements of the system. The system has the option to bypass only the He flow at the output of the reactor or continue along with the other gases to the 6-way valve that allowed introducing the gases and liquid to the reactor or bypassing them.
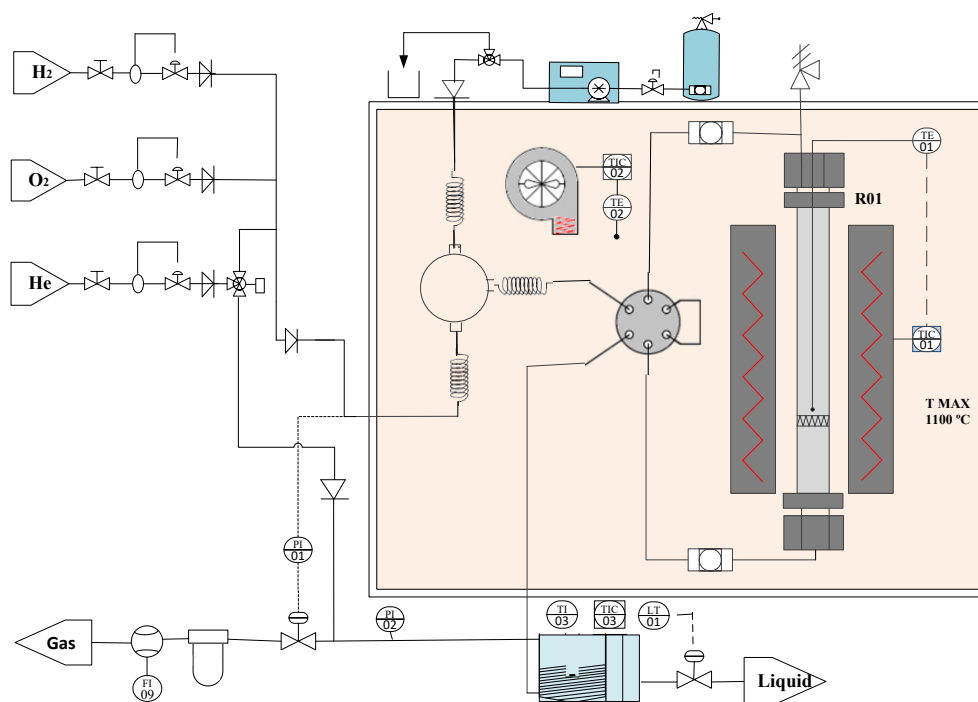

Figure 2.5. Bench-scale reactor process diagram.

2.3.2   Operating Conditions

The evaluation of the catalysts´ performance in the glycerol APR has been achieved through a significant number of tests carried out under different operating conditions in search of the optimal conditions for a better exploitation of the process.

In general, the designed experiments have been carried out under varied reaction conditions in terms of temperature/pressure, space velocity and continuous operating time. More specifically, experiments have been planned modifying the concentration and type of reagent and feeding crude glycerol (see Chapters 6 and 7).

In a typical catalytic test, a weighted amount of catalyst, with particle size between 0.04-0.16 mm, was placed on the stainless steel frit and covered with a quartz wool plug. Before the reaction, the catalyst was reduced *in situ* under 10% H_2-He flow (50 $cm^3 \cdot min^{-1}$) at 600 °C, for 2 h, heating rate 5 °C·min^{-1}, at atmospheric pressure. Subsequently, the pressure was increased to the desired value by flowing He. When the desired pressure was reached, the He flow (40 $cm^3 \cdot min^{-1}$) was switched to bypass and, unless otherwise specified, a 10 wt.% glycerol aqueous solution was pumped into the reactor while the temperature was raised at 5 °C·min^{-1} up to the desired reaction temperature. The reactor exhaust stream, which consisted of a G-L mixed phase, was cooled down to 5 °C by the Peltier cell and the two phases were separated and analysed. The analysis techniques and the equipment used in the analysis of the reaction products are described in section 2.4.

2.4   REACTION PRODUCTS CHARACTERIZATION

An adequate analysis system that facilitates a fast and reliable collection of experimental data has been designed. This section describes the techniques and procedures used to analyse gaseous and liquid products of APR.

2.4.1   Gas Chromatography (GC-MS, GC-FID and μGC)

Gas Chromatograpy (GC) is a technique to separate different components of a mixture. The chromatographic separation relies on the interaction of the sample with a mobile phase and a stationary phase within the GC column. The sample is carried through the column by the mobile phase, typically an inert gas. However, the sample is slowed in its travel through the column as the sample molecules repeatedly adsorb and desorb from the stationary phase in the column. The affinity of a particular molecule for the stationary phase determines its retention time for a given analysis condition. The molecules for each component of the sample travel through the column at nearly the same rate and elute within a narrow time band that is specific to that component (retention time). Thus, compounds with different affinities for the stationary phase (that is, different retention times) are physically separated in the column for presentation to a detector and analyser. To distinguish among the different compounds of a mixture, three types of detectors were launched.

Gas chromatography/mass spectrometry (GC-MS) is the marriage of two analytical methods into a versatile technique for the identification of complex volatile materials. Gas chromatography effectively separates the different constituents of the sample for subsequent analysis and identification by mass spectrometry (MS). In the case of GC-MS, the quadrupole filter can perform a complete mass scan within the duration of a single GC elution band. This system was used, expressly, to identify the compounds obtained in the first screening of catalysts of each condition.

FID and TCD are two universal detectors that have adequate sensitivity, an ample range of linearity and excellent stability. Flame ionization detector (FID) typically uses a H_2/Air flame into which the sample is passed to oxidise organic molecules and produces electrically charged particles (ions). The ions are collected and produce an electrical signal, which is then measured. GC-FID equipment was utilized in the analysis of the liquid product of APR.

Contrastively, TCD is the detector employed by the Agilent μGC system used in the analysis of the gas product of APR. TCD works by having two parallel tubes both containing gas and heating coils. The gases are examined by comparing the heat loss rate from the heating coils into the gas. Normally, one tube holds a reference gas and the sample to be tested is passed through the other. Using this principle, a TCD senses the changes in the thermal conductivity of the column effluent and compares it to a reference flow of carrier gas.

Regardless of the detector used, each peak or band in the chromatogram represents a discrete chemical compound, or a mixture of compounds with identical retention times. The analysis results can be quantified using the area under each peak in the chromatogram, which is proportional to the concentration of the compounds represented by that peak. The concentration for each compound in the sample is calculated from a standard curve of known concentrations established for that compound.

×   Experimental Procedure

The non-condensed gas was analysed online by both a μGC-TCD and a GC-MS. Table 2.3 details the operating conditions of the Agilent 490 μGC equipped with four parallel columns. The characteristic of each column and the conditions of

analysis have been determined for the optimum analysis of the products obtained. All channels, except Channel 4, are equipped with a backflushing system that reverses the flow of the carrier gas after the target compound is detected in order to discharge residual components in the column from the injection port.

Table 2.3. μGC equipment and analysis conditions.

	Channel 1	Channel 2	Channel 3	Channel 4
Chromatograph	Agilent 490 μGC system			
Columns	Molecular sieves HI)	(MS5A	Poraplot (PPQ)	Al_2O_3-KCl
Carrier gas	Ar	He	He	He
Column temperature, °C	70	70	90	80
Column pressure, psi	13	15	15	15
Injector temperature, °C	110	110	110	110
Injection time, ms	20	20	20	100
Backflush time, s	12	11	8	-
Analysis time, s	240	240	240	240
Identified products	H_2 & He	N_2, CH_4 & CO	CO_2 & C_2 compounds	C_{3+} compounds
Control system	OpenLAB CDS (EZChrome edition)			

The methods and the operating conditions employed in GC techniques are specified in Table 2.4. Recall that GC-MS was used to obtain qualitative data. The liquid product was collected at desired times in 2 mL vials, which are kept refrigerated until they are analysed. Liquid analysis was conducted by either GC-FID/GC-MS or HPLC methods.

Table 2.4. GC equipment and analysis conditions for the gas and liquid product analysis.

Chromatograph	Agilent GC-7890B coupled to MS-5977A		Agilent 6890N
Detector	GC-MS	GC-MS	GC-FID
Reaction product analysed	Gas	Liquid	Liquid
Detector conditions			
Temperature, °C	150	250	300
Flow, $cm^3 \cdot min^{-1}$	30.3	17.7	H_2: 40.0 Air: 350.0 Combined flow: 17.0 Makeup Gas: N_2
Carrier gas	He	He	H_2
Columns	CP-Al_2O_3/KCl (25 m x 250 μm x 4 μm)	CP-Wax 57 CB (25 m x 250 μm x 0.2 μm)	HP-Wax Bonded Polyethylene Glycol (25.0 m x 200 μm x 0.40 μm)
Column flow, $cm^3 \cdot min^{-1}$	1.3	1.3	1.0
Oven	40 °C for 30 min.	50 °C for 10 min, up to 190 °C (5 °C·min^{-1}) during 10 min.	80 °C for 4 min, up to 110 °C during 15 min and finally, 200 °C for 10 min. Ramp of 30 °C·min^{-1}.
Loop/ Injection volume	0.25 cm^3	0.1 μL	3 μL
Injector	Split 20:1	Split 20:1	Split 20:1
Analysis time	30 min	48 min	33 min
Control system	MassHunter GC/MS		GC ChemStation

.

2.4.2   Liquid Chromatography (HPLC)

High performance liquid chromatography (HPLC), formerly referred to as high-pressure liquid chromatography, is a technique in analytical chemistry used to separate, identify, and quantify each component in a mixture. This technique has been used to analyse the APR liquid product.

The HPLC system typically includes a sampler, pumps, oven and a detector. The column used was based on the ion exchange, separating molecules based on their respective charged groups (cations or anions) and the eluted compounds were detected by Refractive Index Detector (RI), useful for detecting substances with limited or no UV absorption such as alcohols, sugars, fatty acids, polymers and carbohydrates. Refractive index detector can measure extremely small changes in refractive index to detect the presence of sample.

×   Experimental Procedure

The method used in the HPLC analysis is presented in Table 2.5.

Table 2.5. HPLC equipment and analysis conditions.

HPLC pump	Waters 515
Injector	Waters 717
Injection volume	10 μL
Detector	refraction index, Waters 2414
Detector temperature	50 °C
Columns	Hi-plex H. Strong cation-exchange resin consisting of sulfonated crosslinked styrene-divinylbenzene copolymer in the hydrogen form.
Mobile phase	Water
Column flow	0.2 $cm^3 \cdot min^{-1}$
Column temperature	30 °C
Analysis time	120 min
Control system	Empower Pro v.2

2.4.3   Total Organic Carbon (TOC)

Aqueous-Phase Reforming produces many water soluble intermediates, some of which are difficult to detect or identify from chromatographic analysis. To estimate the total amount of organic products present in the liquid samples, the Total Organic Carbon (TOC) analysis is performed. This widely used parameter is a measure of the total mass of carbon represented by the various organic compounds present in the water solution.

TOC measurement is based on the combustion/non-dispersive infrared gas analysis method. The sample to be analysed is completely oxidized by heating at 680 °C in an oxygen-rich environment inside combustion tubes filled with a platinum catalyst. The carbon dioxide generated absorb infrared radiation of different wavelengths depending upon the bonding condition and kind of atoms constituting each molecule. The amount of rays absorbed is proportional to the density of the gas, according to the Lamberts-Beer`s Law. Therefore, the gas density can be determined by measuring the amount of rays absorbed using an infrared gas analyser (NDIR). The total carbon concentration (TC) in the sample is automatically calculated from a standard calibration curve. NDIR also detects inorganic carbon (IC) after it is converted to carbon dioxide through the sparging process. Finally, the TOC concentration is calculated by subtracting the IC concentration from the TC concentration. This analyser achieves high detection sensitivity, with a detection limit of 4 $\mu g \cdot L^{-1}$. Carbon conversion to gas (X_{gas}) was calculated from the TC analysis, since IC values were negligible.

×   Experimental Procedure

The TC value was measured off-line on a Shimadzu TOC-L series apparatus equipped with an autosampler. Before analysis, 350 μL of liquid samples were diluted in 100 cm^3 of ultrapure water (Milli-Q quality) in order to reach the standard range between 100 and 1000 $mg_{carbon} \cdot L^{-1}$.

2.4.4   Definitions and Calculations

In this work, Weight Hourly Space Velocity (WHSV, h^{-1}) has been calculated as the ratio of the feed mass flow and the catalyst mass:

$$WHSV = \frac{\dot{m}_{feed}}{m_{cat}} \tag{2.15}$$

The total conversion of glycerol (X_{gly}) was calculated on the basis of reactant molar flow using HPLC data, as follows:

$$X_{gly} = 100 \times \frac{F_{gly}^{in} - F_{gly}^{out}}{F_{gly}^{in}} \tag{2.16}$$

The carbon conversion to gas (X_{gas}) accounts the percentage of C atoms fed in glycerol that is present in the gas products, and it was calculated on the basis of carbon molar flow, as follows:

$$X_{gas} = 100 \times \frac{F_C^{in} - F_{C_{liquid}}^{out}}{F_C^{in}} \tag{2.17}$$

Selectivity to gas (S_{gas}) was defined as the fraction of carbon atoms converted into gas phase per converted glycerol moles:

$$S_{gas} = 100 \times \frac{F_C^{in} - F_{C_{liquid}}^{out}}{F_{gly}^{in} - F_{gly}^{out}} \times \frac{1}{3} \tag{2.18}$$

Hydrogen selectivity (S_{H2}) was defined as the number of H atoms as H_2 with respect to the total number of H atoms in the gas product, i.e. compares the H_2 generated with that lost in the production of alkanes:

$$S_{H_2} = 100 \times \frac{2 \times F_{H_2}^{out}}{F_H^{gas}} \qquad (2.19)$$

The selectivity of the C-containing gas product i was defined as the percentage of C atoms in the gas product i with respect to the total C atoms in the gas product, and it was calculated considering the flow of carbon atoms in the product i and in all gas products:

$$S_i = 100 \times \frac{F_{C,i}^{out}}{F_C^{gas}} \qquad (2.20)$$

Hydrogen yield (Y_{H2}) was defined as the ratio between the moles of H_2 produced and moles of glycerol fed to the reactor, multiplied by the stoichiometric reforming factor (RR):

$$Y_{H_2} = 100 \times \frac{F_{H_2}^{out}}{F_{glyc}^{in}} \times RR \qquad (2.21)$$

RR is the stoichiometric requirement of the specific reactant (in moles) per moles of the desired product. Based on equation (1.3), RR=1/7 for glycerol APR.

Yield of liquid product i (Y_i) accounts the percentage of the total C atoms fed as glycerol that exhausted as liquid product i, and it was calculated by dividing the carbon molar flow in the liquid stream by the carbon molar flow in the reactor inlet:

$$Y_i = 100 \times \frac{F_{C,i}^{out}}{F_C^{in}} \qquad (2.22)$$

Calculations developed in Chapter 5 for the liquid-phase WGS experiments were defined following the elemental definitions.

Conversion of CO (X_{CO}) was calculated as follows:

$$X_{CO} = 100 \times \frac{F_{CO}^{in} - F_{CO}^{out}}{F_{CO}^{in}} \qquad (2.23)$$

Yield of CO_2 and CH_4 (Y_i) was defined as the ratio between the moles of product i obtained and moles of CO fed to the reactor:

$$Y_{i_{WGS}} = 100 \times \frac{F_i^{out}}{F_{CO}^{in}} \qquad (2.24)$$

Net hydrogen variation (Y_{H2}) was calculated using the corresponding inlet and outlet hydrogen molar flow:

$$\Delta H_2 = 100 \times \frac{F_{H_2}^{out} - F_{H_2}^{in}}{F_{H_2}^{in}} \qquad (2.25)$$

Chapter 3

COBALT ALUMINATE SPINEL-DERIVED CATALYSTS
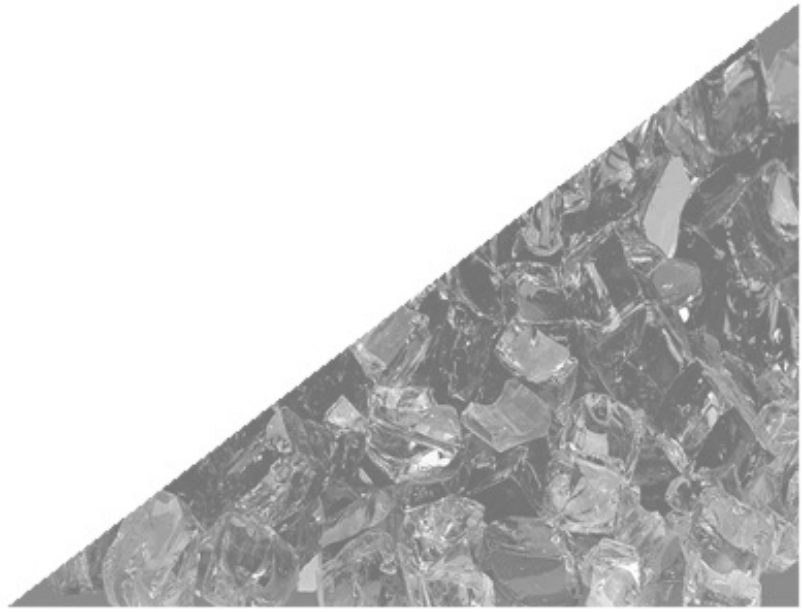
3. COBALT ALUMINATE SPINEL-DERIVED CATALYSTS

Cobalt-based catalysts have been tested in the reforming of oxygenated compounds proving to be active for C-C bond scission and for WGS activity [213-217]. Nevertheless, in liquid-phase reactions, cobalt based catalysts are prone to rapid deactivation due to oxidation and leaching [149]. Moreover, conventional supports such as γ-alumina under APR hydrothermal conditions tends to phase-transform through hydration into the more acidic boehmite (AlOOH) phase, leading to catalyst deactivation [148]. Therefore, the use of a stable structure with low surface acidity, such as the cobalt aluminate spinel, which, after being reduced, led to highly dispersed metallic crystallites on the surface is a promising alternative as a precursor of cobalt-based catalyst to be used in APR process.

Synthesis of the metal spinels have been carried out by coprecipitation from metal salts of the desired elements in basic media. The synthesis route selected for the preparation of these cobalt catalysts is suitable for obtaining nanocrystalline materials of a high catalytic potential for APR. The final characteristics of the catalyst depends largely on the activation protocol followed. In the case of this study, the activation was done by calcination (in order to obtain cobalt aluminate spinels) and then reduction (in order to obtain metallic cobalt), both stages carried out at high temperatures.

In this chapter, the results of an exhaustive study of the textural, structural, redox and metallic properties of the cobalt spinel catalytic precursors and the resulting catalysts are described and discussed. Likewise, the catalytic ability of the prepared catalysts for the glycerol transformation is analysed, with special emphasis on the aqueous-phase reforming of glycerol for the production of hydrogen. In this tenor, firstly, glycerol temperature controlled desorption (glycerol-TPD) has been performed. In the next section, aqueous-phase reforming is evaluated under mild (235 °C/35 bar) and more severe (260 °C/50 bar) reaction conditions. In addition, spent catalysts discarded from the glycerol APR were characterised in order to gain knowledge on the deactivation that will allow the identification of the most appropriate strategies for improving our catalyst formulations.

3.1   CATALYSTS PREPARATION

Spinel-type cobalt aluminates (xCoAl) and bare Co_3O_4 were synthesized by coprecipitation method, using cobalt(II) nitrate hexahydrate ($Co(NO_3)_2 \cdot 6H_2O$) and aluminium nitrate nonahydrate ($Al(NO_3)_3 \cdot 9H_2O$) as precursor salts, and sodium carbonate and sodium hydroxide as precipitating agents.

Various concentrations of cobalt have been chosen by fixing the aluminium concentration to obtain different Co/Al molar ratios (set at 0.25, 0.5 and 0.625) and the plain Co_3O_4.

Scheme 3.1. Diagram of the synthesis method of the *spinel-derived cobalt catalysts.*

shows in a schematic way the synthesis route of cobalt-based catalysts.
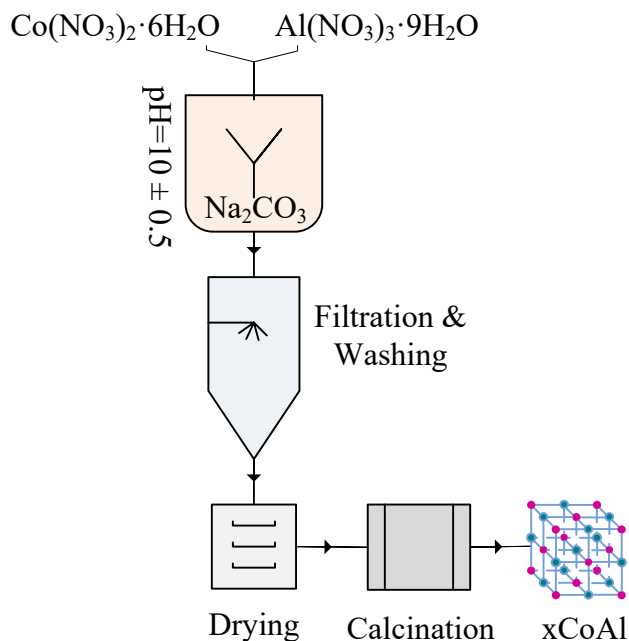
Scheme 3.1. Diagram of the synthesis method of the spinel-derived cobalt catalysts.

For the synthesis, a proper amount of an aqueous solution of $Co(NO_3)_2 \cdot 6H_2O$ and $Al(NO_3)_3 \cdot 9H_2O$ was added dropwise into a beaker containing an aqueous solution of Na_2CO_3 under stirring, for around 2 h, at room temperature and at

constant pH 10 ± 0.5, which was adjusted by adding NaOH solution (2 M). The resulting suspension was aged at room temperature for 24 h, filtered, washed several times with de-ionized water and dried at 110 °C overnight. The solid was ground to fine powders in an agate mortar and then calcined in a muffle furnace at 500 °C (at a heating rate 5 °C·min⁻¹) for 5 h in a static air atmosphere. During calcination, the maximum temperature in the solid did not surpass 505 °C. The as-prepared solids were denoted as xCoAl, where x refers to the nominal Co/Al molar ratio. Remark that the bare Co_3O_4 has been synthesized with the same method without the addition of the aluminium precursor (precipitation). For comparative purposes, γ-Al_2O_3 (prepared by simple calcination of aluminium nitrate in air at 500 °C) and commercial CoO were used as reference.

Certain characterization techniques required a prior *ex situ* treatment of the samples before they were performed. For that, the samples were *ex situ* reduced in a tubular quartz reactor at 600 °C for 1 h (heating rate 5 °C·min⁻¹) into 50% H_2-He, with a total flow of 50 cm³·min⁻¹.

3.2 CATALYSTS CHARACTERIZATION RESULTS

3.2.1 Bulk chemical composition and textural properties

The bulk molar composition (Co/Al molar ratio) and the textural properties in terms of BET surface area (S_{BET}), pore volume (V_P) and pore size (d_P) of the synthesized solids are shown in Table 3.1.

Table 3.1. Molar composition and textural properties of cobalt aluminate spinel samples.

Sample	Co/Al, at·at⁻¹	S_{BET}, m²·g⁻¹	V_P, cm³·g⁻¹	d_P, nm
0.25CoAl	0.267	136.2 (*96.6*)	0.328 (*0.309*)	6.7 (*8.3*)
0.5CoAl	0.498	132.3 (*102.8*)	0.308 (*0.360*)	6.0 (*9.5*)
0.625CoAl	0.634	125.3 (*101.7*)	0.280 (*0.375*)	6.8 (*9.6*)
Co₃O₄	∞	37.7 (*7.4*)	0.263 (*0.032*)	24.4 (*14.0*)

Reduced samples in parenthesis.

The experimental Co/Al molar ratio was very close to the nominal value for all the samples. For calcined samples, the specific surface area of the cobalt aluminate spinels was noticeably larger than that of Co_3O_4. As reported by several authors [218-221], in coprecipitaded binary oxide systems this phenomenon is attributed to a mutual protective effect, that is, the presence of one oxide hinders the crystallization of the other, thus preventing the formation of large particles. As Co/Al decrease, the S_{BET} slightly increase from 125.3 $m^2 \cdot g^{-1}$ for 0.625CoAl to 136.2 $m^2 \cdot g^{-1}$ for 0.25CoAl. Consequently, pore volume decreased (decrease of 14.6% from 0.25CoAl to 0.625CoAl) and pore size enlarged with cobalt increase in the structure.
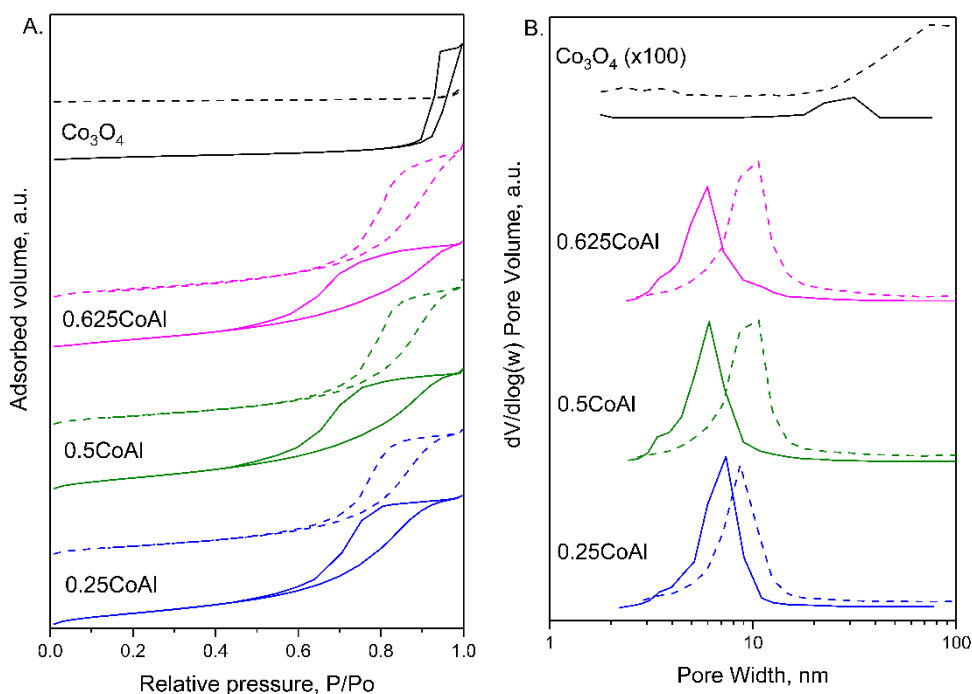
Figure 3.1. Nitrogen adsorption-desorption isotherms (A) and pore size distribution (B) of the calcined (solid lines) and reduced (dashed lines) cobalt aluminate spinel samples.

Figure 3.1.A and B shows the nitrogen adsorption-desorption isotherms and pore size distribution for the calcined and reduced samples. Regardless of Co/Al ratio, calcined samples showed type IV isotherm characteristics of mesoporous solids according to IUPAC classification and H2 type hysteresis loop at high

relative pressures, which is characteristic of disordered porous materials. The t-plot method confirmed that only mesoporous were developed in the synthesized solids. As can be seen in Figure 3.1.B, all aluminium-containing samples displayed a similar unimodal pore size distribution with peaks centred at around 6.5 nm pore size. Conversely, Co_3O_4 had a much broader distribution, with an average pore diameter of 24.4 nm.

After reduction at 600 °C, xCoAl catalysts displayed type IV isotherms and a combination of H1-H2 type hysteresis loop. S_{BET} declined up to 30% (for 0.25CoAl catalyst), caused by the migration of the metallic cobalt from the $CoAl_2O_4$ lattice to the surface [222] and also by the dilution effect [223]. A similar trend can be observed in S_{BET} for all the reduced samples. Interestingly, the samples with higher amount of cobalt suffered a lesser S_{BET} decrease, suggesting that cobalt ions stabilized the spinel structure. As was to be expected, the pore size distribution shifted to larger values. With respect to Co_3O_4 sample, it presented a large decrease (around 80.5% and 87.8%) of its S_{BET} and its pore volume, respectively.

3.2.2   Reducibility of the solids

The reducibility of the xCoAl and Co_3O_4 samples was studied by temperature programmed reduction (H_2-TPR), and the obtained reduction profiles are shown in Figure 3.2. The reduction profile of Co_3O_4 essentially presented two peaks corresponding to a two-step reduction process. The low temperature peak at 300 °C, related to the reduction of surface Co^{3+} to Co^{2+}, and the second broad peak, at higher temperatures (maxima at about 425 °C), attributed to the reduction of Co^{2+} species to metallic cobalt [224]. The ratio between the low and high temperature peak for the prepared Co_3O_4 sample was 0.37, differing from the nominal value of 0.33. This corresponds to a bulk Co^{2+}/Co^{3+} molar ratio of 0.35, somewhat lower than the stoichiometric value ($Co^{2+}/Co^{3+} = 0.5$), which indicates its relative enrichment in Co_2O_3 (42% excess) in detriment of CoO. This would explain its higher than stoichiometric (16.6 mmol·g^{-1}) hydrogen consumption (Table 3.2). These species are likely to be present in small crystallites (below detection limit 2-5 nm) or in amorphous phase, as will be discussed in the XRD analysis.
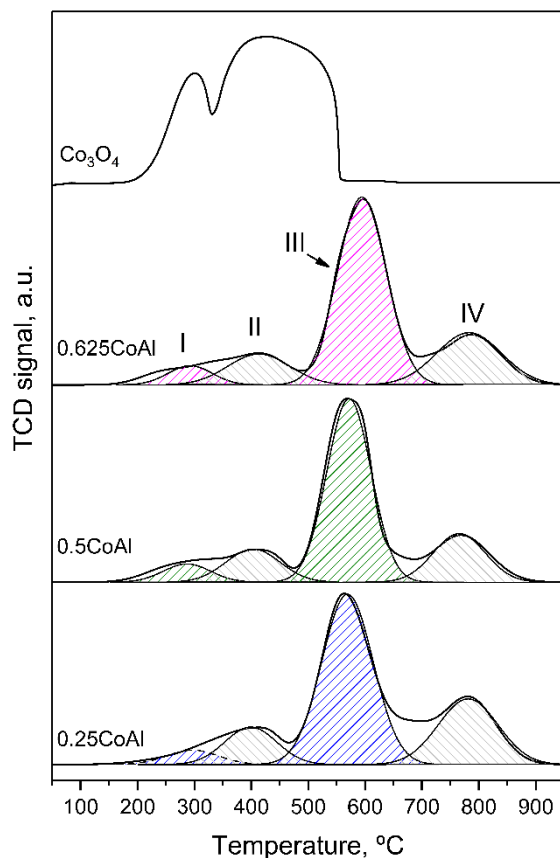
Figure 3.2. H_2-TPR profiles of xCoAl spinel samples.

For a more comprehensive discussion of the profiles obtained in the reduction of xCoAl samples, reducibility of bulk CoO and Co/Al_2O_3 were also analysed (Figure 3.4). CoO was purchased (Alfa Aesar) while Co/Al_2O_3 was synthesized by wet impregnation of γ-alumina, at Co/Al = 0.5 mole ratio, and calcined at 500 and 800 °C. The H_2-TPR profile of CoO exhibited a relatively broad reduction signal in the 250-750 °C range, with two peaks, first at 400 °C and a second, intense and broad peak, with a maximum at 610 °C, in line with literature [225]. For CoO, hydrogen consumption (13.5 mmol$_{H2}$·g^{-1}) was slightly above the stoichiometric value (13.3 mmol$_{H2}$·g^{-1}), which could be ascribed to the complete reduction of Co^{2+} ions to metallic Co and the coexistence of trace amounts of fully oxidized cobalt species on the surface of CoO, as it was observed by FTIR

(discussed below). H$_2$-TPR of Co/Al$_2$O$_3$ calcined at 500 °C (Figure 3.3) exhibited a low temperature peak (355 °C) attributed to reduction of Co^{3+} to Co^{2+} while the Co^{2+} to Co^0 reduction stage showed the contribution of three peaks (at 474 °C, 585 °C and 670 °C) depending on the interaction extent with the support. The formation of CoAl$_2$O$_4$ was clearly detected in the sample calcined at 800 °C. This evidence provided the means to conclude that the counter diffusion of Co and Al ions, necessary to form cobalt aluminate, was promoted by the high calcination temperature.
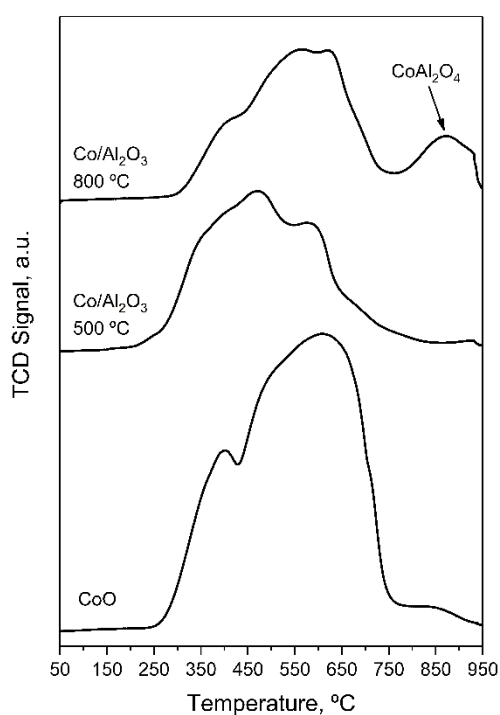
Figure 3.3. H$_2$-TPR profiles of reference samples.

All the xCoAl samples exhibited four reduction peaks. The first two peaks, named peaks I and II and centred at around 300 and 400 °C, respectively, were ascribed to the reduction of Co^{3+} to Co^{2+}. The former was related to the surface cobalt cations without any interaction with the alumina or cobalt aluminate phase. Peak II, meanwhile, was assigned to the reduction of Co^{3+} species in close interaction with alumina and/or cobalt aluminate. This assumption was based on the findings of author Kung et al. [226] who reported that Al^{3+} ions polarize

the Co-O bonds in the spinel-like mixed oxide thus increasing its reduction temperature. The reduction peak at around 580 °C (peak III) was assigned to $Co^{2+} \rightarrow Co°$, and finally, peak IV was assigned to the reduction of cobalt ions in the cobalt aluminate ($CoAl_2O_4$) phase [227].
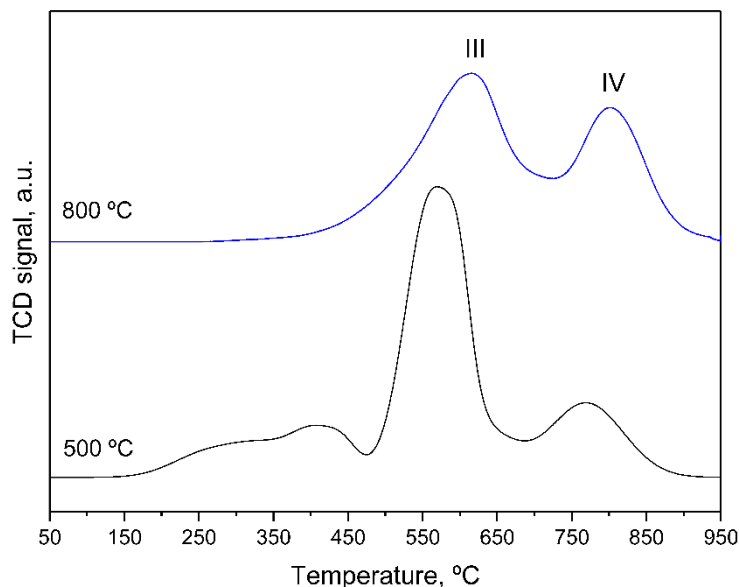
Figure 3.4. H_2-TPR profiles for 0.5CoAl calcined at 500 and 800 °C.

In order to confirm the assignment, the stoichiometric sample (0.5CoAl) was calcined at 800 °C and submitted to H_2-TPR analysis (Figure 3.4). As was be expected, calcination at 800 °C notably decreased the hydrogen consumption at below 600 °C whereas it was increased at high temperature (peak IV). Indeed, formation of $CoAl_2O_4$ phase is favoured at high calcination temperature [228]. Thus, it could be reasonably assumed that peak IV reflects the reduction of cobalt in the cobalt aluminate phase. It is interesting to note that peak III significantly shifted to higher temperatures in the xCoAl samples (by about 150 °C) as compared with bare Co_3O_4. The interaction between the cobalt ions and the support (mixture of alumina and cobalt aluminate) notably hindered both reduction steps, Co^{3+} to Co^{2+} and Co^{2+} to $Co°$. The latter occurred at the highest temperature for catalyst 0.625CoAl. Indeed, this strong Co-support interaction led to an elevated Co dispersion (Table 3.4) and might be attributed to the high cobalt aluminate content of this sample. Co/Al_2O_3 samples prepared

by wet impregnation contained more free cobalt (peak I) than those prepared by coprecipitation. In general, the formation of free Co_3O_4 and cobalt aluminate phases increased with Co loading (Table 3.2). For instance, weight percent of Co_3O_4 accounted for 16.4% in 0.25CoAl and reached up to 34.2% for catalyst 0.625CoAl, while $CoAl_2O_4$ increased from 19.3% to 24.1%, respectively. However, the fraction of cobalt incorporated to the alumina matrix to form cobalt aluminate followed the opposite trend. As a result, the Co mole ratio as $CoAl_2O_4$ to Co_3O_4 significantly decreased from 1.6 to 0.96 with increasing Co/Al. Note that regardless of the Co/Al ratio, the fraction of easily reducible Co_3O_4 particles at the surface remained constant (at around 6%), as inferred from similar contribution of peak I to total hydrogen consumption.
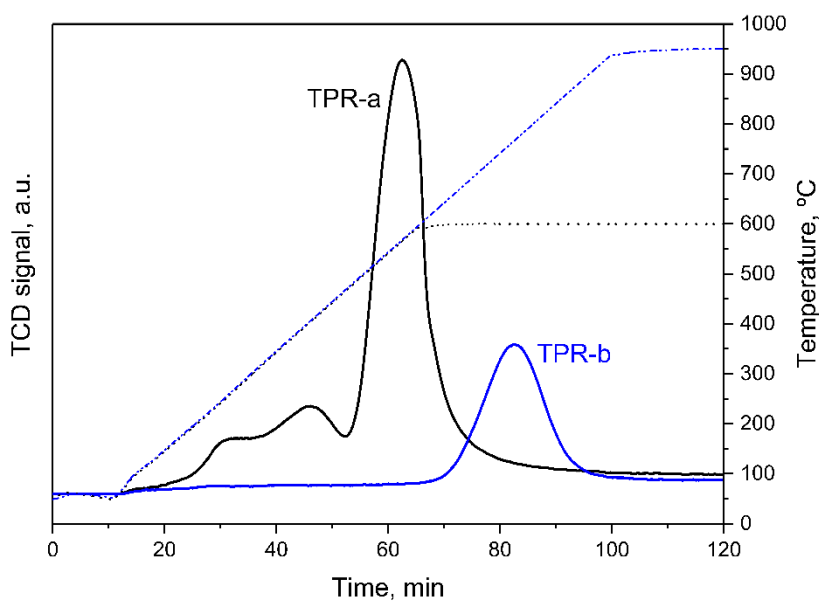
Figure 3.5. H_2-TPR for the sample 0.5CoAl up to 600 °C (TPR-a) and the subsequent at 950 °C (TPR-b).

Based on the above-mentioned H_2-TPR results, xCoAl catalysts were reduced at 600 °C for 2 h prior to catalytic runs. To quantify the amount of reduced cobalt moles after 2 h in 10% H_2 flow at 600 °C (typical pre-treatment in catalyst tests) a double H_2-TPR analysis was carried out for the 0.5CoAl sample: first, at the reduction conditions (600 °C for 2 h, named TPR-a); thereafter, the sample was brought to room temperature in He stream, and then was subjected to a second

Table 3.2. Redox properties of fresh cobalt aluminate spinel samples.

| Sample	H$_2$ uptake, mmol$_{H2}\cdot$g^{-1}					Bulk composition[a]		Co distribution[b]
	Total	Peak I	Peak II	Peak III	Peak IV	Co$_3$O$_4$	CoAl$_2$O$_4$	
0.25CoAl	3.81	0.190 *(291)*	0.492 *(398)*	2.038 *(570)*	1.090 *(780)*	0.164	0.193	1.60
0.5CoAl	5.73	0.348 *(297)*	0.723 *(403)*	3.484 *(572)*	1.175 *(766)*	0.274	0.208	1.03
0.625CoAl	7.04	0.392 *(292)*	0.881 *(413)*	4.407 *(594)*	1.360 *(783)*	0.342	0.241	0.96
Co$_3$O$_4$	17.4	4.70 *(300)*	12.70 *(425)*	0	0	0	0	0

In parenthesis the temperature of the peak (in °C).
[a] weight fraction in catalyst as Co$_3$O$_4$ or CoAl$_2$O$_4$.
[b] Co distribution as bulk CoAl$_2$O$_4$/Co$_3$O$_4$ mole ratio.

reduction step, ramping up to 950 °C, at a heating rate of 10 °C·min^{-1} (named TPR-b). The obtained profiles for 0.5CoAl shown in Figure 3.5 evidenced that the TPR-b only showed the presence of a single reduction peak, centred at 770 °C, corresponding to the reduction of remnant cobalt aluminate spinel. The amount of hydrogen related to this peak was 1.065 mmol$_{H2}$·g^{-1} (giving a reduction degree of 81.4%) which means that all Co$_3$O$_4$ and about 10% of the peak IV, (i.e. that corresponding to CoAl$_2$O$_4$), was readily reduced with the reduction protocol carried out prior to the catalytic runs.

3.2.3   Nature and morphology of the phases
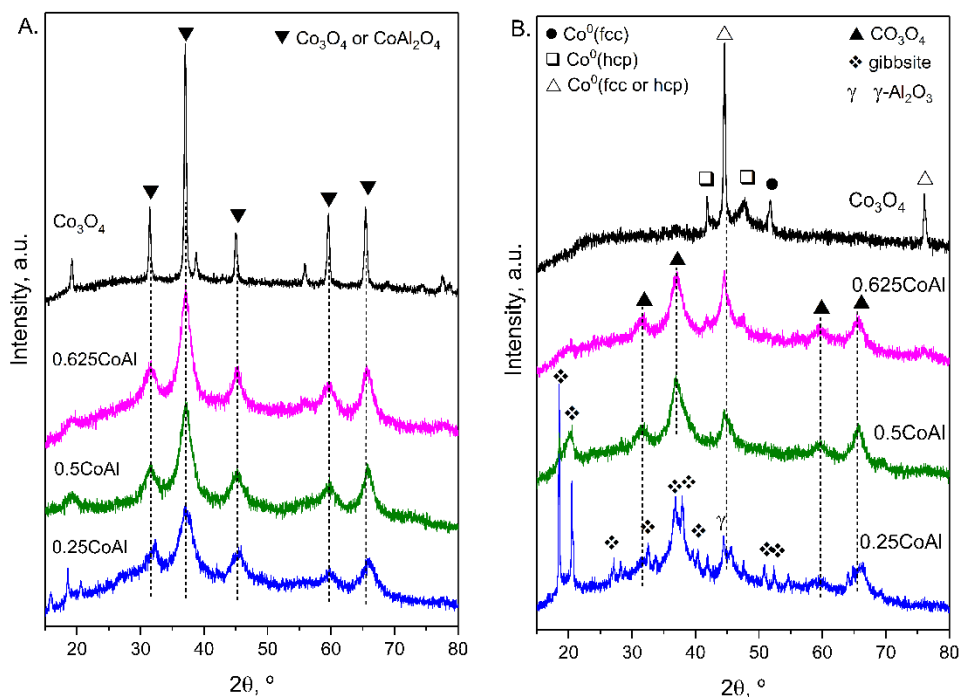
Figure 3.6. XRD patterns of (A) calcined and (B) reduced cobalt aluminate spinels samples.

Figure 3.6 displays XRD pattern of the calcined and reduced samples. All the diffraction peaks of calcined samples were ascribed to both cobalt aluminate (PDF 00-044-0160) and cobalt oxide (PDF 00-042-1467) spinel. It should be pointed out that both Co$_3$O$_4$ and CoAl$_2$O$_4$ crystallize in the same Fd-3m spatial

group and cubic system, which made it difficult to distinguish between both phases by XRD technique.

The crystallite size (d_{spinel}) and lattice parameter (a_{spinel}) of $CoAl_2O_4$ nanocrystals were calculated and tabulated in Table 3.3. Both parameters, d_{spinel} and a_{spinel}, shifted towards higher values as Co/Al ratio increases. The increase in the lattice parameter evidenced a progressive formation of $CoAl_2O_4$ spinel phase. The incorporation of Co^{2+} ions to the $CoAl_2O_4$ lattice brought about its expansion due to the difference in the ionic radii between Co^{2+} (0.74 Å) and Al^{3+} (0.53 Å) [229]. In addition, it seems interesting to note that Co_3O_4 sample showed smaller lattice parameter (0.8059 nm) than that of pure cobalt oxide (0.80837 nm, PDF 00-042-1467), which supports that our sample is non-stoichiometric cobalt oxide.

Table 3.3. Results from XRD studies of the calcined and reduced cobalt aluminate spinel samples.

| Sample	Calcined samples			Reduced samples		
	d_{spinel}, nm	a_{spinel}, nm	I_{220}/I_{440}	$d_{Co(hcp)}$, nm	$d_{Co(fcc)}$, nm	$d_{Co(both)}$, nm
0.25CoAl	3.8	0.7993±0.0058	0.58	*21.0*	*-*	*-*
0.5CoAl	4.1	0.8031±0.0008	0.61	*27.6*	*-*	*18.2*
0.625CoAl	5.0	0.8040±0.0014	0.63	*22.8*	*11.6*	*16.5*
Co_3O_4	19.7	0.8059±0.0008	0.94	*36.4*	*20.1*	*28.3*

The intensity of the (2 2 0) and (4 4 0) planes diffraction was related to the cobalt cations on tetrahedral (T_d) and octahedral (O_h) distribution, respectively [230]. As aforementioned, the ionic radius of Co^{2+} exceeds that of Al^{3+}. Therefore, I_{220}/I_{440} ratio increased with increasing Co^{2+} cations on T_d sites, and the ratio decreased with increasing occupancy of Co^{2+} cations on O_h sites. As deduced from data in Table 3.3, the intensity ratio of these peaks (I_{220}/I_{440}) evidenced a preferential hosting of cobalt in tetrahedral sites. This preference was more pronounced as Co/Al increases. Based on these data, it could be inferred that the spinel corresponded to a mixed structure (intermediated between normal and inverse).

In the reduced Co_3O_4, diffraction lines of metallic cobalt (Co^0) were clearly visible, either in face-centred cubic (*fcc*) (at 51.8°, PDF 00-015-0806) or hexagonal closed packed phase (*hcp*) (at 41.8° and 47.6°, PDF 00-005-0727). However, no diffraction peaks related to oxidized cobalt species (Co_2O_3, Co_3O_4 and CoO) where detected, which implies that all cobalt was reduced. Regarding xCoAl samples, diffraction peaks of spinel phase remained (probably as $CoAl_2O_4$). At the highest Co/Al ratio (0.625CoAl), the presence of both Co^0 phases was confirmed. However, only *hcp* Co^0 was identified in the rest of reduced samples. It has been reported that *hcp* Co^0 crystallites are stable at above 40 nm. Nevertheless, smaller *fcc* metallic cobalt crystallites were measured, which suggests that mixed phases of *hcp* and *fcc* could be present in our catalysts. Ray et al. [231] have reported that *hcp* to *fcc* phase transition of metallic cobalt can occur upon reduction above 400 °C.

0.25CoAl and 0.5CoAl exhibited various diffraction peaks ascribed to gibbsite (PDF 033-0018) and γ-alumina (PDF 01-079-1558). Indeed, water vapour releases during the reduction of cobalt oxide may partially hydrate the γ-Al_2O_3 to gibbsite at high aluminium loading (low Co/Al) [232].

It is noteworthy to point out the notably smaller Co^0 particle size obtained after reduction of xCoAl precursors (between 40–60% smaller than when calcined). Indeed, Co/Al ratio could be used to tune the Co_3O_4 to $CoAl_2O_4$ ratio, and therefore, the environment in which cobalt species are reduced. These results suggested that the strong interaction between Co species and the support in the prepared xCoAl catalysts could effectively improve dispersion of the metallic active phase upon catalysts activation [233]. Growth of the metallic Co nanoparticles was observed, as compared to the parent-calcined spinel, due to the coalescence in the surface of cobalt particles, which migrated from the bulk.
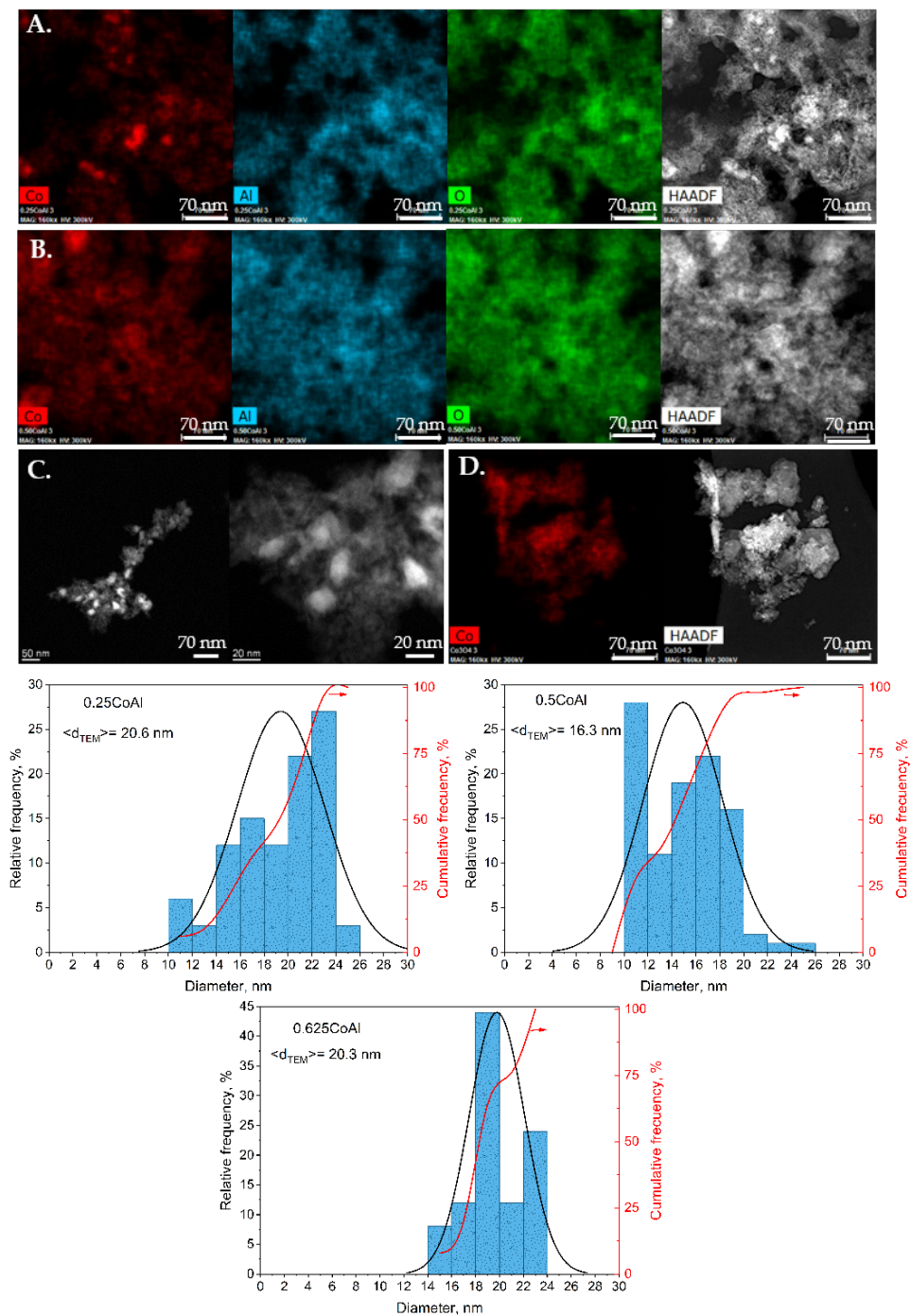
Figure 3.7. STEM micrographs (upper part) and size distribution histogram (lower part) of the reduced catalysts: (A) Co_3O_4, (B) 0.25CoAl, (C) 0.5CoAl and (D) 0.625CoAl.

Scanning transmission electron microscopy (STEM) technique was performed to investigate the morphology of the reduced samples. Figure 3.7 displays their corresponding STEM micrographs and the resulting particle size distribution histograms. Cobalt particles could be optically distinguished from other elements, as STEM mode portrays heavier elements with a brighter reflection. As can be observed, in xCoAl catalysts, cobalt particles were partially dispersed. These catalysts had a general particle size in the range of 10-26 nm, with an average size of 20 nm, very close to the values obtained by XRD. Meanwhile, bulk Co_3O_4 sample presented nearly spherical stacked particles that are difficult to differentiate or measure.

3.2.4   Metallic function

Accessible metallic atoms of the catalysts were titrated by H_2 chemisorption. In addition, the activity of some catalysts, previously reduced, for the dehydrogenation of cyclohexane to benzene was evaluated. Since the latter model reaction is insensitive to the size of the metallic particles, the activity in cyclohexane dehydrogenation is proportional to the number of accessible active metal atoms in the catalysts. Therefore, while the former technique titrates the total accessible metal sites, the latter technique titrates only the active of those sites. The results obtained by these characterization techniques are tabulated in Table 3.4.

Table 3.4. Characterization of the metallic function of the cobalt aluminate spinel catalysts.

Catalyst	Exposed Co atoms [a], at.·g^{-1}	A_{dehyd} [b], mol·h^{-1}·g$^{-1}_{metal}$	TOF_{dehyd} [b], s^{-1}
0.25CoAl	$2.28 \cdot 10^{18}$	1.02	0.34
0.5CoAl	$3.92 \cdot 10^{18}$	1.63	0.43
0.625CoAl	$23.0 \cdot 10^{18}$	1.78	0.59
Co_3O_4	$1.22 \cdot 10^{18}$	0.74	1.61

[a] *from H_2 chemisorption (H:CO = 1:1)*
[b] *from cyclohexane dehydrogenation reaction*

As could be expected, the number of exposed metallic cobalt atoms increased with the Co/Al ratio. Upon reduction, cobalt atoms diffused towards the crystal

surface agglomerating on the solid surface. It is noteworthy, however, that the exposed atoms exponentially increased with cobalt content of binary oxides, and a ten-fold increase was observed from sample 0.25CoAl to 0.625CoAl (2.28×10^{18} to 23.0×10^{18} Co atoms per gram, respectively). Contrarily, bare Co_3O_4 showed the least exposed cobalt atoms, because of sintering, as was explained in the XRD analysis section.

The values of the specific and intrinsic activity obtained in the dehydrogenation of cyclohexane to benzene, indicators of the available active metal sites, are publicised in Table 3.4. The tests were conducted at atmospheric pressure and 250 °C, temperature chosen to minimize cracking/hydrogenolysis reactions. All the catalysts showed a low specific activity, consistent with other results for metallic cobalt [234]. The intrinsic activity (TOF_{dehyd}), based on the number of accessible active metal atoms, was higher for bulk Co_3O_4 catalyst. For xCoAl catalysts, TOF_{dehyd} increased unevenly with increased metal availability. The presence of cobalt oxides in the samples can prevent adequate absorption of cyclohexane, which would explain the low activity of cobalt aluminate catalysts [235].

3.2.5   Structure and coordination state

Infrared spectroscopy was used to verify a particular functional group. The FTIR spectra of calcined and reduced samples are shown in Figure 3.8. Calcined Co_3O_4 sample presented two strong bands in the region of 500-700 cm^{-1}. These bands were due to cobalt-oxygen vibrational mode. The band at 570 cm^{-1} was associated to Co^{2+} (T_d) and the one at 665 cm^{-1} to Co^{3+} in O_h coordination [236]. Sample CoO showed its characteristic broad transmittance band between 400 and 600 cm^{-1}, with a minimum at 465 cm^{-1} [237]. Additional weak band at 660 cm^{-1} was ascribed to Co_3O_4, which was formed by oxidation of surface CoO. Spectra of xCoAl were significantly attenuated in the 400-800 cm^{-1} region, indicating lessening of Co_3O_4. The sharp bands at around 570 and 660 cm^{-1}, characteristics of the spinel phase [238] became more intense as Co/Al ratio increased.

FTIR spectra of reduced xCoAl samples showed broad bands in the 500-800 cm^{-1} range. The shift and growth in adsorption bands may be interpreted as evidence

of cobalt aluminate reduction. Moreover, the absence of CoO and Co_3O_4 was confirmed. As previously shown by XRD data, upon reduction at 600 °C, only metallic Co and cobalt aluminate coexisted. Moreover, a sort of well-defined bands at 3622, 3529, and 3460 cm^{-1} were detected for sample 0.25CoAl, corresponding to the (OH) stretching vibrations of gibbsite [239].
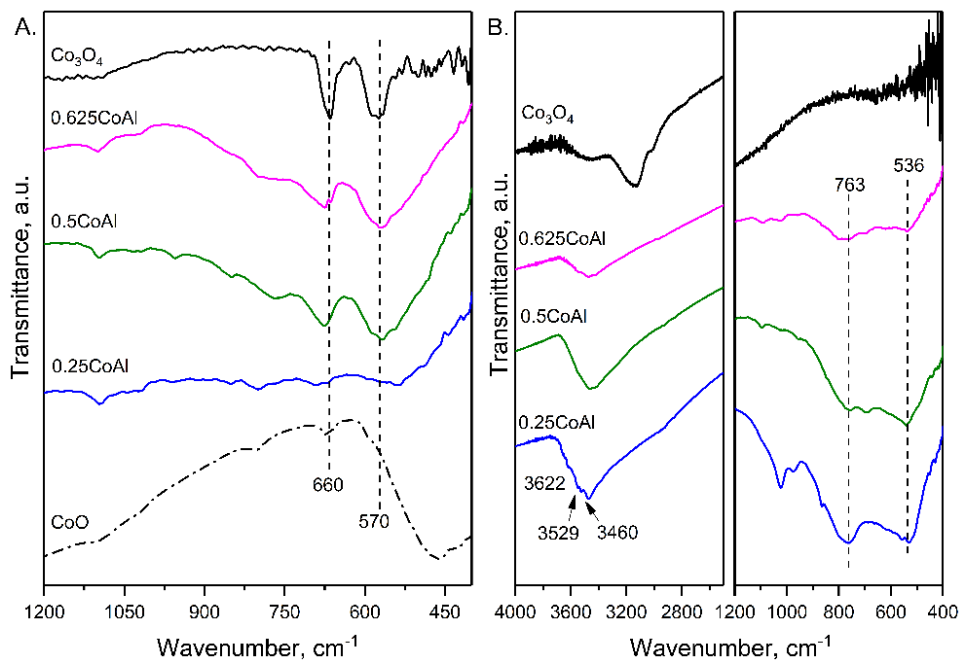

Figure 3.8. Skeletal FTIR spectra of (A) calcined and (B) reduced samples.

Diffuse reflectance UV-vis-NIR spectra of the prepared catalyst and CoO, used as reference, are plotted in Figure 3.9. The spectrum of CoO consisted of two absorption maxima centred at 1265 and 544 nm, with a shoulder at 730 nm. The strong absorption band at 430 nm can be attributed to metal to ligand charge transfers. Accordingly, these bands were assigned to Co^{2+} ions in O_h coordination [240].

Co_3O_4 spectrum showed a broad absorption band at 670 nm attributable to $v_2(^4A_2{\rightarrow}^4T_1(P))$ transition of Co^{2+} (T_d), in agreement with the typical normal spinel structure. Co^{2+} (T_d) was also confirmed in the NIR region (1200-1500 nm) with the presence of a set of bands characteristic of $v_1(^4A_2{\rightarrow}^4T_1(F))$ transition

[240]. Characteristic bands of Co^{3+} (O_h) ions are more difficult to distinguish. According to crystal-field theory Co^{3+} (O_h) shows two bands, at 714 nm and at 434 nm, of comparable intensity associated with $\nu_1(^1A_{1g}{\rightarrow}^1T_{1g})$ and $\nu_2(^1A_{1g}{\rightarrow}^1T_{2g})$, respectively. The presence of octahedral Co^{3+} ions could be deduced from the presence of the broad band, described above, which enclosed the bands of the two Co species (Co^{2+} (T_d) and Co^{3+} (O_h)).
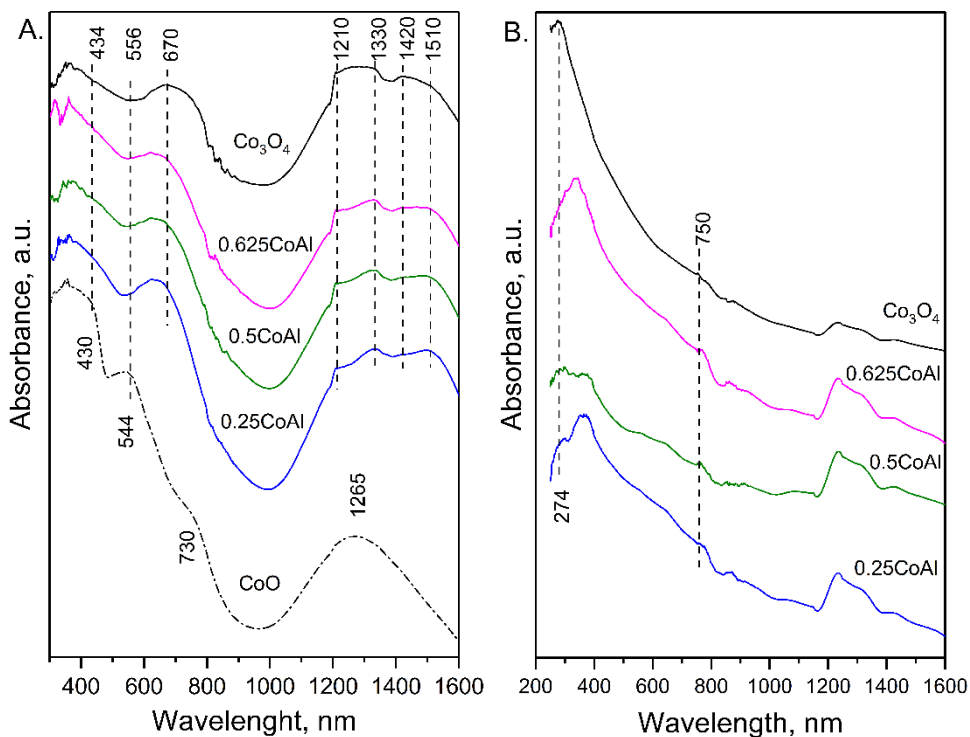
Figure 3.9. DRS spectra of (A) calcined and (B) reduced xCoAl samples.

The spectra of the calcined xCoAl samples was remarkably similar to Co_3O_4. As can be seen from Figure 3.9.A a blueshift occurred in the tetrahedrally coordinated Co^{2+} ions charge transfer transitions (from 670 nm to 556 and 620 nm) and was ascribed to the interaction of such ions with alumina [241]. Two features can be noted at increasing Al content (decreasing Co/Al): (a) The intensity ratio of bands at 1330 to 1210 nm increased, and (b) the ratio 1420 to 1501 nm decreased. Both features could be assigned to the increase in the Co-Al interaction. A more careful analysis of the UV-vis DRS spectra of the calcined xCoAl samples evidenced that the relative intensity of transitions bands in the

UV-vis region with respect to NIR bands decreased with Co/Al ratio. According to Wood and Remeika [242], tetrahedral cobalt structure (which lacks centre of symmetry) exhibits stronger absorption in NIR region than the octahedral cobalt structure (with centre of symmetry). These results indicate an increase in the amount of Co^{2+} (T_d) sites with Co/Al, in line with previously shown in TPR data.

The DRS UV-vis NIR spectra of reduced samples (Figure 3.9.B) confirmed the existence of metallic Co (characteristic absorption band at 274 nm) and the absence of any $Co^{\delta+}$ ionic species (characteristic absorption bands above 300 nm) on Co_3O_4 catalyst surface. However, as could be distinguished by XRD, xCoAl samples presented both above-cited species. In the visible region, all samples showed the characteristic triplet of Co (T_d), although, much less intense than for the calcined counterparts. Furthermore, a new band, ascribed to Co^{3+} (O_h), arose at 750 nm [243]. It is interesting to note that the intensity of NIR region bands corresponding to Co in tetrahedral structure decreased considerable for the reduced samples. This could reflect that the tetrahedral coordination is more easily reducible [244].

Solid-state ^{27}Al NMR was made to inquire about Al coordination in the calcined solids. The spectra (Figure 3.10) showed an intense resonance signal at chemical shift (δ) between 7-9 ppm, characteristic of octahedral site of Al (Al_O). The samples also presented a peak in the region characteristic of tetrahedrally coordinated aluminium (Al_T). For the latter, a shift towards minor values was observed as the Co/Al ratio increased (0.25CoAl= 74.2 ppm; 0.5CoAl= 73.2 ppm; 0.625CoAl= 71.8 ppm), clearly evidencing a transition in the local atomic environments of the cation [245]. The Al^{3+} sites distribution, calculated from the integration of the peaks, resulted in an Al_T percentage of 18.75% for 0.25CoAl, 11.95% for 0.5CoAl and 3.8% for 0.625CoAl sample. The lower peak intensity corresponding to the Al_T for 0.625CoAl sample can be attributed to the increment of cobalt cations on tetrahedral sites (in line with DRS UV-vis-NIR results).

The degree of inversion (γ) of the spinel phase has been determined from the ratio of the intensity of both peaks [246]:

$$\frac{I_{Al_T}}{I_{Al_O}} = \frac{\gamma}{2-\gamma} \tag{3.1}$$

Figure 3.10.B shows that the inversion parameter decreased with the increase of Co/Al, which indicated that the calcined samples had a partially inverted spinel structure, in agreement with the findings from other spectroscopic techniques.
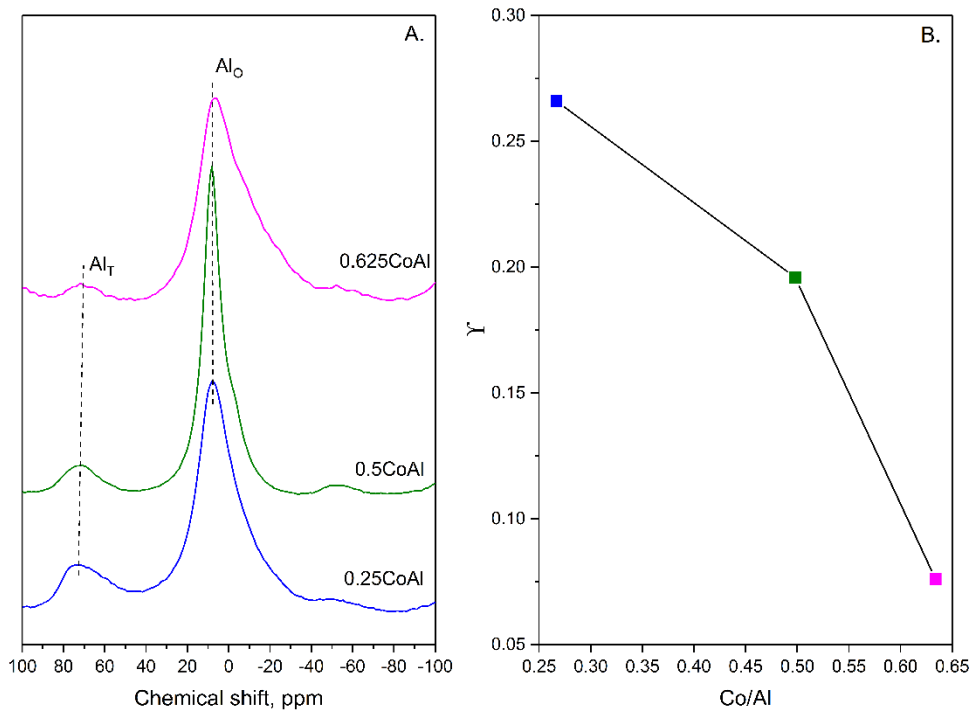

Figure 3.10. ^{27}Al NMR spectra of calcined xCoAl samples (A) and calculated inversion parameters (B).

Surface composition and chemical valence state of the samples was investigated by X-ray photoelectron spectroscopy (XPS). Deconvoluted XPS spectra corresponding to Co 2p for cobalt spinels samples annealed at 500 °C are shown in Figure 3.11. Also, the Co 2p and Al 2p core level binding energy (BE), the spin-orbit separation (ΔE) and other properties are tabulated in Table 3.5. The characteristic peak of Co 2p and Al 2p shifted to higher BE with increasing cobalt loading. The maximum shift observed for 0.625CoAl catalyst confirmed the

strong interaction between Co and Al [247] likely favoured by its high $CoAl_2O_4$ content (as deduced from TPR data). The spin-orbit separation between Co $2p_{3/2}$ and Co $2p_{1/2}$ increased from 15.25 eV for Co_3O_4 to around 15.5 eV for xCoAl samples (Table 3.5), thus confirming a parallel decrease of Co^{3+} [248]. This may be explained by the substitution of Co^{3+} ion by Al^{3+} to form cobalt aluminate on catalyst surface, and the fact that it would result in Co^{2+} enrichment.
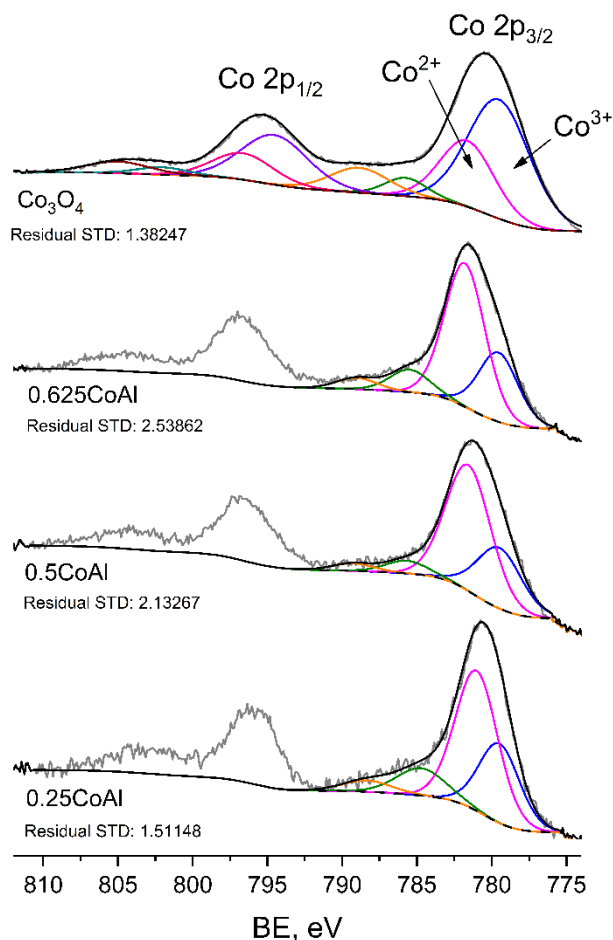
Figure 3.11. XPS spectra corresponding to Co 2p for calcined cobalt aluminate spinel samples.

Table 3.5. Results from XPS analysis for cobalt aluminate spinel samples.

| Catalysts | Al 2p, eV | Co2p$_{3/2}$, eV | | | Co^{3+}/Co^{2+} [a] | Co/Al[b] | Co distribution[c] | Co reduced Fraction[d] |
		Co^{2+}	Co^0	ΔE, eV				
0.25CoAl	75.2 *(74.2)*	780.7 *(781.3)*	*(777.9)*	15.47	0.52	0.124 *(0.041)*	2.9	0.35
0.5CoAl	74.8 *(74.2)*	781.4 *(781.4)*	*(778.2)*	15.45	0.48	0.192 *(0.119)*	3.2	0.27
0.625CoAl	75.6 *(74.2)*	781.6 *(781.3)*	*(778.0)*	15.45	0.48	0.266 *(0.139)*	3.2	0.40
Co$_3$O$_4$	-	780.5 *(779.9)*	*(777.7)*	15.25	2.03	-	-	0.76

Value in parenthesis for reduced samples.

[a] calculated from the contribution of each deconvolution bands to main Co 2p$_{3/2}$ band.

[b] calculated from integrated intensity of Co 2p$_{3/2}$ (with satellite) and Al 2p peaks.

[c] as CoAl$_2$O$_4$/Co$_3$O$_4$ mole ratio. Calculated from Co^{3+}/Co^{2+} assuming formation of stoichiometric Co$_3$O$_4$ and normal CoAl$_2$O$_4$ spinel on catalyst surface.

[d] with respect to total cobalt.
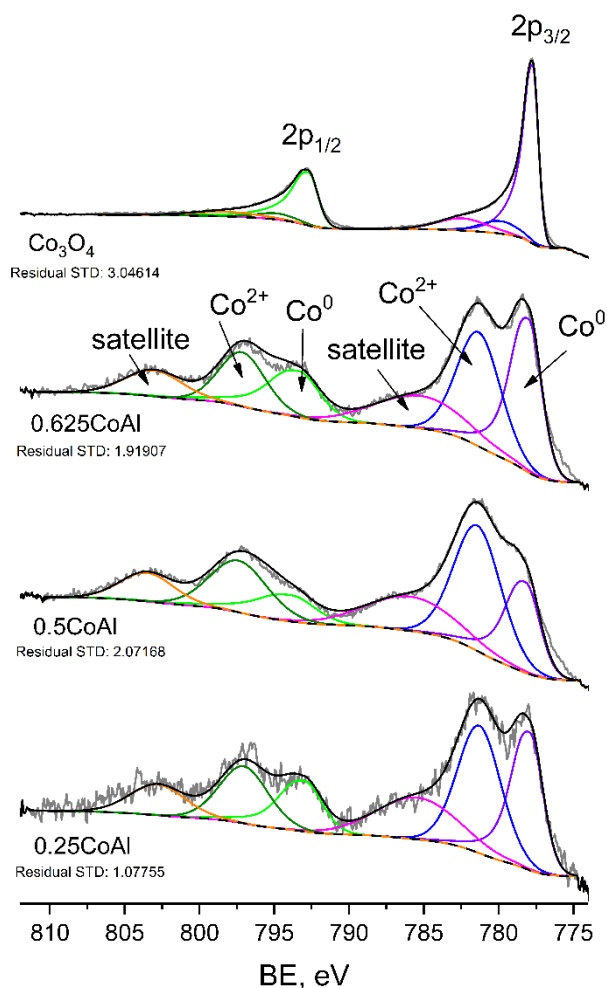
Figure 3.12. XPS spectra corresponding to Co 2p for reduced cobalt aluminate spinel samples.

The asymmetric peak centred at 780.5 eV was split into two components [249]. The peak around 779.5 eV was attributed to Co^{3+} and that occurring at higher BE (around 781.6 eV) was ascribed to Co^{2+} 2p [248]. The satellite features at ≈788 eV supported the presence of Co^{2+} [229]. A relationship between the Co^{3+} and Co^{2+} species was calculated as the ratio of the area of the Co^{2+} and the Co^{3+} signal component Co $2p_{3/2}$ (Table 3.5). Co_3O_4 sample presented a Co^{3+}/Co^{2+} value of 2.03 very close to stoichiometric composition. This value also suggests that Co^{3+} state is octahedrally coordinated to the oxygen anion and Co^{2+} is in tetrahedral positions. On the other hand, and for xCoAl samples, this ratio decreased to

around 0.50 indicating a surface enrichment in Co^{2+} due to increased content of $CoAl_2O_4$ in detriment of Co_3O_4 and suggests that less Co^{3+} ions occupy the O_h positions. Also, the surface cobalt distribution reflected that $CoAl_2O_4$ to Co_3O_4 molar ratio was about 2-3 times larger than bulk composition. It seems interesting to note that contrary to bulk composition, where the $CoAl_2O_4$ to Co_3O_4 ratio decreased with Co loading, on the catalyst surface, it hardly varied among all the prepared xCoAl catalysts.

The overall Co/Al atomic ratio was calculated from Co 2p to Al 2p peak intensities (Table 3.5). In line with the above results, the ratio between Co and Al atoms was lower in surface than in the bulk. This surface enrichment on Al^{3+} ions was attributed to the lower surface free energy of Al as compared to Co [229]. It is interesting to note, however, that the surface Co/Al increased in parallel to bulk Co/Al. TPR data amounted to around 6% of the cobalt loaded that existed as surface $Co^{\delta+}$ species in all the prepared xCoAl samples.

Figure 3.12 shows the normalized Co $2p_{3/2}$ and Co $2p_{1/2}$ XPS spectra for reduced samples. The cobalt 2p spectrum changed substantially as the surface is reduced. As in the calcined samples, the Co 2p emission spectrum was fitted in two spin-orbit doublets. However, after reduction, no peak attributable to Co^{3+} was visible. Therefore, the deconvoluted peaks were assigned to Co^{2+}, Co^0 and shake up satellites. The peak observed at positions 777.8-778.5 eV were attributable to Co^0 and in the region of 785.2-785.9 eV were characteristic satellites of Co^{2+} [250]. The Al 2p peak at the binding energy of 74.2 eV corresponded to Al cations placed at the octahedral sites [251]. Upon reduction, the Co/Al atomic ratio on surface decreased, probably due to the incorporation of metallic species into the porous structure [144]. The calculated fraction of Co^0 is significantly higher for Co_3O_4 sample as could be inferred from H_2-TPR. However, no correlation could be established between reducibility and this fraction for aluminate samples.
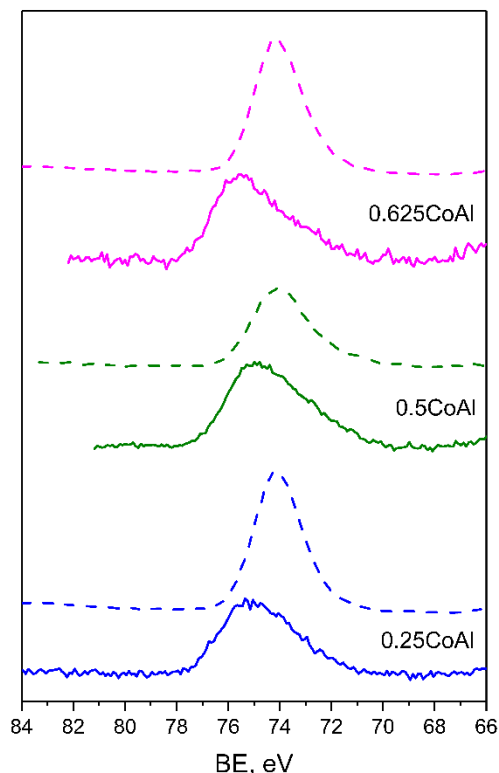
Figure 3.13. XPS spectra of Al 2p for calcined (solid lines) and reduced (dashed lines) cobalt aluminate spinel samples.

3.2.6   Acid-base sites on the catalyst surface

The acid and basic characteristics of the catalysts were evaluated after reduction at 600 °C, and results are summarized in Table 3.6. The exceptionally low acidity of sample Co_3O_4 (0.06 $\mu mol_{NH3} \cdot m^{-2}$) reflects the loss of surface hydroxyls upon reduction. In the case of xCoAl samples, surface density of acid sites decreased with Co loading, from 0.78 $mmol_{NH3} \cdot m^{-2}$ for 0.25CoAl to 0.51 $mmol_{NH3} \cdot m^{-2}$ for 0.625CoAl. This might be related to the formation of Co_3O_4 and cobalt aluminate species instead of alumina. It should be noted that XRD and FTIR analyses revealed the presence of gibbsite at the lowest Co/Al (catalyst 0.25CoAl), which is characterized by large amounts of surface hydroxyl groups that favour acidity [232].

Table 3.6. Acid-basic sites properties of cobalt aluminate spinel samples.

Catalysts	Surface site density		$A_{isom,0}$, $\mu mol \cdot m^{-2} \cdot h^{-1}$
	Acid, $\mu mol_{NH3} \cdot m^{-2}$	Basic, $\mu mol_{CO2} \cdot m^{-2}$	
0.25CoAl	0.78	2.20	3.44
0.5CoAl	0.60	1.95	2.46
0.625CoAl	0.51	1.90	2.84
Co_3O_4	0.06	2.01	51.0
γ-alumina	0.55	0.23	n.d.

The strength of surface acidic sites was assigned as follows: weak acidity (< 300 °C), intermediate acidity (300-650 °C) and strong acidity (> 650 °C), as indicated in Figure 3.14. In the case of γ-alumina, different temperature ranges were used and NH_3-TPD profile was also deconvoluted into three desorption peaks, with maxima at 185 °C, 280 °C and a large peak at 640 °C. Overall, the prepared catalysts contain mainly weak and medium acidity. The general trend suggests that Co loading increased the number of weak acid sites, at the expense of intermediate and strong sites, which significantly decreased as Co/Al ratio increased (specially the medium strength site density). It was assumed that this was due to the increased presence of cobalt on surface (the number of exposed cobalt atoms increased with Co/Al) which would shield the bare alumina.

The model reaction of skeletal isomerization of 33DM1B was performed to titrate the Brønsted acid sites, as Lewis centres are not involved in this reaction. As can be seen in Table 3.6 the initial isomerization activity ($A_{isom,0}$) of Co_3O_4 was much greater than that of xCoAl samples. The reason of the outstanding isomerization activity of Co_3O_4 was not noticeably clear. The most probable reason was its very low S_{BET} (7.4 $m^2 \cdot g^{-1}$). An incomplete reduction of Co_3O_4 to Co^0 in the pre-treatment stage before isomerization activity measurements could also be involved. xCoAl presented a very low activity confirming that Lewis type acidity prevail in these catalysts [252].
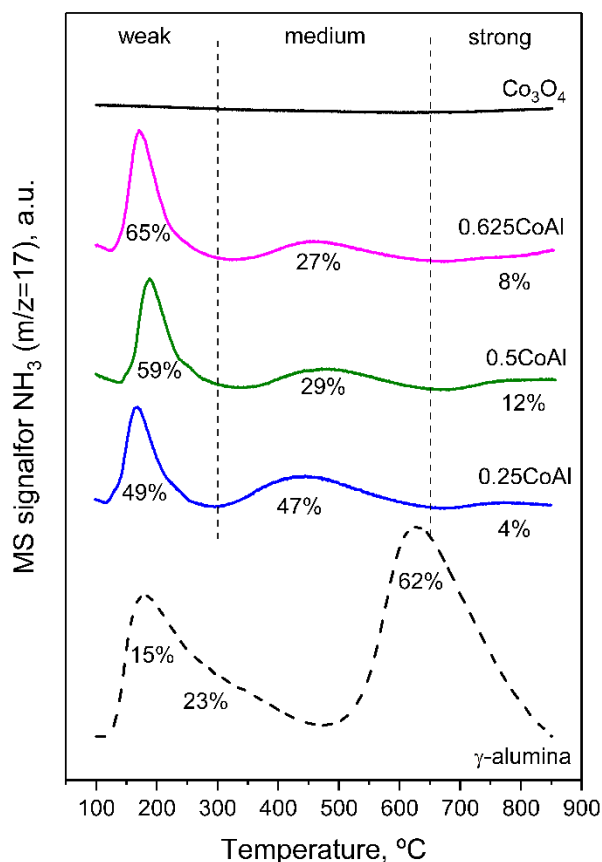
Figure 3.14. NH_3-TPD profiles of reduced xCoAl samples.

The density and nature of surface basic sites was studied by CO_2-TPD. Bare γ-alumina and Co_3O_4 contained the lowest number of basic sites. Co_3O_4 hardly adsorbed CO_2; however, due to its considerably low surface area, surface density of basic sites amounted 2.01 $\mu mol_{CO2} \cdot m^{-2}$. The surface density of basic sites decreased as Co/Al increased. It is interesting to note the predominance of surface basic functionalities in the prepared xCoAl catalysts, as compared to acid ones (sites density ratio basic/acid is around 4:1) [253].

The strength of surface basic sites was evaluated from the CO_2 desorption temperatures (Figure 3.15). The assignment of basic sites was as follows: weak basicity (< 300 °C), intermediate basicity (300-650 °C) and strong basicity (> 650 °C). The low temperature desorption peak of γ-alumina (152 °C, 0.173 $\mu mol_{CO2} \cdot m^{-2}$) was assigned to decomposition of bicarbonates, while the

peak at 670 °C was due to decomposition of unidentate carbonate species adsorbed on strong basic sites [254,255]. On the other hand, xCoAl catalysts contain mainly weak basic sites (> 45%), and a small fraction of strong sites (< 22%). Contrarily to acid sites, the formation of medium strength basic sites was favoured by the Co/Al ratio.

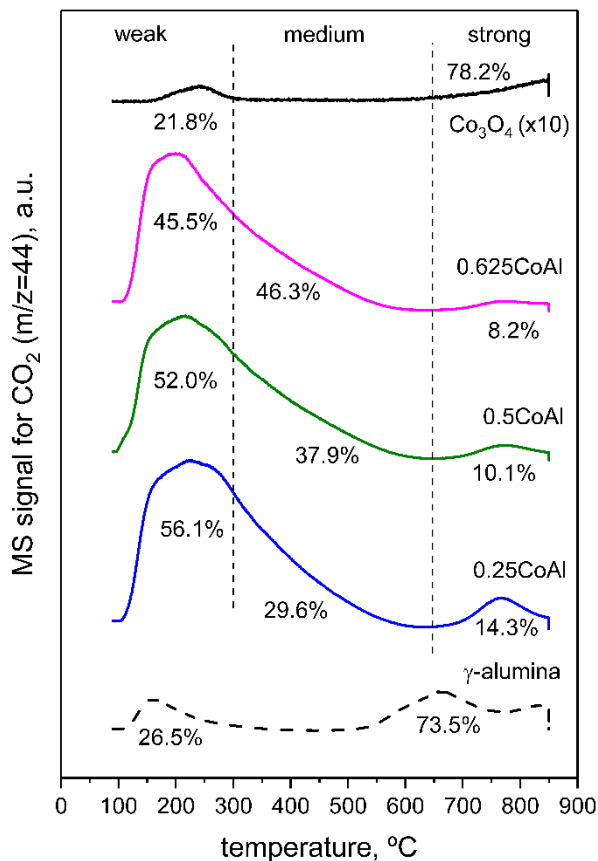**Figure 3.15.** CO_2-TPD profiles of reduced xCoAl samples.

3.3   GLYCEROL DEHYDRATION/DEHYDROGENATION REACTIONS

Glycerol desorption experiments were performed to evaluate the catalytic capacity of cobalt aluminates and cobalt oxide catalysts in the dehydration/dehydrogenation activity. These experiments were conducted in a thermogravimetric (TG) setup coupled with temperature-programmed

desorption (TPD) and online MS analysis. TPD-TG-MS is an agile and feasible methodology to elucidate the viability of catalysts in the APR process.
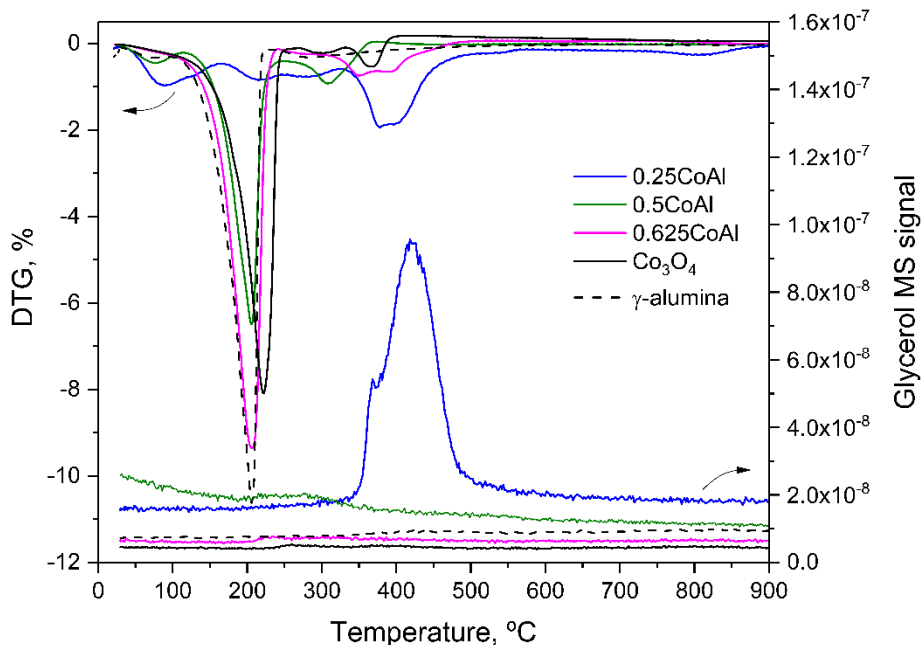
Figure 3.16. DTG-TG and TPD-MS profile of glycerol desorbed.

Glycerol-TPD-TG-MS studies were carried out at constant heating rate of $10\,°C\cdot min^{-1}$ from room temperature up to 900 °C in He flow, upon catalyst sodden by 10 wt.% glycerol/water solution (Section 2.2.8). The mass variation profile was recorded and the desorbed products were monitored by mass spectrometry using the following mass fragments: H_2 (2), H_2O (18), CH_4 (15), formic acid (29), methanol, ethanol and propanol, grouped as R-OH (31), hydroxyacetone (43), CO_2 (44), acrolein (56), propanal (58) and glycerol (61).

The DTG and released glycerol TPD-MS profiles of all the catalysts are shown in Figure 3.16. The DTG profiles presented two main weight loss steps. The first at a temperature below 300 °C and the other in the 300-500 °C range. In the low temperature region, weight loss was around 10 wt.% for catalysts 0.25CoAl and between 30-45% for catalysts with higher Co content. Above 300 °C, 0.25CoAl sample presented the highest weight loss with its maximum at 390 °C, concurring with a strong desorption peak of glycerol.
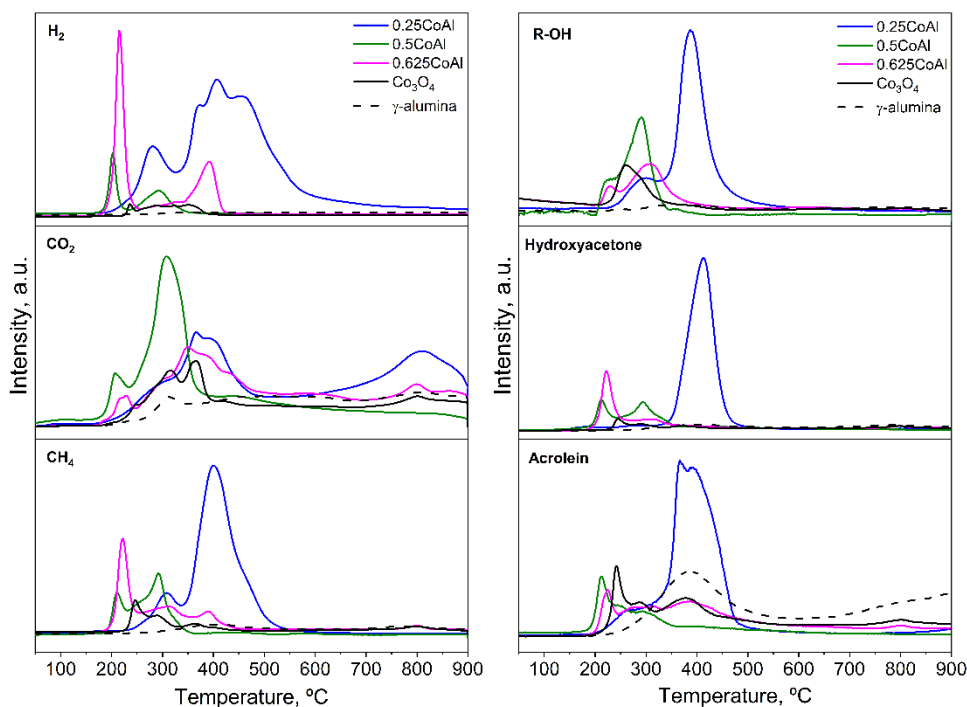
Figure 3.17. MS signals of different species released during Glycerol-TPD analysis.

Based on the aforementioned and analysing the released products (Figure 3.17), it could be inferred that the low temperature weight loss was due to the decomposition of glycerol via dehydration, dehydrogenation and oxidation; while the high temperature weight loss corresponded to both the decomposition and desorption of glycerol. It should be noted that species released in the high temperature interval were likely produced by gas phase reactions since the reaction system approaches the glycerol boiling temperature (290 °C). Therefore, and considering, that the glycerol APR is carried out at low temperatures, the detailed analysis of the products focused on temperatures below 300 °C.

Due to the different MS sensitivity for each desorbing species, the MS signals were normalized giving the value of 1.00 to the largest area of the corresponding MS profile and the results are reported in Table 3.7. The highest yield was attained by 0.5CoAl and 0.625CoAl samples. Catalyst 0.625CoAl showed the highest yield to hydrogen (threefold larger than the second most active 0.5CoAl), methane and hydroxyacetone, while 0.5CoAl catalyst showed

maximum yield to oxidation products such as CO_2, formic acid and alcohols (R-OH). Sample 0.25CoAl manifested a limited glycerol conversion with low yield for all the mass fractions analysed. Even so, this catalyst exhibited a higher relative yield than the Co_3O_4 sample. For alumina calcined at 500 °C, all the desorption products have considerably low intensity (the most prominent peaks corresponded to acrolein and water), which pointed towards the main role of the cobalt.

Table 3.7. Relative yield of products desorbed below 300 °C during glycerol TPD-TG-MS.

Compound	0.25CoAl	0.5CoAl	0.625CoAl	Co_3O_4	γ-alumina
H_2	0.15	0.31	1.00	0.04	0.01
CO_2	0.17	1.00	0.38	0.15	0.14
CH_4	0.23	0.60	1.00	0.18	0.02
R-OH	0.12	1.00	0.59	0.35	0.08
Hydroxyacetone	0.36	0.65	1.00	0.13	0.02
Acrolein	0.28	1.00	0.70	0.60	0.12

The first product released (at lowest temperature) was H_2, with its maximum at about 200-215 °C. Desorption of CH_4 occurred concurrently to hydroxyacetone and acrolein and at a slightly higher temperature than that observed for hydrogen release. Both are primary liquid products of the dehydration pathway [256]. However, desorption of other partial oxidation products such as methanol, ethanol and propanol occurred slightly delayed which reveals these are end chain by-products. A manifest shift in peak maximum to higher temperature was observed for Co_3O_4 catalyst compared to xCoAl samples. The peak maximum for H_2 and acrolein release proceeded at about 205 °C and 210 °C, respectively, for catalysts 0.5CoAl, whereas it occurred at around 233 °C and 243 °C for Co_3O_4. This fact and the higher yield obtained with xCoAl samples demonstrate that cobalt-aluminium interaction improved activity during glycerol reforming. No direct correlation between catalytic performance and total acidity was observed, implying that metal properties strongly affected catalytic activity [257-259].

3.4   GLYCEROL APR

The evaluation of the performance of the synthesized catalysts in the glycerol aqueous-phase reforming reaction has been carried out under two reaction conditions. The catalysts were initially evaluated at 235 °C/35 bar and subsequently, increased to 260 °C/50 bar. These temperature and pressure values were chosen to discern the catalytic behaviour of the samples at both moderate and severe conditions. For both T/P conditions, a 10 wt.% glycerol/water feed and a weight hour space velocity (WHSV) of 24.5 h^{-1} have been used. The chosen large WHSV responds to the purpose of obtaining high concentrations of both gas and liquid products, which assist us in the elucidation of the reaction pathway. The Weisz−Prater and Mears criterion confirmed the absence of internal and external mass transfer limitations (Appendix, Table A.1). The time on stream (TOS) for each reaction T/P condition was 3 h, although the reported data correspond to 1 h TOS, unless otherwise specified. Catalyst pre-treatment, reaction system setup and products characterization techniques are detailed in Chapter 2.

Firstly, aiming to evaluate the homogeneous APR, the reaction was carried out with no catalyst loaded into the reactor; secondly, the APR performance of bare γ-alumina was evaluated. Both runs showed almost null activity, which reflected the critical role of the metallic function during the glycerol conversion by APR. In case of γ-alumina, traces of hydroxyacetone were observed under the most severe conditions, dehydration product owing to its acid property (surface acid sites density 0.55 $\mu mol_{NH3} \cdot m^{-2}$, surface basic sites density 0.17 $\mu mol_{CO2} \cdot m^{-2}$).

3.4.1   Effect of calcination/reduction temperature

A first screening was carried out with the 0.5CoAl catalysts to determine the effect of the calcination temperature and the subsequent reduction in the catalytic performance of glycerol APR. It is a known fact that the complete formation of the $CoAl_2O_4$ spinel-type structure occurs at temperatures above 800 °C [260]. Nevertheless, the main objective in sample preparation was to obtain a spinel-type structure that, after reduction, exerts as a stable support for the extracted metallic cobalt. According to the characterization data previously

discussed, annealing the samples at 500 °C achieves a catalyst with the appropriate characteristics to display high APR performance

In order to visualize in terms of catalytic activity the possible variations caused by the temperature chosen for both calcination and reduction steps, glycerol APR reaction was carried out over 0.5CoAl sample, previously calcined at 500 °C and reduced *in situ* to 600 °C (labelled 500-C_R600). The results have been compared with those obtained from the samples prepared with the same Co/Al molar ratio, calcined at 800 °C and reduced to 600 °C (labelled 800-C_R600) and 700 °C (labelled 800-C_R700).
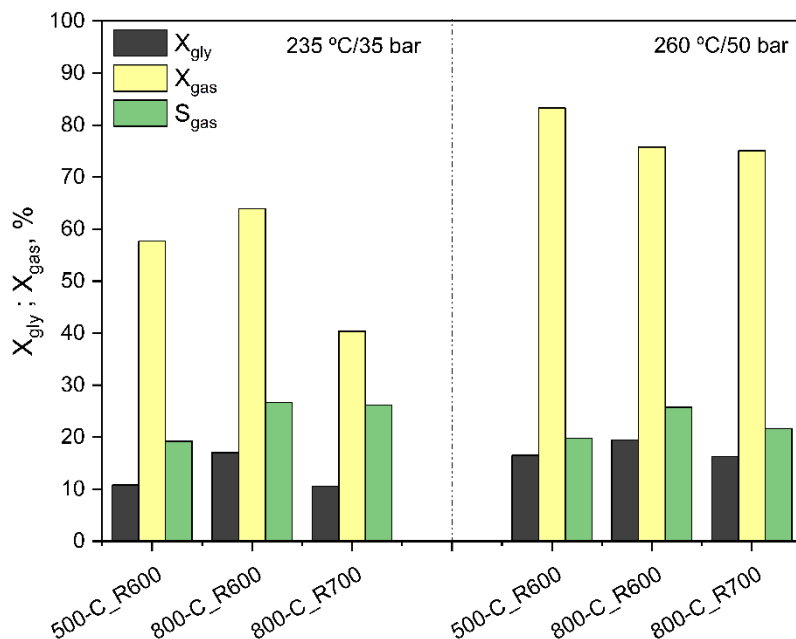
Figure 3.18. Effect of calcination/reduction on glycerol APR activity (glycerol total conversion, carbon conversion to gas and selectivity to gas) at 235 °C/35 bar and 260 °C/50 bar. Reaction conditions: $m_{cat} = 0.5$ g, $L = 0.2$ cm^3·min^{-1}, 10 wt.% glycerol/water, WHSV = 24.5 h^{-1}.
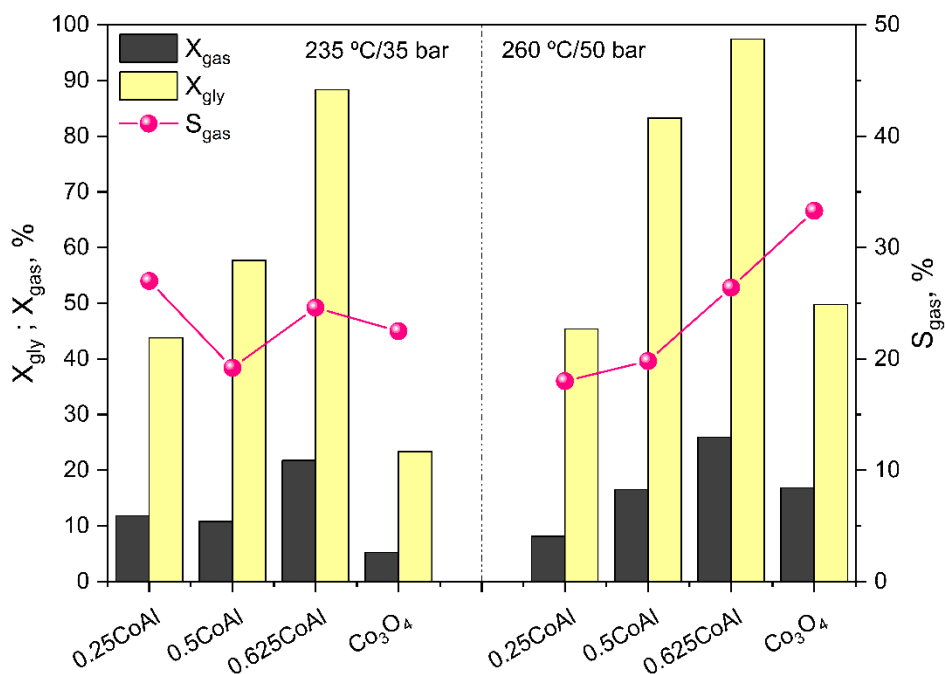
Figure 3.18 shows glycerol total conversion (X_{gly}), carbon conversion to gas (X_{gas}) and selectivity to gas (S_{gas}) of the catalysts at two operating conditions. At 235 °C/35 bar, catalyst labelled 800-C_R600 exhibited slightly higher glycerol conversion than the catalyst labelled 500-C_R600 (64% to 58%) and the highest

carbon conversion to gas (17%). The data obtained at 260 °C/50 bar, showed an increase in both glycerol conversion and conversion to gas for each catalysts (i.e. X_{gly} increased 44.3% for 500-C_R600 and 18.6% for 800-C_R600). However, selectivity to gas remained almost constant, for both catalysts, regardless of operating condition. Catalyst calcined at 800 °C and reduced to 700 °C presented the lowest catalytic activity in both tested conditions, possibly due to the resulting low surface area after reduction (17.8 $m^2 \cdot g^{-1}$).

From the H_2-TPR data, it is known that the sample calcined at 800 °C consumes less hydrogen at temperatures below 600 °C than that calcined at 500 °C. Hence, a higher dispersion of the metallic cobalt is estimated which could explain the greater initial catalytic activity of sample 800-C_R600. To sum up, from an energy requirement point of view, it is not justified to calcine the samples at 800 °C when similar or even better results are obtained by calcining at 500 °C.

3.4.2   Effect of Co/Al molar ratio

The APR potential of the catalysts prepared at different Co/Al molar ratios has been evaluated. Catalytic performance (X_{gly}, X_{gas} and S_{gas}) of these samples are plotted in Figure 3.19. At 235 °C/35 bar, the most active catalyst was 0.625CoAl (X_{gly} = 88.4%; X_{gas} = 21.7%). Glycerol conversion decreased as follows: 0.625CoAl > 0.5CoAl > 0.25CoAl > Co_3O_4. Similar order for conversion to gas was observed: 0.625CoAl > 0.5CoAl≈0.25CoAl > Co_3O_4. At 260 °C/50 bar, the activity of Co-rich catalysts (0.625CoAl, 0.5CoAl, Co_3O_4) increased while performance of catalyst 0.25CoAl hardly varied. S_{gas} varied in the 18–27% range for all the catalysts and both reaction conditions. It seems interesting to note that although the high bulk Co content of catalyst Co_3O_4, its APR performance was much lower than optimum cobalt-aluminate spinel catalyst. The low number of surface exposed Co^0 atoms of Co_3O_4 (i.e. twenty times lower than 0.625CoAl, Table 3.4) could be responsible in spite of its high number of accessible active metal atoms per area. Moreover, Co_3O_4 showed negligible acidity, which is known to facilitate glycerol conversion through the dehydration mechanism. Indeed, it produced the least amounts of hydroxyacetone, which is formed through this mechanism [261]. It could be concluded, therefore, that both metal and acid sites were required for a good APR performance.

Figure 3.19. Catalytic activity of glycerol APR (glycerol total conversion, carbon conversion to gas and selectivity to gas) at 235 °C/35 bar and 260 °C/50 bar. Reaction conditions: m_{cat} = 0.5 g, L = 0.2 cm^3·min^{-1}, 10 wt.% glycerol/water, WHSV = 24.5 h^{-1}.

Conversion to gas was below 30% for the prepared catalysts, thus it could be concluded that xCoAl catalysts decomposed glycerol mainly into liquid oxygenated products, at the employed high WHSV. The effect of WHSV on glycerol APR performance will be further discussed in Chapter 6. High conversion to gas has been related to favourable textural properties [262]. Large surface area would facilitate the adsorption of intermediate molecules onto highly dispersed active phase nanoparticles, facilitating their further conversion into gaseous products. The moderate specific surface area (around 100 m^2·g^{-1}) of the prepared catalysts could limit their gasification potential. It is interesting to note that conversion to gas proportionally increased with the glycerol conversion. That is, the higher the glycerol molecules decomposed, the higher the fraction of C atoms in the feed that were converted into gaseous products. The prepared xCoAl catalysts converted around 24% of the glycerol into gaseous products, regardless of the used catalyst and operation T/P conditions (Figure 3.20).
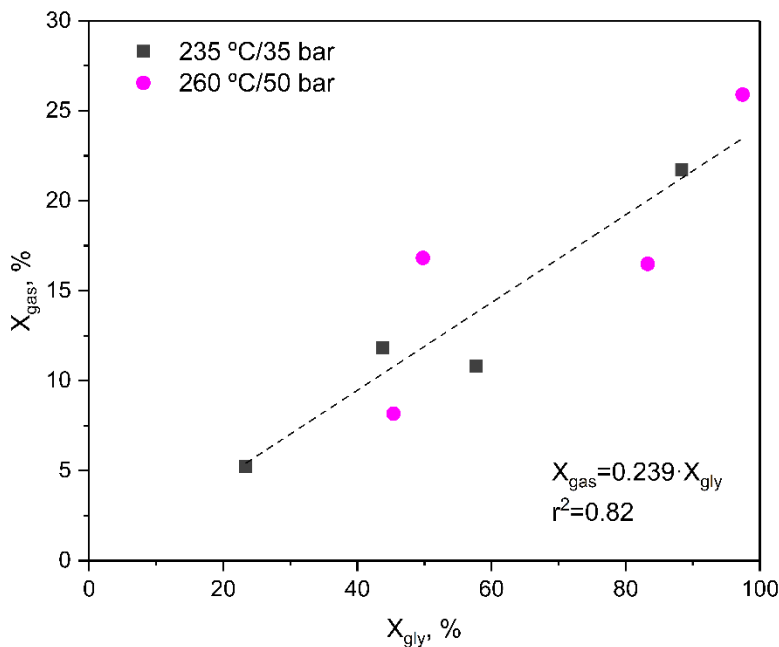
Figure 3.20. Correlation between conversion to gas and glycerol conversion.

It is interesting to note that Co-rich catalysts (0.5CoAl, 0.625CoAl and Co_3O_4) were more sensitive to APR operating conditions. This way, the gasification capability and hydrogen production significantly increased under severe conditions (260 °C/50 bar), while for Co-lean catalysts, the influence of operation conditions was limited.

Table 3.8 reported the relevant parameters of the gaseous products. The main components of the gaseous products were: $H_2 > CO_2 > CH_4 > CO \gg C_{2+}$ (which includes alkanes and alkenes of two or more carbons). Hydrogen concentration in the gaseous stream varied in the 52–63% and 60–75% ranges, under moderate and severe conditions, respectively. The second main product of the gas phase was CO_2 (10–30%), followed by CH_4 (8–14%), CO (0.6–2.3%) and small C_{2+} hydrocarbons (< 6%). Traces of ethane, ethylene, propane, and butane were also detected. The main carbon-containing product was CO_2.

All the catalysts presented a high hydrogen selectivity (greater than 60%). Catalysts Co_3O_4 gave the lowest S_{H2} in both conditions. At this point, it is

important to recall that hydrogen selectivity was defined as the ratio of molar flows in the gas stream of H_2 and H-containing products, that is, the fraction of H atoms that comes out as H_2 with respect to all H atoms in the gas phase. Therefore, any decrease in S_{H2} responds to an increase in the production of methane and other alkanes. In fact, selectivity towards alkanes was also high (S_{alk} = 58.5% and 49.8%, at 235 °C/35 bar and 260 °C/50 bar, respectively). It must be kept in mind that methane is thermodynamically the most favoured compound under APR conditions, especially under low temperature APR conditions [124]. Moreover, cobalt catalysts are known by their high methanation activity [263]. This fact, and the high concentration of strong basic sites (which are known to facilitate methanation [264] at the surface of this assay), would explain the high selectivity to alkanes measured for Co_3O_4 and the increase in the H_2/CH_4 ratio by increasing operation temperature observed for these catalysts.

Catalyst 0.625CoAl, which contained the highest number of exposed Co atoms (23×10^{18} surface Co^0 atoms·g^{-1}, Table 3.4), gave the highest hydrogen yield under both moderate and severe conditions, 10.8% and 14.9%, respectively. The high Co dispersion and the low ratio of acid to basic sites of 0.625CoAl (0.51/1.90) facilitated the initial dehydrogenation of the substrate and somewhat limitation of the side reactions.

Methanation and Fischer–Tropsch reactions take place under similar reaction conditions to APR. Moreover, there is evidence of similar reaction intermediates in both reactions [265,266]. Indeed, the observed behaviour suggested that cobalt could be active for the above two reactions under APR conditions. If WGS occurred, a ratio H_2/CO_2 of 2.33 could be expected at the APR reactor outlet. However, it was 1.73 for 0.625Co/Al what supports H_2 consumption through the above-mentioned side reactions.

Table 3.8. Gas products stream characteristics on glycerol APR at 1 h TOS.

Reaction conditions	Catalysts	S_{H2}, %	Y_{H2}, %	S_{alk}, %	Gaseous products, %				H_2/CO_2 ratio	H_2/CH_4 ratio
					H_2	CO_2	CH_4	CO		
235 °C/35 bar	**0.25CoAl**	70.4	9.5	53.4	61.0	25.8	7.70	1.41	2.36	7.95
	0.5CoAl	66.3	6.8	51.3	54.5	27.6	12.8	0.64	1.98	4.27
	0.625CoAl	64.3	10.8	44.9	52.2	30.1	11.1	0.93	1.73	4.71
	Co₃O₄	60.9	9.4	58.5	62.6	17.0	14.0	2.30	3.69	4.47
260 °C/50 bar	**0.25CoAl**	75.0	10.9	62.2	75.4	9.52	8.80	2.04	7.96	8.57
	0.5CoAl	75.1	10.4	52.4	63.0	22.8	10.0	1.83	2.76	6.29
	0.625CoAl	69.7	14.9	39.3	59.6	24.9	12.0	0.92	2.39	4.98
	Co₃O₄	65.0	13.3	49.8	64.1	17.4	12.7	1.90	3.69	5.06

× Liquid products

Liquid products yields in the condensable phase is shown in Figure 3.21.A and B. The most abundant liquid product was propylene glycol, followed by hydroxyacetone and ethylene glycol. In addition, trace amounts of ethanol, methanol, acetone, acetaldehyde, propanal, 1-propanol and 2-propanol were also detected for all the catalysts. Overall, there was a clear predominance of oxygenated C_3 compounds as compared to C_2 or C_1 compounds, which would reflect a weak to moderate capability of cobalt aluminate catalysts for direct C-C bond cleavage.
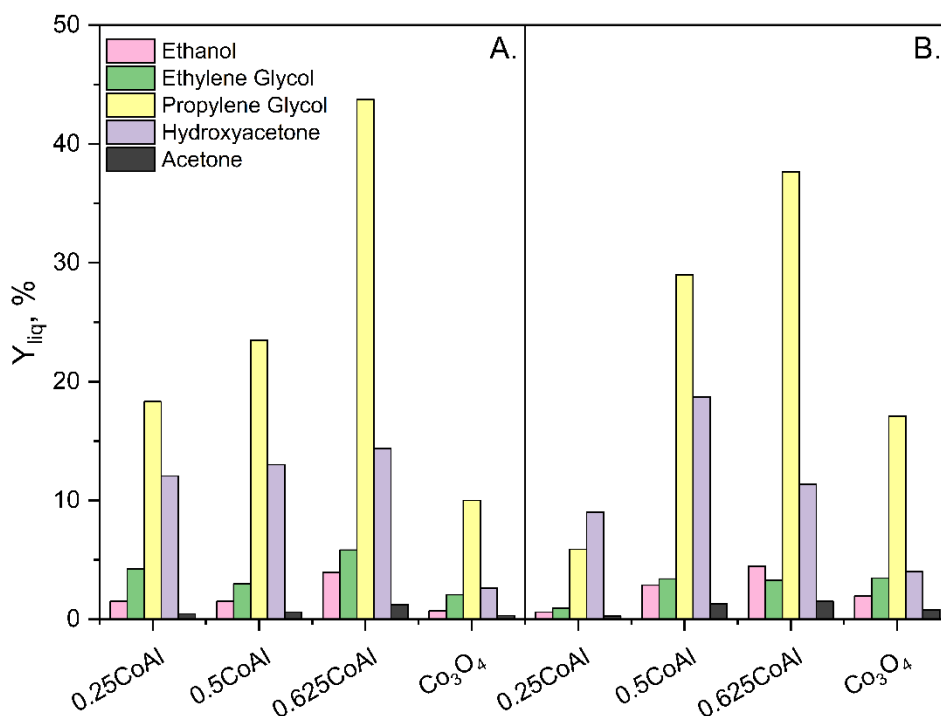
Figure 3.21. Liquid products yields of glycerol APR at (A) 235 °C/35 bar and (B) 260 °C/50 bar. Reaction conditions: $m_{cat} = 0.5$ g, $L = 0.2$ cm^3·min^{-1}, 10 wt.% glycerol/water, WHSV = 24.5 h^{-1}.

The wide variety in the obtained liquid products confirmed the complexity of the glycerol APR process, where reactions of dehydration, dehydrogenation and hydrogenolysis take place, together with the reforming of the intermediate compounds. Based on the obtained product distribution, a possible reaction

pathway for our bifunctional catalysts is depicted in Scheme 3.2, which comprises two main routes: dehydrogenation to glyceraldehyde, preferably on metal sites, and dehydration to hydroxyacetone, mainly on acid sites. The comparatively higher yield to hydroxyacetone and propylene glycol of all the assayed catalysts indicated that the dehydration route was dominant. This can be seen in Figure 3.22, where the ratio between products from direct dehydration (propylene glycol and hydroxyacetone) to dehydrogenation (ethylene glycol) in the liquid-phase clearly exceeded unity (varied in 4-10 range). Moreover, a linear correlation was found between this ratio and the density of surface acid sites. It is accepted that hydroxyacetone is formed by elimination of primary hydroxyl group of glycerol while 3-hydroxypropanal is formed by elimination of the secondary. 3-hydroxypropanal was not detected among the condensable phase products, which implies a higher reactivity of the primary hydroxyl by our catalysts. Also, as previously noted, these catalysts have a majority of Lewis sites, which were reported to favour dehydration towards hydroxyacetone rather than to 3-hydroxypropanal [267]. This could explain the absence of the latter among the condensable phase products. Also, the very scarce acidity of Co_3O_4 (Table 3.6), would explain the much lower production of hydroxyacetone and propylene glycol by this catalyst. Unlike glycerol TPD experiments, acrolein was not produced during glycerol APR reactions. It should be pointed out that H_2 and acrolein production during Glycerol-TPD (Section 3.3) occurred at different temperatures, whereas during glycerol APR this aldehyde may have been hydrogenated to 1-propanol.

According to Scheme 3.2, propylene glycol is formed by the hydrogenation of hydroxyacetone. Since hydrogen is consumed for the formation of propylene glycol, high yield to this by-product could be in direct relation to a high hydrogenolytic capacity accompanied by limited hydrogen production. However, 0.625CoAl still presented the highest hydrogen yield, which reflected that both routes of dehydration/hydrogenation and dehydrogenation were present. The moderate concentration in liquid product of ethylene glycol, which was produced from dehydrogenation/decarbonylation of glycerol, would support the abovementioned idea. It also points to the high C–C, C–H cleavage activity of catalyst 0.625CoAl, accompanied by an increased production of hydrogen.
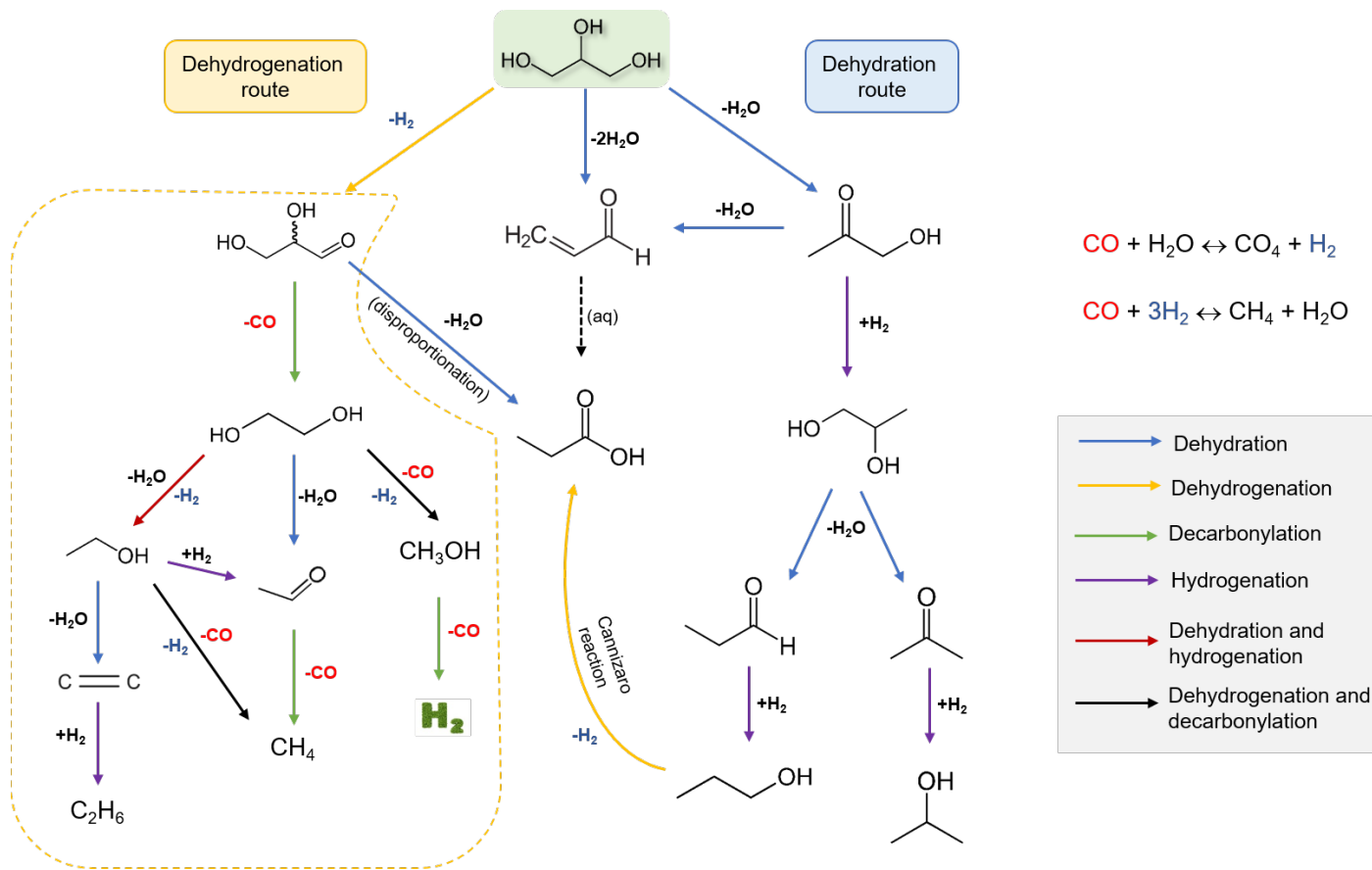
Scheme 3.2. Reaction pathways for glycerol APR over cobalt aluminate spinel-derived catalysts.
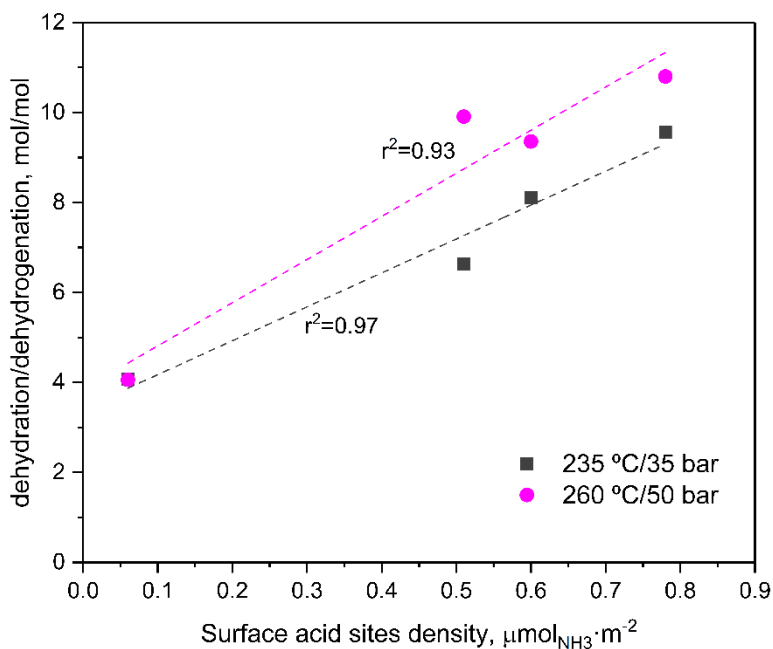
Figure 3.22. Ratio of dehydration to dehydrogenation in the liquid products as a function of surface acid sites density.

As previously noted, 0.5CoAl and 0.625CoAl catalysts were characterized by the lowest total acidity but the largest surface density of weak and medium strength acid sites. Indeed, these catalysts led to the formation of moderate amounts of oxygenated hydrocarbons in the liquid-phase, which suggests a predominant role of weak and medium strength acid sites (i.e. Lewis sites) in C-O cleavage mechanism rather than strong sites. For the most active catalyst 0.625CoAl, at 260 °C/50 bar, the yield to hydroxyacetone and propylene glycol decreased as compared to that at 235 °C/35 bar (propylene glycol: 0.37 vs 0.43; hydroxyacetone: 0.11 vs 0.14). This behaviour coincided with an important increase in the hydrogen yield of 0.625CoAl with the increase of reaction temperature (Table 3.8: 10.8% vs. 14.9%) what suggests that dehydrogenation, which competes with dehydration route, was significantly favoured under severe conditions. Overall, our experimental results show that catalyst that promoted dehydration reactions led to low hydrogen selectivity, as oxygenated intermediates could be hydrogenated to form alkanes.

3.4.3   Long-term catalytic study over 0.625CoAl

Once the effectiveness of spinel-derived cobalt catalysts has been verified for glycerol APR and, especially, for the production of hydrogen, the stability of the 0.625CoAl catalyst has been studied. As was well stated in the previous section, 0.625CoAl catalyst presented the most advantageous catalytic results. Long-term catalytic runs were conducted at the same WHSV (24.5 h^{-1}) and in both conditions (at 235 °C/35 bar and 260 °C/50 bar). Results, depicted in Figure 3.23, revealed a significant loss of catalytic performance with reaction time, and at substantially lower temperature and pressure.
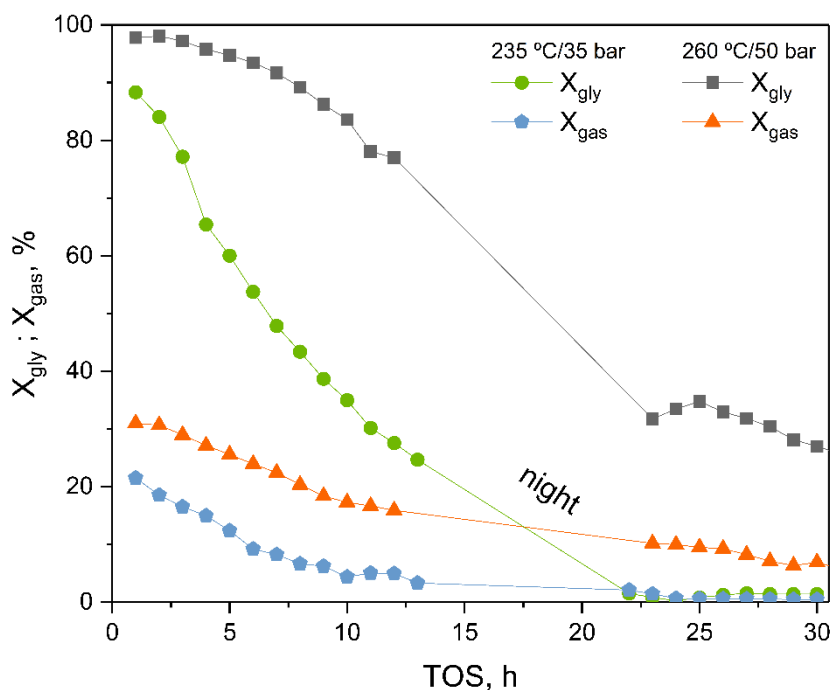
Figure 3.23. Evolution with TOS of glycerol conversion and carbon conversion to gas for 0.625CoAl catalysts at 235 °C/35 bar and 260 °C/50 bar. Reaction conditions: $m_{cat} = 0.5$ g, L = 0.2 cm³·min^{-1}, 10 wt.% glycerol/water, WHSV = 24.5 h^{-1}.

At 235 °C/35 bar, glycerol conversion dropped dramatically from 88.3% in the first hour to 43.4% at 8 h TOS. Obviously, in the course of the same time frame, carbon conversion to gas also exhibited a marked decrease of around 70%. During the first 3 h of reaction, at 260 °C/50 bar, glycerol conversion remained

high, at around 98%, with conversion to gas and selectivity to gas, both showing values of around 30%. Afterwards both X_{gly} and X_{gas} values gradually decreased. After 30 h TOS, both parameters dropped to 27% and 7%. Consequently, the gas outflow decreased from 11 cm³ (STP)·min⁻¹, during the first 3 h, to around 4.7 cm³ (STP)·min⁻¹ at the end of the test. Besides, another symptom of deactivation was the increase of liquid product yield. The reaction network of glycerol APR has consecutive steps; first obtaining liquid intermediates and then subsequent gas products. Thus, decrease in the latter and increase in the former yield pointed to intrinsic deactivation. With regard to the conversion data obtained for both conditions, the research is focused on the most favourable condition for catalytic activity and stability.
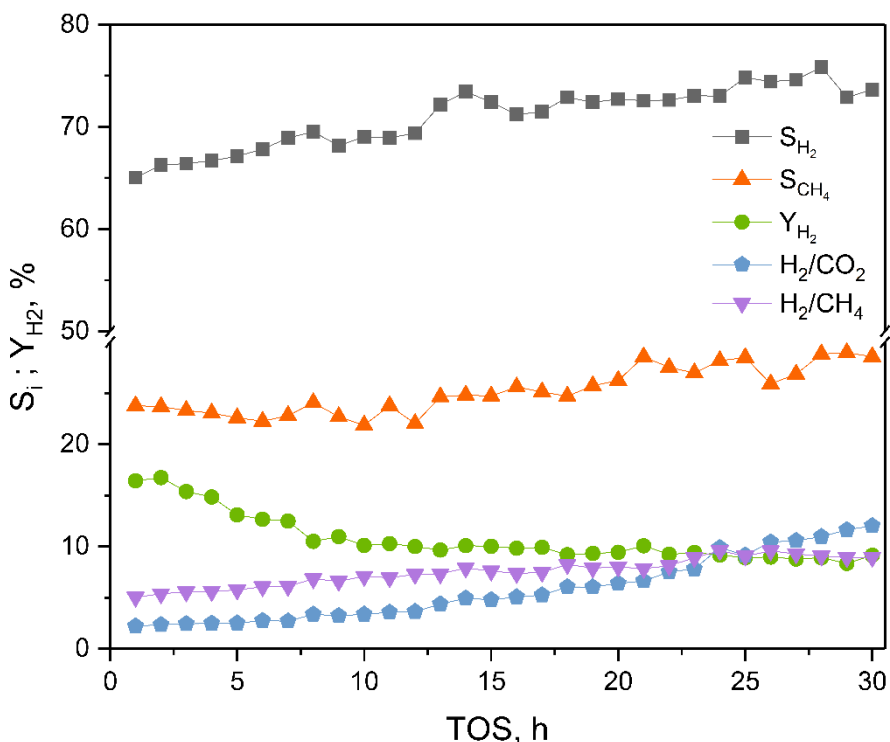
Figure 3.24. Evolution with TOS of S_{H2}, Y_{H2}, S_{CH4} and molar H_2/CO_2 and H_2/CH_4 in the gas phase. Data for 0.625CoAl catalyst at 260 °C/50 bar. Reaction conditions: m_{cat} = 0.5 g, L = 0.2 cm³·min⁻¹, 10 wt.% glycerol/water, WHSV = 24.5 h⁻¹.

The data regarding the composition of the gas and liquid-phase for glycerol APR at 260 °C/50 bar are plotted in Figure 3.24 and Figure 3.25. It is interesting to note that H_2/CO_2 ratio remained very close to the theoretical value ($H_2/CO_2 = 2.3$) at the initial stages of APR reaction and markedly increased (up to $H_2/CO_2 = 12$) with TOS, indicating that secondary reactions have taken on a greater degree.

Regarding the condensable phase (Figure 3.25.A), propylene glycol was the main species among the liquid products throughout all the reaction period (30 h). It is accepted that hydroxyacetone is produced directly from glycerol through the dehydration route. Subsequent hydrogenation of hydroxyacetone can yield propylene glycol [268]. Thus, it suggested that hydroxyacetone was readily hydrogenated over the metallic active sites of 0.625CoaAl catalyst. It was found that concentrations of both propylene glycol and hydroxyacetone increased during the first hours of reaction (i.e. propylene glycol increased up to 38% during the initial 7 h TOS) and at prolonged TOS, dropped off. Other liquid products such as ethylene glycol, ethanol (both from the dehydrogenation route in Scheme 3.2) and acetone (dehydration route) progressively declined throughout all the reaction period. This behaviour reflects that predominant reactions during the initial stages of reaction were different from those measured at prolonged TOS values. It could be interpreted as the hydrogenation reactions (i.e. of hydroxyacetone in Scheme 3.2) occurring more rapidly than dehydration (i.e. of propylene glycol, glycerol) on the acid functionalities on catalyst surface. However, this trend changed as reaction proceeded, and propylene glycol dropped off to around 8%. Such a loss of hydrogenation activity was likely caused by the loss of metallic active sites.

The intense decrease with TOS of X_{gas} and the continuous downward trend in the ethylene glycol concentration, which was formed through the dehydrogenation route, support the above idea. It seems interesting to note that the dehydrogenation rate (that is C-C and C-H cleavage capacity) was more affected by catalyst deactivation as suggested by the progressive decrease on the levels of ethylene glycol, and its derivate ethanol in the liquid-phase. Moreover, the stable profile of hydroxyacetone within all the reaction time, suggests that catalyst still preserved surface acidity. Contrarily, as previously pointed out, propylene glycol and hydroxyacetone yields increased with time during a part of reaction. We hypothesize that this could be due to enhanced acid property on

the catalyst surface, as well as to the oxidation and leaching of cobalt [149] in APR. It has been reported that a part of γ-alumina in the support can be transformed into boehmite as APR reaction proceeds [269]. The surface hydroxyl groups of the latter would increase acidity [148], which would drive reaction mechanism towards the dehydration mechanism. According to Scheme 3.2, the formation of ethylene glycol requires the formation of glyceraldehyde. However, the latter was not detected in the liquid stream. It could be due to its rapid decarbonylation to yield ethylene glycol favoured by the high C-C cleavage activity of Co [270].

The variability of the gaseous phase composition also evidenced these alterations on the reaction mechanisms. Hydrogen concentration continuously increased throughout the long-term APR reaction. C_1 and C_2 gaseous products (i.e. CO, ethylene, ethane), as a result of high C-C cleavage activity, initially increased and levelled off at around 12 h of TOS (Figure 3.25). Contrarily, methane showed the inverse trend, and decreased with TOS. Considering these dynamic conditions, data collected during the first 12 h of TOS were used to calculate the partial correlation matrix (IBM SPSS Statistics 24 software package) and seek correlations between the formation/consumption of the oxygenated hydrocarbons. The obtained Pearson coefficients and p values are shown in Appendix B. A strong and significant correlation was observed between propylene glycol and hydroxyacetone (r: 0.877, $p < 0.001$), which supports that both are intermediate products of the same decomposition route (i.e. dehydration of glycerol). There is also an alternative route in which the glycerol molecule undergoes dehydrogenation/decarbonylation to yield ethylene glycol. Significant and strong correlation existed between ethylene glycol and ethanol/acetone (r: 0.984/0.954, $p < 0.001$) suggesting all of them participate in this reaction chain. Moreover, the correlation between propylene glycol, hydroxyacetone and the latter species was low and statistically not significant (propylene glycol r −0.274 and r −0.197; hydroxyacetone r −0.495 and r −0.449 for ethanol and acetone, respectively). This lack of correlation could be interpreted as being that both the dehydration and dehydrogenation mechanism occurred simultaneously, and independently, in our catalytic system.
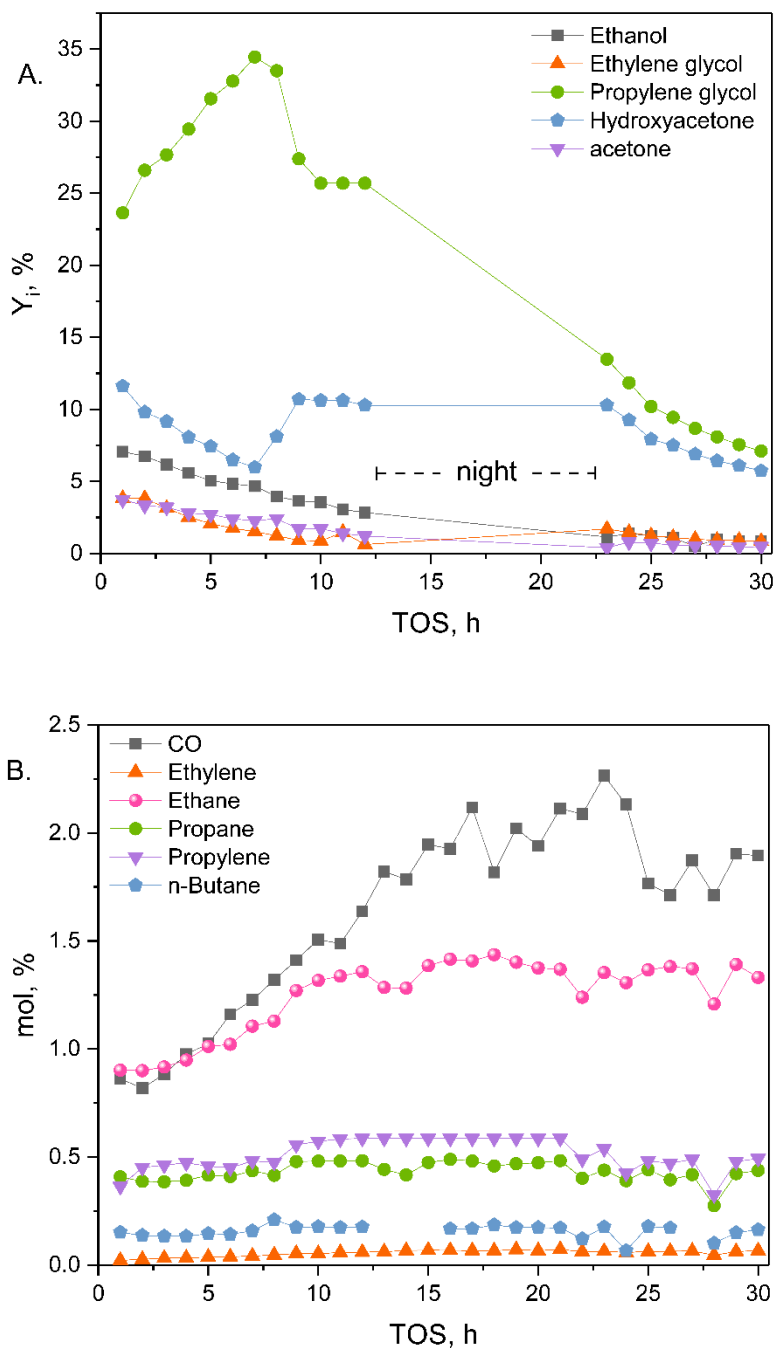
Figure 3.25. Evolution with TOS of (A) liquid yield and (B) gas phase composition. Data for 0.625CoAl catalyst at 260 °C/50 bar. Reaction conditions: m_{cat} = 0.5 g, L = 0.2 cm³·min⁻¹, 10 wt.% glycerol/water, WHSV = 24.5 h⁻¹.

Finally, the correlation between liquid products and those in the gas phase was also analysed. A significant correspondence between levels of the main gaseous products and ethylene glycol, ethanol and acetone in the liquid phase was found to exist. On the contrary, no correlation existed with respect to hydroxyacetone and propylene glycol levels, suggesting that contribution of the dehydration route to production of small gas products was marginal. Indeed, dehydrogenation of glycerol was the main route that produced gas flow.

Regarding the species in the gaseous stream, it is worth pointing to the strong correlation observed between H_2 and CO_2 (r -0,988, $p < 0.001$). The negative value implies the existence of an opposite trend, where selectivity to H_2 increased at the time CO_2 in the gas phase was reduced. This behaviour suggests that WGS reaction, which simultaneously produces H_2 and CO_2, did not pose a relevant role in this catalytic system. The increase with time of CO levels would support the idea of WGS activity decay of the catalyst. As could be expected, a positive and significant correlation between H_2 and alkanes and alkenes (ethane, ethylene, propylene) was found as the latter are formed through hydrogen reforming reaction of intermediate compounds.

3.5   CHARACTERIZATION OF SPENT CATALYSTS

After reaction, the catalysts have been recovered and extensively characterized by specific techniques in order to better know their particular behaviour. The textural properties obtained from the nitrogen adsorption isotherms and the leached metal content obtained by chemical analysis of the liquid product are reported in Table 3.9. The specific surface area and pore volume notably increased after usage, whereas the average pore size decreased. Increase in the specific surface area was more pronounced for samples prepared at low Co/Al (S_{BET} increased by 194% for 0.25CoAl, and about 70% for 0.5CoAl and 0.625CoAl samples). On the contrary, specific surface area decreased by around 21% for sample Co_3O_4. This behaviour suggests that aluminium-based compounds could be involved in such a surface area increase. It is well known that γ-alumina could be hydrated to either the boehmite or gibbsite phase under hydrothermal conditions, as hydroxides are thermodynamically more stable than γ-alumina [271].
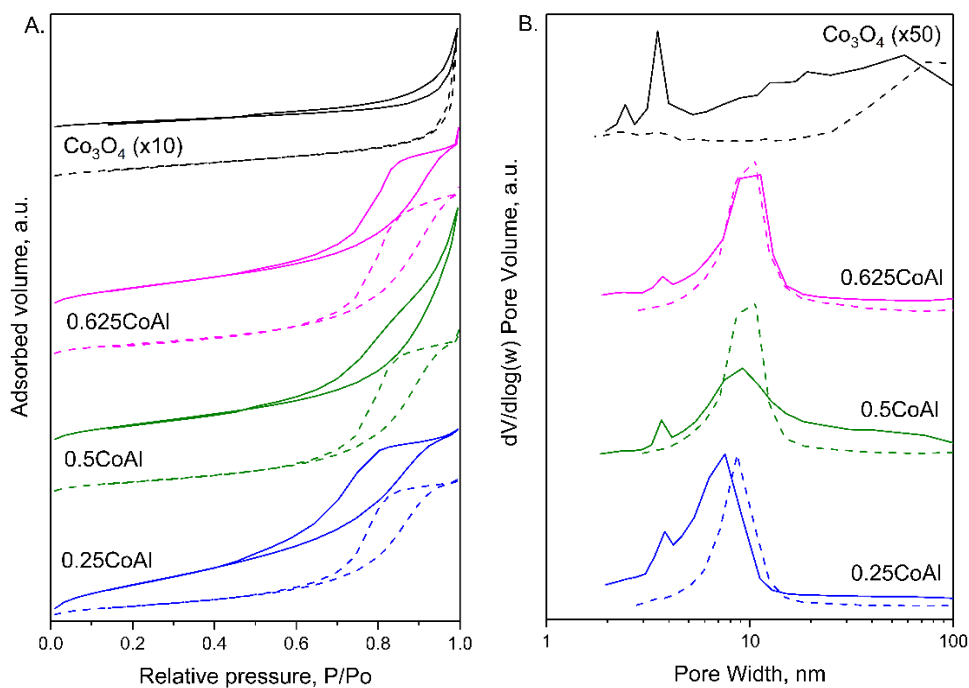
Figure 3.26. Nitrogen adsorption-desorption isotherms (A) and pore size distribution (B) of the reduced (dashed lines) and used (solid lines) samples.

Table 3.9. Textural properties and leached metals concentration from the spent cobalt aluminate spinel samples.

Sample	S_{BET}, $m^2 \cdot g^{-1}$	V_P, $cm^3 \cdot g^{-1}$	d_P, nm	Leached metals, wt.%	
				Al	Co
0.25CoAl	284.4 *(+194%)*	0.456 *(+48%)*	5.7 *(-31%)*	2.2	2.1
0.5CoAl	172.6 *(+68%)*	0.524 *(+46%)*	10.5 *(-11%)*	13.7	3.2
0.625CoAl	178.2 *(+75%)*	0.411 *(+10%)*	8.0 *(-17%)*	1.5	1.6
Co₃O₄	5.8 *(-21%)*	0.022 *(-31%)*	13.0 *(-7%)*	-	0.3

In parenthesis, percentage variation respect freshly reduced samples.

Moreover, hydration of γ-alumina is enhanced in an acidic medium, as occurred in our catalytic system (liquid product stream initial pH: 6.6; final pH: 2.6) due

to the presence of soluble oxygenated compounds and dissolved CO_2. In addition, the aluminium hydroxide can leach from catalysts surface, assisted by acid media [272], which would generate extra porosity in the solid and, thus, increase its specific surface area.
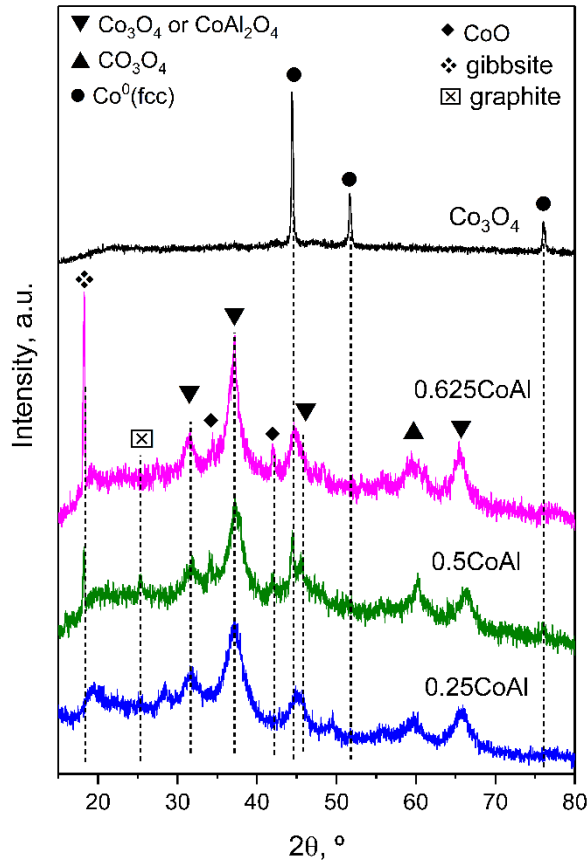
Figure 3.27. XRD patterns of spent cobalt aluminate spinel catalysts.

XRD diffraction lines of *fcc* metallic cobalt were still observed in all spent catalysts (Figure 3.27). Note that both *fcc* and *hcp* phases were detected in fresh samples, which supports the idea of the *fcc* phase being thermodynamically more stable than *hcp* [273]. For all the spent catalysts the cobalt crystallite size notably increased (largest value for Co_3O_4, with d_{Co} = 43 nm, as compared to 20.1 nm as freshly reduced) (Table 3.10). It occurred by coarsening of large particles at the expense of smaller ones [150]. This phenomenon has been

reported to be favoured at high pressures and by the support hydrolysis which breaks the metal-support anchoring [274]. The formation of CoO (PDF 042-1300) and gibbsite was clearly observed for the cobalt aluminate-based catalysts. Under hydrothermal conditions, water can act as a strong oxidizing agent, even in presence of high hydrogen concentration in the gas stream [148].

Table 3.10. Metallic evaluation data of spent cobalt aluminate spinel catalysts.

Catalyst	$d_{Co(fcc)}$, nm	H_2 uptake, $mmol_{H2} \cdot g^{-1}$	Exposed Co atoms, atoms$\cdot g^{-1}$
0.25CoAl	n.d.	3.19	$4.08 \cdot 10^{17}$ *(-82%)*
0.5CoAl	34.4	4.90	$7.71 \cdot 10^{17}$ *(-80%)*
0.625CoAl	25.7	4.98	$9.92 \cdot 10^{17}$ *(-95%)*
Co_3O_4	43.0	1.81	$9.40 \cdot 10^{17}$ *(-23%)*

In parenthesis percentage variation respect freshly reduced samples.

H_2-TPR profiles of the samples after glycerol APR reaction are shown in Figure 3.28 and the quantified hydrogen uptakes are listed in Table 3.10. Spent Co_3O_4 catalyst showed a single reduction peak, centred at 272 °C, which could be ascribed to $Co^{\delta+}$ species with very weak interaction with the support, product of the re-oxidation of the metallic cobalt [275]. It is known that oxidation of cobalt by water may occur, as anticipated by the low values of the Gibbs free energy [149]. Also, the C-O cleavages that occur on the metal particles could contribute to its oxidation [276]. The observed H_2 consumption suggests that around 10% of total cobalt was re-oxidised in this sample. Regarding spent xCoAl catalysts, the amount of easily reducible $Co^{\delta+}$ species, formed as due to the re-oxidation of metallic cobalt during APR of glycerol [141], was notably lower. For instance, in the case of catalyst 0.625CoAl, it accounted for around 3% of cobalt oxide measured in the fresh sample. For catalyst 0.25CoAl, these species were undetected, probably caused by its limited formation, due to low Co loading and leaching favoured by such an acid media. It seems interesting to note the increased H_2 consumption of spent catalyst at high temperatures (at above 600 °C) as compared to fresh samples. Integration of the TPR profile allowed quantifying the cobalt aluminate enrichment at around 31-35% for the exhausted xCoAl catalysts. Moreover, reduction peaks shifted to higher temperatures. We

hypothesize that the lessening of surface cobalt species due to leaching could have limited the spillover phenomena. Also, the observed reduction profile reflects that re-oxidation of metallic cobalt occurred in close contact to aluminium species to form cobalt aluminate. Based on the significant differences in the catalytic performance of Co_3O_4 and xCoAl catalysts, it seems reasonable to assume that alumina species could also have a significant role in the reaction mechanism.
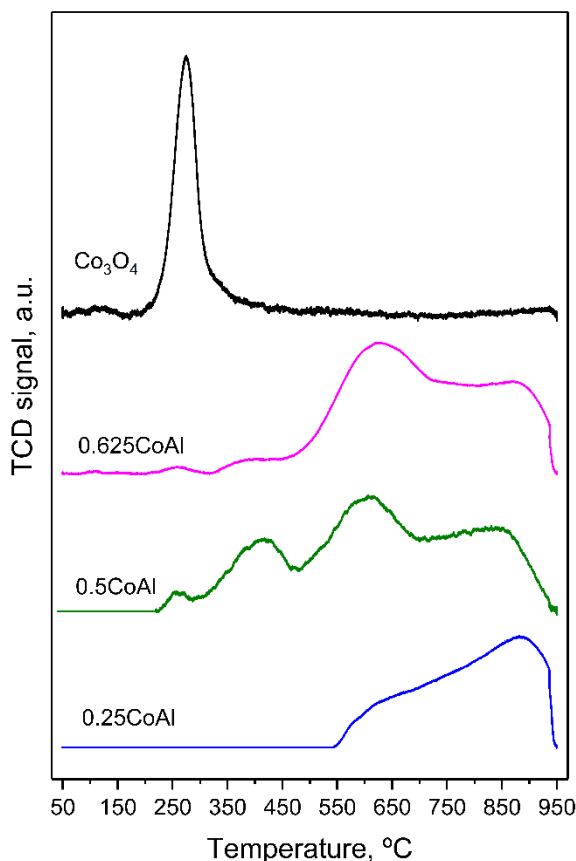
Figure 3.28. H_2-TPR profiles of cobalt aluminate spinel catalysts after glycerol APR.

H_2 chemisorption analyses revealed a decrease of around 80-95% in the exposed Co metallic area for xCoAl catalysts, and much less for bare Co_3O_4. Such a significant loss of active sites would imply a sound re-oxidation of Co particles accompanied by leaching. It was hypothesized that rapid deactivation of the

catalyst when the reaction was carried out at 235 °C/35 bar could be related to a greater leaching of cobalt under these conditions, since the reaction temperature influences leaching [277].

However, the amount of Co leached was not significant, and remained in the 1.6-3.2% range (Table 3.9). Moreover, TPR analyses showed that hydrogen consumption of spent catalyst was not decreased to a large extent. In hot-compressed water, where solubility of inorganic oxide materials is low, it can be expected that hydroxylated alumina that leached off can be re-deposited on the catalyst surface [269]. Indeed, this could have diminished the number of accessible metallic cobalt atoms. For practical application, regeneration of our catalyst, essentially by a reduction treatment [276], would be required to overcome cobalt re-oxidation.

3.5.1   Carbonaceous material deposition

Deposition of carbonaceous materials onto catalyst surface was investigated by Raman spectroscopy (Figure 3.29). Two bands at around 1340-1400 cm^{-1} and 1540-1600 cm^{-1} were observed which were related to the defect/amorphous (D-band) and graphite (G-band) modes of carbon, respectively [278]. According to literature, D-band could be associated to non-deactivating carbon, whereas G-band corresponds to deactivating graphitic carbon [279]. In the Raman spectra of the spent catalysts, both D and G bands of the deposited coke at 1340 cm^{-1} and 1604 cm^{-1}, respectively, were clearly observed. This was in agreement with XRD data of spent catalysts which confirmed the formation of graphitic carbon (2θ = 26.4°) on 0.25CoAl and 0.5CoAl catalysts. In addition, a strong band emerged at 985 cm^{-1} in FTIR analysis of the spent 0.625CoAl (after 30 h TOS), confirming the presence of acrolein, a precursor of coke (Figure 3.30).
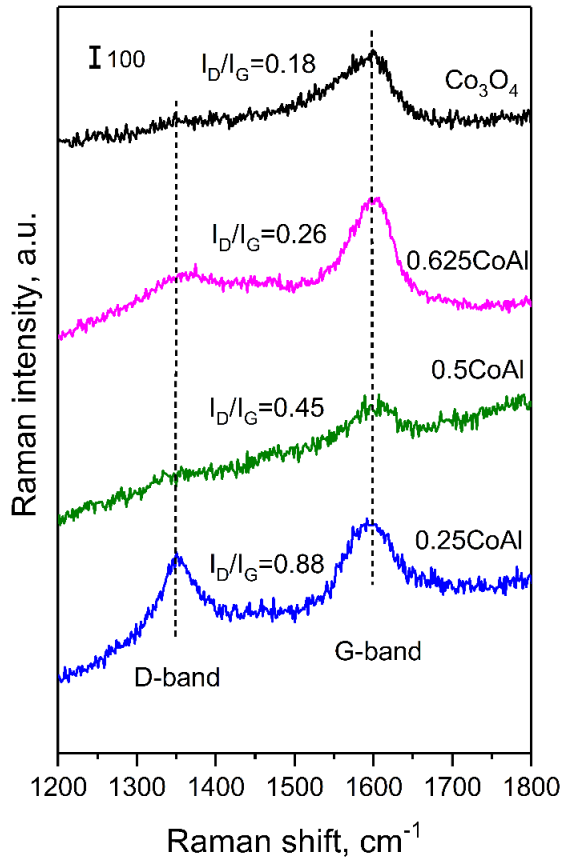
Figure 3.29. Raman spectra of used cobalt aluminate spinel catalysts.

Resuming Raman analysis, bands were considerably broad, which indicated that the coke was highly inhomogeneous in nature. The intensity ratio of D/G (I_D/I_G) bands was used to obtain the coke distribution profiles. The fact that I_D/I_G value was in all cases lower than unity (0.18-0.88 range), suggested deposition mainly of graphitic carbon. Moreover, this ratio decreased with Co/Al. This would also help to understand the observed strong deactivation during the long-term run. Indeed, after long-term run, a greater amount of carbonaceous deposits was quantified when conducted at 235 °C/35 bar (faster deactivation) compared to that carried out at 260 °C/50 bar (9.9 vs 5.3 $\mu mol_C \cdot g_{cat}^{-1}$). As shown in Table 3.6, density of total surface acid sites decreased with Co/Al, being notably low for the reduced Co_3O_4 sample. It could be reasonably hypothesized that carbon deposits were more readily formed during dehydration reactions

over the acid sites, with some contribution of metallic cobalt, being the latter the unique contribution to carbon deposits on Co_3O_4. Coke formation in APR occurs to a much lesser extent than in gas phase reforming, due to higher H_2O/carbon and lower operation temperatures. Carbon deposits were detected in our catalysts, probably formed by polymerization of reaction intermediates on acidic sites.
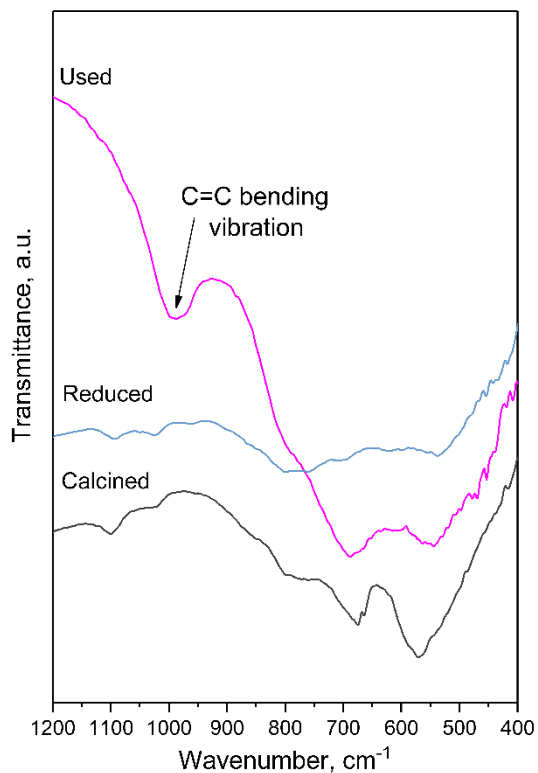
Figure 3.30. FTIR spectrum from 0.625CoAl spent catalyst after 30 h TOS.

3.6   GLOBAL VISION AND SUMMARY

Cobalt aluminate spinels were synthetized by coprecipitation at varying Co/Al ratios with the aim of obtaining active, selective and stable catalysts for the aqueous-phase reforming of glycerol. The catalysts were characterized after calcination, reduced and used.

The compositional and structural characterization of the catalytic precursors has validated the suitability of the synthesis method. The textural analysis has determined that the solids present a mesoporous structure with a moderate specific surface area (around 130 $m^2 \cdot g^{-1}$), which slightly decreased through reduction at 600 °C (to around 100 $m^2 \cdot g^{-1}$ for all the samples).

The reduction of cobalt species in the mixed spinel shifted to higher temperatures as compared to the bare Co_3O_4 reflecting a strong Co-O-Al interaction in the mixed spinels. The formation of spinel structure in the xCoAl series were confirmed by XRD, UV-vis-NIR DRS and FTIR analyses. Moreover, spectroscopic techniques showed a partially inverted spinel structure.

Incorporation of aluminium hindered the crystallization of the Co_3O_4, preventing the formation of large particles. XPS revealed that surface $CoAl_2O_4$ to Co_3O_4 molar ratio was about 2-3 times larger than bulk composition. Consequently, improved Co dispersion was achieved in the cobalt aluminate spinel-based catalysts, with the maximum number of exposed Co atoms in catalyst 0.625CoAl (ten-fold that of Co_3O_4).

The results obtained by temperature programmed desorption of both CO_2 and NH_3 suggest that xCoAl catalysts maintained the surface basicity of metallic cobalt, while the strong acidity of alumina was attenuated. Resultant acid sites were mainly weak and medium strength sites, and the low isomerization activity of 33DM1B denoted a Lewis-type acidity, what could inhibit undesired dehydration and other side reactions.

Glycerol TPD-TG-MS experiments did not show glycerol desorption below 300 °C. Catalyst 0.625CoAl showed higher yields towards H_2, CH_4 and hydroxyacetone, while the 0.5CoAl catalyst showed a higher activity towards glycerol oxidation products.

Cobalt aluminate calcined at 500 °C and reduced at 600 °C proved to be competent for APR performance if the methanation/Fischer-Tropsch activity could be inhibited. For all the catalysts, hydrogen was the foremost gaseous product and the main compounds in liquid stream were propylene glycol and hydroxyacetone. Catalyst 0.625CoAl showed the most promising results with

high X_{gly} and X_{gas}. Furthermore, high Y_{H2} and low selectivity to alkanes were obtained with this catalyst.

It could be concluded that reduction of the Co species on xCoAl catalysts prepared at a Co/Al ratio above the stoichiometric value produced smaller and more stable metallic Co which was more resistant to sintering and coke formation. Long-term catalytic runs (30 h) reported remarkable deactivation, which was mainly attributed to sintering and re-oxidation of active phase with some leaching of Co nanoparticles, favoured by the acidity of the media, and carbon deposition, mainly on acid sites.

The reaction conditions studied (WHSV of 24.5 h^{-1}) made the development of a reaction pathway feasible. Glycerol APR over transition metal catalysts occurs through two main paths: (i) dehydrogenation to glyceraldehyde, promoted by metallic sites, which undergoes C-C scission and subsequently WGS reaction; and (ii) dehydration of terminal hydroxyl groups, and succeeding hydrogenation to yield propylene glycol.

Chapter 4

COBALT ALUMINATE SPINEL-DERIVED CATALYSTS MODIFIED BY CERIUM
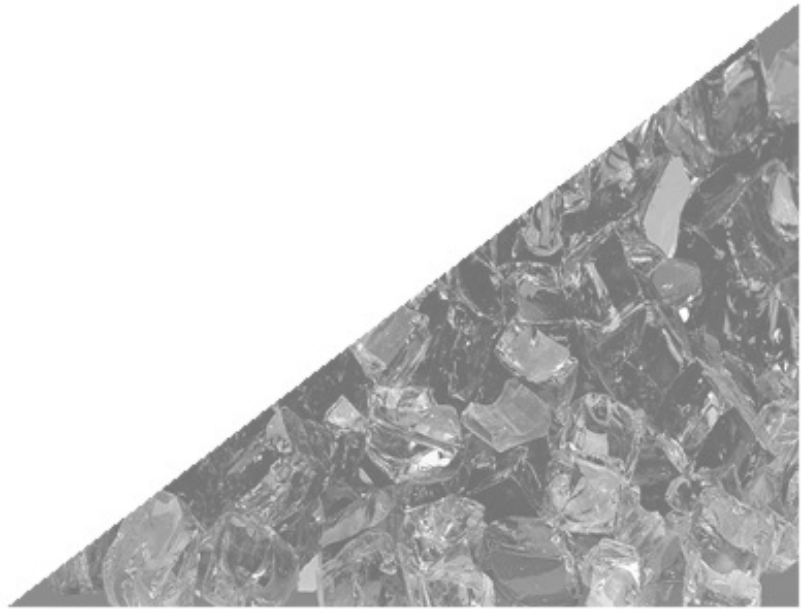
4. COBALT ALUMINATE SPINEL-DERIVED CATALYSTS MODIFIED BY CERIUM

In the previous chapter, the effectiveness of cobalt-based catalysts for glycerol APR, especially the catalyst with the highest cobalt content (Co/Al molar ratio = 0.625), was proven. Nevertheless, this catalytic system has to be improved to overcome long-term catalyst stability limitations caused by cobalt re-oxidation and leaching, together with coke formation. Since promoters can increase the metal-support interaction and the active dispersion of the metal and can also tune the acid/base character of the catalysts [280], adding a promoter is an economical and time-efficient strategy that would prevent leaching and avoid other deactivation phenomena, as well as enhance activity [281].

Several researchers have used cerium to improve the activity and stability of its catalysts in APR and have reported a positive effect, attributed, mainly, to oxygen vacancies in the cerium oxide (CeO_2) lattice that may promote reforming to H_2 and WGS reaction. [119,168,282,283]. Furthermore, its high oxygen mobility promotes H_2O adsorption and dissociation, improving hydrothermal stability and avoiding formation of unsaturated hydrocarbons that are coke precursors [182,284].

Considering the promising results obtained with the catalysts 0.625CoAl and taking into account the aforementioned characteristics of cerium, it was decided to dope the cobalt aluminate spinel with Ce and analyse the effect of dopant content on the catalyst performance in glycerol APR.

4.1 CATALYSTS PREPARATION

Spinel-derived cobalt catalysts modified by cerium were prepared by coprecipitation. For the synthesis of these catalysts, the aforementioned cobalt and aluminium nitrates and cerium(III) nitrate hexahydrate ($Ce(NO_3)_3 \cdot 6H_2O$) were used. As a base, Co/Al molar ratio has been established at 0.625, modifying the centesimal concentration of cerium in the sample.

$$Ce(NO_3)_3 \cdot 6H_2O$$

$$Co(NO_3)_2 \cdot 6H_2O \qquad Al(NO_3)_3 \cdot 9H_2O$$

pH=10 ± 0.5

Na₂CO₃

Filtration &
Washing

Drying   Calcination   xCeCoAl
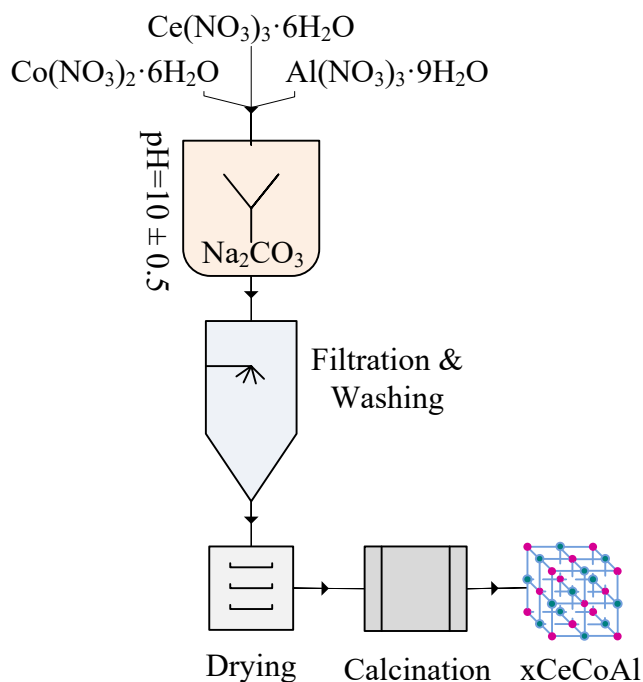
Scheme 4.1. Diagram of the synthesis method of cobalt aluminate spinel catalysts modified by cerium.

Such as in the preparation of the spinel-derived cobalt aluminate solids, proper amounts of aqueous solutions of precursor nitrates were coprecipitated, dropingwise into a sodium carbonate solution. Solution pH was adjusted to 10 ± 0.5, with sodium hydroxide solution (2 M). As can be seen in Scheme 4.1, the resulting suspension was aged at room temperature for 24 h and subsequently, filtered, washed several times with de-ionized water, dried at 110 °C overnight and calcined in a muffle furnace at 500 °C for 5 h, at heating rate of 5 °C·min⁻¹, in a static air atmosphere. This sample was abbreviated xCeCoAl, where x denotes the weight percentage of cerium in the sample. As a reference, CeO_2 was also synthetized by precipitation following the same protocol.

4.2   CATALYSTS CHARACTERIZATION RESULTS

4.2.1   Bulk chemical composition and textural properties

Table 4.1 lists the values corresponding to the chemical analysis, specific surface area, pore volume and average pore size for the prepared samples. Actual metal content measured experimentally by ICP-OES revealed a variation with respect to the nominal value lower than 4.5% for cerium, and a Co/Al ratio slightly higher than nominal.

Table 4.1. Ce content and textural properties of Ce-modified catalysts.

Sample	Ce, wt.%	Co/Al, at·at^{-1}	S$_{BET}$, m^2·g^{-1}	V$_P$, cm^3·g^{-1}	d$_P$, nm
0.625CoAl	0	0.634	125.3 (*101.7*)	0.280 (*0.375*)	6.8 (*9.6*)
0.3CeCoAl	0.29	0.637	148.1 (*138.3*)	0.341 (*0.403*)	6.7 (*8.7*)
0.7CeCoAl	0.67	0.643	162.2 (*130.7*)	0.388 (*0.375*)	7.0 (*8.5*)
2.1CeCoAl	2.15	0.640	146.4 (*131.8*)	0.371 (*0.423*)	7.8 (*9.7*)

Reduced samples in parenthesis

All the isotherms of the calcined solids (Figure 4.1.A) were characteristic of mesoporous materials presenting IV type, with the P/P$_0$ position of the inflection point corresponding to a mesoporous range diameter. The hysteresis shape suggested that the mesopores were randomly distributed and formed by nanoparticles assembling. Except 2.1CeCoAl assay, the other two Ce-doped solids presented the same pore size distribution than pristine 0.625CoAl (Figure 4.1.B), unimodal centred on 6.8±0.2 nm. However, sample 2.1CeCoAl presented a bimodal distribution with a main peak at 7.8 nm and another around 13 nm. The coprecipitation of Co, Al and Ce leaded to an increase in the S$_{BET}$ as compared to 0.625CoAl counterpart (between 17% and 29% increase). Likewise, an increase in pore volume was observed (between 22% and 39% increase). Noteworthy, the increase on S$_{BET}$ and V$_P$ was not monotonic, increasing up to 0.7 wt.% Ce loading and further addition caused lower increase. Only 2.1CeCoAl sample significantly varied the pore size of 0.625CoAl.

After reduction (at 600 °C, 2 h), the specific surface area of Ce-doped solids slightly dropped (up to 19%) as compared to calcined counterparts, with a concomitant increase in the mean pore size values (increase by 21-41%). It should be noted that said increase was less pronounced than that revealed by 0.625CoAl sample (41% vs 21-29%). Compared to 0.625CoAl assay, S_{BET} of xCeCoAl reduced samples was 29-36% higher. Therefore, up to this point, we can conclude that the addition of Ce by coprecipitation notably improved the textural properties of the solid both in calcined and reduced conditions.
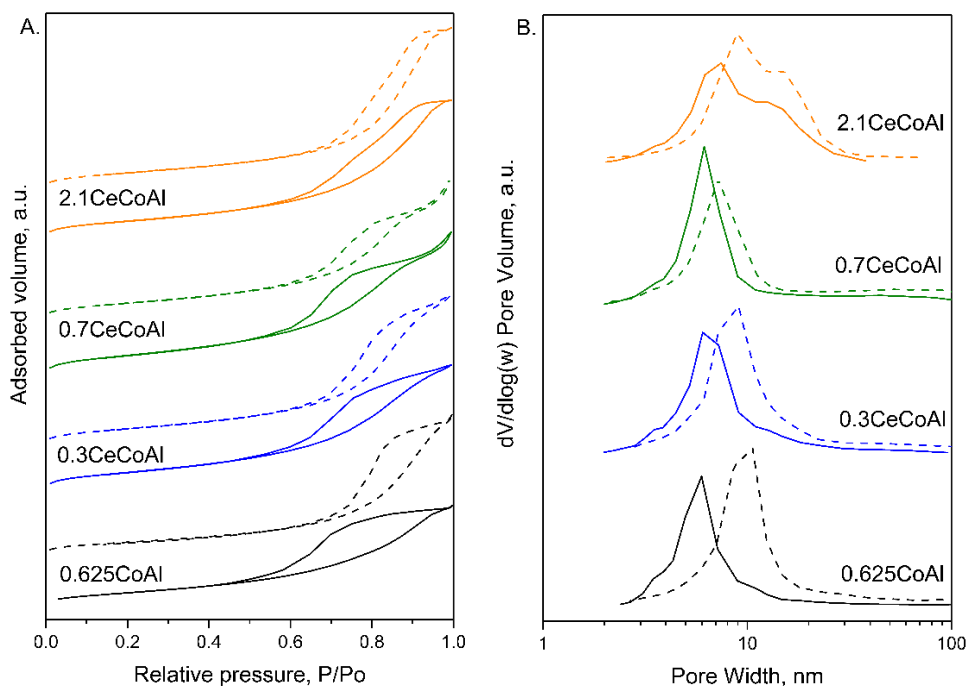
Figure 4.1. Nitrogen adsorption-desorption isotherms (A) and pore size distribution (B) of the calcined (solid lines) and reduced (dashed lines) spinels samples doped by Cerium.

4.2.2   Reducibility of the solids

Figure 4.2 displays the H_2-TPR profiles for 0.625CoAl and Ce-modified samples. In addition, an amplified profile of CeO_2 (prepared by precipitation from $Ce(NO_3)_3 \cdot 6H_2O$, calcined at 500 °C/5 h) is shown for comparison purposes. Reference CeO_2 showed two reduction temperature ranges: one at temperature

below 550 °C, and the other at a high temperature, above 800 °C, in line with literature [285]. The low temperature peak, centred at 496 °C, corresponded to the reduction of surface caps of ceria and the high temperature peak, centred at 845 °C, was due to the reduction of the innermost layers (bulk) of the ceria. For Ce-doped samples, both peaks could be overlapped by cobalt reduction peaks. As the pristine 0.625CoAl sample, Ce-doped samples clearly showed four reduction peaks. These peaks were attributable to the cobalt species previously described in Chapter 3.
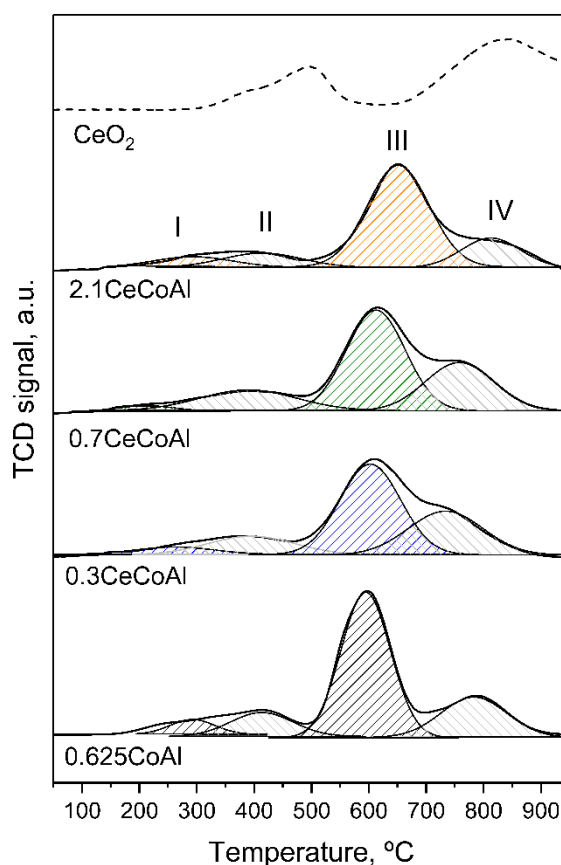
Figure 4.2. H$_2$-TPR profiles of spinels samples modified by cerium.

Strictly calculating, H$_2$ consumption due to ceria reduction should be subtracted. However, the highest consumption was 0.076 mmol$_{H2}$·g^{-1} for sample 2.1CeCoAl, which represented 1% of the total H$_2$ uptake, for this reason the total

consumption is shown. As can be consulted in Table 4.2, the addition of a small amount of cerium (0.3 and 0.7 wt.%) shifted to lower temperatures the peaks corresponding to reduction of Co^{3+} to Co^{2+} (Peaks I and II), indicating promotional effect of ceria on both kinds of Co^{3+} species reduction. Nevertheless, for these same peaks, the 2.1CeCoAl sample did not show any significant shift from 0.625CoAl (292 vs 295 °C for peak I and 413 vs 414 °C for peak II). In the case of the reduction temperature of Co^{2+} to Co^0 (peak III), all the Ce-doped catalysts showed reduction peaks at temperatures higher than those exhibited by 0.625CoAl assay. For the reduction peak of cobalt species in $CoAl_2O_4$ phase, 2.1CeCoAl required the highest temperature among all samples. This higher temperature requirement led to a lower degree of reduction of this sample when reduced at 600 °C (conditions in which the activation process is carried out before the catalytic experiments). Overall, Ce-modified samples would achieve a smaller reduction than pristine 0.625CoAl.

Table 4.2. H_2-TPR analysis results of Ce-containing samples.

Sample	H_2 uptake, mmol$_{H_2} \cdot g^{-1}$					Degree of reduction[a], %
	Total	Peak I	Peak II	Peak III	Peak IV	
0.625CoAl	7.04	0.392 (292)	0.881 (413)	4.407 (594)	1.360 (783)	62.6
0.3CeCoAl	7.05	0.371 (262)	0.997 (395)	3.572 (603)	2.110 (734)	60.2
0.7CeCoAl	7.12	0.185 (213)	1.207 (390)	3.694 (612)	2.035 (758)	56.1
2.1CeCoAl	7.09	0.498 (295)	0.787 (414)	4.582 (652)	1.223 (813)	45.9

In parenthesis the temperature of the peak (in °C).
[a]H_2 consumption at 600 °C with respect to 950 °C.

4.2.3   Nature and morphology of the phases

The diffractograms of Ce-doped and pristine cobalt aluminate spinel samples, in their oxidised and reduced forms, are displayed in Figure 4.3. All the calcined samples exhibited the characteristic peaks for cobalt spinels (superimposed signals from Co_3O_4 and $CoAl_2O_4$). Catalysts with higher Ce content were

characterised by the presence of far less intense peaks at 47.5 and 56.3° (2θ) attributable to cubic cerianite CeO_2 phase (PDF 00-034-0394), indicating the presence of segregated phase of the latter. These peaks were not observed for sample 0.3CeCoAl, which confirmed that Ce ions were uniformly substituted in spinel lattice sites. Literature data indicated a limit of molar Ce/Co = 0.03 for the cerium solubility into spinel phase [286]. A careful inspection of (3 1 1) peak of spinel phase showed a slight negative shift in the positions of peak indicated (0.625CoAl: 37.0637°, 2.1CeCoAl: 37.0238°) which determined that the distance between the lattice planes was increased.
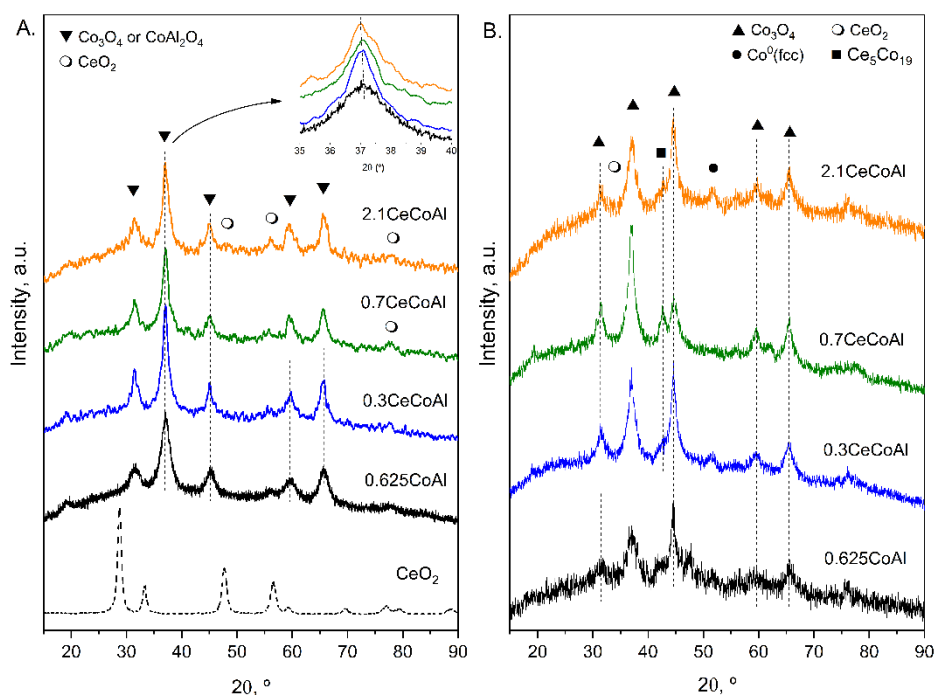
Figure 4.3. XRD patterns of (A) calcined and (B) reduced Ce-modified spinel samples.

The crystallite average size (Table 4.3) of spinel (without distinction between $CoAl_2O_4$ and Co_3O_4) increased with Ce content (between 28-40%). In like manner, Ce-doping generated a growth in the spinel lattice parameter, in agreement with negative shift of the peak. This could be attributed to the larger ionic radius of Ce^{4+} ions (101 pm) as compared to Co^{2+} (79 pm), Co^{3+} (69 pm) and Al^{3+} (67.5 pm) host ions. The average crystallite sizes of ceria phase were not

determined due to their weak intensities. Undoubtedly, lattice changes would affect spinel structure. On the other hand, the intensity ratio of the (2 2 0) and (4 4 0) planes diffraction increased as Ce-content augmented, indicating a preferential arrangement of cobalt ions in tetrahedral coordination.

Table 4.3. XRD analysis results of the calcined and reduced xCeCoAl samples.

Sample	Calcined samples			Reduced samples		
	d_{spinel}, nm	a_{spinel}, nm	I_{220}/I_{440}	$d_{Co(hcp)}$, nm	$d_{Co(fcc)}$, nm	$d_{Co(both)}$, nm
0.625CoAl	5.0	0.8040 ±0.0014	0.63	*22.8*	*11.6*	*16.5*
0.3CeCoAl	6.4	0.8055 ±0.0014	0.71	*4.7*	*5.8*	*9.8*
0.7CeCoAl	6.7	0.8056 ±0.0011	0.75	*9.6*	*12.2*	*5.1*
2.1CeCoAl	7.0	0.8059 ±0.0018	0.76	*n.d.*	*9.3*	*7.2*

After the reduction treatment, peaks assignable to metallic cobalt emerged in all samples, whereas in samples 0.7CeCoAl and 2.1CeCoAl, the formation of a more stable structure denominated Ce_5Co_{19} (PDF 026-1084) was observed. The formation of this stable phase, more difficult to reduce, would explain the shift at higher temperatures of peaks III and IV observed in the H_2-TPR study (Table 4.2). Ce-doped catalysts also had a smaller metallic cobalt crystal size than the pristine 0.625CoAl sample.

STEM micrographs and the resulting particle size distribution histograms are depicted in Figure 4.4. The identification of the nanoparticles was also confirmed by EDX analysis. Cobalt nanoparticles (cubic/cuboid shape) in Ce-doped catalysts were found to be homogenously distributed, as were the tiny cerium nanoparticles that were found completely scattered throughout the sample. Regarding the particle size distribution, samples continued to have an overall size of between 10 and 26 nm and 75% of the nanoparticles are smaller than 20 nm. Ce-modified catalysts had a broader distribution curve, which was also reflected by the variation in the Co^0 crystallite sizes evaluated by XRD depending on chosen phase of Co^0 (*hcp*, *fcc* or both). Among Ce-doped samples, 0.7CeCoAl presented the largest average size.
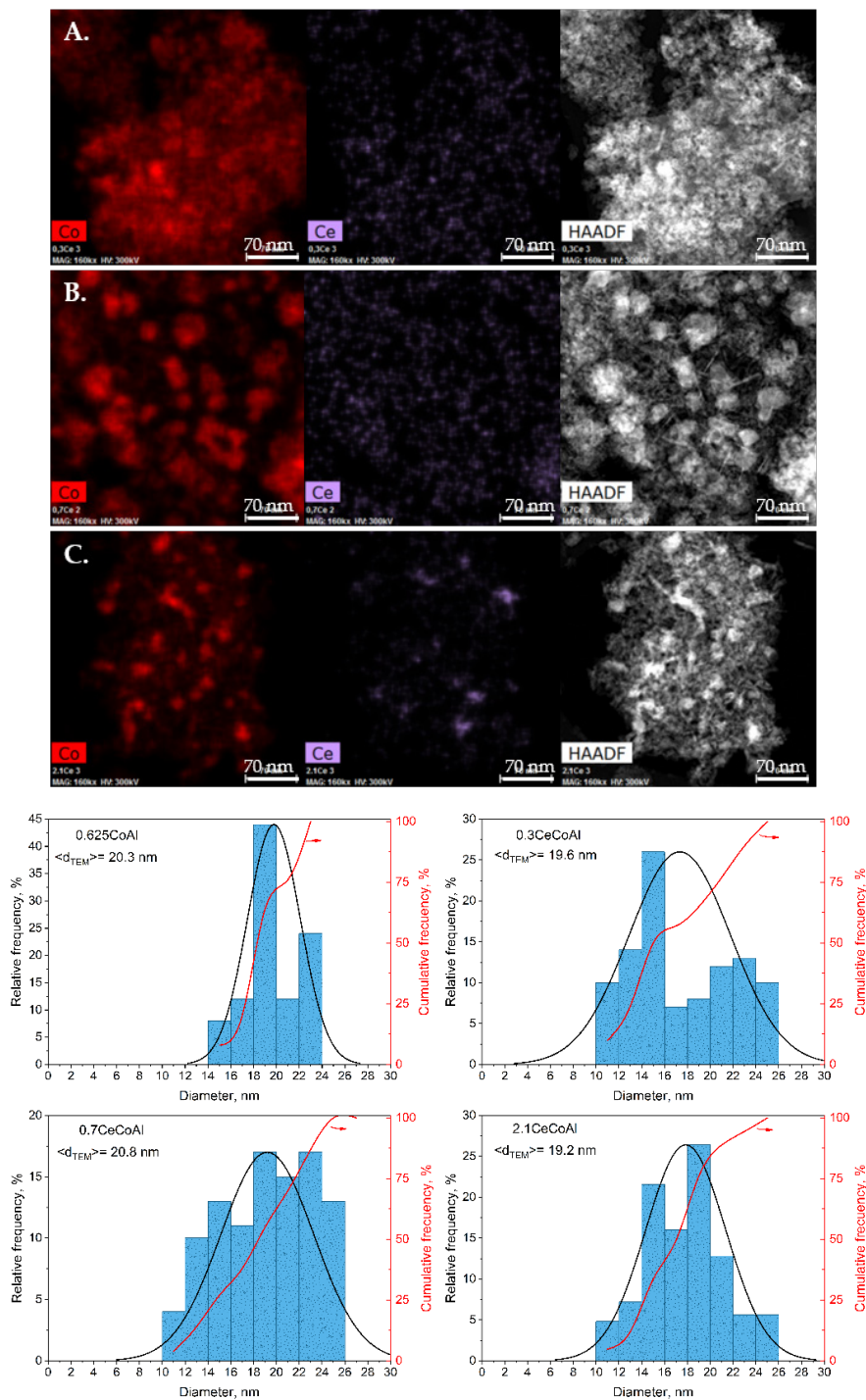
Figure 4.4. Stem micrographs of Co^0 for reduced catalysts (upper part): (A) 0.3CeCoAl, (B) 0.7CeCoAl and (C) 2.1CeCoAl; and its size distribution histogram (lower part).

4.2.4   Metallic function

The total amount of exposed metal, calculated as a whole by isothermal H_2 pulse chemisorption, is gathered in Table 4.4. Consistent with the reducibility results discussed above, Ce addition remarkably decreased the available metal. This depletion was around 35% for the samples with a lower cerium load, reaching 44% for the sample with 2.1% cerium load.

Table 4.4. Characterization of the metallic function of xCeCoAl catalysts.

Sample	Exposed metal site, atoms·g^{-1}	A_{dehyd}, mol·h^{-1}·g^{-1}$_{metal}$	TOF$_{dehyd}$, s^{-1}
0.625CoAl	23.0·10^{18}	1.78	0.59
0.3CeCoAl	14.6·10^{18}	2.91	0.84
0.7CeCoAl	15.0·10^{18}	2.33	0.66
2.1CeCoAl	12.9·10^{18}	3.33	0.90

The activity of catalysts in cyclohexane dehydrogenation model reaction are also indicated in Table 4.4. Despite the lower availability of metal measured by chemisorption, Ce-modified samples showed good performance in this type of reaction. The activity, expressed as TOF$_{dehyd}$, increased between 42-52% for 0.3CeCoAl and 2.1CeCoAl catalysts, while 0.7CeCoAl sample led to an increase of 12%. The positive effect of the small Ce nanoparticles present in these catalysts cannot be ruled out.

4.2.5   Structure and coordination state

The FTIR spectra of calcined and reduced xCeCoAl samples are plotted in Figure 4.5. For calcined samples, well-resolved bands continued to be observed around 575 and 660 cm^{-1}, without any change in the band positions, after Ce-modification. These transmittance bands were attributed to the Co-O vibration modes in the cobalt spinel structure. The presence of bands ascribable to the strength of Ce-O bond was not apparent in any of the catalysts [287]. In the case of the reduced catalysts, the samples Ce-doped presented a distinctive profile from that shown by 0.625CoAl sample, characterized by very broad bands and a myriad of weak peaks in the range of 400-800 cm^{-1}.
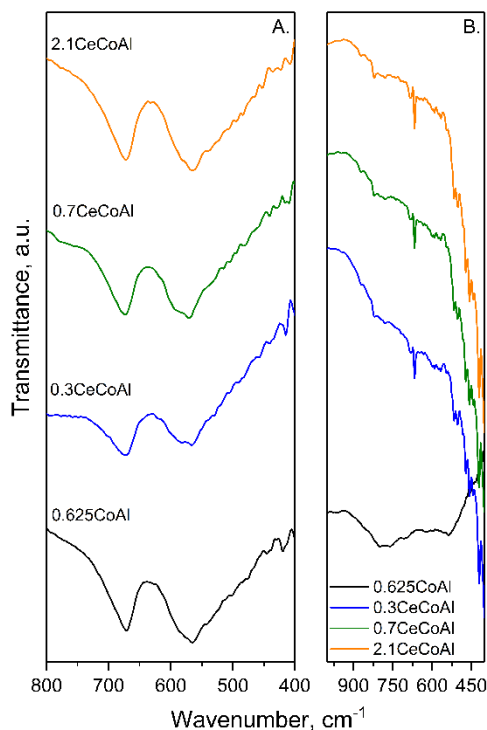
Figure 4.5. FTIR spectra of (A) calcined and (B) reduced xCeCoAl samples.

Figure 4.6 illustrated the UV-vis DRS spectra of calcined catalysts. CeO_2 sample, used as a reference, showed two absorbance bands below 400 nm. Bands at 257-278 nm are attributable to O-Ce charge transfer transitions involving Ce^{3+} (≈255 nm) and Ce^{4+} ions (≈278 nm) with different coordination numbers, whilst at 328 nm a characteristic vibration of interband transitions in CeO_2 was observed [288]. This latter band was also seen in xCeCoAl samples, in addition to two broad bands in the UV region centred around 420 and 635-644 nm. Furthermore, these catalysts exhibited characteristic cobalt aluminate bands in the NIR region (1200-1500 nm). These bands were found to be less intense than those shown by pristine 0.625CoAl assay with a slight band shift from 1420 to 1460 nm, indicative of Ce incorporation in the structure.

The direct band gap (E_g) for all samples was estimated by Tauc plot. A band gap of ≈1.38 eV was estimated for pristine 0.625CoAl and decreased to 0.81, 0.73 and 0.48 eV for samples with 0.3, 0.7 and 2.1% of cerium, respectively. The lower

E_g values for Ce-doped samples could be attributed to the incorporation of metal cations into the framework of cobalt spinel crystal [289].
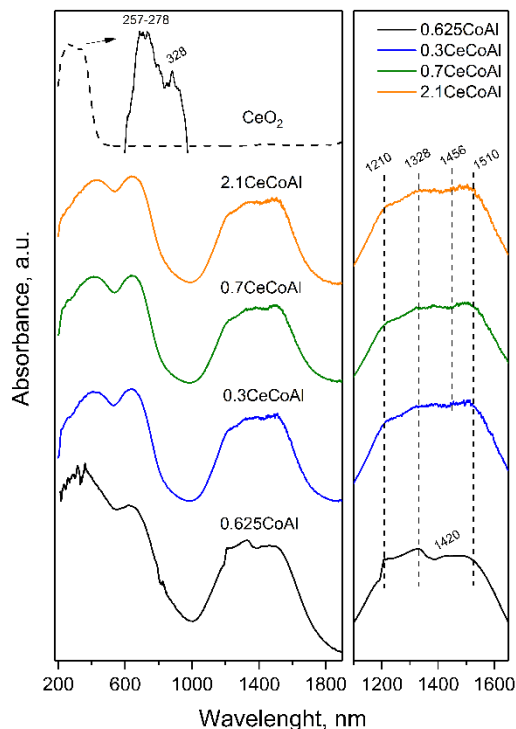
Figure 4.6. DRS spectra of calcined Ce-modified samples.

XPS spectroscopy was employed to obtain further information on the oxidation state and surface composition of xCeCoAl. The BE of the photoelectron peaks for both calcined and reduced samples have been gathered in Table 4.5. Before reduction, spin-orbit splitting between Co $2p_{3/2}$ and Co $2p_{1/2}$ peaks was 15.67 eV for 0.3CeCoAl and decreased with increasing cerium loading to 15.35 for sample 2.1CeCoAl. The satellite peak of Co $2p_{3/2}$ is located approximately 4-5 eV higher than the main Co $2p_{3/2}$ peak, which is characteristic of Co^{2+} in $CoAl_2O_4$ framework. The peaks in the Al 2p region of Ce-containing catalysts were lower in binding energy than those of 0.625CoAl, suggesting a greater interaction between elements in these samples.

The spectra corresponding to Co 2p of reduced samples are displayed in Figure 4.7. After reduction, one more Co $2p_{3/2}$ feature assigned to metallic cobalt

emerged. This peak located at 778.0 eV for 0.625CoAl catalyst shifted to higher BE for samples xCeCoAl. Striking is the small shift presented by sample 0.7CeCoAl ($\Delta E = 0.1$ eV), which differed from the rest of Ce-containing samples ($\Delta E = 0.7$-1.1 eV). In addition, for xCeCoAl, deconvolved Co^0 peak was less intense than for 0.625CoAl catalyst, in agreement with H_2-TPR results.
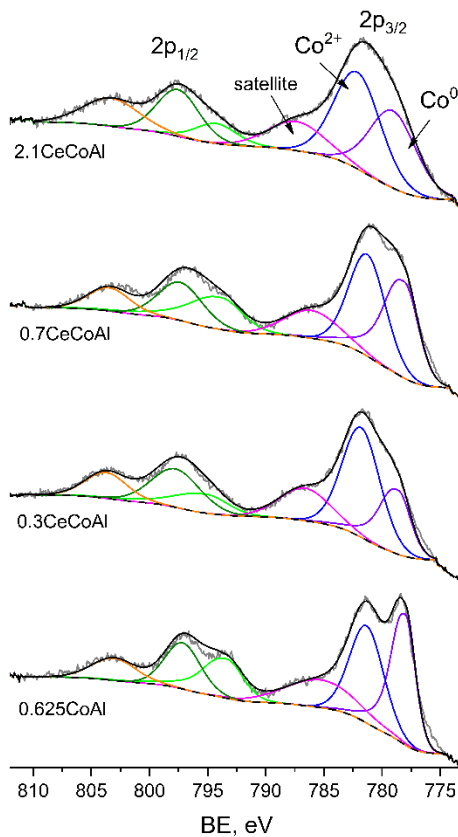
Figure 4.7. XPS spectra corresponding to Co 2p of reduced cobalt aluminate spinel samples modified with cerium.

A quantitative evaluation of surface chemical composition of Co and Al was calculated for the calcined and reduced samples (Table 4.5). As seen for other catalysts, the compositional ratio on the surface of calcined catalysts is lower than the ratio (≈ 0.634) measured by ICP-OES. Evidently, after reduction, this ratio decreased even more, but to a lesser extent for Ce-coprecipitated samples, suggesting less segregation of the trivalent cations on the catalyst surface.

Table 4.5. XPS analysis results for cobalt aluminate spinel samples modified by cerium.

Catalysts	Al 2p, eV	Co 2p$_{3/2}$, eV		Ce 3d$_{5/2}$, eV	Co/Al at surfaceᵇ
		Co^{2+}	Co^{0}	Ce^{3+}	
0.625CoAl	75.6 (74.2)	781.6 (781.3)	(778.0)	-	0.266 (0.139)
0.3CeCoAl	74.2 (74.2)	781.3 (781.8)	(778.7)	884.6 (885.9)	0.223 (0.213)
0.7CeCoAl	74.2 (74.2)	781.3 (781.3)	(778.1)	885.7 (885.5)	0.268 (0.209)
2.1CeCoAl	74.0 (73.9)	781.8 (782.1)	(779.1)	885.0 (884.5)	0.243 (0.207)

Value in parenthesis for reduced samples.

ᵃ calculated from the contribution of each deconvolution bands to main Co 2p$_{3/2}$ band

ᵇ calculated from integrated intensity of Co 2p$_{3/2}$ (with satellite) and Al 2p peaks.
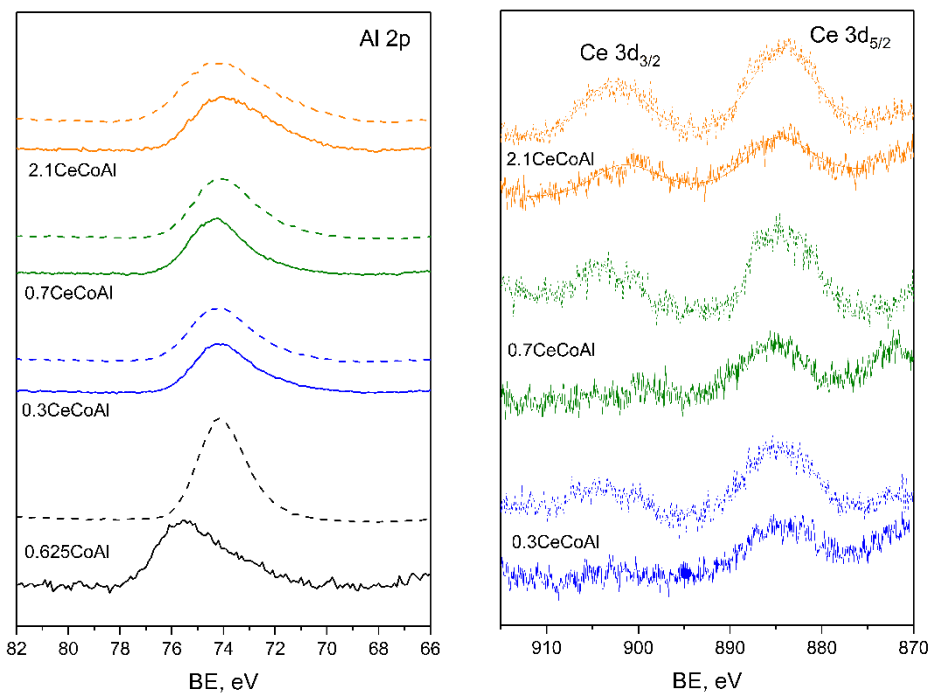
Figure 4.8. XPS spectra of Al 2p (left) and Ce 3d (right) for calcined (solid lines) and reduced (dashed lines) Ce-modified cobalt aluminate spinel samples.

The Ce 3d features collected for calcined and reduced samples are displayed in Figure 4.8. For both calcined and reduced samples, the Ce $3d_{3/2}$ and $3d_{5/2}$ spectra had significantly low intensity (signal close to noise), making deconvolution of the peaks difficult. However, the observed separation was around 18.2 eV in good agreement with other reports [290-292]. Unambiguously, no characteristic photoelectronic peaks of tetravalent states of Ce^{4+} (generally located around 882.3 and 900.6 eV, 888.6 and 906.9 eV, 898.3 and 916.7 eV) [293] were detected. Instead, the characteristic peak of Ce^{3+} were observed at around 902.7±0.5 and 885.2±0.7, this latter the result of Ce $3d^9 4f^1$ O $2p^6$ final state [290].
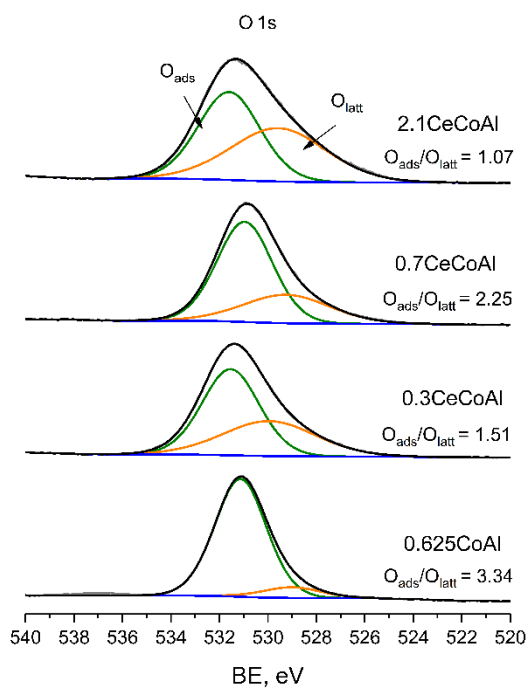
Figure 4.9. O 1s spectra of reduced xCeCoAl samples.

Two typical bands could be observed in the O 1s XPS spectrum of reduced samples (Figure 4.9). The first peak at 530.9-531.6 eV corresponded to adsorbed oxygen (O_{ads}) species and the other, located at lower BE coincided with surface lattice oxygen (O_{latt}) [294]. O_{ads} species has greater mobility than O_{latt}, and are considered responsible for maintaining the charge balance in the structure, [295,296]. The ratio between the two kinds of oxygen species (O_{ads}/O_{latt}) was

lower for Ce-containing samples (1.07-2.25) compared to their counterpart 0.625CoAl catalyst (3.34), which implied a decrease in oxygen vacancies.

4.2.6   Acid-base sites on the catalyst surface

The acid-base properties of the reduced solids are summarised in Table 4.6 and the strength distribution, according to desorbed (CO_2 or NH_3) profiles, is displayed in Figure 4.10. Recall that the numbers of weak, medium and strong catalyst acid/basic sites are estimated from the area under their TPD curves for the temperature range of 90-300 °C, 300-650 °C and > 650 °C, respectively. Ce-doping led to an increase in the total amount of surface acidity and a change in the distribution of the acid centres. Ce-doped solids exhibited a higher density of medium and strong acid centres compared to their counterpart. For example, in percentage terms, strong acid sites increased from 8.1% for sample 0.625CoAl to 25.9-33.0% for Ce-containing samples. Morterra et al. [297] found that Ce-doped alumina had more acidity than parent γ-alumina, and ascribed this to the modified environment of Al cations by cerium.

Table 4.6. Acid-basic properties of Ce-doped spinels samples.

Catalyst	Surface site density		$A_{isom,0}$, $\mu mol \cdot m^{-2} \cdot h^{-1}$
	acid, $\mu mol_{NH3} \cdot m^{-2}$	basic, $\mu mol_{CO2} \cdot m^{-2}$	
0.625CoAl	0.51	1.90	2.84
0.3CeCoAl	0.79	1.91	252.4
0.7CeCoAl	0.58	2.08	2.53
2.1CeCoAl	0.88	2.03	191.0

Evaluation of Brønsted acidity by skeletal isomerization of 33DM1B showed a large difference between the samples. With the exception of the 0.7CeCoAl sample that exhibited a similar activity to the 0.625CoAl sample (2.53 vs 2.84 $\mu mol \cdot m^{-2} \cdot h^{-1}$), the rest of Ce-containing solids were 70-90 times more active for 33DM1B, making evident their predominant Brønsted acidity.

Ce addition induced an increase in total amount of surface basicity (up to 10%). As for the strength of these centres, weak basicity prevailed. Nevertheless, the

samples with 0.3 and 2.1% cerium showed a higher density of strong basic centres compared to the 0.625CoAl sample. This was consistent with the XPS evidence, since unlike Ce^{4+}, which is a weak base, Ce^{3+} is a strong base [298].
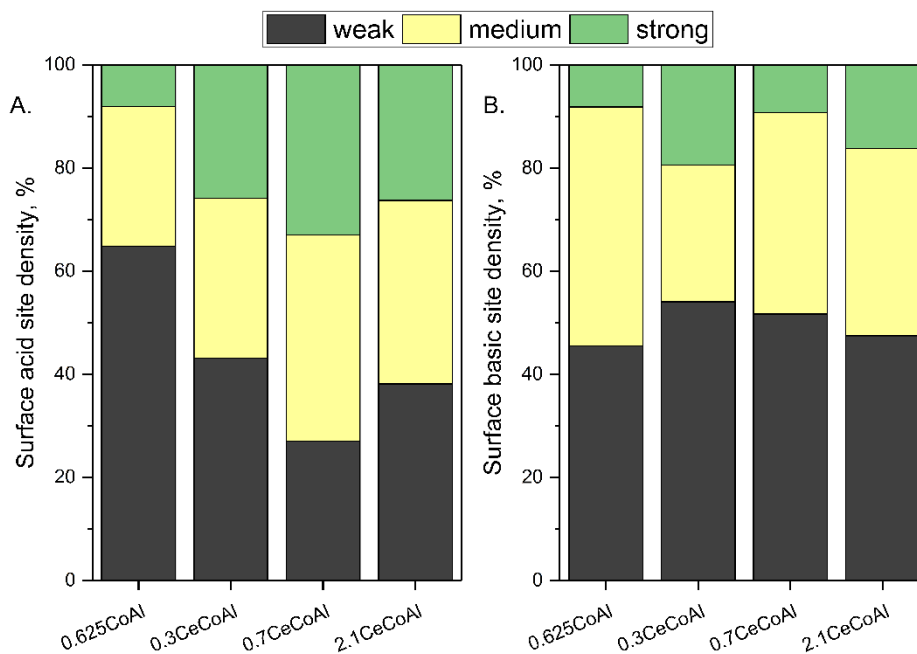
Figure 4.10. Strength distribution of (A) surface acid sites and (B) surface basic sites for xCeCoAl catalyst.

4.3 GLYCEROL APR

The catalytic APR performance of the samples was studied using 10 wt.% glycerol/water feedstream under two experimental conditions (235 °C/35 bar and 260 °C/50 bar) at 24.5 h^{-1}, during 3 h of reaction. The data obtained in terms of X_{gly} and X_{gas} for each catalyst and TOS are plotted in Figure 4.11.

At first glance, the superiority of the 0.625CoAl catalyst under all investigated conditions was appreciable. At 235 °C/35 bar, during the first hour of reaction, catalyst 0.625CoAl presented 20% higher glycerol conversion than Ce-modified catalysts. As the reaction time elapsed, this difference became more pronounced, as bare cobalt aluminate catalyst remained more stable (X_{gly} for 0.625CoAl, at 1 h = 88.3% and 77.2% at 3 h). Among Ce-modified catalysts, samples with a

lower cerium load showed slightly higher glycerol conversion (at 1 h TOS, $X_{gly}=$ 66.3% for 0.7CeCoAl vs 62.2% for 2.1CeCoAl). The same trend was observed for X_{gas}. The decrease in this conversion for Ce-containing catalysts with respect to sample 0.625CoAl was greater than 40%, evidently sample 2.1CeCoAl being the one that presented the greatest drop (around 48% for all TOS).
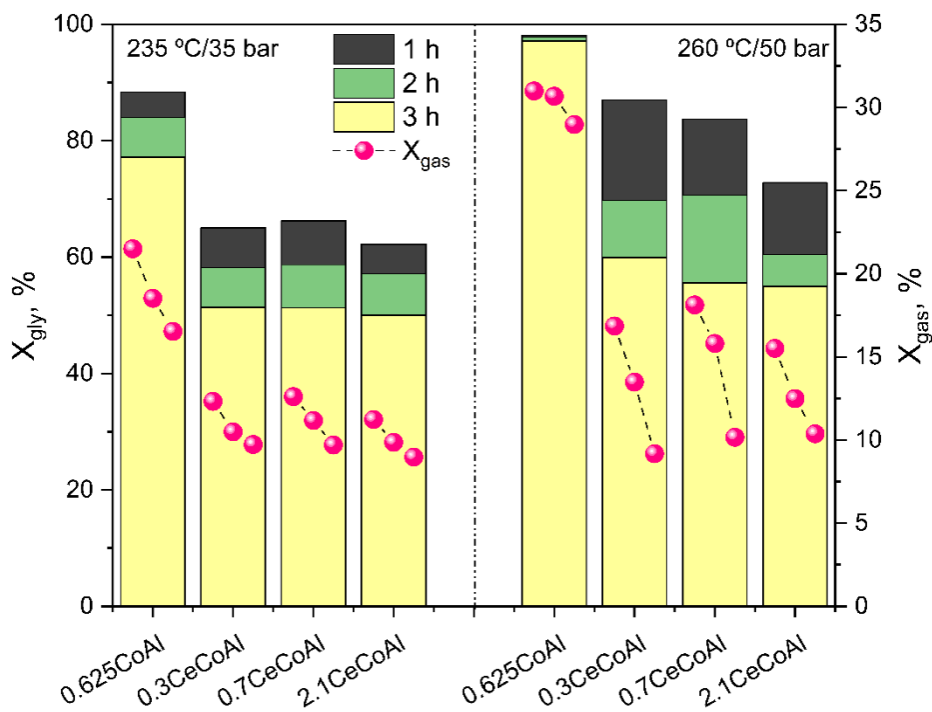
Figure 4.11. Effect of doping Ce over cobalt aluminate spinels on glycerol APR activity (conversion to gas and glycerol total conversion) at 235 °C/35 bar (left) and 260 °C/50 bar (right). Reaction conditions: $m_{cat} = 0.5$ g, $L = 0.2$ cm³·min⁻¹, 10 wt.% glycerol/water, WHSV = 24.5 h⁻¹.

By modifying the reaction conditions, an increase in conversions was achieved. In the first hour under this condition (260 °C/50 bar), it was the Ce-modified catalysts that had the highest conversion increase since they were the catalysts with the greatest scope for improvement. For instance, at 1 h TOS, X_{gly} for 0.3CeCoAl increased from 65.1% (235 °C/35 bar) to 87.0% (260 °C/50 bar). Nevertheless, as TOS progresses, the deactivation becomes more evident and X_{gly} fell to values close to those obtained at mild condition. As a comparative, for 0.7CeCoAl at the third hour of TOS, X_{gly} was 55.6% vs 51.3% at 235 °C/35 bar.

Focusing on X_{gas} at 260 °C/50 bar, unlike the 0.625CoAl catalyst, which exhibited a slight decrease of 6.5% throughout this reaction, Ce-modified catalysts suffered drops of around 45% for samples with 0.3 and 0.7% of cerium.

Regardless of the rapid deactivation shown, the low initial activity of the Ce-containing catalysts may be related to the stabilizing effect of ceria on the Co^{2+} ion, delaying its reduction to Co^0, as could be seen by H_2-TPR. Furthermore, and related to the above, available metallic area was lower than that displayed by catalyst 0.625CoAl.

It seemed evident that cerium was responsible of the lower glycerol conversion activity of xCeCoAl catalysts. The decrease in APR activity upon Ce-doping would be related to the interaction between Co and Ce ions into the spinel framework, likely giving less productive metallic Co particles. Moreover, a higher acid/basic sites density ratio and a greater predominance of Brønsted centres may have influenced the activity of these catalysts.

For sake of simplicity, the detailed analysis of the products obtained is shown for the third hour of reaction (Table 4.7). At both operation conditions S_{H2}, calculated on the H atoms basis as the ratio between H_2 produced and the sum of H-containing gases (including alkanes) was considerably high for all catalysts ($S_{H2} > 60\%$). Moreover, catalysts with cerium showed higher S_{H2} than pristine 0.625CoAl, being 0.3 wt.% the optimum Ce load to maximize hydrogen selectivity. However, despite the fact that Ce-containing catalysts presented a high S_{H2}, selectivity towards alkanes increased with cerium content, which was evidenced by the decrease in Y_{H2}. With the increase in temperature and consequently in pressure, an increase in selectivity to H_2 (around 6%) and alkanes (between 10-14%) was observed. Regarding Y_{H2}, the lowest value (10.2%) was obtained for catalyst 2.1CeCoAl. This catalyst, instead, showed the maximum selectivity to alkanes, with 54% under the most severe conditions.

Table 4.7. Gas products stream characteristics, at 3 h TOS, on glycerol APR.

Reaction conditions	Catalysts	S_{H2}, %	Y_{H2}, %	S_{alk}, %	Gaseous products, %				H_2/CO_2 ratio	H_2/CH_4 ratio
					H_2	CO_2	CH_4	CO		
235 °C/ 35 bar	0.625CoAl	61.8	13.4	32.3	54.9	29.3	12.1	0.82	1.87	4.53
	0.3CeCoAl	65.8	11.9	36.6	57.2	27.9	11.6	1.71	2.05	4.95
	0.7CeCoAl	65.4	11.2	40.6	63.5	20.6	12.4	1.14	3.08	5.12
	2.1CeCoAl	63.0	11.1	46.4	63.1	18.7	12.9	0.74	3.37	4.89
260 °C/ 50 bar	0.625CoAl	66.4	15.8	36.5	62.9	23.9	10.1	0.83	2.63	6.22
	0.3CeCoAl	70.3	13.5	40.5	64.9	20.5	10.9	1.97	3.17	5.95
	0.7CeCoAl	69.9	12.6	46.3	66.3	17.1	12.1	1.67	3.88	5.48
	2.1CeCoAl	66.3	10.2	54.0	67.9	16.8	12.5	0.20	4.04	5.43

Hydrogen concentration in the gaseous stream was larger, for each catalyst, when reaction temperature was higher, whereas the CO_2 concentration was lower at higher temperatures. Therefore, H_2/CO_2 ratio was positively away from theoretical value, which corroborated higher incidence of secondary reactions of glycerol decomposition. Undoubtedly, the presence of Ce did not enhance WGS reaction to the extent expected, probably due to the lack of Ce^{4+} since the coexistence of the cerium states improves its redox properties [299] and phase formation of Ce_5Co_{19}-type stable structure.

× <u>Liquid products</u>
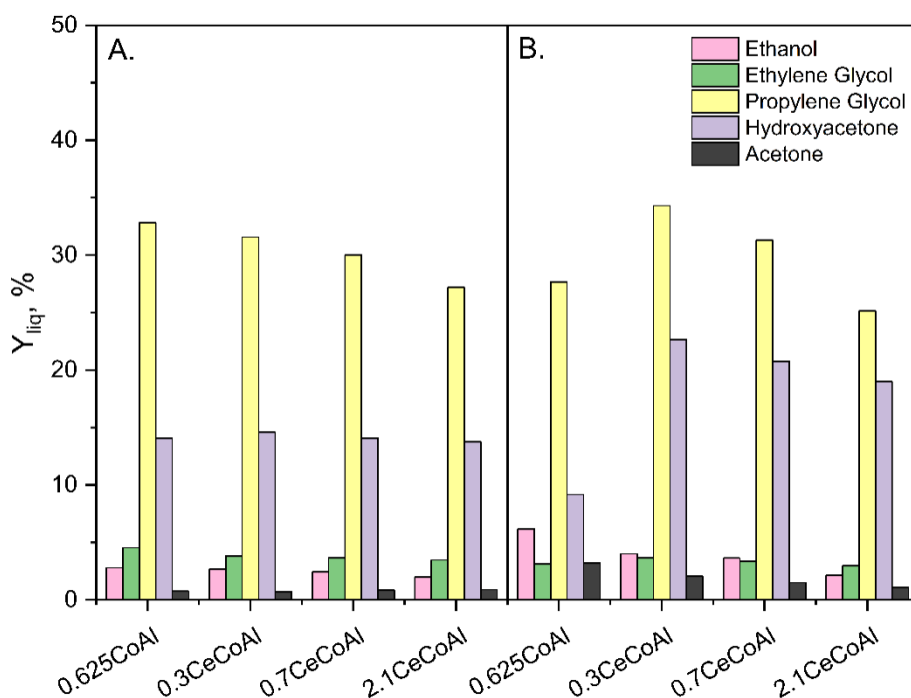
Figure 4.12. Liquids products distribution at 3 h TOS of glycerol APR at (A) 235 °C/35 bar and (B) 260 °C/50 bar. Reaction conditions: $m_{cat} = 0.5$ g, L = 0.2 cm³·min⁻¹, 10 wt.% glycerol/water, WHSV = 24.5 h⁻¹.

The yield of the leading liquid products is depicted in Figure 4.12. Ce-doped catalysts had a distribution similar to that obtained with bare cobalt aluminate catalysts. Under both operation conditions, propylene glycol was the product with the highest yield, followed by hydroxyacetone. The high yields to both

compounds, in addition to acetone, demonstrated a high activity of these catalysts for glycerol dehydration, as they were early compounds from dehydration route in the reaction Scheme 3.2.

As the operation temperature/pressure increased, catalyst 0.625CoAl presented the same trend seen in the previous chapter (at 1 h TOS), that is, a decrease in hydroxyacetone (from 14% to 9%) and propylene glycol (from 33% to 27%) yields and a concomitant increase in ethanol (from 2.8 to 6.2%) and acetone (from 1% to 3%) yields. In the case of Ce-doped catalysts, the increase in ethanol yield was low compared to catalyst 0.625CoAl (i.e.: for 0.3CeCoAl from 2.7 to 4.0%) and dehydration product yields also increased. According to the proposed reaction pathway (Scheme 3.2), the presence of cerium favoured the dehydration pathway, by slight increase on surface acid/basic sites ratio, even under conditions in which cobalt aluminate based-catalysts had shown greater dehydrogenation activity.

4.4   CHARACTERIZATION OF SPENT CATALYSTS

In order to shed light on the catalytic behaviour evidenced by Ce-doped catalysts, the characterization of said used catalysts was carried out. Table 4.8 lists the results obtained by nitrogen physisorption and ICP-MS. As for bare cobalt aluminate catalysts, these samples showed an increase in S_{BET} area and pore volume whereas pore size decreased.

As can be seen in Figure 4.13.B spent catalysts possessed a bimodal pore structure reaching maximums at approximately 3-4 nm and 8-10 nm. The former narrow peak was more pronounced for samples with higher amount of cerium. Two phenomena could explain this evolution of the textural properties: hydration of the alumina and deposition of carbonaceous material.

Ce-containing catalysts underwent greater leaching of all contained metals. Cobalt was the most leached metal and the percentage of leaching in the Ce-containing samples was 2-3 times higher than for catalysts 0.625CoAl. The greatest loss of aluminium occurred in sample 0.7CeCoAl. Meanwhile, the amount of Ce leaching out from the catalysts increased in proportion to the amount of Ce in the samples.
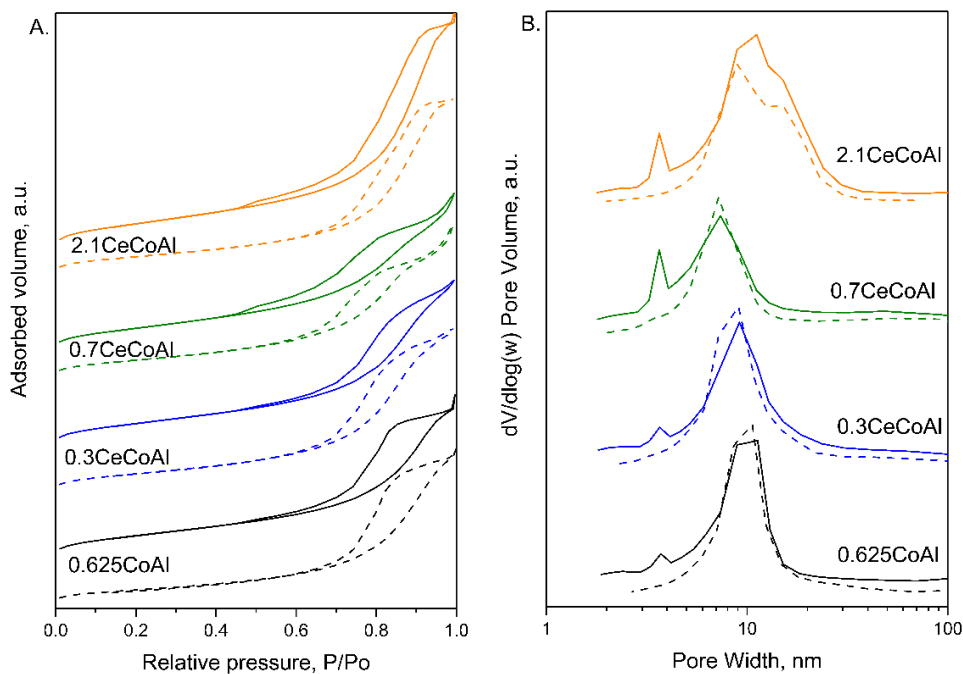
Figure 4.13. Nitrogen adsorption-desorption isotherms (A) and pore size distribution (B) of the freshly reduced (dashed lines) and used (solid lines) samples.

Table 4.8. Textural properties and leaching concentration of xCeCoAl used samples.

Catalyst	S_{BET}, $m^2 \cdot g^{-1}$	V_P, $cm^3 \cdot g^{-1}$	d_P, nm	Leached metal, wt.%		
				Al	Co	Ce
0.625CoAl	178.2 *(+75%)*	0.411 *(+10%)*	8.0 *(-17%)*	1.5	1.6	-
0.3CeCoAl	174.4 *(+26%)*	0.414 *(+3%)*	7.8 *(-10%)*	2.1	3.5	0.12
0.7CeCoAl	178.4 *(+36%)*	0.397 *(+6%)*	7.0 *(-18%)*	3.5	4.8	0.22
2.1CeCoAl	206.7 *(+57%)*	0.598 *(+41%)*	9.3 *(-4%)*	2.3	4.8	0.63

In parenthesis, percentage variation respect freshly reduced samples

XRD diffractograms (Figure 4.14), for all catalysts, showed the well-known characteristic peaks of cobalt spinel. For Ce-containing catalysts, peaks indexed to the Ce_5Co_{19} phase structure weakened. Samples 0.625CoAl and 0.3CeCoAl maintained peaks assignable to metallic cobalt, which, however, were not visible for samples with higher Ce-content. In the latter, peaks attributable to the

hexagonal phase of cerium carbonate hydroxide (Ce(CO$_3$)OH) (PDF 32-0189) arose and became more significant for sample 2.1CeCoAl.
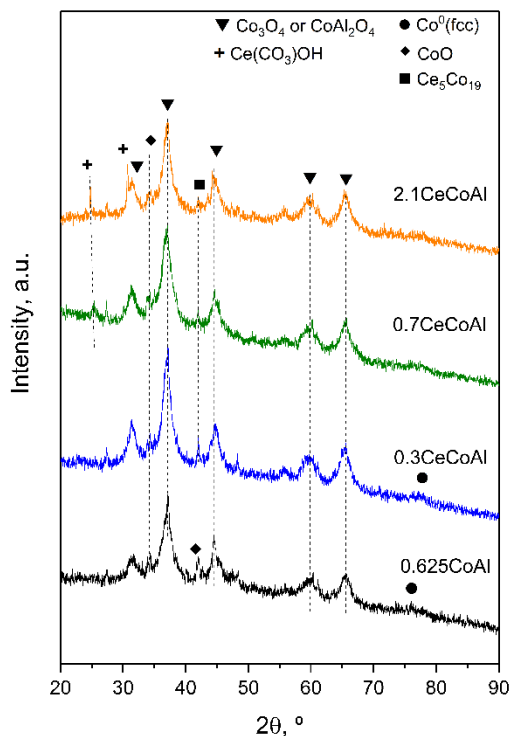
Figure 4.14. XRD patterns of used cobalt aluminate spinel catalysts modified by cerium.

The H$_2$-TPR profiles of used catalysts are shown in Figure 4.15 and the calculated hydrogen consumptions are reported in Table 4.9. Total hydrogen consumption was higher than expected (deduced through the reducibility degree) after a reduction process, which implies a re-oxidation of the samples. Also noteworthy was the redistribution of the profiles with higher consumption at temperatures above 600 °C. Indeed, the reduction profiles showed negligible consumption below 500 °C. Other authors [300] have investigated reduction temperature range after and before reactions, concluding that spent catalysts show a shift towards higher temperatures compared to fresh one due to the aggregation or sintering of metal cluster. Overall, the metallic availability of all catalysts was seriously compromised, as was also confirmed by H$_2$

chemisorption that revealed a decrease of about 64% for catalyst 2.1CeCoAl and up to 96% for monometallic 0.625CoAl.

Table 4.9. Metallic evaluation data of spent Ce-modified cobalt aluminate spinel catalysts.

Sample	H$_2$ uptake [a], mmol$_{H2}\cdot$g^{-1}		Exposed metal sites [c], atoms$\cdot$g^{-1}
	Total[a]	Expected[b]	
0.625CoAl	4.98	2.63	$9.92\cdot10^{17}$ (*-96%*)
0.3CeCoAl	6.59	2.80	$4.10\cdot10^{18}$ (*-72%*)
0.7CeCoAl	5.48	3.13	$2.04\cdot10^{18}$ (*-86%*)
2.1CeCoAl	5.26	3.84	$4.68\cdot10^{18}$ (*-64%*)

[a] *from H$_2$-TPR of spent catalysts*

[b] *estimated from the reducibility degree calculated in Table 4.2*

[c] *from H$_2$ chemisorption. Values in parenthesis percentage variation respect freshly reduced samples.*
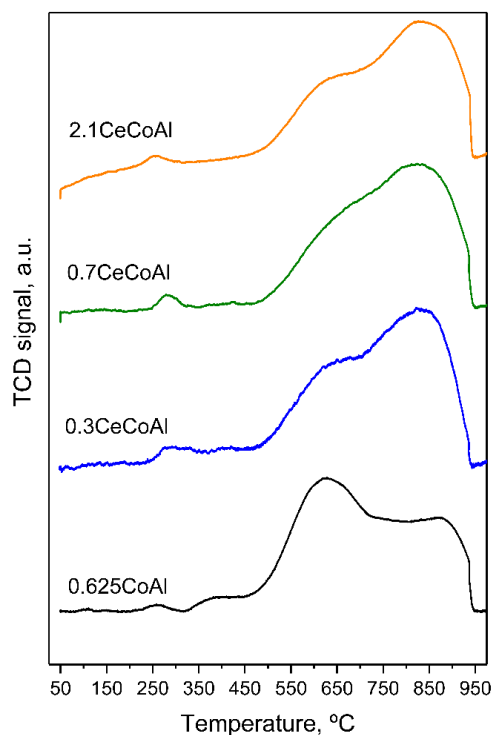
Figure 4.15. H$_2$-TPR profiles of used Ce-modified cobalt aluminate spinel catalysts.

4.4.1   Carbonaceous material deposition

The recorded Raman spectra of used catalysts (Figure 4.16) exhibited the typical carbon peaks, D and G bands, at ca. 1350 and 1590-1600 cm^{-1}. The shape of the spectra was similar for all catalysts with a very broad D-band and a more intense G-band. A dissonant feature (D_3) appeared, for sample 0.7CeCoAl, at ca. 1480 cm^{-1} assigned to structural defects of aromatic domains with poor organization [301]. As well as the shoulder observed at 1710 cm^{-1} in the sample 2.1CeCoAl that several authors attribute to an overtone of an M point phonon, not directly measured by Raman [302,303]. The degree of graphitization of carbonaceous materials was estimated by the relative intensity ratio of D and G bands (I_D/I_G inset in Figure 4.16). The I_D/I_G values obtained were in the range of 0.22-0.38 and did not show correlation with the composition of the samples.
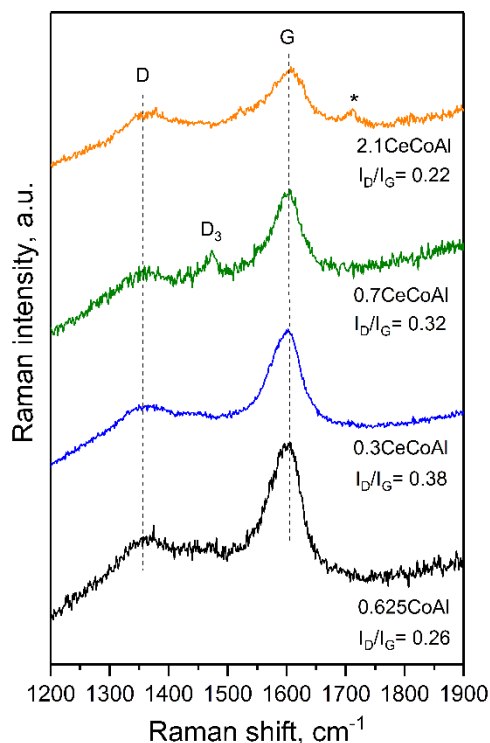
Figure 4.16. Raman spectra of used xCeCoAl catalysts.

4.5 GLOBAL VISION AND SUMMARY

In this chapter, the effect of Ce-coprecipitation to improve the activity and selectivity of cobalt aluminate-based catalysts for glycerol APR was discussed. Ce-modification of the 0.625 CoAl catalyst caused an increase in S_{BET} of approximately 16-30% and in other textural parameters. By means of XRD, an increase in the spinel crystallite size also verified. Furthermore, for the reduced sample, in addition to cobalt aluminate and metallic cobalt species, a structural phase of Ce_5Co_{19} was identified. Concerning acid-basic sites, Ce addition increased both total acidity and basicity and the conversion obtained by isomerization of 33DM1B indicated a high density of Brønsted centres for Ce-containing samples, except for catalyst 0.7CeCoAl.

In all tested conditions, Ce-modified catalysts exhibited lower glycerol conversion and carbon conversion to gas than their counterpart, 0.625CoAl. This behaviour could be due to a lower reducibility and, therefore, a lower metal availability of these samples as demonstrated by the H_2-TPR and H_2 chemisorption. In comparison, monometallic 0.625CoAl, xCeCoAl catalysts showed a higher S_{H2}, but in turn, S_{Alk} was also high, resulting in a lower Y_{H2}. Besides, a notable deactivation of these doped catalysts could be verified during the 3 h of reaction under each condition. Like bare cobalt aluminate catalysts, post-reaction characterization has verified an increase in S_{BET} and a change in the pore size distribution that can be attributed to the hydration of the alumina and deposition of carbonaceous material on the surface of catalysts. In addition, at the hydrothermal conditions that the reactions were performed $Ce(CO_3)OH$, was formed. Further confirmed fact was that despite the addition of cerium, the catalysts continued to exhibit re-oxidation and leaching phenomena, which explains the remarkable deactivation over time.

It was established that doping with Ce did not enhance catalytic activity, perhaps due to the type of interaction with cobalt and aluminium influenced by the preparation method used. Hence, the use of an ulterior method of preparation could result in better promotion of the catalyst, probably by impregnating Ce at the catalyst surface instead of bulk doping, in order to leave CeO_2 available for reactants.

Chapter 5

COBALT ALUMINATE SPINEL-DERIVED CATALYSTS MODIFIED BY PLATINUM
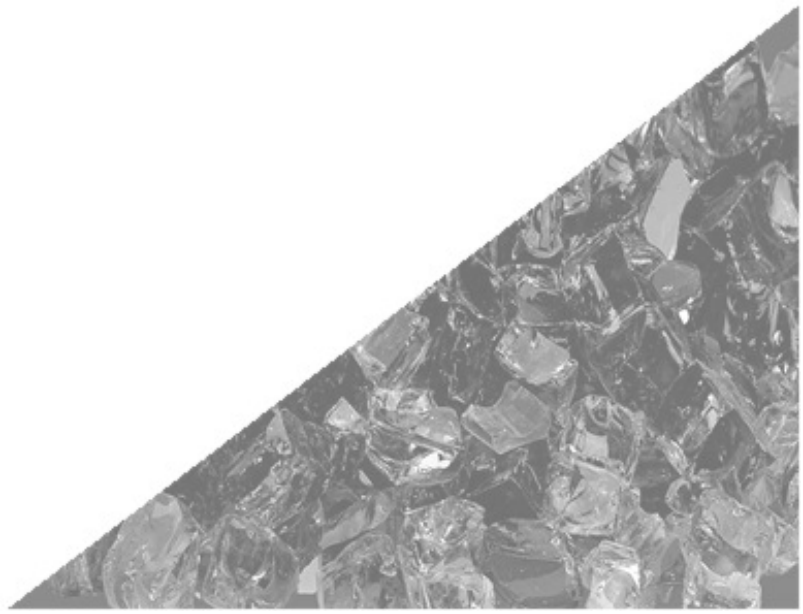
5. COBALT ALUMINATE SPINEL-DERIVED CATALYSTS MODIFIED BY PLATINUM

The results presented in the previous chapters have revealed that the cobalt aluminate-based catalyst system, and especially 0.625CoAl catalyst, exhibits suitable chemical properties for glycerol aqueous phase reforming. However, stability is a weakness that has not yet been solved. To face this drawback, the addition of another metal to the cobalt spinel with proven qualities for the reforming of oxygenated compounds has been proposed.

Catalytic systems based on platinum-group metals have been shown to be effective for hydrogen production by aqueous phase reforming of oxygenated hydrocarbons thanks to their ability to cleave C-C bonds and to boost the water-gas shift activity [124]. Among these noble metallic elements, it is beyond any doubt that platinum has been the most investigated metal, becoming the benchmark catalysts for this process [69,132]. The standing of this precious metal as a catalyst for the APR process is endorsed by its high overall activity in polyols conversion and hydrogen yield [141,304]. Knowing the goodness of platinum, the impregnation of said metal on cobalt spinel augurs a synergistic effect that enhances the activity and stability for the glycerol APR.

The main objective of this chapter is to evaluate the long-term catalytic behaviour of Pt-impregnated cobalt aluminate catalysts. In line with this, firstly, the method for preparing modified catalysts and the main characterization results are developed. Then, APR catalytic results carried out during 100 h TOS and the characterization of spent catalysts are presented. Given the importance of the WGS reaction in the APR process, a section was reserved to show the results obtained in carrying out said reaction in the liquid phase state.

5.1 CATALYSTS PREPARATION

The synthesis of the platinum-modified catalysts was conducted by impregnation on cobalt aluminate with a Co/Al ratio of 0.625. As way of reminder, proper amounts of aqueous solutions of $Co(NO_3)_2 \cdot 6H_2O$ and $Al(NO_3)_3 \cdot 9H_2O$ were coprecipitated with sodium carbonate at pH 10. The resulting suspension was aged at room temperature for 24 h, filtered, washed

several times with de-ionized water, dried at 110 °C for 17 h and calcined in a muffle furnace at 500 °C (heating rate 5 °C·min^{-1}) for 5 h in a static air atmosphere. This sample was abbreviated 0.625CoAl.
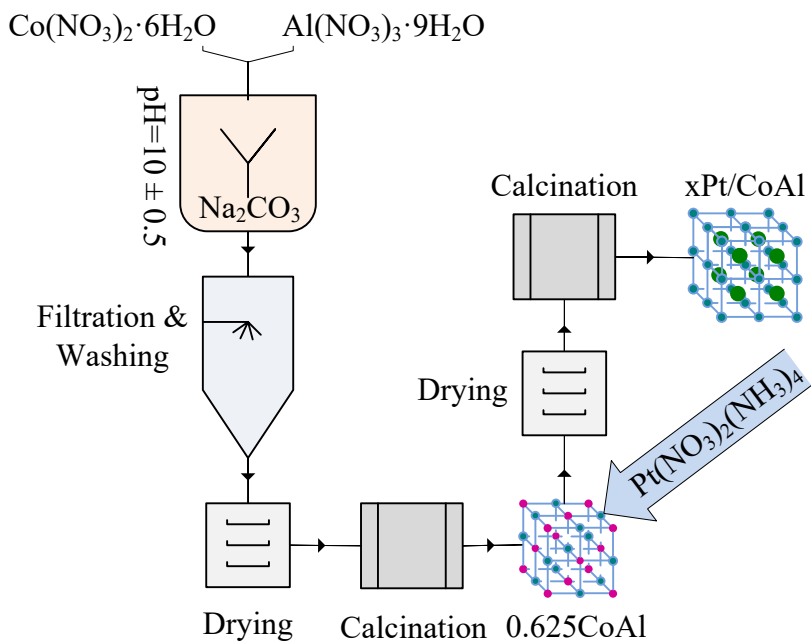
Scheme 5.1. Schematic representation of the synthesis of platinum-modified cobalt aluminate spinel catalysts.

Pt (with nominal contents of 0.3, 1 and 3 wt.%) was added to above prepared cobalt aluminate spinel (0.625CoAl) by wet impregnation method, using tetraammineplatinum(II) nitrate (Pt(NH$_3$)$_4$(NO$_3$)$_2$) as the metal precursor, dissolved in deionized water. After impregnation, the solids were dried at 110 °C for 17 h and finally, calcined at 350 °C in a muffle furnace (heating rate 5 °C·min^{-1}) for 3 h to anchor metal ions to surface. These samples were abbreviated xPt/CoAl, where x denoted the nominal wt.% of platinum. For comparative purposes, γ-Al$_2$O$_3$-supported Pt catalyst was prepared by simple calcination of (Al(NO$_3$)$_3$·9H$_2$O) in air at 500 °C for 4 h (heating rate 5 °C·min^{-1}) and subsequently impregnated with 0.3% platinum. This solid was calcined under the same conditions as the as-prepared xPt/CoAl and was abbreviated 0.3Pt/Al.

The sample reduction protocol has been maintained, the xPt/CoAl catalysts have been reduced at a temperature of 600 °C and the sample 0.3Pt/Al at 300 °C.

5.2   CATALYSTS CHARACTERIZATION RESULTS

5.2.1   Bulk chemical composition and textural properties

Table 5.1 and Figure 5.1 show the results of the textural characterisation, by N_2 adsorption-desorption experiments, for all the prepared samples. The Pt-modified catalysts showed mesoporous characteristics with S_{BET} values ranging from 134 to 146 $m^2·g^{-1}$. After Pt loading into the 0.625CoAl spinel, surface area and pore volume size increased. S_{BET} increased up to 17%, being the highest at the lowest platinum content. After reduction, S_{BET} values decreased at the expense of larger pores. Moreover, it was observed that textural properties of the 0.625CoAl spinels were stabilised upon Pt loading. For instance, upon reduction, S_{BET} of catalyst 0.625CoAl, 0.3Pt/CoAl and 3Pt/CoAl samples decreased by around 19%, 10% and 5%, respectively.

Table 5.1. Platinum loading and textural properties of Pt-modified catalysts.

Catalyst	Pt, wt.%	S_{BET}, $m^2·g^{-1}$	V_P, $cm^3·g^{-1}$	d_P, nm
0.625CoAl	-	125.3 *(101.7)*	0.280 *(0.375)*	6.8 *(9.6)*
0.3Pt/CoAl	0.29	146.3 *(131.0)*	0.561 *(0.521)*	12.7 *(14.8)*
1Pt/CoAl	1.09	138.6 *(126.1)*	0.541 *(0.553)*	12.8 *(14.9)*
3Pt/CoAl	3.01	134.4 *(127.4)*	0.537 *(0.514)*	13.2 *(14.7)*
0.3Pt/Al	0.36	138.4 *(138.1)*	0.192 *(0.198)*	3.9 *(4.0)*

In parenthesis, values for reduced samples.

The addition of Pt shifted the pore size of the xPt/CoAl samples towards higher values. After reduction, modification of the average pore size was also smaller in Pt loaded samples. Regarding the alumina supported reference catalyst (0.3Pt/Al), it showed the smallest pores. For this sample, both S_{BET} and pore size were preserved upon reduction.
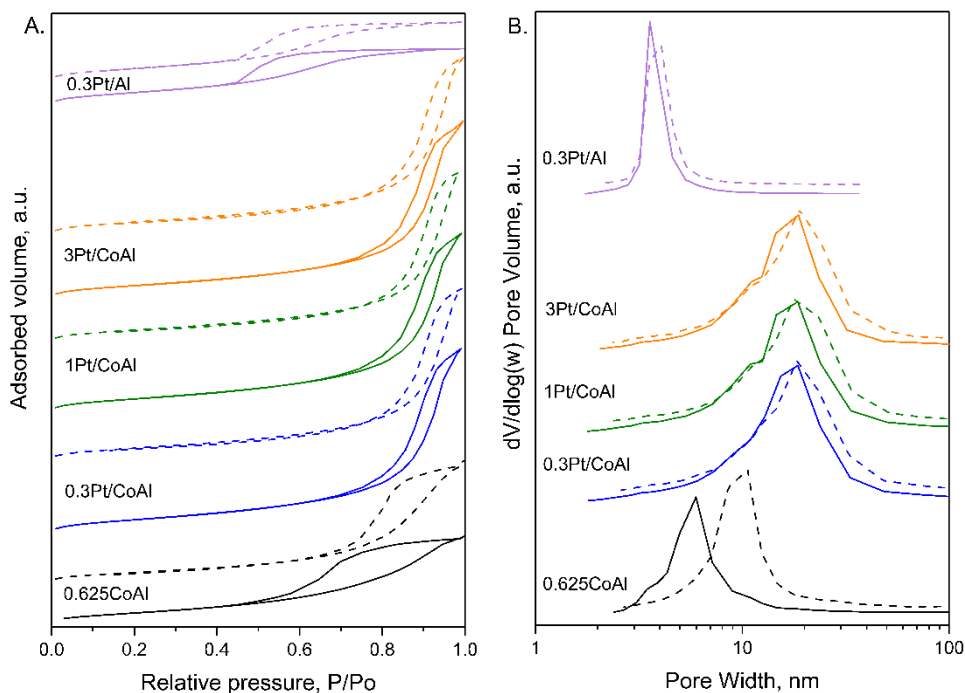
Figure 5.1. Nitrogen adsorption-desorption isotherms (A) and pore size distribution (B) of the calcined (solid lines) and reduced (dashed lines) xPt/CoAl samples.

5.2.2   Reducibility of the solids

The reduction profiles of the samples obtained by H_2-TPR are shown in Figure 5.2 and quantification of resulting peaks is given in Table 5.2. Catalyst 0.3Pt/Al exhibited three exceptionally low intensity peaks (for better viewing, it has been five-fold enlarged). The two low temperature peaks were related to the reduction of platinum species (PtOx). The peak at 227 °C was ascribed to the reduction of highly dispersed platinum species with little interaction with the support, while the peak at 375 °C was ascribed to the reduction of platinum species greatly interacting with alumina [305]. The high temperature peak, at around 660 °C, was related to the reduction of alumina, assisted by hydrogen spillover on Pt [306].

As described in Chapter 3, the reduction profile of 0.625CoAl sample showed four peaks centred at 292, 413, 594 and 783 °C. After Pt loading, a temperature peak emerged below 200 °C. This low temperature peak exceeded the theoretical

H_2 consumption of platinum species (PtO species were assumed), what suggested the concomitant Co^{3+} to Co^{2+} reduction of free surface cations promoted by platinum, due to hydrogen spillover from the Pt^0 surface. As calculated (Table 5.2), the promotional effect was largest at the lowest Pt loading (0.3 wt.%).
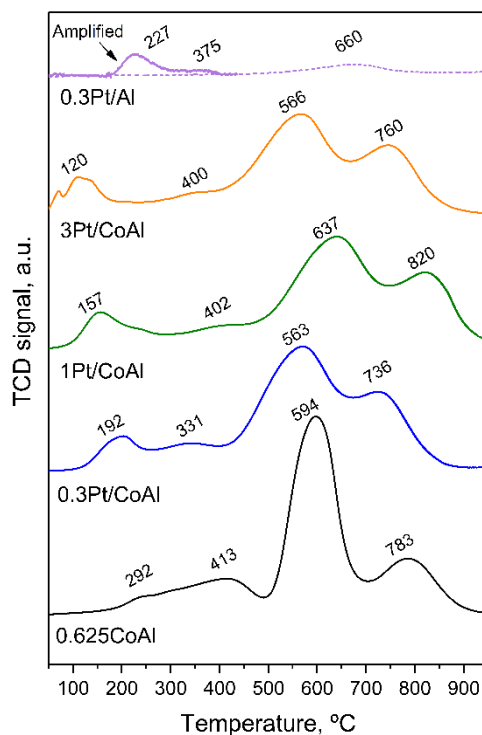
Figure 5.2. H_2-TPR profiles of xPt/CoAl samples.

However, Pt-Co catalysts showed disparate results in the less reducible Co species. For instance, taking as reference 0.625CoAl catalyst, the reduction temperature of Co^{2+} to Co^0 for 0.3Pt/CoAl and 3Pt/CoAl decreased by around 30 °C while for 1Pt/CoAl this temperature increased from 594 to 637 °C. The same behaviour was observed for the reduction temperature of Co ions in the spinel phase. Notwithstanding this opposite effect, all Pt-Co samples presented a degree of reduction at 600 °C (reduction protocol before reaction) superior to sample 0.625CoAl (62.6%), indicating the promotional effect of Pt (Table 5.2). The greatest reducibility at this temperature was shown by the 0.3Pt/CoAl

sample (68.6%). In conclusion, in the 0.3Pt/CoAl system, reducibility of the metal species (Pt, Co) was significantly promoted, as deduced from the increased low temperature hydrogen consumption, likely due to a strong Pt-Co interaction.

Table 5.2. H_2 consumptions and reducibility of the xPt/CoAl samples.

Catalyst	Total H_2 uptake, $mmol_{H2} \cdot g^{-1}$	Consumption below 250 °C, $mmol_{H2} \cdot g^{-1}$	Degree of reduction[a], %
0.625CoAl	7.04	-	62.6
0.3PtCoAl	7.29	0.516 (0.0149)	68.6
1PtCoAl	7.36	0.659 (0.0559)	65.3
3PtCoAl	7.37	1.126 (0.1547)	65.2
0.3Pt/Al	0.35	0.0195 (0.0185)	n.a.

In parenthesis, the theoretical amount assuming PtO species.
[a]H_2 consumption at 600 °C with respect to 950 °C.

5.2.3 Nature and morphology of the phases

The phase composition and morphology of the samples was evaluated by XRD, and the obtained diffraction patterns are shown in Figure 5.3. Independent of the support, none of the Pt-containing samples showed any diffraction peak of platinum species, which pointed to a high Pt dispersion, as expected by the low loadings applied (1000 x Pt/Co mole ratio=2.3, 7.7 and 22.1). Catalyst 0.3Pt/Al showed characteristics peaks of γ-alumina with a clear baseline elevation indicative of its amorphous nature. Calcined cobalt-containing samples presented the characteristic diffraction peaks of cobalt aluminate (PDF 00-044-0160) and cobalt oxide (PDF 00-042-1467) spinel. Both species, with cubic crystal system and Fd3m space group, have almost the same diffraction angles and could only be distinguished by their different lattice parameters (smaller for Co_3O_4). The calculated parameter for the bare 0.625CoAl sample was 0.8040 nm, which was lower than the lattice constant of standard stoichiometric $CoAl_2O_4$ (0.8104 nm). This could be due to the non-stoichiometric composition of 0.625CoAl, caused by the higher Co/Al mole ratio (0.634) compared to the corresponding stoichiometric one. After the addition of Pt, the lattice parameter increased slightly, proportionally to platinum content, suggesting that Pt strongly interacted with the support.

As can be seen in Table 5.3, the spinel crystallite size of the calcined samples increased between 26 and 30% with the addition of platinum. On the contrary, the size of metallic cobalt crystallite noticeably decreased, suggesting that Pt acts as a structural promoter that decreases metallic Co particle size.
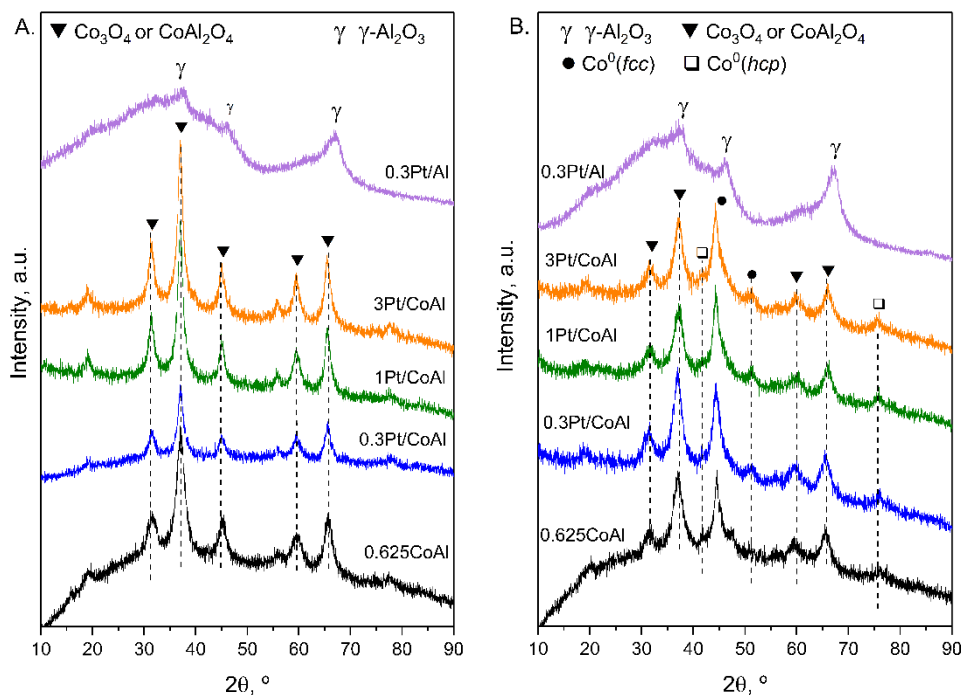
Figure 5.3. XRD patterns of (A) calcined and (B) reduced Pt-containing catalysts.

Regarding the reduced assays, cobalt-containing catalysts showed diffraction peaks ascribed to metallic Co, prevailing in the *fcc* phase with respect to the *hcp* phase. In addition, the aforementioned cobalt spinel phase was still identifiable. However, as for the calcined samples, any signal of Pt species was absent.

Table 5.3. XRD analysis results of the calcined and reduced xPt/CoAl samples.

Sample	Calcined samples			Reduced samples		
	d_{spinel}, nm	a_{spinel}, nm	I_{220}/I_{440}	$d_{Co(hcp)}$, nm	$d_{Co(fcc)}$, nm	$d_{Co(both)}$, nm
0.625CoAl	5.0	0.8040 ±0.0014	0.63	22.8	11.6	16.5
0.3Pt/CoAl	6.3	0.8052 ±0.0011	0.57	8.0	2.1	6.9
1Pt/CoAl	6.3	0.8063 ±0.0006	0.78	7.5	5.1	6.5
3Pt/CoAl	6.5	0.8065 ±0.0005	0.70	9.1	4.9	7.0

Figure 5.4 shows the STEM micrographs and the resulting particle size distribution histograms of the reduced catalysts. The surface morphology of cobalt aluminate support is basically preserved after Pt addition. The energy dispersive X-ray spectra (EDX) analysis confirmed the metallic composition of the Pt nanoparticles. The analysis revealed the presence of well-dispersed metallic particles of homogeneous size. Overall particle size of metallic cobalt nanoparticles were in the range of approximately 14-24 nm (average size of 20.3 nm) having cube/cuboid shape; in contrast, Pt nanoparticles showed a near-spherical shape, and a much smaller size, in concordance with the absence of diffraction peaks in XRD. Overall particles size ranged between 0.5-3.5 nm, with a mean size of 1.62 nm for 0.3Pt/CoAl, 1.88 nm for 1Pt/CoAl and 2.35 nm for 3Pt/CoAl. Pt nanoparticles coexisted homogeneously dispersed on large Co nanoparticles, as can be seen in the STEM images. For the monometallic 0.3Pt/Al sample, most of the nanoparticles were uniform with an average size of 1.84 nm.
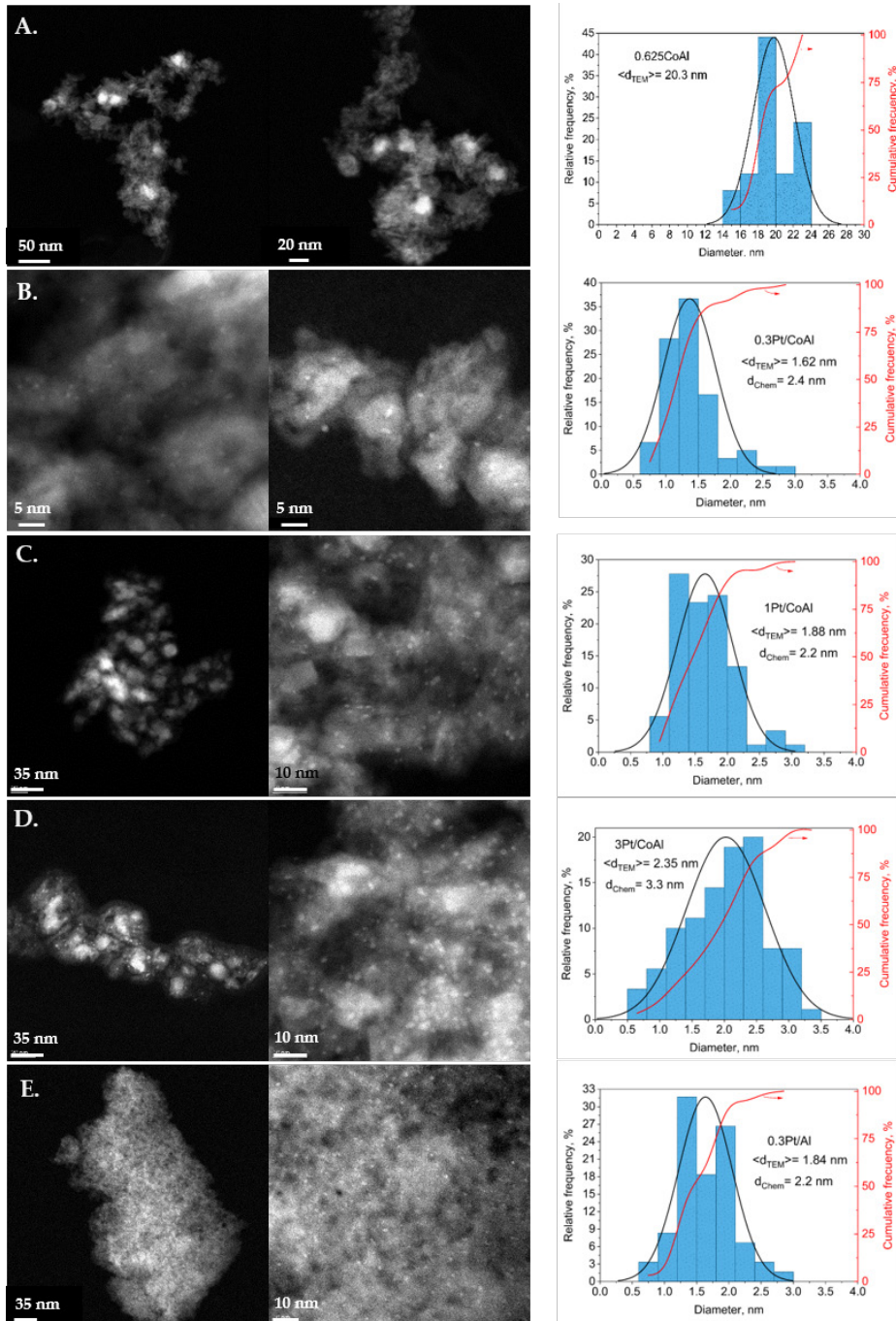
[2]**Figure 5.4.** STEM micrographs and size distribution histogram of the reduced catalysts: (A) 0.625CoAl, (B) 0.3Pt/CoAl, (C) 1Pt/CoAl, (D) 3Pt/CoAl and (E) 0.3Pt/Al.

---

[2] $d_{CHEM} = \dfrac{6000}{\rho_{Pt} \cdot n_{sb,Pt} \cdot S_{Pt}}$, where $\rho_{Pt} = 21.45 \text{ g} \cdot cm^{-3}$

$S_{Pt} = 0.0655 \text{ nm}^2 \cdot at_{Pt}^{-1}$

5.2.4   Metallic function

This fundamental parameter of metal catalysts was estimated from H_2 chemisorption. Platinum particle size was also calculated by this chemical technique, obtaining a mean diameter in the range 2.2-2.4 nm for 0.3 and 1% of Pt loading and 3.3 nm for 3Pt/CoAl sample, slightly larger than calculated from STEM (Figure 5.4). This discrepancy could be due to the diminished hydrogen adsorption capacity due to the strong Pt-Co interactions, likely alloy formation. This discrepancy was more evident in 0.3Pt/CoAl catalyst, suggesting stronger Pt-Co interaction, in agreement with H_2-TPR. Available metallic Pt sites increased proportionally to Pt loading. Thus, we hypothesize that Pt-Co interaction, especially at low Pt loadings, not only promoted the reducibility of the catalyst but also increased the amount of available metallic Co species.

Pt dispersion estimated from the H_2 chemisorption was in agreement with the values obtained with the STEM technique. The largest difference between techniques was for 0.3Pt/CoAl catalyst, which gave a slightly lower value (58%) than 1Pt/CoAl. Possibly, the dispersion measured by H_2 chemisorption was under-estimated, due to the high Co-Pt interaction.

The data for the metal function evaluation by the model reaction of cyclohexane dehydrogenation is also displayed in Table 5.4. As can be dissected from both A_{dehyd} and TOF_{dehyd}, Pt-impregnation undoubtedly enhanced catalytic activity for this reaction. This higher dehydrogenating activity confirms the synergistic effect of Pt-Co alloy revealed by H_2-TPR and H_2 chemisorption.

Table 5.4. Characterization of the metallic function of the Pt-modified catalysts.

Catalyst	Exposed metal site[a], atoms·g^{-1}		D$_{Pt}$, %		A$_{dehyd}$ [c], mol·h^{-1}·g^{-1}$_{metal}$	TOF$_{dehyd}$ [c], s^{-1}
	Co°	Pt°	Chem[a]	TEM[b]		
0.625CoAl	23.0·10^{18}	-	-	-	1.78	0.59
0.3PtCoAl	30.4·10^{18}	5.2·10^{18}	58	72	8.35	2.29
1PtCoAl	25.5·10^{18}	20.7·10^{18}	62	63	7.92	2.20
3PtCoAl	30.7·10^{18}	38.7·10^{18}	42	50	12.3	3.55
0.3Pt/Al	0	6.9·10^{18}	62	64	7.17	0.61

[a] *from H$_2$ chemisorption.*

[b] *estimated by TEM[3].*

[c] *from cyclohexane dehydrogenation model reaction.*

[3] $D_{Pt} = \dfrac{6 \cdot V_{bulk}}{\left(1 / n_s \right) \cdot < d_{TEM} >}$, where $V_{bulk} = \dfrac{M_{me}}{\rho_{Pt} \cdot N_A}$ and assuming spherical shape n$_s$= 1.3·10^{19} number of Pt atoms per unit area.

5.2.5   Structure and coordination state

The FTIR measurements of Pt-containing samples were carried out to identify the possible modification in the structure of the spinel. Skeletal FTIR spectra of calcined and reduced samples are shown in Figure 5.5. For calcined samples, after Pt addition, characteristic bands of Co(Al)-O vibrations were maintained while the typical signal of C-O-H bending mode shifted from 1399 to 1386 cm^{-1}, due to the Pt-ligand chemical bonds [307]. Furthermore, the presence of the Pt oxide species generates shoulder peaks at low energies (420-400 cm^{-1}). After reduction, a growth in the bands between 800-500 cm^{-1} was evidenced.
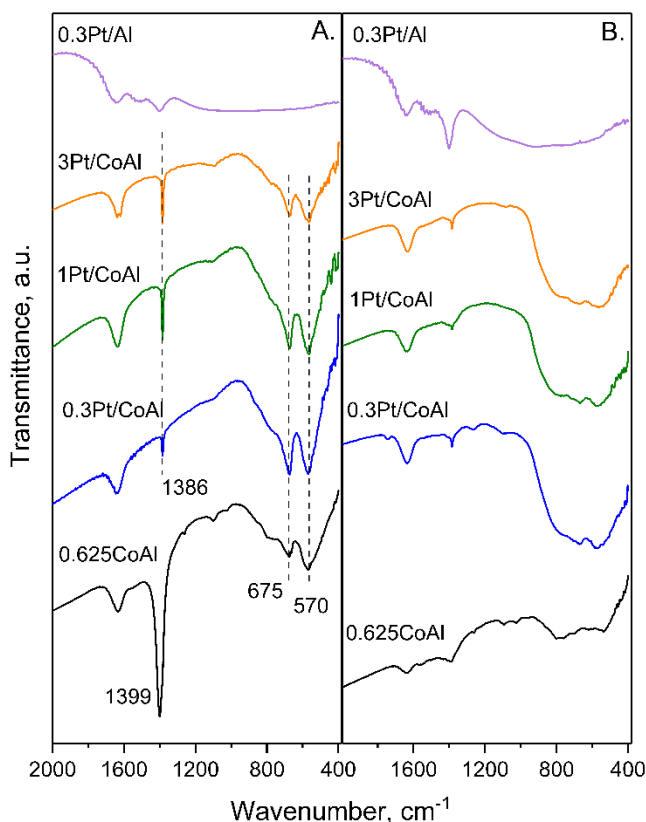
Figure 5.5. Skeletal FTIR spectra of (A) calcined and (B) reduced cobalt aluminate spinel samples modified by platinum.

^{27}Al NMR solid-state spectroscopy was used to study the structure of the aluminium cations in the calcined catalysts. Figure 5.6 depicts the obtained

spectra and in the inset table, the quantification of Al^{3+} ions in different coordination structures are shown. Bare alumina presented three peaks at 7.5, 33.6 and 61.8 ppm, related to octahedral (Al_O), pentahedral (Al_P) and tetrahedral (Al_T) Al^{3+} species, respectively [308].

Sample	Al^{3+} sites distribution, %		
	Al_O	Al_P	Al_T
0.625CoAl	96.2	0	3.8
0.3Pt/CoAl	84.3	8.1	7.6
1Pt/CoAl	87.1	7.2	5.7
3Pt/CoAl	89.2	7.9	2.9
0.3Pt/Al	65.4	16.9	17.7
γ-alumina	58.6	18.6	22.8
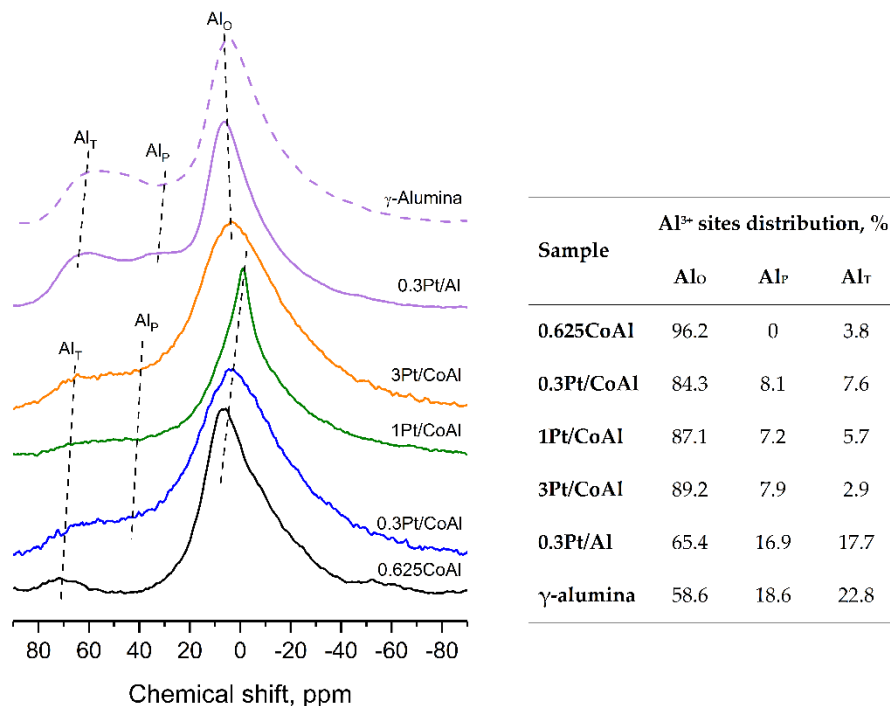
Figure 5.6. ^{27}Al-NMR spectrum of calcined xPt/CoAl samples and the distribution of differently coordinated Al^{3+} sites (from the peak areas).

Nevertheless, 0.625CoAl spinel, as could be seen in Chapter 3, exhibited only two peaks at 6.9 and 71.8 ppm, strongly prevailing the octahedral symmetry (Al_O/Al_T = 96/4). Also, the low symmetry of the main peak of 0.625CoAl indicated different Al^{3+} surrounding environments. In addition to the peaks shown by the 0.625CoAl sample, the ^{27}Al NMR spectra of xPt/CoAl samples revealed the existence of a very low relative intensity (about 8%) peak at around 33 ppm representing Al^{3+} ions in unsaturated pentahedral coordination (Al_P). Also, bimetallic assays contained relatively less amount of Al_O as compared to bare 0.625CoAl, suggesting that Pt ensembles anchor on these sites. In comparison to bare 0.625CoAl, Al_T and Al_O peaks of xPt/CoAl samples shifted

to the right. These results clearly indicated that the deposition of platinum ions caused changes in the distribution and coordination of Alo sites of the cobalt aluminate spinel.

Figure 5.7.A displays the recorded Co 2p spectra of calcined samples, and the binding energies (BE) of the Al, Co and Pt species and the surface Co/Al atomic ratios are tabulated in Table 5.5. The Co 2p spectrum of the calcined catalysts presented the characteristic pattern of cobalt oxide, with the Co $2p_{3/2}$ peak at 781.1-781.6 eV and a strong shake up feature between 785.1 and 786.5 eV. Interestingly, the Co^{2+} $2p_{3/2}$ binding energy of xPt/CoAl samples is slightly shifted to lower BE by adding Pt. The higher values of 0.625CoAl can be due to the strong interaction between aluminium and cobalt [165].
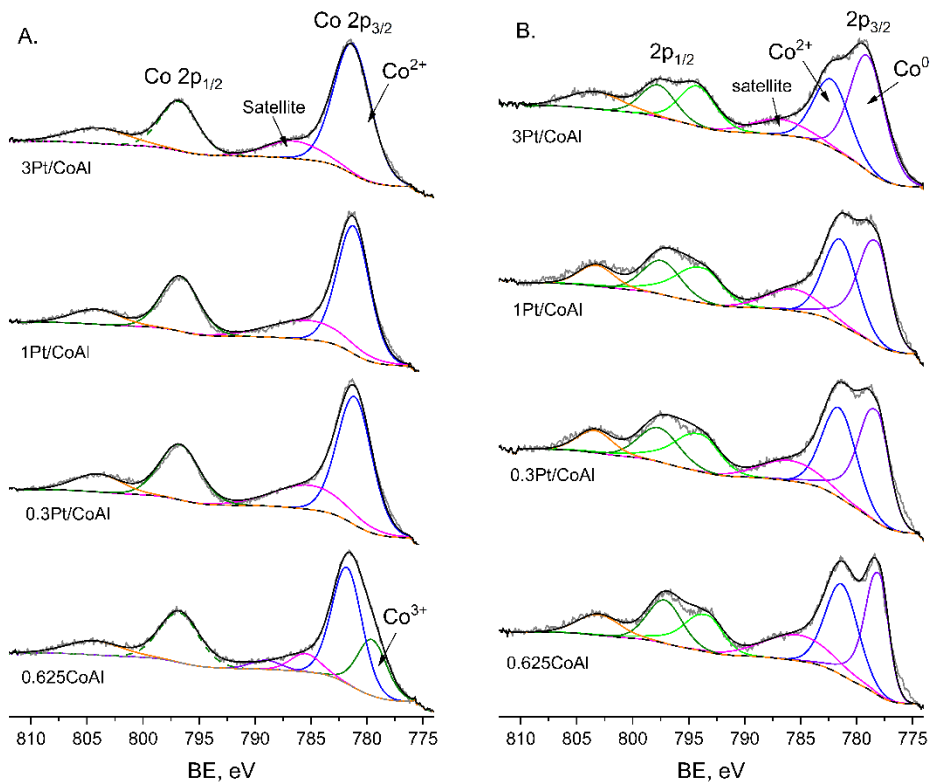
Figure 5.7. XPS spectra corresponding to Co 2p for calcined (A) and reduced xPt/CoAl samples.

The XPS Co 2p for reduced samples are shown in Figure 5.7.B. The spectra of reduced samples were deconvoluted into Co^0, Co^{2+} and shake up satellites; however, no peaks could be assigned to Co^{3+}, probably due to the self-reduction in the high vacuum chamber. Co 2p peaks of the xPt/CoAl samples shifted to higher binding energies compared to parent 0.625CoAl. This upshift could be attributed to the electron transfer from less electronegative Co to Pt atoms that decreased electron density at the Co site [309]. Thus, this supported the above noted Pt-Co interaction in the investigated system. Al 2p level binding energy was measured at 74.2 eV, which is typically ascribed to Al^{3+} cations placed at the octahedral sites [310]. It is known that the Al 2p photoelectron line of alumina can mask the most prominent photo-emitted electron of platinum (Pt 4f) [311], due to that, the Pt $4d_{5/2}$ was analysed instead. Although limited due to the low platinum content, the spectra of Pt 4d region showed peaks located at 314.0 ± 0.2 eV for the Pt-containing catalysts (Figure 5.8), which can be ascribed to the Pt^0 phase [312].

Table 5.5. XPS analysis results for Pt-modified cobalt aluminate spinel catalysts.

Catalyst	Al 2p, eV	Co $2p_{3/2}$, eV		Pt $4d_{5/2}$, eV		Co/Al at surface
		Co^{2+}	Co^0	Pt^{2+}	Pt^0	
0.625CoAl	75.6 (74.2)	781.6 (781.3)	(778.0)	-	-	0.266 (0.139)
0.3Pt/CoAl	74.2 (74.2)	781.1 (781.6)	(778.2)	316.8	(314.0)	0.271 (0.184)
1Pt/CoAl	74.2 (74.2)	781.2 (781.5)	(778.2)	317.7	(314.2)	0.271 (0.186)
3Pt/CoAl	74.0 (74.1)	781.3 (782.3)	(779.0)	317.4	(314.5)	0.251 (0.187)
0.3Pt/Al	74.0 (73.5)	-	-	315.5	(313.8)	-

Values in parenthesis for reduced samples.

As was also seen in Chapter 3 for the xCoAl samples, the overall surface Co/Al atomic ratio, calculated from Co 2p to Al 2p peak intensities (Table 5.5), decreased as compared to bulk composition (evaluated by ICP-OES). The surface enrichment on Al^{3+} ions was attributed to the lower surface free energy of Al as compared to Co [229]. Moreover, Co/Al atomic ratio on surface

decreased upon reduction. This behaviour has been related to the incorporation of metallic species into the porous structure [144], which would also explain the decrease in pore volume. Furthermore, it is interesting to note the higher Co/Al values measured for the bimetallic assays (as compared to parent 0.625CoAl) in the reduced state.
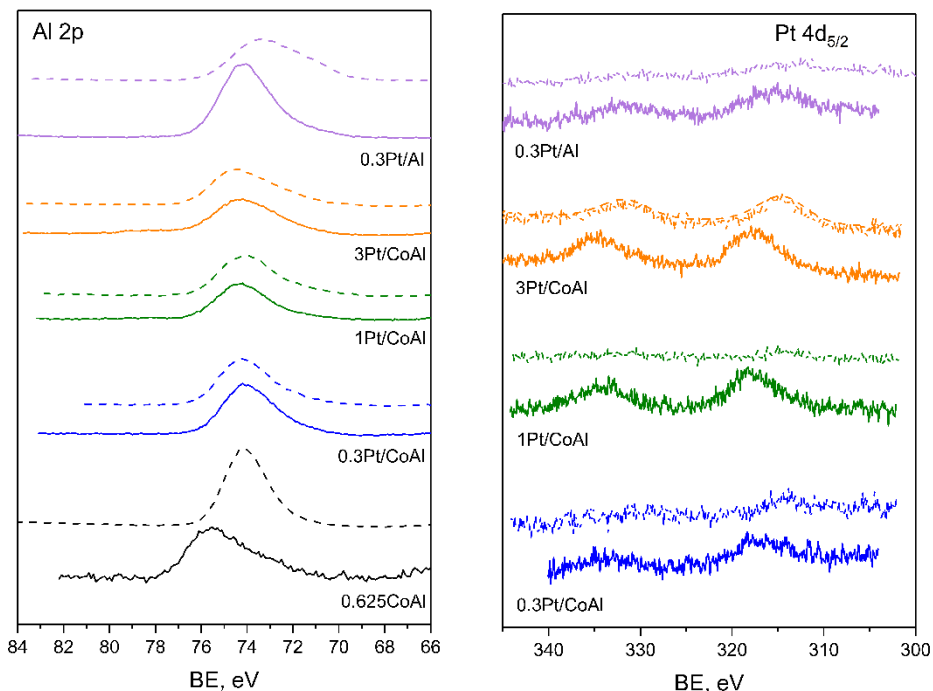
Figure 5.8. XPS spectra of Al 2p (left) and Pt 4d (right) for calcined (solid lines) and reduced (dashed lines) Pt-modified spinel samples.

5.2.6   Acid-base sites on the catalyst surface

Table 5.6 lists the values obtained in the evaluation of acidity and basicity of the catalysts. Cobalt-containing catalysts exhibited a remarkably similar surface acid sites density with predominantly weak and medium strength. Both 0.3Pt/CoAl and 0.3Pt/Al catalysts showed high activity in the isomerization of 33DM1B, the model reaction carried out to evaluate Brønsted acidity.

Table 5.6. Acid-basic properties of Pt-modified cobalt aluminate spinel samples.

| Catalyst | Surface site density | | | | | | | | $A_{isom,0}$, $\mu mol \cdot m^{-2} \cdot h^{-1}$ |
| | acid, $\mu mol_{NH3} \cdot m^{-2}$ | | | | basic, $\mu mol_{CO2} \cdot m^{-2}$ | | | | |
	Total	Weak	Medium	Strong	Total	Weak	Medium	Strong	
0.625CoAl	0.51	0.33	0.14	0.04	1.90	0.86	0.88	0.16	2.84
0.3Pt/CoAl	0.56	0.24	0.24	0.08	1.16	0.70	0..32	0.13	85.6
1Pt/CoAl	0.68	0.21	0.30	0.17	1.34	0.59	0.69	0.06	2.10
3Pt/CoAl	0.53	0.15	0.25	0.12	1.05	0.28	0.72	0.05	4.51
0.3Pt/Al	0.34	0.03	-	0.31	0.32	0.03	0.17	0.12	165.6

Weak: T < 300 °C; Medium: 300 - 650 °C; Strong: T > 650 °C.

Regarding basicity, the lowest density of surface basic sites corresponded to catalyst 0.3Pt/Al (0.32 $\mu mol_{CO2} \cdot m^{-2}$). On the opposite side, 0.625CoAl sample showed the highest density of surface basic sites, with 1.90 $\mu mol_{CO2} \cdot m^{-2}$. xPt/CoAl samples presented around 30-45% lower density than monometallic 0.625CoAl.

5.3   GLYCEROL APR
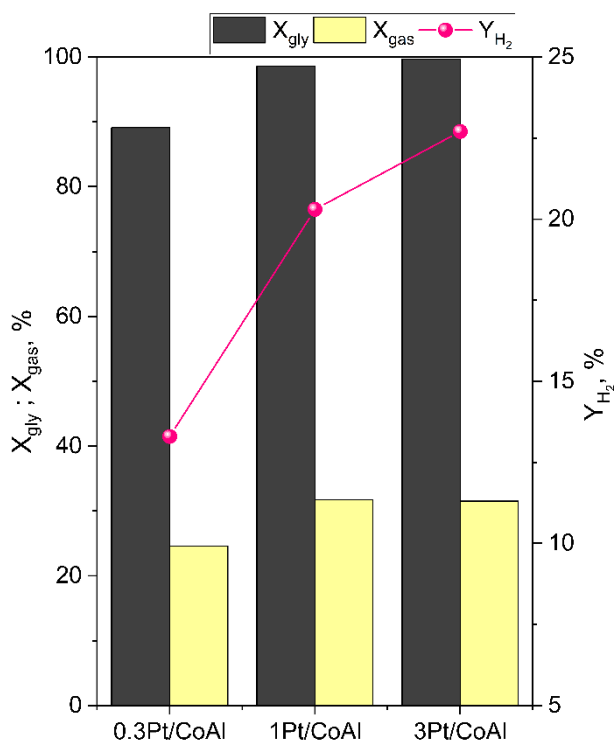
Figure 5.9. Catalytic activity of glycerol APR (glycerol total conversion, carbon conversion to gas and selectivity to gas) over xPt/CoAl at 260 °C/50 bar after 3 h TOS. Reaction conditions: $m_{cat} = 0.5$ g, $L = 0.2$ cm$^3 \cdot$min^{-1},   10 wt.%   glycerol/water, WHSV = 24.5 h^{-1}.

The first APR performance screening with cobalt aluminate spinels modified by platinum were performed at 260 °C/50 bar and WHSV of 24.5 h^{-1} (same as in Chapter 3). The results shown in Figure 5.9 exhibit a high glycerol conversion for all the samples. As could be expected, the sample with the least amount of Pt presented the lowest conversion of glycerol and to gas. Although the

3Pt/CoAl sample showed the best results in terms of glycerol conversion and hydrogen yield (X_{gly} = 99.7% and Y_{H2} = 22.7%), these results are not noticeably superior to those obtained with catalyst 1Pt/CoAl (98.6% and 20.3% for X_{gly} and Y_{H2}, respectively). On analysing the activity improvement by increasing the platinum content from 1 to 3%, it was concluded that the improvement was not significant due to the increase in metal content that it entails. Therefore, for the following catalytic tests, the 3Pt/CoAl catalyst was put aside.

The catalytic study continued with the performance of long-duration reactions (100 h TOS). For these reactions, the pressure and temperature conditions (260 °C/50 bar) have been maintained and the WHSV was established in 0.68 h^{-1}.

The evolution of glycerol total conversion and carbon conversion to gas with TOS is shown in Figure 5.10. The investigated catalysts proved high glycerol APR activity with a very high conversion of glycerol (above 99%) for the duration of the entire test. In addition, Pt-doped samples remained stable throughout the entire test whereas 0.625CoAl suffered a weak deactivation at above 70 h TOS.
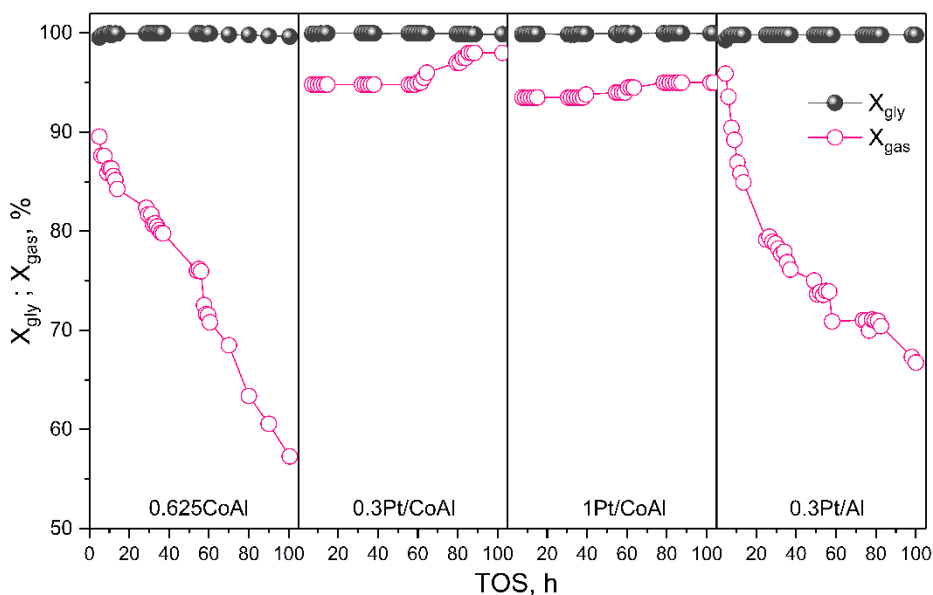
Figure 5.10. Total glycerol conversion (solid circles) and X_{gas} (open circles) evolution with TOS. Reaction conditions: 260 °C/50 bar, 10 wt.% glycerol, WHSV = 0.68 h^{-1}.

Significant differences existed in the carbon conversion capability of the catalysts. Again, both Pt-Co bimetallic catalysts showed the highest and more stable carbon conversion to gas (around 95%). Catalyst 0.625CoAl, with an initial X_{gas} value of 89.5% suffered 36% decay (X_{gas} of 57.3% at 100 h TOS). Reference 0.3Pt/Al catalyst also displayed moderate decay in X_{gas}, from 95.9% at the beginning of the reaction to 66.8% at 100 h TOS (30% decay). As previously noted, bimetallic catalysts showed very stable operation over 100 h TOS, moreover, a subtle increase in X_{gas} was appreciated. Overall, such stable performance in the glycerol conversion and gasification suggested a relevant role of Pt species in catalyst stabilisation.

A summary of gaseous product parameters is given in Table 5.7 at 10 h and 100 h TOS, and the evolution with TOS of the main gaseous product is displayed in Figure 5.11. Hydrogen was the main gaseous product for all the tested catalysts, with concentrations of around 60% by 0.625CoAl and 0.3Pt/Al, which dropped off to around 38% after incorporation of 1 wt.% Pt. Selectivity to hydrogen was also highest for these assays. CO_2 was the second most abundant gas product, throughout the whole reaction time.

Table 5.7. Gaseous products characteristics at 10 h/100 h TOS. Reaction conditions: 260 °C/50 bar, 10 wt.% glycerol, WHSV = 0.68 h^{-1}.

Catalyst	S_{H2}, %	S_{alk}, %	Y_{H2}, %	$[H_2]$, %	H_2/CO_2 ratio
0.625CoAl	67/86	29/16	55/89	61/78	2.8/4.7
0.3Pt/CoAl	49/53	34/38	37/44	50/52	2.0/2.0
1Pt/CoAl	32/49	40/36	21/36	37/49	1.8/1.8
0.3Pt/Al	65/65	31/29	57/46	60/62	2.7/2.8

Light alkanes (mainly methane) were formed in appreciable amounts, especially by the bimetallic catalysts. We believe such product distribution might be due to factors such as: (i) the very low spatial velocity, which enabled a large contact time between catalyst and reactants, pushing forward the hydrogenation reactions of the liquid intermediates, and (ii) the high reaction temperature employed in this work, where the CO hydrogenation is kinetically favoured

[313]. Theoretically, H_2/CO_2 ratio for the glycerol APR is 7/3. Lower values indicated hydrogen was consumed in parallel reactions (i.e. hydrogenation), while higher values indicated glycerol was partially reformed, to yield intermediates that release hydrogen but hold carbon atoms in the skeleton. It was observed that both monometallic samples gave the highest H_2/CO_2 values (> 2.4), while this ratio decreased to 2.0 and 1.3, for 0.3Pt/CoAl and 1Pt/CoAl, respectively. This behaviour coincided with their higher alkane production. It is likely that the small crystallites of cobalt particles and Pt-Co alloying in the bimetallic samples was involved in such methane production [314]. This behaviour was much more marked at the longest TOS (S_{alk} 36-38% vs. 16%).
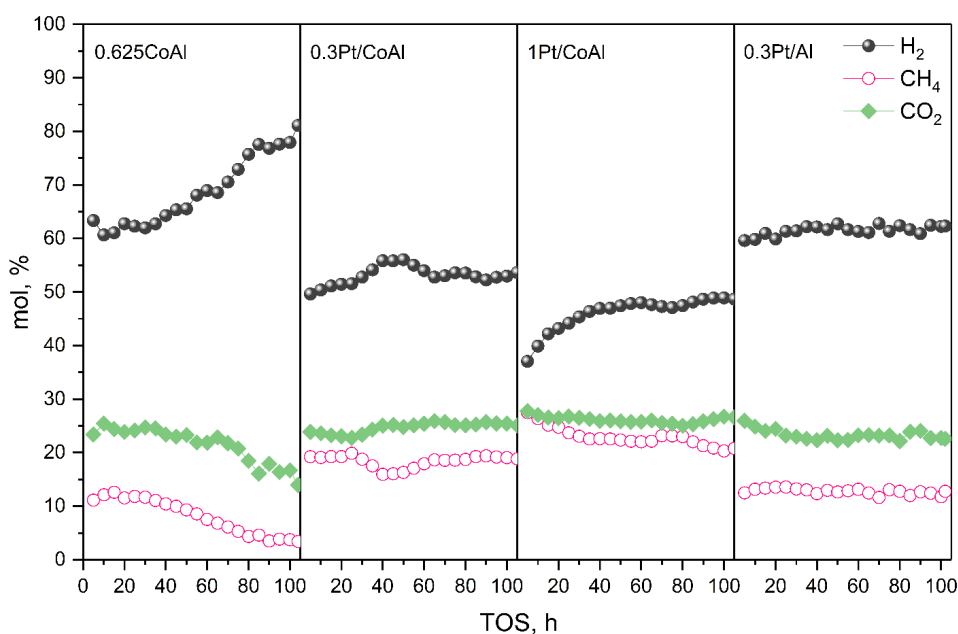
Figure 5.11. Evolution with TOS of the main gas phase compounds. Reaction conditions: 260 °C/50 bar, 10 wt.% glycerol, WHSV=0.68 h^{-1}.

Liquid product yields, evaluated as carbon moles in the liquid compounds ($F_{C,liq}$), are tabulated in Table 5.8. As can be observed, all the catalysts exhibited considerably low values under the investigated conditions. These results agreed with the high conversion to gas achieved by these catalysts. It is worth pointing to the significantly higher liquid flow rate obtained by monometallic catalysts (0.625CoAl and 0.3Pt/Al) as compared to bimetallic samples, reflecting the

decisive role of catalyst formulation on product distribution. Moreover, $F_{C,liq}$ varied with TOS, especially for monometallic assays, which showed three-fold increase during the catalytic run, showing a clear trade-off with X_{gas} (Figure 5.10). Interestingly, $F_{C,liq}$ for bimetallic samples remained almost constant, as evidence of its stability in the glycerol APR.

Liquid intermediates obtained by the cobalt-containing catalysts comprised mainly C_3 (i.e. acetone, propanols) compounds, which reflected a low decarbonylation activity. With respect to reaction pathways, it seemed that dehydration/hydrogenation route (Scheme 3.2) was predominant, which proceeded though glycerol dehydration reaction over acid sites. The highest amount of C_3 liquid intermediates was attained by catalyst 0.625CoAl with the concomitant increase of the H_2/CO_2 ratio, at above theoretical values. 0.625CoAl was the unique assay that contained propanoic acid in the liquid stream, which was formed through the dehydrogenation of 1-propanol and subsequent Cannizzaro reaction [315]. With regards to the reference catalyst 0.3Pt/Al, it produced comparable yields of C_2 and C_3 products. The main liquid product of the monometallic 0.3Pt/Al catalyst was ethanol, a secondary product obtained via the decarbonylation of hydroxyacetone, and favoured by metallic function. Regarding the xPt/CoAl assays, at the lowest Pt/Co ratio, yield to acetone dominated. As Pt loading increased, 2-propanol became the main liquid compound, which was likely formed through the hydrogenation of acetone.

Table 5.8. Liquid products characteristics at 10 h/100 h TOS. Reaction conditions: 260 °C/50 bar, 10 wt.% glycerol, WHSV = 0.68 h^{-1}.

Catalyst	$Y_{ethanol}$, %	$Y_{acetone}$, %	$Y_{propanols}$, %	$Y_{propanoic\ acid}$, %	$F_{C,liq}$, $\mu mol_C \cdot min^{-1}$
0.625CoAl	0.2/0	2.8/2.6	2.5/1.9	5.5/13.8	9.0/28.4
0.3Pt/CoAl	0/0	1.1/0.9	0.5/0.4	0/0	3.5/1.3
1Pt/CoAl	0/0	0.6/0.4	3.4/2.7	0/0	4.3/3.3
0.3Pt/Al	1.4/4.1	0.9/1.0	0.7/1.7	0/0	8.8/22.1

At high values of TOS the intensification of the dehydration route for both monometallic catalysts was evidenced by an increased yield of liquid products ($F_{C,liq}$) displaying a significantly higher selectivity to propanoic acid (0.625CoAl)

and ethanol (0.3Pt/Al). Gas phase product distribution also changed with TOS, especially for the monometallic 0.625CoAl catalyst. In this case, the selectivity to H_2 notably increased, up to 86%. It is noteworthy that although X_{gas} declined with TOS for catalyst 0.625CoAl, the H_2 yield increased (up to 89% for 0.625CoAl). However, for the monometallic catalyst 0.3Pt/Al selectivity to H_2 remained unchanged and thus, the H_2 yield decreased with TOS. Interestingly, bimetallic xPt/CoAl system showed a more stable performance with TOS. For instance, yield to liquid products remained at similar values, or even diminished. Concomitantly, the yield to H_2 increased to around 50%.

The obtained product distribution in APR experiments was hardly correlated with the surface acidity, conceivably due to the small differences among them. Instead, it was suggested that the product distribution depended on the balance between acid sites and metallic sites.

5.4   CHARACTERIZATION OF SPENT CATALYSTS

The catalysts used in the long-term reaction were characterized by N_2-physisorption, XRD, H_2-TPR, H_2-Chemisorption, TPH and Raman spectroscopy. The textural properties of spent catalysts are shown in Figure 5.12 and summarised in Table 5.9. Catalyst 0.3Pt/Al suffered the most drastic alterations with around 70% decrease in the specific surface area and pore volume. This behaviour was certainly ascribed to formation of boehmite [316]. 0.625CoAl spinel showed the opposite behaviour with a substantial increment of its S_{BET}, likely aided by a reduction of the average pore size (from 9.6 to 7.6 nm) and minor decrease of its pore volume. Finally, the bimetallic xPt/CoAl catalysts showed an intermediate behaviour. That is, both specific surface area and pore volume decreased after usage, though moderately (within 6-14% decrease). Pore size hardly varied, indicative of a higher textural and surface stability of bimetallic catalysts compared to monometallic ones.
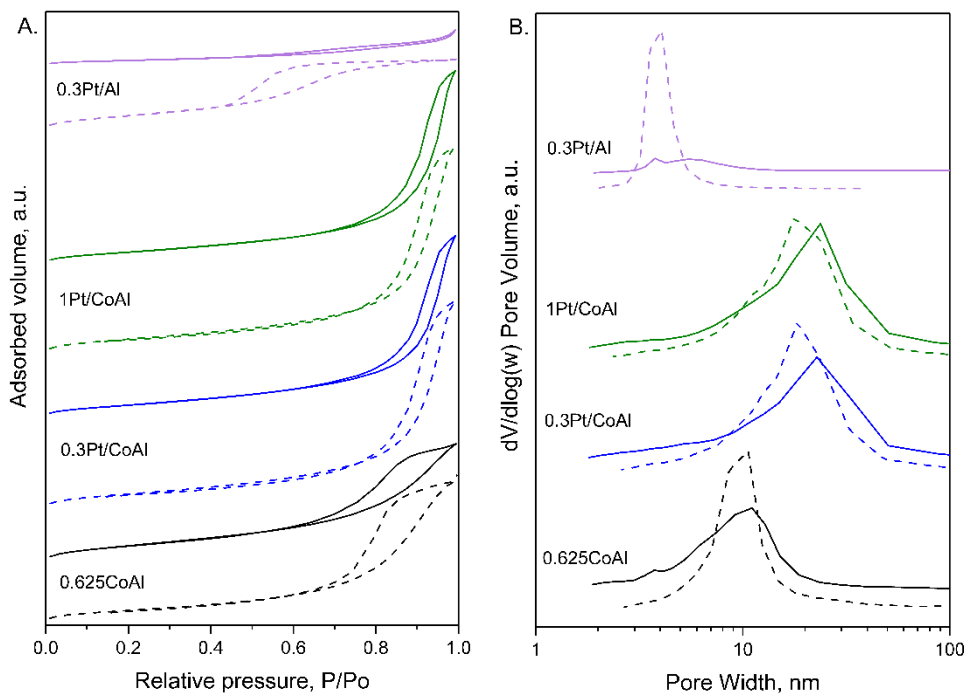
Figure 5.12. Nitrogen adsorption-desorption isotherms (A) and pore size distribution (B) of the reduced (dashed lines) and used (solid lines) samples.

Table 5.9. Textural properties and leaching values for used platinum-modified cobalt spinel catalysts.

Sample	S_{BET}, $m^2 \cdot g^{-1}$	V_P, $cm^3 \cdot g^{-1}$	d_P, nm	Leached metals, wt.%		
				Al	Co	Pt
0.625CoAl	142.1 *(+40%)*	0.309 *(-18%)*	7.6 *(-21%)*	0.6	2.7	-
0.3PtCoAl	112.7 *(-14%)*	0.457 *(-12%)*	13.5 *(-9%)*	0.3	1.6	0.1
1PtCoAl	113.4 *(-10%)*	0.485 *(-12%)*	14.5 *(-3%)*	0.1	5.7	0.06
0.3Pt/Al	42.7 *(-69%)*	0.093 *(-53%)*	7.7 *(+93%)*	0.4	-	0.02

In parenthesis, percentage variation with respect freshly reduced samples.

One of the most promising results of the assays investigated is their limited metal (Al, Co and Pt) leaching despite the long run duration (100 h). The amount

of Pt and Al leached out from the fresh catalyst was less than 0.1% and 0.6%, respectively. Co leaching is an issue during the aqueous phase reforming [317]. Cobalt-based catalysts showed restrained Co leaching with values in the 1.6-5.7% of the cobalt loaded. These results are more advantageous than those reported by others author in similar processes [149]. Thus, it is clear that the effectiveness of alternative catalyst formulations requires a careful assessment in order to better anchor the metal.

Figure 5.13. XRD pattern of the used samples.
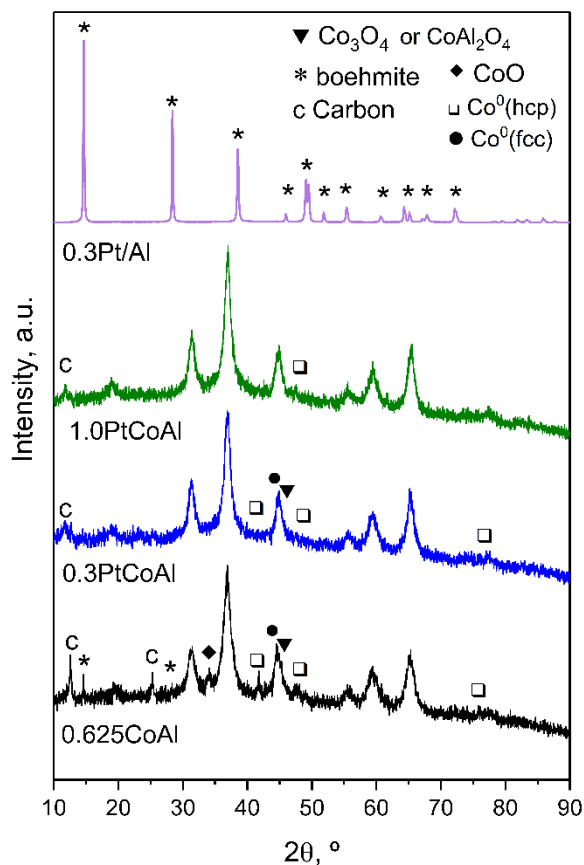
XRD diffractograms are displayed in Figure 5.13. As occurred in the parent fresh samples, no peaks of platinum were observed for any of the spent catalysts. Cobalt-containing catalysts showed wide and asymmetric peaks, as in the fresh samples. From data summarised in Table 5.10 an increase of the spinel crystal size was observed, with a maximum increase of 38% measured for catalyst

0.625CoAl. Characteristic peaks of metallic cobalt could be still detected, although, too weakly to perform quantitative analysis. Additionally, boehmite phase was identified in both monometallic catalysts, especially in sample 0.3Pt/Al. Indeed, the spinel structure can hinder the hydration of alumina to boehmite. Taking into consideration that diffraction peaks of boehmite were not observed for the bimetallic samples, it is likely that the presence of Pt could further inhibit the hydration. Also, it is worth noting that only monometallic assays, and particularly catalyst 0.625CoAl, exhibited the characteristic diffraction peak of carbon, at $2\theta = 25.5°$.

Table 5.10. Summary of metallic properties of xPt/CoAl samples.

Catalyst	d_{spinel}, nm	H_2 uptake, $mmol_{H2} \cdot g^{-1}$	Co species oxidized, %	Exposed metal atoms, atoms·g⁻¹
0.625CoAl	6.9 *(+38%)*	3.07	35.7	$1.1 \cdot 10^{18}$ *(-95%)*
0.3Pt/CoAl	7.8 *(+24%)*	4.37	27.1	$6.4 \cdot 10^{18}$ *(-82%)*
1Pt/CoAl	7.2 *(+14%)*	502	29.6	$40 \cdot 10^{18}$ *(-13%)*
0.3Pt/Al	-	0	-	$6.5 \cdot 10^{18}$ *(-6%)*

In parenthesis, percentage change respect to freshly reduced.

From the H_2-TPR profiles of the spent catalysts (Figure 5.14) some hydrogen consumption at below 600 °C was evidenced, which reflected that re-oxidation of the metal species occurred (it must be noted that fresh catalysts were reduced at 600 °C). As expected, 0.3Pt/Al was not re-oxidized. It is known that oxidation of Pt in aqueous phase is difficult, even in the presence of hydrogen [277]. This was also supported by the fact that the amount of available metal after APR was preserved for catalyst 0.3Pt/Al (Table 5.10). Considering this, it is assumed that Pt-Co alloys were also resistant to oxidation under APR conditions [317], thus, it can be hypothesized that the reduction peaks at below 600 °C were due to re-oxidized cobalt species not interacting with Pt. The contribution of coke hydrogenation should not be discarded, as suggested by the identification of carbonaceous deposits by Raman. Thus, the oxidation percentages of Co given in Table 5.10 could be somewhat overestimated. Also, the reduction peak at about 750 °C observed for all the cobalt containing samples, was ascribed to the reduction of cobalt species in the $CoAl_2O_4$ spinel phase, not reduced by the

pre-treatment (reduction) before catalytic run. Interestingly, bimetallic catalysts suffered less oxidation under APR conditions than the parent monometallic 0.625CoAl. In quantitative terms, for the most favourable assay, the oxidation of cobalt species was diminished by around 25% upon Pt doping (from 35.7 to 27.1%, for 0.625CoAl and 0.3Pt/CoAl, respectively). This behaviour was also consistent with the dramatic decrease in the exposed metal atoms (95% decrease) of the former.
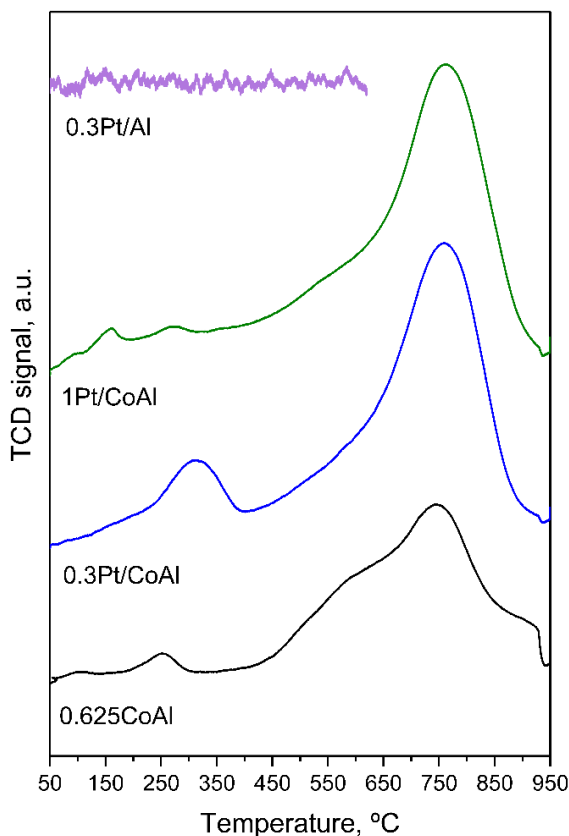
Figure 5.14. H2-TPR profiles of used samples.

5.4.1   Carbonaceous material deposition

The nature of the above mentioned carbon deposits was investigated by Raman spectroscopy. The Raman spectra (Figure 5.15) of both monometallic catalysts showed the typical D and G. The spectra of the spent bimetallic catalysts were

quite different and showed very low intensity in both bands, indicating negligible formation of carbonaceous deposits on the catalyst surface. It seemed clear that the strong Pt-Co interaction inhibited the coke formation during APR of glycerol [183].
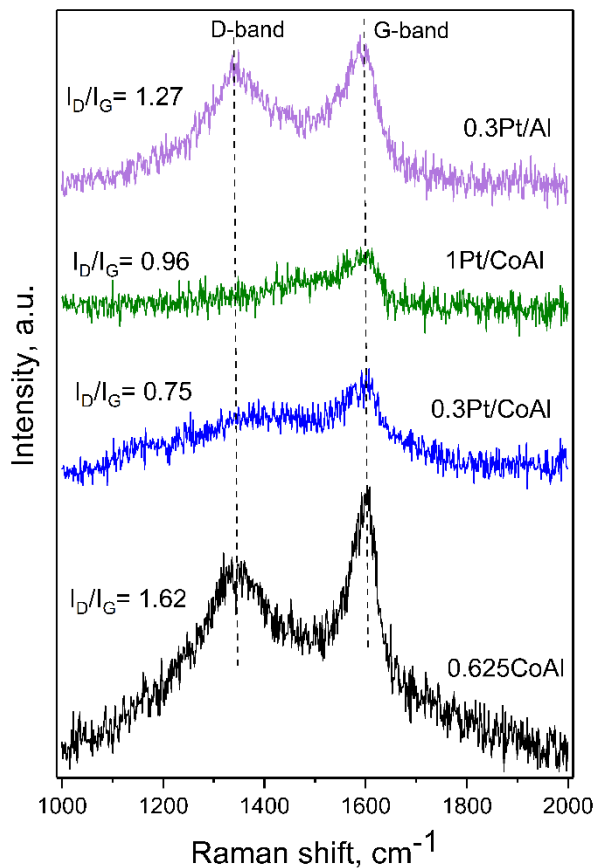
Figure 5.15. Raman spectra of the spent catalysts

According to the ratio of intensity of D-Band to G-Band (I_D/I_G), it could be concluded that the carbonaceous deposits on all the spent catalysts were predominantly amorphous, as I_D/I_G values were above or near unity. In the case of 0.625CoAl catalysts, the amorphous carbon would coexist with graphitic carbon, as the diffraction peak at $2\theta = 25.5°$ suggested. The absence of diffraction peaks of graphitic carbon for bimetallic catalysts must be related to the low amount of deposits.
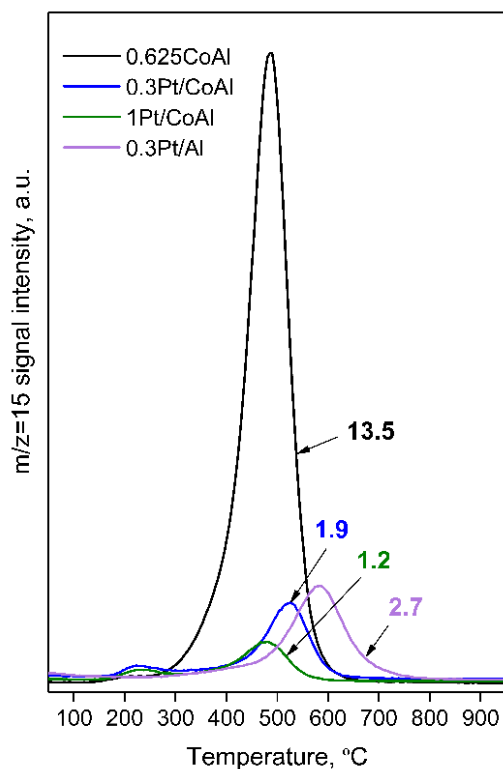
Figure 5.16. TPH profiles of the spent catalysts and the amount of surface carbon deposits given in $\mu mol_C \cdot g_{cat}^{-1}$.

The carbonaceous deposits were quantified by Temperature Programmed Hydrogenation (TPH) coupled to MS. Figure 5.16 shows the evolution, with temperature, of methane (m/z = 15 signal) formed from the hydrogenation of the surface carbonaceous materials and the quantification of carbon deposits on the surface ($\mu mol_C \cdot g_{cat}^{-1}$). Methane was released in the 200-700 °C range. Such a wide temperature range suggested the presence of different reactivity carbonaceous species, in agreement with the presence of two Raman peaks. The low temperature peak (at around 200 °C) could be ascribed to hydrogenation of the more amorphous carbon, while the high temperature peak (between 500 and 600 °C) was attributed to the hydrogenation of more polymerized carbonaceous deposits that need higher temperatures for its removal [318].

It is interesting to note that only Pt-containing assays showed the low temperature peak, which suggests it could correspond to the hydrogenation of

carbon deposited in the proximity of well dispersed Pt centres, which, in turn could dissociate and spillover hydrogen on the surface and favour hydrogenation of the carbonaceous precursor. Therefore, the high temperature peak was ascribed to the hydrogenation of carbon deposits located in farthest positions from the metallic centres [319]. Notably, catalysts 0.625CoAl showed the largest methane yield, of around 13.5 $\mu mol_C \cdot g_{cat}^{-1}$. The attained decrease upon Pt loading as highly significant, with around ten-fold decrease (1.2-1.9 $\mu mol_C \cdot g_{cat}^{-1}$), in line with previous XRD and Raman results.

5.5   LIQUID-PHASE WGS REACTION

WGS reaction generates great interest in the energy field and, particularly, in research pertaining to reforming. Thanks to the WGS reaction, a boost in hydrogen yield is achieved in the aqueous phase reforming of oxygenated compounds. It is for this reason, and due to the lack of research on liquid phase WGS, that this reaction has been studied at the same conditions that APR is carried out to expand the knowledge of said process. In addition, CO hydrogenation capacity of these catalysts was also investigated.

5.5.1   Mechanistic approach and Gas-Liquid Equilibrium

Two general mechanisms are commonly accepted for the gas-phase WGS reaction over noble metals supported on oxides: (i) regenerative mechanism, where the labile oxygen from the support oxidizes CO adsorbed on the metal and the formed oxygen vacancy is re-oxidized by water; (ii) associative mechanism, where adsorbed CO reacts with terminal hydroxyl groups of the support to form a C-containing intermediate that is decomposed to CO_2 and H_2. Thus, both the dispersed metal and the support participate in the reaction. Scheme 5.2 depicts the schematic representation of the WGS reaction when water reacts from the vapour or liquid phase. Davda et al. [186] contemplated the idea that WGS occurred in the gas bubbles formed within the liquid-phase reactor (Scheme 5.2.A), with the vapour water amount dictated by its liquid-vapour saturation. In Scheme 5.2.B, water reacts from the liquid phase and CO reacts from the gas phase, which implies that the reaction takes place at the gas-liquid-solid interface [126]. In both schemes, the CO reactant and the obtained products were partially dissolved in liquid water, dictated by the

vapour/solution equilibrium (Henry's law). Partial pressures of water, CO and H_2, and the liquid/gas distribution of CO and H_2 for each experiment, are given in Table 5.12. As can be seen, the high partial pressure of water, when close to operating pressure, could have a large impact on the CO and H_2 partial pressures, which are very low.

For CO hydrogenation, two mechanisms are usually proposed: (i) associative, where carbonyl combines with H_{ads} followed by C-O bond cleavage, and (ii) dissociative, where C-O bond breaking takes place directly on the metal, before the hydrogenation step [320].
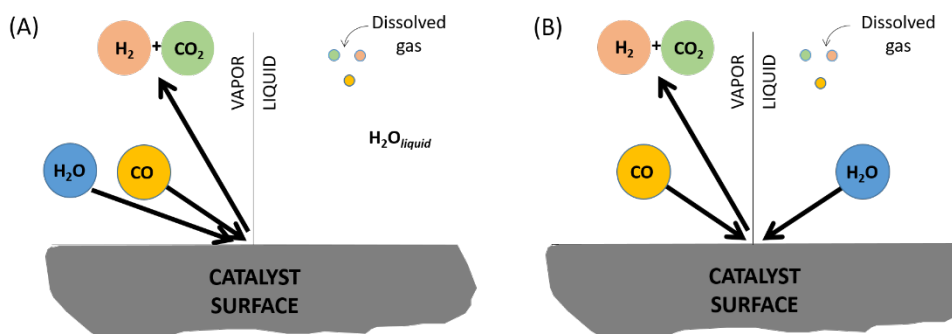
Scheme 5.2. Schematic representation of the water–gas shift (WGS) reaction mechanisms for aqueous-phase reforming (APR) reacting H_2O from liquid (A) or vapour (B) phase.

An important parameter in two-phase flow reactions is the liquid holdup. This parameter represents the total amount of liquid in the reactor volume at any given time [321]. Liquid holdup is influenced by pressure and liquid and gas flow rates but is independent of conversion, reaction temperature and reaction rate [322]. The follow empirical correlation, that take into consideration the positive effect of pressure and the specific gas mass flow rates, L' and G', was used to estimate the liquid holdup:

$$\varepsilon_L = \left[0.0254 + 0.0771\left(1 - e^{-7.72L'}\right)\right]\left(\frac{P}{G'}\right)^{0.14} \tag{5.1}$$

In order to gain knowledge on their solubility in water, Henry´s law constants (H) for the CO, CO_2, H_2 and CH_4 gases were estimated, from the experimental data in reference [323]. The units of the constants were bar/mole fraction in gas. The temperature dependence of the constants has been described by the Van't Hoff equation, which in its integrated form is the following:

$$H(T) = H^{ref} \cdot e^{\left[\frac{-\Delta_{sol}H}{R} \left(\frac{1}{T} - \frac{1}{T^{ref}} \right) \right]}$$

(5.2)

H^{ref} is the Henry's constant at a reference temperature $T^{ref} = 298.15$ K, and $\Delta_{sol}H$ is the enthalpy of dissolution. Table 5.11 shows the estimated H values.

Table 5.11. Estimated H values and vapour pressure of water.

H, bar/mole fraction ($\cdot 10^{-4}$)	@ 220 ºC	@ 235 ºC	@ 245 ºC	@ 260 ºC
CO	32.0	34.6	36.4	39.0
CO₂	4.0	4.7	5.1	5.8
H₂	14.3	14.8	15.1	15.5
CH₄	49.2	55. 1	59.2	65.6
Vapour pressure of Water, bar	23.20	30.78	36.77	47.36

The total pressure in the gas phase is due to the partial pressures of the gas compounds and to the partial pressure of the water vaporized in equilibrium with the liquid phase. Assuming liquid-vapour equilibrium for the water phase, the vapour pressure of water was calculated by the Antoine equation, and the obtained values are given in Table 5.11. As reflected, the solubility in water of the gases decreased with temperature. Among them, CO_2 and CH_4 were the most and least soluble, respectively, the latter being the most sensitive to temperature. Interestingly, the solubility of H_2 is almost twice of that of CO, which would decrease the H_2/CO mole ratio in the gas phase. Indeed, the partial pressures of CO and H_2 decreased with the increase of temperature, due to the increase in the partial pressure of water vapour.

Table 5.12. Liquid holdup (ε_L), vapour composition and liquid/vapour distribution of CO and H_2.

exp #	H_2/CO ratio	T, °C	P, bar	ε_L, %	P_{H2O}, bar	P_{co}, bar	P_{H2}, bar	L/V distribution, mol/mol	
								CO	H_2
1	0	260	50	16.4	47.36	2.64	0	$1.05 \cdot 10^{-04}$	0
2	1.33	260	50	16.2	47.36	1.13	1.51	$4.49 \cdot 10^{-05}$	$1.13 \cdot 10^{-04}$
3	2.33	260	50	16.1	47.36	0.79	1.85	$3.14 \cdot 10^{-05}$	$7.88 \cdot 10^{-05}$
4	4.0	260	50	15.8	47.36	0.53	2.11	$2.11 \cdot 10^{-05}$	$5.29 \cdot 10^{-05}$
5	4.0	245	50	18.8	36.78	2.64	10.58	$1.13 \cdot 10^{-04}$	$2.71 \cdot 10^{-04}$
6	4.0	235	50	15.8	30.78	3.84	15.38	$1.72 \cdot 10^{-04}$	$4.03 \cdot 10^{-04}$
7	4.0	220	50	15.8	23.2	5.36	21.44	$2.60 \cdot 10^{-04}$	$5.80 \cdot 10^{-04}$
8	4.0	220	40	15.3	23.2	3.36	13.44	$1.63 \cdot 10^{-04}$	$3.64 \cdot 10^{-04}$
9	4.0	220	35	15.1	23.2	2.36	9.44	$1.14 \cdot 10^{-04}$	$2.55 \cdot 10^{-04}$
10	4.0	220	25	14.4	23.2	0.36	1.44	$1.74 \cdot 10^{-05}$	$3.89 \cdot 10^{-05}$

5.5.2   Liquid-phase WGS activity in the absence of hydrogen ($H_2/CO = 0$)

The WGS performance of the prepared catalysts was evaluated at 260 °C and 50 bar (which corresponded to 2.64 bar above saturation), with water/CO mole ratio of 15/1 in the feedstream and a space-time of 76.8 $kg_{cat} \cdot s \cdot mol_{CO}^{-1}$.

The obtained CO conversion (X_{CO}), CO_2 yield (Y_{CO2}) and CH_4 yield (Y_{CH4}) at 10 h TOS are shown in Figure 5.17. Among the catalysts tested, the monometallic 0.3Pt/Al catalyst exhibited the lowest activity in the aqueous-phase WGS, with a 29.9% conversion of CO. The platinum-free monometallic 0.625CoAl catalyst was the most active assay, with 51.2% conversion. Bimetallic catalysts performed better; thereby, after the addition of 0.3% Pt, CO conversion increased to 63.8%. Moreover, it was further improved by 1% Pt loading, which reached 97.1% conversion, close to thermodynamic equilibrium (99.9%). It was evidenced that Pt loading on Co-based sample produced a promotional effect in the WGS activity and also, confirmed the strong influence of the support on the catalytic behaviour. The activation of the water molecule, a critical step in the WGS reaction, can occur either on the oxygen vacancies (reducible support) or on the metal particle. The H_2-TPR results indicated the very low reducibility of the 0.3Pt/Al catalysts, which suggested that the support did not provide sufficient oxygen vacancies for the activation of water molecules, as cobalt-containing catalysts did. Therefore, the WGS activity of the 0.3Pt/Al catalyst should be related mainly to the available Pt particles, with competitive adsorption of both CO and H_2O. The apparent reaction rate, normalized per Pt site (on the H_2 chemisorption basis), was calculated and used to compare the WGS activity for both catalysts with similar Pt content (0.3%). The obtained values (0.31 s^{-1} vs. 0.88 s^{-1} for 0.3Pt/Al and 0.3Pt/CoAl, respectively) supported the hypothesis of the active participation of the support in the reaction mechanism. On the other hand, the apparent reaction rates normalized per Co site (based on H_2 chemisorption) for the 0.625CoAl and 0.3Pt/CoAl catalysts were very similar (around 0.16 s^{-1}) and increased to 0.27 s^{-1} for the 1Pt/CoAl catalyst.

The acid/basic character of the surface can also affect the WGS catalyst activity [169,324]. Among our samples, the surface basic site density of 0.3Pt/Al (0.32

$\mu mol_{CO2} \cdot m^{-2}$) was lower than the cobalt-containing catalysts (1.16–1.90 $\mu mol_{CO2} \cdot m^{-2}$). The basic sites can polarize the water molecule and induce its dissociation to hydroxyl [169], which is the kinetically limiting step in WGS. The excellent WGS catalytic performance of the Pt-Co ensemble was ascribed to its improved ability for water dissociation (by the alloyed cobalt surface) as well as by a lowered CO binding energy, in comparison to monometallic catalysts [317].
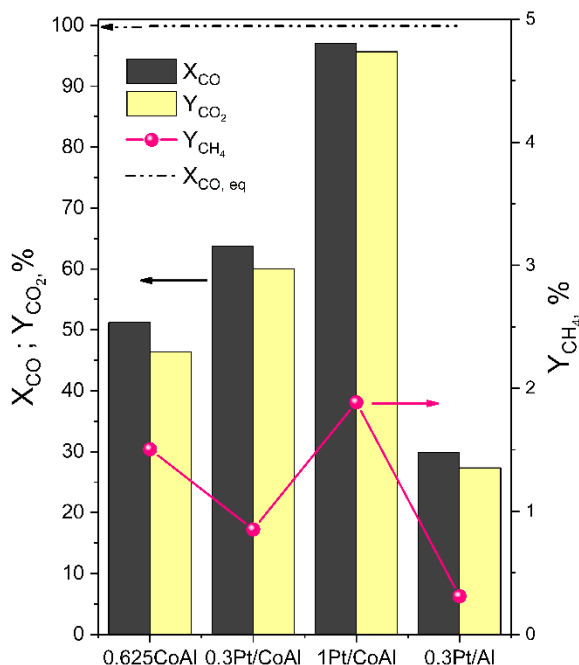
Figure 5.17. CO conversion and product yields in liquid phase WGS reaction at 260 °C/50 bar and TOS = 10 h. Feedstream: H_2O/CO = 15/1 mol ratio, space-time = 76.8 $kg_{cat} \cdot s \cdot mol_{CO}^{-1}$.

Under the investigated operation conditions, all the catalysts showed high CO_2 yield (ranging from 27.4% for 0.3Pt/Al to 95.7% for 1Pt/CoAl). Moreover, CO_2 selectivity was above 90% for all the catalysts. Thus, the CO_2 yields indicated a satisfactory product distribution, with mainly H_2 and CO_2 in the gas product stream. Methane was also detected, though to a much lesser extent. Methane yield increased as follows: 0.3Pt/Al (0.3%) < 0.3Pt/CoAl (0.9%) < 0.625CoAl (1.5%) < 1Pt/CoAl (1.9%).

Under the investigated conditions (i.e., feedstream containing only CO and water), the negligible hydrogenation of CO was associated with the low availability of the in-situ produced hydrogen that, in fact, competed for the metal sites. Moreover, not all the hydrogen produced in the gas phase was readily available for CO hydrogenation, as it was partly dissolved in the aqueous phase. Henry's constants (Table 5.11) indicate the higher solubility of hydrogen gas as compared to CO. Nevertheless, the fraction of CO and H_2 dissolved in the liquid phase was four orders of magnitude lower than that remaining in the liquid phase (Table 5.12). This was reflected in the large Y_{CO2}/Y_{CH4} yields ratio for all the samples (Table 5.13), between 30.8 (for 0.625CoAl) and 88.1 (for 0.3Pt/Al), indicating the superior CO hydrogenation activity of cobalt in a hydrogen-lean scenario. Further investigation was carried out to simulate real APR operation conditions (high H_2/CO ratio) and elucidate whether high hydrogen availability could overcome such CO hydrogenation limitations. The results are presented in the following section.

5.5.3   Liquid-phase WGS activity in the presence of hydrogen ($H_2/CO > 0$)

CO hydrogenation capacity of the catalysts was investigated under real APR conditions. H_2 was co-fed at different H_2/CO mole ratios (1.33, 2.33 and 4.0), based on the stoichiometric ratio in a typical APR process. Figure 5.18 displays the CO conversion reached as a function of the H_2/CO ratio for all the catalysts assayed, evaluated at 260 °C and 50 bar and after 10 h TOS. For comparison purposes, the X_{CO} values attained for the hydrogen-free feedstream are also depicted ($H_2/CO = 0$). For all the catalysts, the achieved CO conversion was lower than that obtained in the absence of hydrogen in the feedstream. Additionally, a decreasing trend of X_{CO} with H_2/CO was observed. The figure shows that bimetallic xPt/CoAl catalysts remained as the most active, independent of the H_2/CO ratio. The achieved CO conversion values varied as follows: 1Pt/CoAl $\gg$ 0.3Pt/CoAl $\gg$ 0.625CoAl > 0.3Pt/Al. It is interesting to note that the monometallic 0.625CoAl catalyst was the most sensitive to the feedstream composition (it had the largest negative slope in the figure). Catalyst 0.625CoAl showed the most considerable drop, of around 50% (X_{CO} = 39.4% and dropped to 19.9% by passing from H_2/CO = 2.33 to 4.0). The decrease was quite similar for 0.3Pt/Al (29%) and 0.3Pt/CoAl (25%) catalysts. As noted, 1Pt/CoAl

was the least sensitive to H_2/CO ratio, with only an 11% decrease in X_{CO}. A possible explanation for the negative effect of H_2/CO ratio on X_{CO} could be the lower residence time of the gas phase (as H_2/CO increased) and the competition between H_2 and CO for the available metal sites. In addition, the higher H_2/CO ratio decreased the CO partial pressure, which also might negatively affect the reaction rate. At these reaction conditions, CO was converted by both the WGS and CO hydrogenation reactions. It is well known that CO poses a negative reaction order in the methanation reaction, whereas it is slightly positive for H_2 [325]. The apparent reaction order with respect to CO was positive for all the catalysts and ranged between 0.12 and 0.17 for the bimetallic catalysts and 0.57 for the monometallic 0.625CoAl catalyst, while the order with respect to H_2 was negative (between -0.34 and -0.80 for bimetallic catalysts).
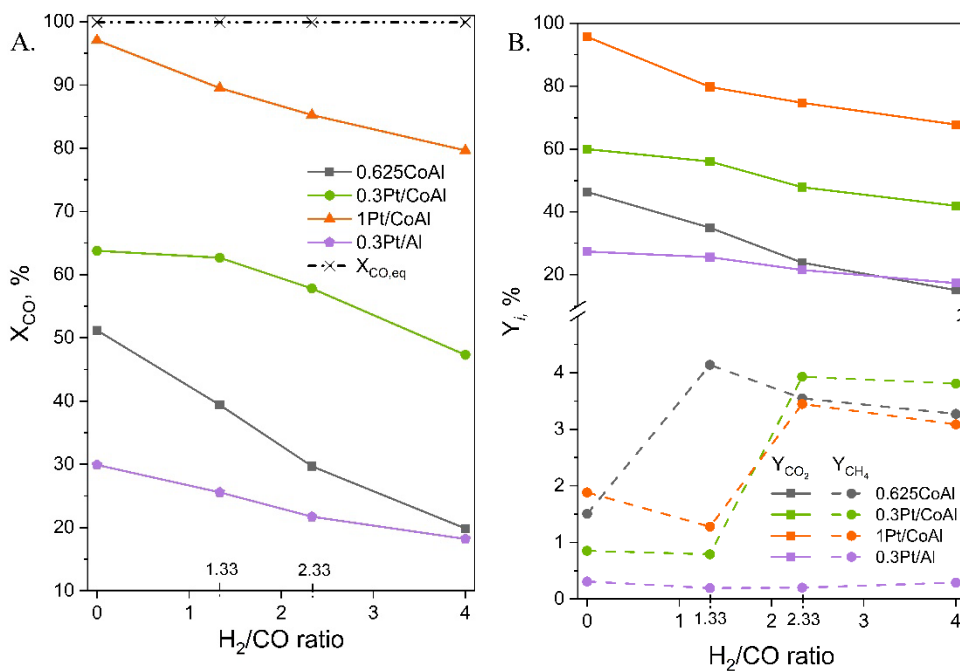
Figure 5.18. Catalytic activity in the WGS reaction at 260 °C/50 bar and H_2 co-feeding: (A) CO conversion and (B) product yield. Reaction conditions: m_{cat} = 0.2 g, L_{H2O} = 0.04 cm³·min⁻¹, G_{CO} = 3.5 cm³·min⁻¹.

Regarding product distribution, unreacted H_2 and CO, together with produced CO_2, CH_4 and traces of ethane, were detected in the reactor outlet. The very low

production of C_{2+} alkanes indicated inferior Fisher-Tropsch activity of the catalysts at these reaction conditions. Indeed, the production of methane was notably higher than under the hydrogen-free feed conditions, except for the 0.3Pt/Al catalysts, for which it slightly decreased. Several studies have shown that in the gas phase, the CO hydrogenation rate is higher than CO_2 hydrogenation, evidencing that high concentration of CO in the reaction bed could inhibit the reaction of CO_2 [320]. On this basis, we assumed that methane was only formed from CO hydrogenation. In this scenario, CO was converted by both WGS and CO hydrogenation reactions. Figure 5.18.B shows the trend in the CO_2 and CH_4 yields with H_2/CO ratio. The CO_2 yield showed a similar decreasing trend to X_{CO}. As occurred for $H_2/CO = 0$ (hydrogen was not fed), the bimetallic xPt/CoAl catalysts remained the most selective to CO_2, independent of the H_2/CO ratio, while both monometallic catalysts showed similar values of Y_{CO2}, especially at $H_2/CO \geq 2.33$.

Methane yield (Y_{CH4}) was used as representative of the CO hydrogenation activity. The Y_{CH4} obtained clear evidence that hydrogenation activity was more pronounced for Co-containing catalysts, in agreement with literature [326]. Not in vain, cobalt is one of the most used catalysts for CO hydrogenation [327]. On the opposite side, the 0.3Pt/Al catalyst showed very low Y_{CH4}. For example, at the highest H_2/CO ratio of 4.0, catalyst 0.3Pt/Al showed 0.29% of methane yield, whereas the rest of the investigated catalysts ranged in the 3.1-3.8% interval. Among the cobalt-containing catalysts, the different behaviour of Y_{CH4} for the monometallic 0.625CoAl is noticeable when changing H_2/CO from 0 to 1.33 — that is, for bimetallic catalysts, methane yield slightly decreased as H_2 availability increased, while for the 0.625CoAl catalyst, methane yield was boosted—. This behaviour could be related to the size of the cobalt particles, which was two-fold larger in the monometallic sample. Indeed, the hydrogenation of CO is known to be favoured onto large cobalt particles [328]. Note that, even in the case of more available hydrogen (higher H_2/CO), Y_{CH4} reached a plateau for the bimetallic catalysts. The effect on Y_{CH4} of the H_2/CO ratio change from 1.33 to 2.33 for cobalt-containing catalysts was also noticeable and could be related to the formation of cobalt carbide-like species at low hydrogen partial pressures [329].

Table 5.13. Effect of feedstock on Y_{CO2}/Y_{CH4} yields ratio.

Catalyst	H$_2$/CO ratio			
	0	1.33	2.33	4.0
CoAl	30.8	8.5	6.7	4.6
0.3Pt/CoAl	70.3	70.7	12.2	11.0
1Pt/CoAl	50.7	62.4	21.7	21.9
0.3Pt/Al	88.1	131.7	106.7	59.4

As previously noted, it can be considered that the CO_2 hydrogenation rate was negligible with respect to CO hydrogenation. In addition, no carbon deposits were detected in the spent catalysts. Therefore, the yield ratio (Y_{CO2}/Y_{CH4}) could be assumed as representative of the selectivity to WGS reaction (instead of CO hydrogenation): higher Y_{CO2}/Y_{CH4} indicated higher selectivity to WGS—that is, the CO was converted preferably by WGS rather than by CO hydrogenation—. Table 5.13 shows the obtained Y_{CO2}/Y_{CH4} values. Regardless of the catalyst, selectivity to WGS decreased with increasing hydrogen concentration in the feed, as more hydrogen is available for hydrogenation. It is interesting to note that the bimetallic xPt/CoAl catalysts experienced the highest drop in Y_{CO2}/Y_{CH4} values (84.4% and 64.9% for 0.3 and 1% Pt loading, respectively). Even so, they presented high WGS activity, only surpassed by the monometallic Pt sample.

Net hydrogen change (ΔH_2) has been defined as the difference in hydrogen molar flow between the reactor outlet and inlet: it can be either positive or negative depending on the net generation or consumption of hydrogen in the reaction system. In addition, the ΔH_2 parameter reflects the hydrogenation activity. CO hydrogenation (methanation) is a highly hydrogen-consuming reaction and pulls the ΔH_2 parameter to negative values. As can be seen in Figure 5.19, for cobalt-containing catalysts, ΔH_2 decreased with the increase of H$_2$/CO, due to the hydrogenation capability of cobalt, boosted by the hydrogen excess. Among all catalysts, both bimetallic xPt/CoAl catalysts presented positive ΔH_2, independent of the H$_2$/CO used. The largest positive ΔH_2 corresponded to the bimetallic 1Pt/CoAl catalysts, in agreement with its highest activity and selectivity to the WGS reaction, with a maximum value of 33.9% for H$_2$/CO = 1.33. Catalyst 0.3Pt/Al presented slightly negative ΔH_2 at a low H$_2$/CO

ratio (-1.02% at $H_2/CO = 4/3$), which turned slightly positive (+0.52%) for the highest hydrogen to CO mole ratio.
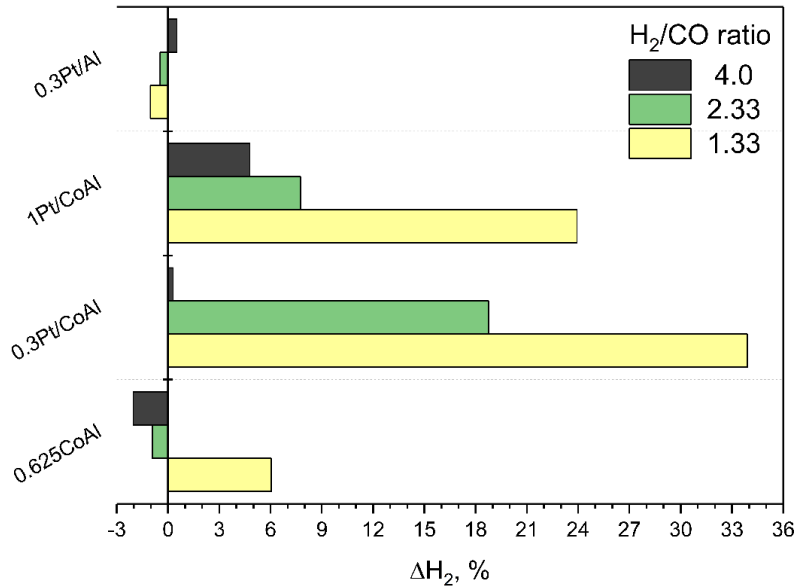
Figure 5.19. Net hydrogen variation in WGS reaction feeding H_2 at 260 °C/50 bar. Reaction conditions: $m_{cat} = 0.2$ g, $L_{H2O} = 0.04$ cm^3·min^{-1}, $G_{CO} = 3.5$ cm^3·min^{-1}.

5.5.4   Effect of temperature and pressure

Both the reaction temperature and pressure have a strong influence on the polyol APR activity and product distribution [330]. Whether the effect is related to reforming or to WGS is of great interest in order to understand the APR behaviour. With this aim, further experiments were carried out with catalyst 0.3Pt/CoAl in order to investigate the influence of temperature and pressure on the WGS activity and with H_2 co-feeding.

CO conversion achieved at 50 bar at different reaction temperatures and at $H_2/CO = 4.0$, is displayed in Figure 5.20. The observed initial increase in the conversion (which lasted about 3 h) was due to unsteady operation due to the reaction protocol, where the temperature was ramped while holding pressure. Thereafter, the conversion of CO remained stable. Noticeably, the increase in the reaction temperature led to increased CO conversion values. However, the obtained values were far from the equilibrium, indicating a kinetically

controlled reaction regime under these operation conditions. At low reaction temperatures, the higher overpressure may play a negative role in the catalytic activity, as the products desorption from the catalyst surface was hindered [331]. In addition, the water solubility of the reactants (CO and H_2) increased according to Henry´s law (Table 5.11). The fact that these values barely varied with temperature (from 2.2 at 220 °C to 2.5 at 260 °C) suggested that solubility issues hardly affected the H_2/CO mole ratio in the gas phase (Table 5.12).
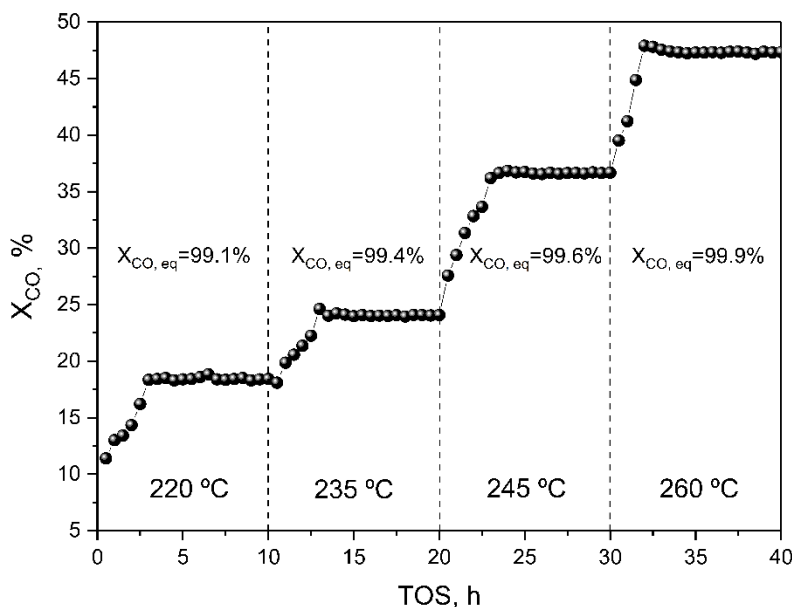
Figure 5.20. Conversion of CO in WGS reaction feeding H_2 over 0.3Pt/CoAl catalyst at 50 bar. Reaction conditions: m_{cat} = 0.2 g, L_{H2O} = 0.04 cm^3·min^{-1}, G_{CO} = 3.5 cm^3·min^{-1}, G_{H2} = 14 cm^3·min^{-1}.

According to Table 5.14, the Y_{CO2}/Y_{CH4} ratio increased with the operation temperature, i.e., it became more selective to WGS. This trend could be explained by two reasons: firstly, the thermodynamics of the CO hydrogenation reaction (highly exothermic reaction), which is highly favourable at lower temperatures; secondly, the increased partial pressure of water in the gas phase, which would shift the WGS equilibrium towards the products.

Table 5.14. Y_{CO2}/Y_{CH4} yields ratio for temperature/pressure experiments.

Temperature effect at 50 bar		Pressure effect at 260 °C	
Temperature, °C	Y_{CO2}/Y_{CH4}	Pressure, bar	Y_{CO2}/Y_{CH4}
220	0.97	25	8.2
235	3.5	35	2.4
245	6.0	40	2.1
260	11.0	50	0.97

Temperature, °C	$r_{app,CO}$, s^{-1}
220	0.255
235	0.332
245	0.507
260	0.654

Activation energy: 51.5 kJ·mol⁻¹
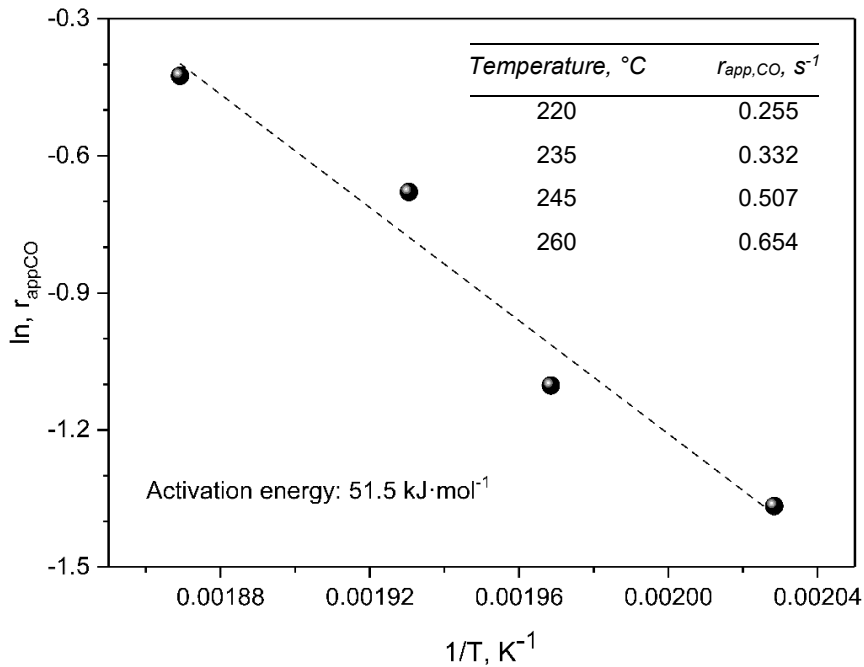
Figure 5.21. Arrhenius plot for WGS reaction feeding H_2 over 0.3Pt/CoAl catalyst at 50 bar and Apparent reaction rate normalized per Pt site ($r_{app,co}$) on the H_2 chemisorption basis. Reaction conditions: m_{cat} = 0.2 g, L_{H2O} = 0.04 cm³·min⁻¹, G_{CO} = 3.5 cm³·min⁻¹, G_{H2} = 14 cm³·min⁻¹.

The apparent reaction rate normalized per Pt site ($r_{app,co}$) (on the H_2 chemisorption basis) was calculated for each reaction temperature, at 50 bar and

$H_2/CO = 4.0$ in the feedstream. Obtained values are shown in Figure 5.21, and they revealed that $r_{app,CO}$ was strongly affected by the reaction temperature, as supported by the activation energy value of 51.5 kJ·mol^{-1} calculated from the Arrhenius plot. As far as is known, this is the first approach to the experimental determination of the apparent activation energy for the liquid-phase WGS, making the data hard to compare with similar works. It is of interest to note the inhibitory effect of hydrogen on the intrinsic reaction rate, as $r_{app,CO}$ decreased from 0.88 (for hydrogen-free feedstream) to 0.654 s^{-1} (for $H_2/CO = 4.0$).
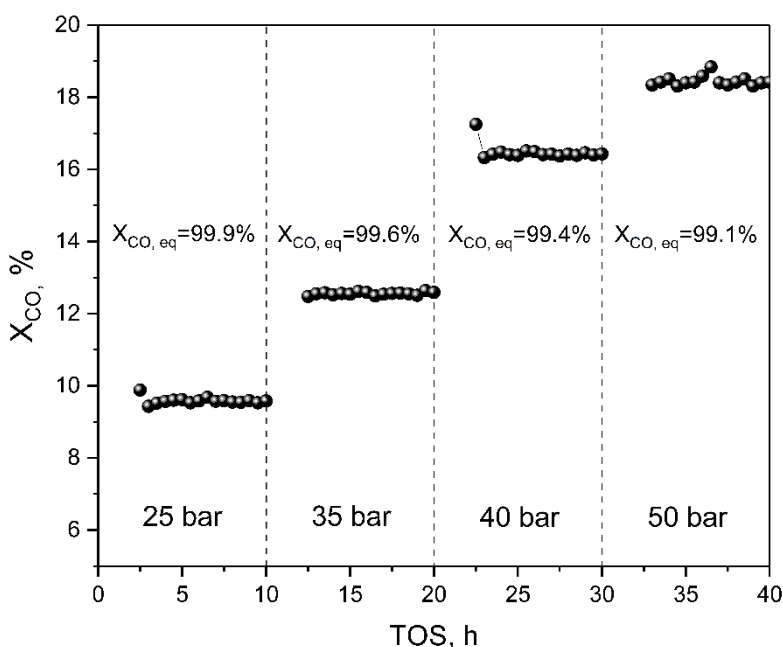
Figure 5.22. Conversion of CO in the presence of hydrogen over 0.3Pt/CoAl catalyst at 220 °C. Reaction conditions: m_{cat} = 0.2 g, L_{H2O} = 0.04 cm^3·min^{-1}, G_{CO} = 3.5 cm^3·min^{-1}, G_{H2} = 14 cm^3·min^{-1}.

Figure 5.22 shows CO conversion at 220 °C for different reaction pressures, with $H_2/CO = 4.0$. The observed gap in the first 2.5 h of reaction at each pressure is because the reactor outlet flow valve was shut until the desired pressure was achieved. Notably, CO conversion increased with operation pressure, at a constant reaction temperature. For example, at 25 bar, the obtained CO conversion was 9.6% and increased two-fold at 50 bar. The achieved CO conversions were far from the equilibrium (which decreased from 99.2% at 25

bar to 89.0% at 50 bar), which was a result of slow kinetics due to the low reaction temperature.

Product yields (Y_{CO_2} and Y_{CH_4}) for 0.3Pt/CoAl at different temperatures (A) and pressure (B) values are displayed in Figure 5.23. CO_2 yield turned out to be more sensitive to temperature than to pressure changes. For example, CO_2 yield increased by 95% by passing from 220 to 235 °C. In like manner, a further increase in temperature to 260 °C caused an increase of about 140%. On the contrary, methane yield hardly varied with temperature, though a slight tendency to decrease with increasing temperature could be deduced. This led to a substantial increase in Y_{CO_2}/Y_{CH_4}, with an approximate ten-fold increase in the 220 to 260 °C range. As a result, the increase in WGS activity with respect to hydrogenation activity with increasing temperature is conclusive (Table 5.14).
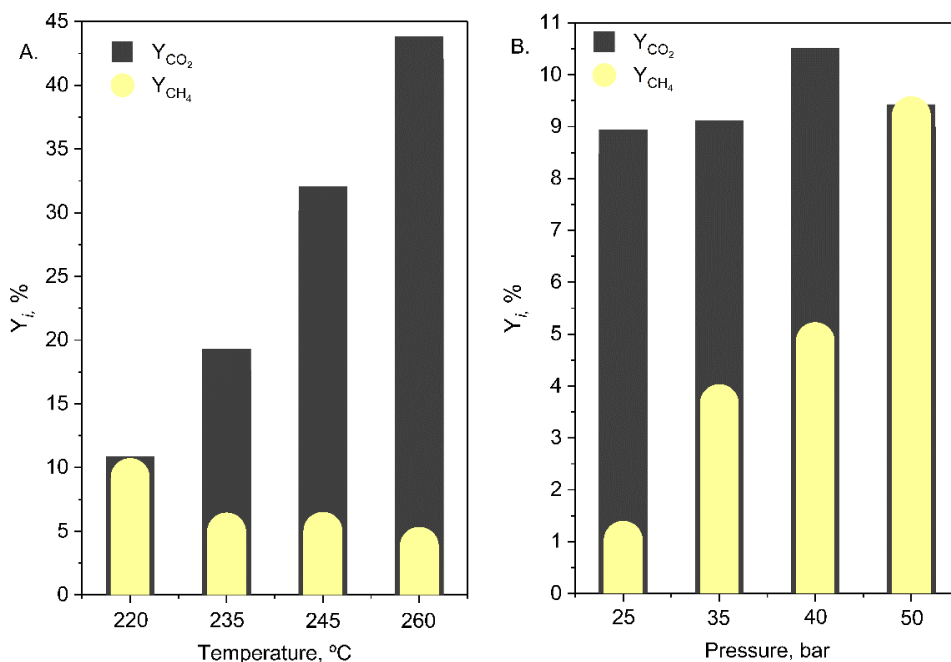
Figure 5.23. Evolution of product yields as a function of (A) temperature at P = 50 bar and (B) pressure at T = 220 °C over 0.3Pt/CoAl. Reaction conditions: m_{cat} = 0.2 g, L_{H_2O} = 0.04 cm³·min⁻¹, G_{CO} = 3.5 cm³·min⁻¹, G_{H_2} = 14 cm³·min⁻¹.

Regarding the influence of pressure on the product distribution, Figure 5.23.B shows that CO_2 yield slightly increased with pressure. Methane yield, however,

increased ten-fold, from 25 to 50 bar. Therefore, the increased CO conversion at high pressure was due to a favoured hydrogenation activity (i.e., ten-fold increase of Y_{CH4} in the 25 to 50 bar range) rather than the WGS. Note that, at a constant temperature, the vapour pressure of water remains constant, thus the increase in the operating pressure is accomplished by increasing the partial pressures of the CO and H_2 (Table 5.12). Although the water solubility of hydrogen is twice that of CO, its effect on the available hydrogen in the gas phase could be offset due to the high partial pressure of H_2 under the established reaction conditions. Moreover, the fact that CO can react via WGS and produce even more hydrogen would also increase the hydrogenation rate [325]. The Y_{CO2}/Y_{CH4} data in Table 5.14 clearly shows that the higher the overpressure, the less selectivity towards WGS, which is the opposite effect of the temperature increase.
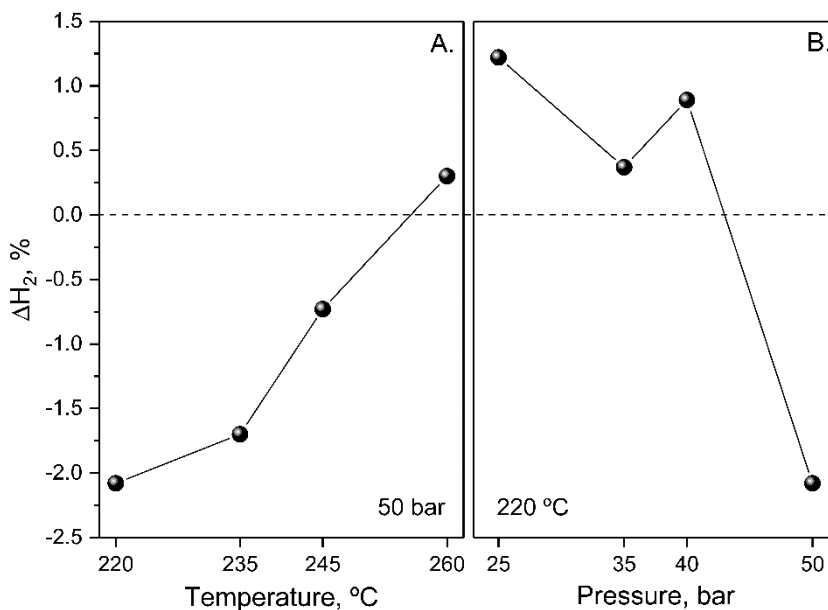
Figure 5.24. Net hydrogen variation in experiments with H_2 co-feeding over 0.3Pt/CoAl catalyst at (A) 50 bar and (B) 220 °C. Reaction conditions: m_{cat} = 0.2 g, L_{H2O} = 0.04 cm³·min⁻¹, G_{CO} = 3.5 cm³·min⁻¹, G_{H2} = 14 cm³·min⁻¹.

The evolution of the net hydrogen variation is shown in Figure 5.24. A large net hydrogen consumption ($\Delta H_2 < 0$) was observed at low temperatures due to the

high hydrogenation activity. It was verified that methane production decreased at increasing temperatures. Moreover, hydrogen consumption progressively decreased until a positive balance was obtained at the highest temperature screened. In agreement with the observed trend in the CO_2 and CH_4 yield, an increase in pressure favoured selectivity towards CO hydrogenation. Hence, at the maximum working pressure, the rate of hydrogen consumption overtook that of production.

5.6   GLOBAL VISION AND SUMMARY

Spinel type cobalt catalyst was impregnated with different amounts of platinum. The characterization of these samples revealed that Pt loading stabilized the textural and structural properties of the cobalt spinel-supported catalysts. In addition, the strong Pt-Co interaction promoted reducibility and increased the availability of both metallic species. Acid and basic sites are primarily weak and medium strength.

Bimetallic catalysts showed a very high catalytic activity and proved to be stable for glycerol APR, unlike 0.625CoAl and 0.3Pt/Al catalysts that exhibited a decline in activity. The incorporation of Pt to Cobalt spinels also increased methane production. Even so, hydrogen was the main product for all the assayed catalysts, followed by CO_2. The importance of the conjunction between the metal part and the acid-base sites of the catalysts is reaffirmed.

Examination of spent catalysts, after glycerol APR, revealed that xPt/CoAl bimetallic catalysts preserved their structural and textural properties, whereas APR conditions significantly deteriorated those of monometallic ones. The total available metal atoms decreased considerably for catalysts devoid of or with a lower platinum content. H_2-TPR confirmed the oxidation of metallic cobalt active centres, which was probably the first step in leaching this metal. Amorphous carbonaceous deposits were detected by Raman spectroscopy and quantified via methane formation using temperature-programmed hydrogenation. Obtained results corroborated that Pt-containing catalysts formed less amount of carbon deposits, as they could be hydrogenated by hydrogen spillover from Pt.

The catalytic performance of the liquid-phase Water-Gas Shift (WGS) reaction and CO hydrogenation was investigated over bimetallic Pt-Co catalysts and their monometallic counterparts. Bimetallic xPt/CoAl catalysts clearly outperformed monometallic ones in all the investigated operating conditions (220 to 260 °C, 25 to 50 bar). The improved activity of these catalysts can be explained by the high density of basic sites, smaller particle size and the nature of the support.

It was concluded that bimetallic catalysts were more selective towards the WGS reaction than CO hydrogenation, despite the high availability of hydrogen in the reaction mixture. These results suggest that the methane formation in APR of these catalysts would mainly occur by cleavage of C-C from acetaldehyde by decarbonylation. Furthermore, catalytic runs over 0.3Pt/CoAl with excess hydrogen in the feedstream demonstrated the positive effect of increasing temperature on WGS activity. The opposite effect was reported with increasing pressure, which led to improved methane production.

Chapter 6

EFFECT OF OPERATING VARIABLES ON APR
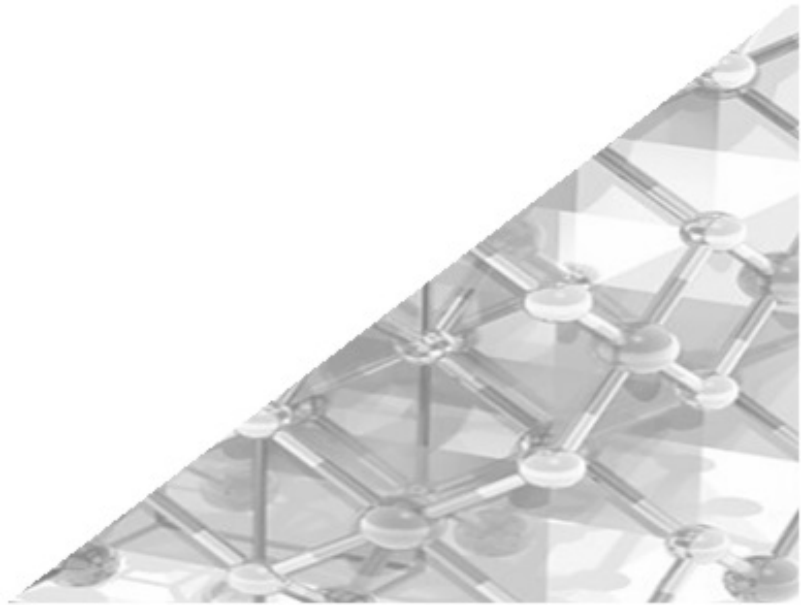
6. EFFECT OF OPERATING VARIABLES ON APR

The activity and selectivity in the APR process strongly depend on the catalyst characteristics such as the metallic surface, acidic-basic sites density, and type of support, among others. In addition to the catalyst's characteristics, APR process is also influenced by the operation conditions and the concentration and type of substrate fed.

As seen in Chapter 5, Pt/CoAl catalytic system are active and stable for APR glycerol. Of those samples, catalyst 0.3Pt/CoAl has been chosen to be used in research on the influence of the operating conditions on this catalytic system. Among the variables that can condition the selectivity of the reforming process, in this chapter we will look into the glycerol concentration in the feedstream, the couple temperature-pressure, the space velocity (WHSV) and the substrate structure. The effect of the former three effects was studied for glycerol feedstream. The effect of substrate structure on APR was analysed by comparing the results obtained with ethylene glycol, glycerol, and sorbitol, under the same operating conditions, focusing on the hydrogen production.

6.1   EFFECT OF GLYCEROL CONCENTRATION

The influence of feedstock concentration on the catalytic reaction was explored at 260 °C/50 bar, WHSV = 6.8 h^{-1} (flowrate: 0.1 cm^3·min^{-1}, catalyst mass: 0.9 g) for three glycerol concentrations: 5, 10 and 20 wt.% in water. Table 6.1 shows the APR global results after 3 h TOS for the three glycerol concentrations. Glycerol conversion was very high (> 99%), independent of its initial concentration. Conversion to gas showed a decreasing trend with glycerol concentration in the feedstream. Specifically, increasing the glycerol content from 5 to 10 wt.%, X_{gas} decreased by 18.4%, while increasing from 10% to 20% the decrease is practically insignificant (by 1.2%). The total gas flow (F_{gas}) did not increase in proportion to the increase in glycerol concentration. For instance, when glycerol concentration is 20 wt.%, around twice F_{gas} obtained with 5% was produced (719.7 vs 359.1 μmol·(g_{cat}·min)$^{-1}$), when by stoichiometry, a 4-fold increase would be expected. Calculating F_{gas} per mole of fed glycerol, it followed an opposite trend with glycerol concentration.

Table 6.1. Overall results of glycerol APR over 0.3Pt/CoAl. Influence of the glycerol content in the feed.

	Glycerol wt.%		
	5	10	20
X_{gly}, %	99.4	99.9	99.8
X_{gas}, %	40.8	33.4	33.0
Y_{H2}, %	50.6	41.3	26.7
S_{H2}, %	88.8	89.8	85.2
S_{CH4}, %	14.9	12.3	10.1
F_{gas}, $\mu mol \cdot (g_{cat} \cdot min)^{-1}$	359.1	524.9	719.7
F_{H2}, $\mu mol \cdot (g_{cat} \cdot min)^{-1}$	217.9	355.2	460.0
Gaseous products, % mol			
H_2	75.1	70.8	67.1
CO_2	20.5	24.5	27.3
CH_4	3.72	3.61	3.37
CO	0.06	0.07	0.69
C_{2+}	0.62	1.02	1.54
H_2/CO_2	3.66	2.89	2.46
H_2/CH_4	20.2	19.6	19.9
Liquid products yield, %			
Methanol	0.30	0.46	0.42
Ethanol	4.57	9.19	6.31
Acetic acid	4.39	3.63	1.55
Acetaldehyde	0.57	1.24	0.58
Acetone	3.50	4.89	3.84
1-Propanol	2.02	3.39	2.06
2-Propanol	0.23	0.46	0.18
Propanal	0.21	0.31	0.53
Hydroxyacetone	4.00	9.12	9.11

Continuation Table 6.1			
Propylene glycol	4.29	10.8	14.7
Propanoic acid	29.0	26.1	13.3

For more diluted feedstock the availability of the active sites increases, thus reactions involved in the APR proceed more extensively to obtain more volatile (gas phase) compounds. Consequently, it can be deduced that feedstock with low glycerol concentration is more advantageous for gas production, while more concentrated would be preferred for liquid production. It could also be observed that for the WHSV values used in this study, 10 wt.% or higher concentration of glycerol did not have enough available active sites to further decompose intermediate molecules, thus reaching a constant X_{gas}. Hydrogen yield showed lineal decrease with glycerol concentration (r^2 = 0.996, slope = -1.57). Consequently, in line with the above idea, in terms of hydrogen yield, feedstock with low glycerol concentration was more advantageous.

Regarding distribution of the gas products, an increase in glycerol concentration affected CO_2 and H_2 concentration in the opposite way, increasing the former and decreasing the latter. If we take a look at the H_2/CO_2 ratio and CO content, the former decreased while the latter increased with the glycerol concentration. This would indicate lower availability of the metallic centres with the increase of glycerol concentration, since the WGS and CO hydrogenation occur in these type of centres. Even so, the lowest hydrogen concentration in the gas product was 67%, feeding 20 wt.% glycerol/water mixture. Likewise, CH_4 content decreased slightly with the increase of glycerol content. This trend combined with the fact that the CO and C_{2+} products augmented, may suggest a lower hydrogenation activity of terminal $C-CH_3$ and CO when the glycerol concentration increases.

As was expected regarding the liquid products, a greater concentration of said products was obtained by increasing the glycerol content in the feed stream. The yield of dehydration products had a more pronounced rise with glycerol concentration than those obtained via dehydrogenation. For example, an increase in glycerol concentration produced an increment in hydroxyacetone (primary product from glycerol dehydration) and propylene glycol

(hydroxyacetone hydrogenation) yields. As we previously discussed in Chapter 3, hydrogenations seemed to occur more rapidly than dehydrations for cobalt aluminate catalysts. Propylene glycol can undergo further dehydration/hydrogenation to produce 1-propanol and 2- propanol. This same route can also form, via Cannizzaro type disproportionation, propanoic acid from propanal [315,332], one of the main liquid products. These aforementioned products practically did not change as glycerol content increased from 10 to 20%. The ratio of dehydrogenation products to dehydration products (Figure 6.1) presented a maximum at 10 wt.% glycerol. Therefore, it can be concluded that this glycerol concentration provides a balance between these two routes.
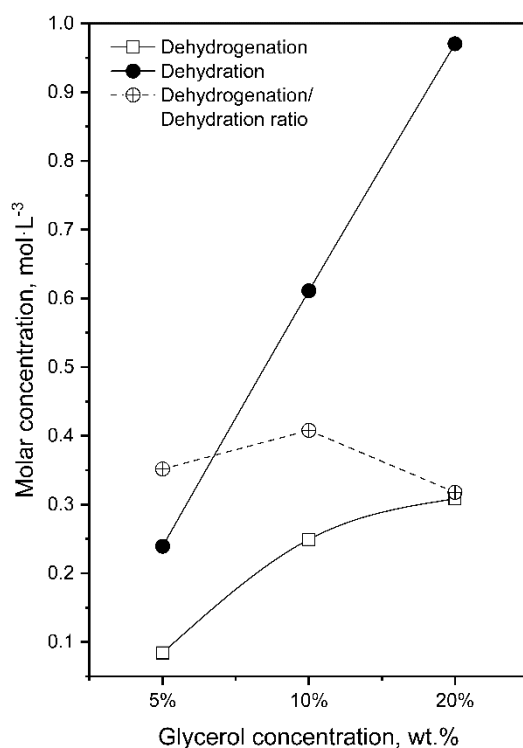
Figure 6.1. Ratio of dehydration to dehydrogenation in the liquid products in function of glycerol content. Reaction conditions: 260 °C/50 bar, WHSV = 6.8 h⁻¹.

6.2   EFFECT OF TEMPERATURE/PRESSURE COUPLE

The experiments to determine the effect of operation variables on APR performance were conducted with a solution 10 wt.% glycerol/water, at constant

WHSV of 6.8 h^{-1} (0.1 cm$^3 \cdot$min^{-1} of glycerol, 0.9 g of catalyst). Four experiments in the temperature range of 220 to 260 °C were carried out, maintaining the necessary pressure to assure liquid phase, with 1.8-4.2 bar above the bubble point of the feedstock. Therefore, the isolated effect of pressure was not analysed, but that of the coupled temperature-pressure was. In detail, the temperature/pressure pairs studied were (°C/bar): 220/25; 235/35; 245/40 and 260/50.
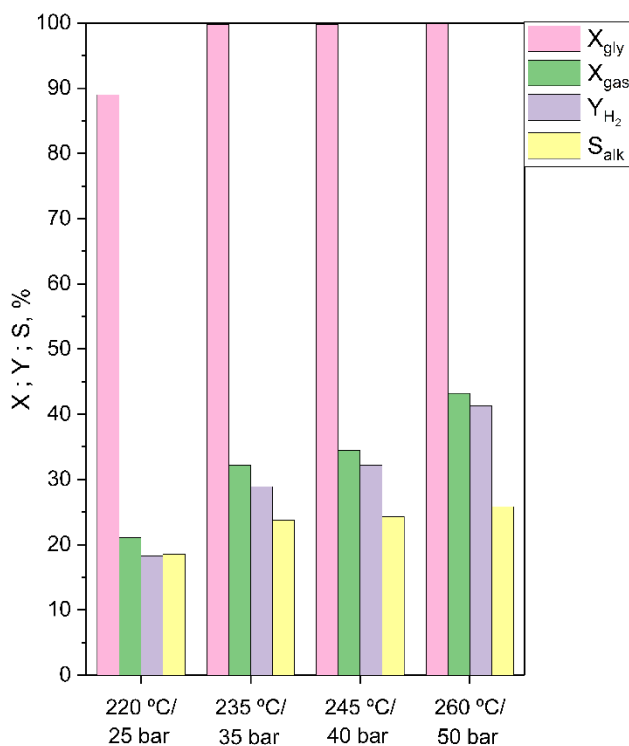
Figure 6.2. Glycerol APR catalytic results as a function of temperature/pressure reaction. Operating conditions: WHSV = 6.8 h^{-1}, 10 wt.% glycerol/water.

Figure 6.2 shows that conversion of glycerol increased with temperature, from 89% at 220 °C/25 bar to 99.8% at 235 °C/35 bar. Complete glycerol conversion was achieved at higher temperature conditions. Correspondingly, carbon conversion to gas exhibited a non-monotonic increase with temperature, reaching a maximum of 43.2% at the most severe conditions (260 °C/50 bar). High temperatures enhanced the reforming of glycerol and intermediate liquids,

by promotion of C-C and C-O bonds cleavage to obtain more volatile compounds.

Hydrogen yield was strongly enhanced by temperature. For instances, from 220 °C/25 bar to 260 °C/50 bar an overall increment of 126% was attained. The increase on the operation temperature moderately increased the selectivity to alkanes, with methane as the most representative of them. The production of alkanes, therefore, led to a consumption of the hydrogen. However, selectivity to hydrogen did not show a clear trend with temperature.

Regarding the C numbers of the produced alkanes, the majority corresponded to methane, which accounted for 63% at the lowest temperature and 71% at the highest, once again suggesting that C-C scission reaction were promoted by temperature.

Table 6.2. Gas phase composition over 0.3Pt/CoAl at different temperature/pressure reaction.

	220 °C/ 25 bar	235 °C/ 35 bar	245 °C/ 40 bar	260 °C/ 50 bar
F_{H2}, $\mu mol_{H2} \cdot (g_{cat} \cdot min)^{-1}$	157.5	249.1	277.5	355.2
H_2, % mol	70.4	68.9	69.5	70.8
CO_2,% mol	25.1	24.8	24.4	24.5
CO, % mol	0.16	0.10	0.04	0.07
CH_4, % mol	3.47	5.22	4.89	3.61
C_2+, % mol	0.87	0.98	1.17	1.02
S_{H2}, %	87.7	82.8	83.9	89.8
H_2/CO_2	2.80	2.78	2.85	2.89

Table 6.2 summarizes the gas product composition at each analysed condition. Hydrogen is, by far, the most abundant product, with around 70%, independent of the reaction conditions. Also, H_2 selectivity was considerably high, with no clear trend with operation T/P, ranging between 83-90%. Thanks to the increase in conversion to gas, H_2 outflow increased with temperature/pressure. CO_2 was the main carbon-containing product, followed by methane, which was the most

abundant alkane. Traces of ethane, ethylene, propane, and butane were also detected (compiled as C_{2+}). The formation of C_{4+} compounds suggested that Pt-Co catalysts had some activity in C-C coupling reaction, in addition to their recognized great activity in WGS reaction. The latter could be confirmed from the very low CO content in the gaseous product (< 0.2%) for all the temperatures studied. The subtle decrease on CO concentration with temperature could indicate the slightly endothermic condition of the WGS, which would be attained when water reacts from the liquid phase.
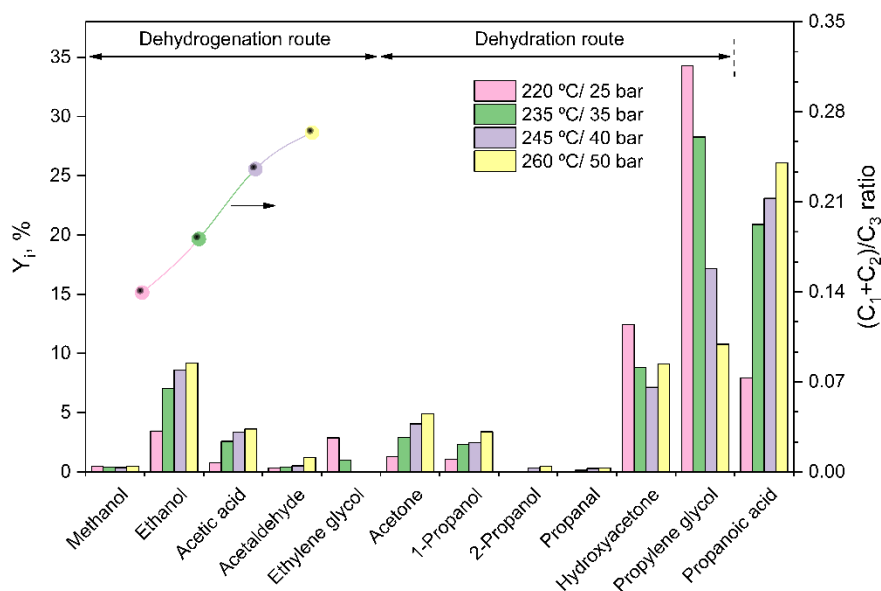
Figure 6.3. Liquid products distribution (bars) and $(C_1+C_2)/C_3$ ratio (line) as a function of reaction temperature/pressure couple. Operating conditions: WHSV = 6.8 h^{-1}, 10 wt.% glycerol/water.

Depending on the working conditions, 57-79% of the carbon contained in the glycerol fed was converted into liquid products. This considerable production of intermediate oxygenated liquids was related to the WHSV used, as will be shown in Section 6.3. The identified liquid products comprised acids (acetic, propanoic), ketones (acetone, hydroxyacetone), aldehydes (propanal, acetaldehyde), C_3 alcohols (propylene glycol, 1-propanol, 2-propanol) and C_1-C_2 alcohols (ethylene glycol, ethanol, methanol). Other peaks detected by chromatography, which accounted for less than 5% of the total area, could not

be identified. The wide variety in the obtained liquid products reflected the complexity of the glycerol APR reaction network. Figure 6.3 displays the liquid products yield at each condition, showing a strong influence of temperature-pressure couple on the liquid products distribution.

The liquid stream was mainly composed by C_3 products. On the other hand, the $(C_1+C_2)/C_3$ compounds ratio in the liquid stream indicated monotonous increase with the operation temperature (Figure 6.3) confirming the temperature promoted C-C cleavage. The reaction temperature increased the majority of the liquid products concentration. However, the products resulting from the direct dehydration of glycerol (hydroxyacetone) and its subsequent hydrogenation (propylene glycol) shown a marked decrease in concentration as reaction temperature increased. These results indicated that an increase in reaction temperature favoured the dehydrogenation pathway and explained the improvement in hydrogen yield at higher temperatures.

×   Characterization of spent catalysts

After each reaction, the spent catalyst was analysed by N_2 adsorption-desorption (Figure 6.4), ICP and TPH analyses. As can be seen in Table 6.3, catalysts underwent morphological changes during glycerol APR. The specific surface area of the spent catalyst increased when the reaction was performed at the mildest condition (220 °C/25 bar) while decreased for the other conditions tested. At lower temperatures, a greater decrease in the average pore diameter was also observed, which has a tendency to increase with the reaction temperature without reaching the value of its reduced state.

Metal leaching in the liquid product was also investigated by ICP-MS. The results showed that the reaction conditions influenced cobalt leaching. Although the overall results confirmed low metal leaching, cobalt was found to be more leachable at low reaction temperatures (cobalt leaching was 2.30% after reaction at 220 °C vs 0.74% at 235 °C). These apparently inconsistent results were, however, consistent with the results obtained with catalyst 0.625CoAl after 30 h TOS at 235 °C and 260 °C (Chapter 3). A comprehensible explanation can be found in the re-deposition of hydroxylated alumina. At higher temperatures, pH of the reaction medium increased, thus greater leaching was expected. However,

in hot water the solubility of the inorganic oxide materials is low, which facilitates the re-deposition of leached alumina, decorating the cobalt and therefore protecting it from leaching [269]. As for the other metals, both platinum and aluminium had a low percentage of leaching, understanding that the platinum conferred the stability of the catalyst during reaction.
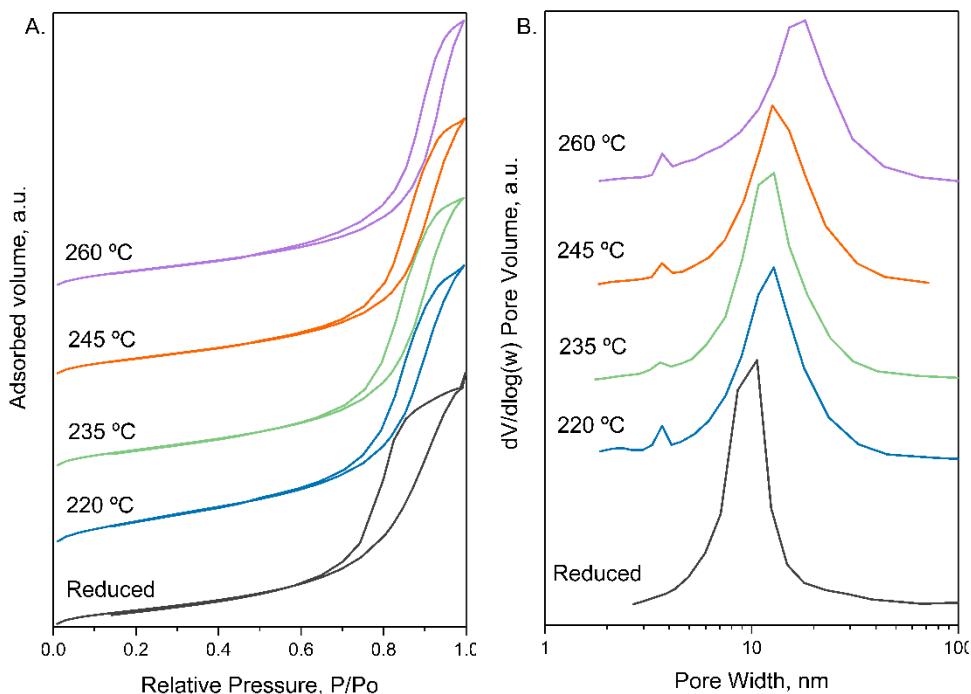
Figure 6.4. Nitrogen adsorption-desorption isotherms (A) and pore size distribution (B) of used samples.

The results obtained by temperature-programmed hydrogenation (TPH) did not show any relation to the reaction condition. The samples with the highest amount of carbonaceous deposits correspond to those of the reactions at 235 and 245 °C. Surprisingly, the samples after the reaction at 260 °C had a content of carbonaceous material very similar to that used in the reaction at 220 °C. It is worth highlighting the much lower (three to four orders of magnitude) coke deposits in glycerol APR as compared to glycerol steam reforming [333,334]. This was due to the ability of hot compressed water to dissolve carbonaceous deposits [269].

Table 6.3. Physico-chemical properties of spent catalyst. Influence of temperature/pressure.

Reaction Temperature, °C	S_{BET}, $m^2 \cdot g^{-1}$	V_P, $cm^3 \cdot g^{-1}$	d_P, nm	Leached, wt.%			$C_{deposits}$, $\mu mol_C \cdot g_{cat}^{-1}$
				Pt	Co	Al	
220 °C	155.0 *(+18%)*	0.424 *(-19%)*	9.5 *(-36%)*	-	2.30	0.02	1.62
235 °C	119.7 *(-9%)*	0.402 *(-23%)*	10.7 *(-28%)*	$1.77 \cdot 10^{-3}$	0.74	0.01	4.39
245 °C	116.2 *(-11%)*	0.378 *(-27%)*	11.1 *(-25%)*	$1.77 \cdot 10^{-3}$	0.67	0.01	5.25
260 °C	112.7 *(-14%)*	0.398 *(-24%)*	12.1 *(-18%)*	$4.13 \cdot 10^{-3}$	0.37	0.01	1.75

In parenthesis percentage variation respect freshly reduced sample.

6.3   EFFECT OF CONTACT TIME

The effect of contact time was studied in terms of WHSV (higher WHSV, shorter contact time), varying the flowrate of the feedstream from 0.02 to 0.5 cm³·min⁻¹ over 1.80 g of 0.3Pt/CoAl catalyst. The experiments were performed at 260 °C/50 bar with a 10 wt.% glycerol in the feedstream. Results of glycerol conversion, carbon conversion to gas, hydrogen yield and selectivity to alkanes are shown in Figure 6.5.
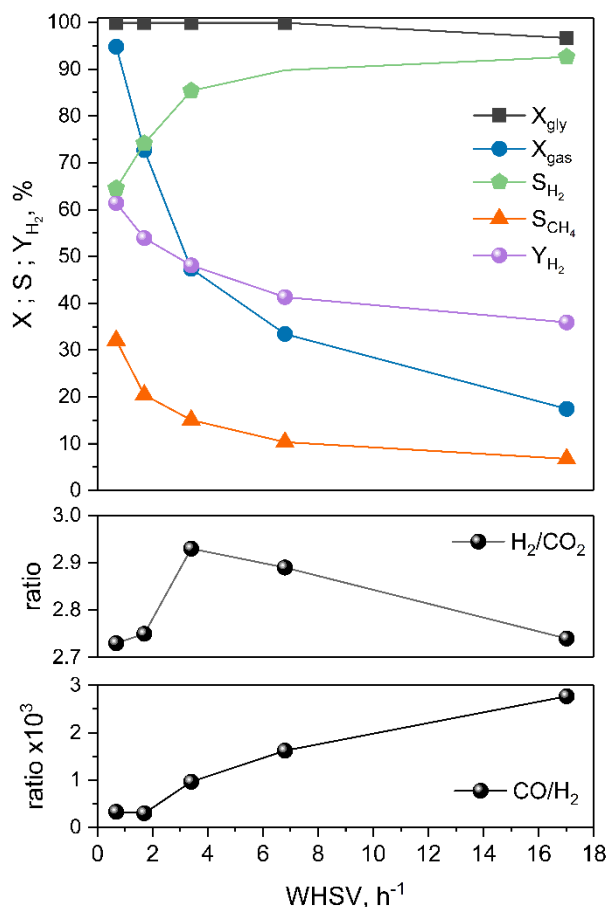
Figure 6.5. Effect of space velocity (WHSV) on catalytic results of glycerol APR. Reaction conditions: 260 °C/50 bar, 10 wt.% glycerol/water.

The effect of WHSV was very noticeable in all the parameters represented, except in X_{gly}, which remained practically at 100% for a wide range of WHSV,

and only decayed to 97% for WHSV = 17 h^{-1}. These results indicated the pronounced activity of this catalyst to glycerol decomposition, even working at very high WHSV. Nevertheless, carbon conversion to gas was highly sensitive to contact time: as WHSV increased, carbon conversion to gas decreased. Augmenting feed flowrate from 0.02 to 0.1 cm^3·min^{-1} (WHSV = 0.68 and 3.4 h^{-1}, respectively) resulted in a 50% drop in the carbon conversion to gas. Further increase in WHSV resulted in a less severe decay in X_{gas}. Operating with large WHSV (short contact time) there were fewer consecutive reactions of the intermediate liquid products, thus resulting in fewer gas compounds and more liquid products. Analogous to X_{gas}, a decrease in hydrogen yield and selectivity to methane could be observed with WHSV, with a concomitant increase on CO and CO$_2$. As a consequence, selectivity to hydrogen increased with WHSV. At lower WHSV, the contact time between the intermediate liquids, gases and catalyst was higher, thus enhancing the hydrogen consumption reactions which decreased the hydrogen yield.

As can be seen in Figure 6.5, CO/H$_2$ molar ratio in the gas stream increased with WHSV. This implies that the WGS reaction requires long contact time, so this reaction occurs to a lesser extent at high WHSV. H$_2$/CO$_2$ ratio might indicate the catalysts ease for C-C or C-O cleavage [187]. This value was slightly higher than the theoretical one and practically remained stable regardless of the WHSV used, which demonstrated that this catalyst had a high capacity for C-C bonds breakage prior to C-O bond breakage.

The liquid products yields at different WHSV is provided in Figure 6.6. As seen before, a low WHSV presented an exceptionally high carbon conversion to gas, and therefore, the concentration of liquid products was insignificant. Largely, the yield of the liquid products increased with WHSV, in accordance with X_{gas} decrease. At higher WHSV a wide variety of liquid products could be distinguished. Among the products obtained, a noticeably high yield of hydroxyacetone and propylene glycol could be noted at shorter contact times (Y_i at 17 h^{-1} was 37.6% and 41.5%, respectively). The yields of both compounds increased in similar way with WHSV, which suggests that at such short contact times, dehydration and hydrogenation reactions predominate at the same rate to the detriment of C-C cleavage. This lower activity for C-C bonds scission caused a drop in the yield of C$_2$ products from 13.4% at 6.8 h^{-1} to 5% at 17 h^{-1}.

Yields of propanoic acid, ethanol, acetone and both 1-propanol and 2-propanol reached their maxima at 3.4 and 6.8 h^{-1}, respectively, then decreasing dramatically as WHSV achieved 17.0 h^{-1}. It is evident that at short contact times less fragmentation of the initial molecule takes place. Contrariwise, for the longest contact time (0.68 h^{-1}), it is only possible to detect compounds resulting from several reaction stages such as propanols and acetone.
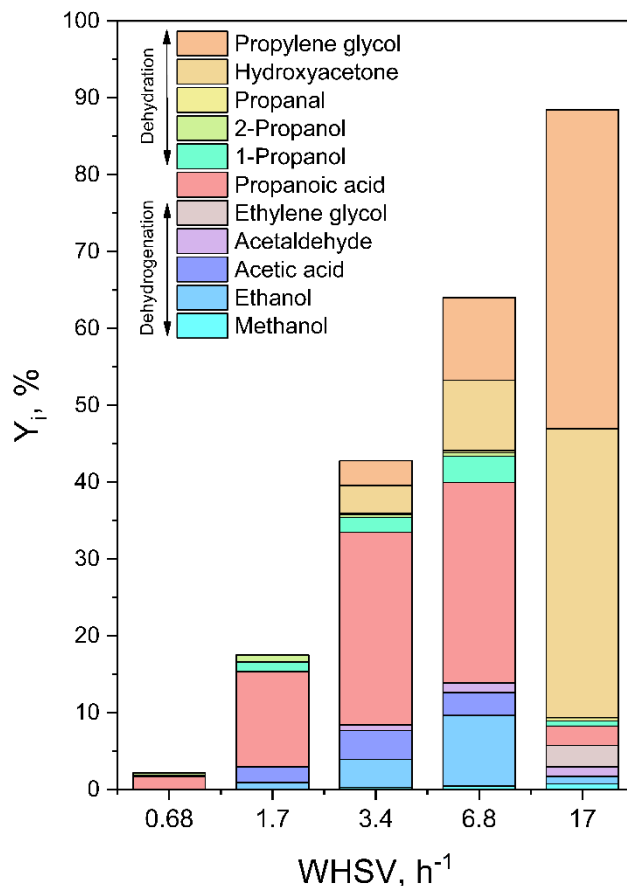
Figure 6.6. Liquid products distribution as a function of WHSV. Reaction conditions: 260 °C/50 bar, 10 wt.% glycerol/water.

6.4   EFFECT OF SUBSTRATE STRUCTURE

Dumesic and co-workers demonstrated that hydrocarbons with a C:O ratio of 1:1 and H:C > 1 were more susceptible to C-C bond cleavage favouring hydrogen production [124]. Besides glycerol ($C_3H_8O_3$), ethylene glycol ($C_2H_6O_2$) and sorbitol ($C_6H_{14}O_6$) are feasible compounds for the APR process. All three are important industry feedstocks that can be derived from sustainable biomass. Indeed, the three polyols can be derived from glucose, a primary product from the cellulosic biomass hydrolysis [335]. Sorbitol and glycerol are compounds of great interest in biorefinery, as they present a significant market opportunity for hydrogen and alkane production [265,336,337]. Meanwhile ethylene glycol is a model molecule for studies of aqueous-phase reforming reactions, since it contains the same functionalities as a larger polyol [131,338]. According to the stoichiometry of the overall APR of an oxygenated compound, 5 moles of H_2 could be produced per mole of ethylene glycol, which increased to 7 and 13 for glycerol and sorbitol, respectively. Figure 6.7 shows the 3D structures of the three polyols studied.
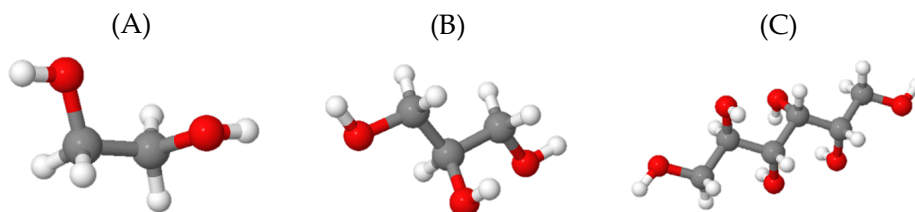
Figure 6.7. 3D structures of (A) ethylene glycol; (B) glycerol; and (C) sorbitol.

The aqueous phase reforming of ethylene glycol, glycerol and sorbitol was performed at 260 °C/50 bar, WHSV = 6.8 h^{-1} (0.1 cm^3·min^{-1} of subtract, 0.9 g of catalyst) and a 10 wt.% content of the polyol in the feed. The overall results of the tested polyol are listed in Table 6.4. In this section, we do not delve into the discussion about the reaction paths for ethylene glycol and sorbitol APR. The sorbitol APR reaction paths and the distribution of liquid products is discussed in more detail in Chapter 8. At the conditions in which the experiments were performed, the overall conversion of the substrate was very high (near 100%) for the three substrates. Sorbitol, in accordance with the complexity of its structure, exhibited a slightly lower conversion than the other polyols. More evident

differences were found in both the conversion to gas and hydrogen yield, both decreasing with the polyol complexity. The smallest substrate, ethylene glycol, showed X_{gas} superior to 85%, and decreased down to 25.1% for sorbitol. Y_{H2} levelled off from 76.1% for ethylene glycol to 15.6% for sorbitol. Decrease in both parameters could be explained by the lower probability of hydrogen-consuming side reactions occurring with the decrease of the chain length of the initial substrate and subsequent liquid intermediates. Same trend was found in the seminal work on APR from the group of Dumesic [98] and later corroborated by others [276,339-341].

Table 6.4. Influence of the polyol fed on APR global results.

# Carbon	2	3	6
Substrat	**Ethylene glycol**	**Glycerol**	**Sorbitol**
X_{polyol}, %	99.8	99.9	98.6
X_{gas}, %	85.9	43.2	25.1
Y_{H2},%	76.1	41.3	15.6
S_{H2}, %	89.5	89.8	90.4
S_{Alk},%	25.0	25.8	27.4
F_{H2}, $\mu mol_{H2} \cdot (g_{cat} \cdot min)^{-1}$	693.3	355.2	128.8
Composition			
H_2, % mol	70.5	70.8	73.2
CO_2,% mol	23.4	24.5	20.0
CO, % mol	0.07	0.07	0.16
CH_4, % mol	5.40	3.61	5.94
C_2+, % mol	0.63	1.06	0.70
H_2/CO_2	3.0	2.9	3.7

Obviously, because of that higher hydrogen production was achieved when shorter carbon substrates were reformed. For ethylene glycol, F_{H2} was 693.3 $\mu mol_{H2} \cdot (g_{cat} \cdot min)^{-1}$, almost twice that obtained for glycerol and five times higher than that for sorbitol. Therefore, undoubtedly, sorbitol had the lowest hydrogen production capability by APR, among the polyols investigated. Very high

selectivity to hydrogen could be achieved from the three subtracts, around 90%, increasing only slightly with the polyol size. Selectivity to alkanes increased very slightly with the substrate chain length, remained in a close range regardless of the polyol used, showing that the complexity of the molecule does not play a predominant role in this parameter. Related to this, the gas phase composition for all substrates was quite similar.

The results of the liquid composition for each substrate are shown in Figure 6.8. Significant changes in the liquid phase product composition were detected. The only products detected in liquid phase during ethylene glycol APR were methanol, ethanol, acetaldehyde, acetone, and 1-propanol. Notably, C_1 compound (methanol) represents the majority in the aqueous phase followed by ethanol. Scheme 6.1 shows a simplified diagrammatic network of the reaction pathways involved in C_2-C_6 oxygenated compounds. A more detailed reaction pathway including C_3 compounds was discussed in Chapter 3 (Scheme 3.2). Methanol is produced via ethylene glycol dehydrogenation/decarbonylation while ethanol is formed through the dehydration/hydrogenation route [124]. The rest of the products were in considerably low concentrations. According to the literature, 1-propanol can be formed by hydroformylation of ethylene using carbon monoxide and hydrogen in the presence of a cobalt catalyst [342].
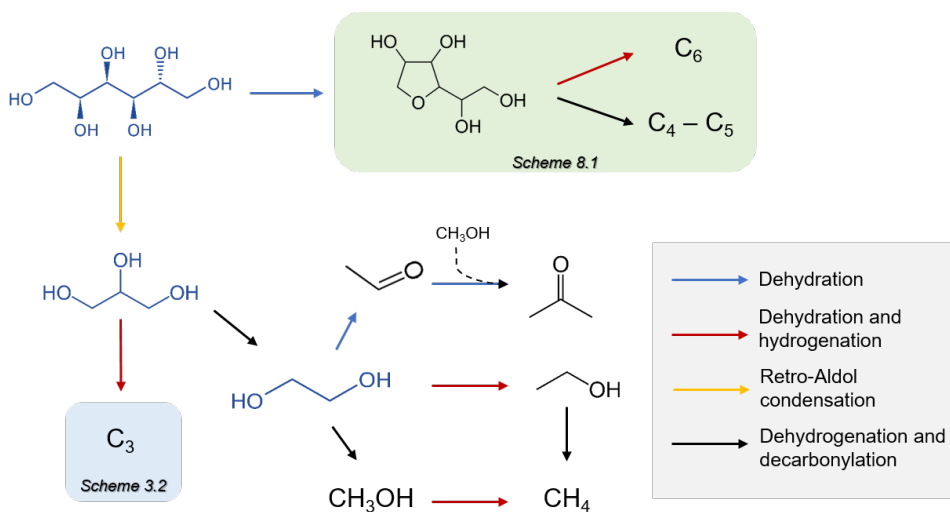
Scheme 6.1. Summary of reaction pathways involved in the APR of oxygenated hydrocarbons.

Glycerol APR presented a higher concentration of C_3 products. Propanoic acid, propylene glycol and hydroxyacetone were the main C_3 products detected. Ethanol is the second largest concentration product in the liquid phase. Contrary to the results obtained for APR of ethylene glycol, the concentration of C-O cleavage products was higher than that of C-C cleavage products in glycerol APR. The distribution of liquid products obtained from the sorbitol APR is displayed in Figure 6.8.C. Polyols with a long chain of carbon atoms give more intermediates. Sorbitol reforming can undergo dehydration to produce sorbitan and by subsequent hydrodeoxygenation reactions generate C_{4+} higher oxygenated and heterocyclic compounds [343]. However, the determination and accurate quantification of C_{4+} liquid products were difficult to carry out with the equipment used (only 40% mass balance in liquid products achieved for sorbitol APR). It is well known that sorbitol, through retro-aldol condensation, can be derived into glycerol and other smaller species [265]. The glycerol yield obtained was quite low (0.58%), however, the yield of other C_1-C_3 products was remarkable (ΣY_{C3} = 22.9%). As for the other subtracts tested, a high yield of hydroxyacetone and propylene glycol was obtained. Overall, among the quantified liquid products, C_3 compounds were the majority. The identification of products generated from the cleavage of C-C such as ethylene glycol and methanol demonstrated the high activity of this catalyst for obtaining gases and light compounds. Other sizeable products identified were propanoic acid (4.3%), ethanol (2.6%), ethylene glycol (1.4%) and acetone (1.3%).
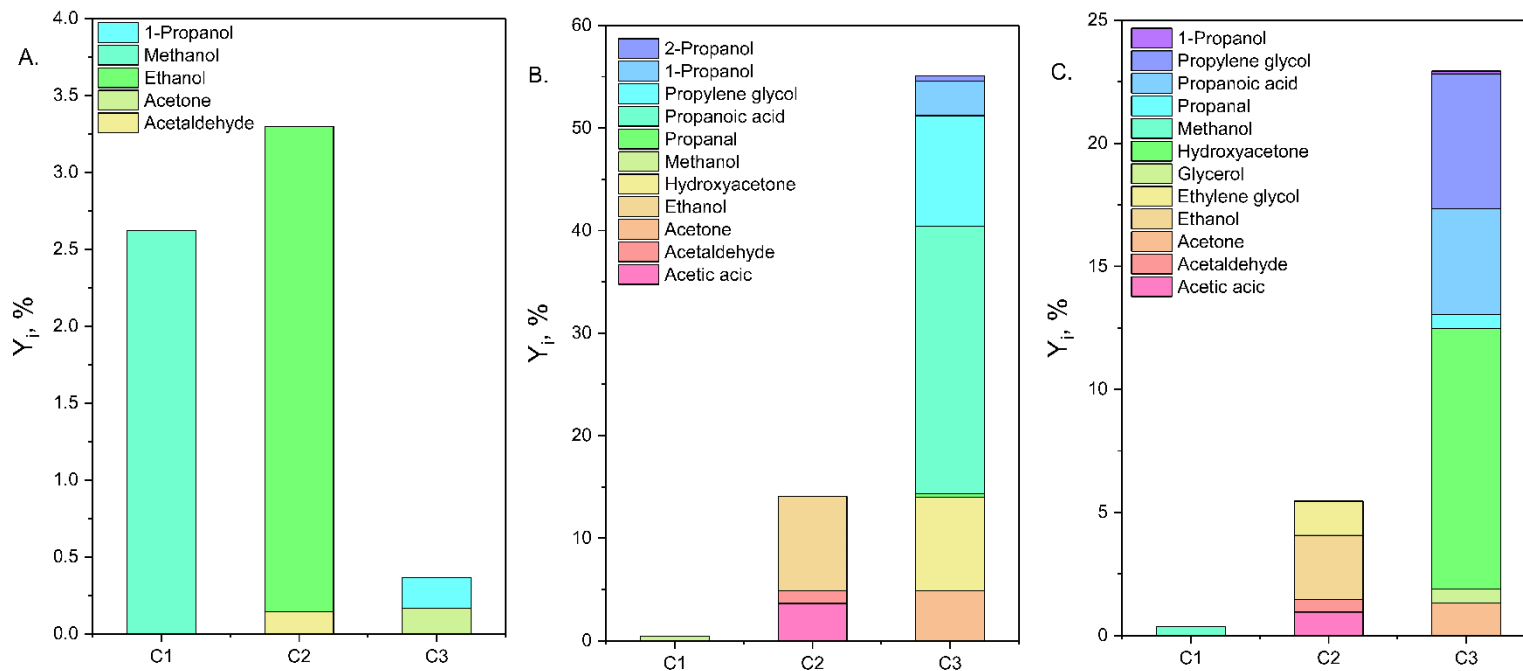
Figure 6.8. Liquid products distribucion in the APR of (A) ethylene glycol, (B) glycerol and (C) sorbitol over 0.3Pt/CoAl. Reaction conditions: 260 °C/50 bar, WHSV = 6.8 h^{-1}, 10 wt.% substracte/water.

6.5   GLOBAL VISION AND SUMMARY

This chapter has focused on the study of the different experimental conditions. After validating the stability of the 0.3Pt/CoAl catalyst and its high catalytic activity in the previous chapter, various reactions were carried out modifying the following reaction parameters: glycerol content, temperature/pressure, space velocity (WHSV) and type of polyol fed. The effect of each parameter was studied while maintaining the rest of the operating conditions constant.

Under the conditions studied (260 °C/50 bar), the glycerol conversion did not show significant variation when the glycerol concentration was modified from 5 to 20 wt.% or when the WHSV used was increased from 0.68 to 6.8 h^{-1}. The reactions with other compounds (ethylene glycol or sorbitol) did not show notable differences in the total conversion with respect to the use of glycerol (total conversion between 98.6 and 99.9 for all the polyols). Only at 220 °C/25 bar (WHSV = 6.8 h^{-1}, 10 wt.% glycerol/water) did the glycerol conversion drop below 90%.

Regarding carbon conversion to gas, the best results were achieved at a lower glycerol concentration in the feed, high temperatures/pressures, or a lengthy contact time. Furthermore, ethylene glycol reforming showed better results than the other oxygenated compounds tested. As expected, the conditions where the highest conversion to gas was achieved were the ideal ones to obtain higher hydrogen yield.

Increasing the glycerol concentration in the feed from 5 to 20% (260 °C/50 bar, 10 wt.% glycerol/water, WHSV = 6.8 h^{-1}) also showed an increase in the yield of the liquid products formed through the dehydration/hydrogenation of glycerol such as hydroxyacetone and propylene glycol. Conversely, by increasing temperature/pressure from 220 °C/25 bar to 260 °C/50 bar (10 wt.% glycerol/water, WHSV = 6.8h^{-1}) propylene glycol yield decreased while ethanol yield increased. As well, higher hydrogen yield was obtained at a higher temperature. This behaviour is expected, as it is an endothermic process. On the topic of post-reaction characterization, temperature/pressure conditions undoubtedly affected cobalt leaching. However, further investigation must be conducted to clearly establish the leaching mechanism.

Increasing the feed flowrate, and consequently the WHSV used, (at 260 °C/50 bar and maintaining glycerol concentration at 10 wt.%) did not change the composition of the outflow gases. However, due to the shorter contact time, the production of liquids increased, especially the liquids obtained by the direct reaction of glycerol (hydroxyacetone and propylene glycol). Finally, the comparison between oxygenated compounds showed that ethylene glycol (which has a lower number of carbons) presented a higher hydrogen yield. Compounds with larger carbon numbers, such as sorbitol, can be reformed to obtain, in addition to hydrogen, a huge number of intermediate compounds. Several of which are value-added chemicals that can be harnessed.

Chapter 7

CRUDE BIOGLYCEROL APR OVER 0.3Pt/CoAl CATALYST
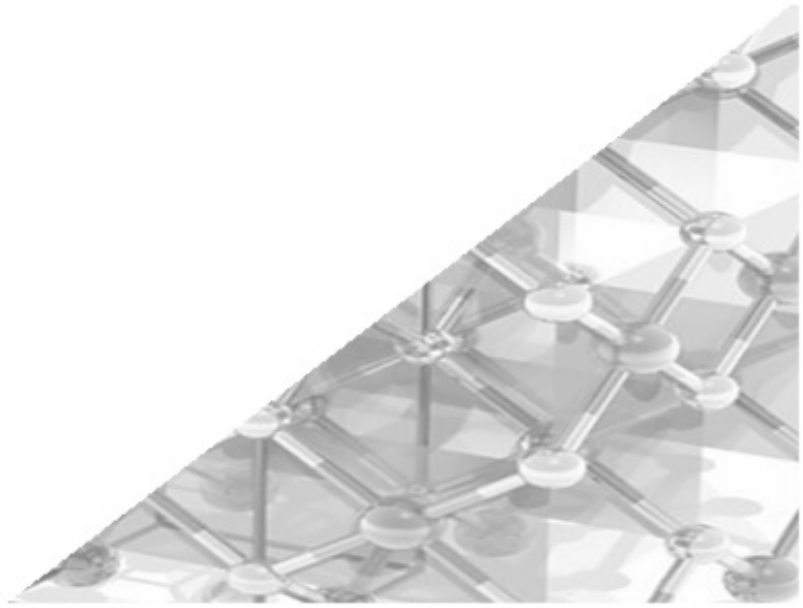
7. CRUDE BIOGLYCEROL APR OVER 0.3Pt/CoAl CATALYSTS

Heretofore, activity tests with synthetic glycerol solutions demonstrate the efficacy of cobalt aluminate spinel-based catalysts for the production of hydrogen by the aqueous phase reforming. Additionally, the optimised 0.3Pt/CoAl catalysts has also shown its ability to treat synthetic feeds of other polyols. Nevertheless, glycerol obtained as waste in biodiesel production units (in advance called "bioglycerol") is a crude fraction, and contains a number of impurities, which depends on the process used such as inorganic salts and other organic compounds that can undermine the performance of the APR process. The impact of these impurities on the catalytic process can be very complex, hypothesizing poisoning phenomena associated with inorganic salts and inhibition of catalytic activity due to the presence of organic compounds related to competitive adsorption mechanisms in the active centres. In addition, unpurified feedstreams can cause operational problems in the reactor and downstream systems (i.e. clogging, corrosion). Therefore, although pre-treatment is necessary, it is convenient to design efficient reforming technologies in the treatment of complex feedstreams, and thus reduce the operating costs derived from rigorous purification methods.

Considering the importance of knowing the effect of impurities in the feedstream on the performance of catalysts, this chapter deals with the characterization and pre-treatment of bioglycerol, and subsequent APR catalytic tests. The viability of the APR process with feedstreams from biodiesel production units will be determined, while the physico-chemical properties and catalytic performance between synthetic glycerol and bioglycerol are compared.

7.1 CHARACTERIZATION OF BIOGLYCEROL

The composition and physico-chemical characteristics of bioglycerol can vary significantly depending on the raw material and the type of process (i.e. base or acid catalysts, transesterification efficiency, impurities in the feedstock, purification methods) used [344,345]. A crude bioglycerol aqueous solution has been obtained from local biodiesel plant (Bionor S.L.). No additional information about the nature nor composition of the bioglycerol was obtained. Due to the

characteristics of its composition, crude bioglycerol solution was treated by saponification (by adding NaOH 2M) in order to convert the free fatty acids into soaps. The saponification was carried out in a beaker under constant stirring at 60 °C for 30 min until pH 12.0 was reached. Then, the solution was left overnight until complete separation of the two phases was achieved, and finally filtered. The soaps were discarded and the filtered fraction (in advance called "treated" bioglycerol) was neutralized by acetic acid addition. The use of this organic acid was preferred to other inorganic acids such as sulphuric or phosphoric acid to prevent possible catalyst poisoning. Physico-chemical properties of both the as-received and the treated samples were determined by a sort of analytical techniques, and compared with 10 wt.% synthetic glycerol/water solution (the same as used in previous chapters), used as reference.

The pH value was measured by a digital pH & Ion-meter (GLP 22, Crison), at room temperature. Density was determined by measuring the volume and weight of the sample, at room temperature. A viscometer Mettler Toledo RM180 Rheomat was employed to measure viscosity, also at room temperature. The quantification of the overall concentration of glycerol, acetic acid and methanol was carried out by HPLC with refraction index detector (previously described in Chapter 2). The ash content was determined by calcining approximately 1 g of sample in a furnace at 750 °C for 3 h, following the standardized ISO 2098:1972 method [346]. Ash composition was determined by Wavelength Dispersive X-ray Fluorescence (WDXRF) (AXIOS, PANalytical), using the fusion method.

The detailed analysis of the chemical composition was performed in the Alava unit of Central Analysis Service (SGIker). For this, each sample was fractionated into aqueous and organic fractions. Briefly, 170 μg of sample was saponified adding 2 mL KOH 2M and then acidified with a proper amount of HCl 2M. The recovery of the organic fraction was achieved by petroleum ether extraction. The solvent was removed in a rotary evaporator, and the obtained organic fraction was derivatized with BSTFA (N,O-bis-(trimethylsilyl)trifluoroacetamide) and analysed by gas chromatograph (Agilent 7890A) with mass spectrometry detector (Agilent 5975C).

For the GC-MS analysis, each sample (2 μL) was injected into an HP-5MS column (30 m, 0.25 mm) at an injection temperature of 300 °C. The column

temperature was ramped from 90 to 300 at 15 °C·min^{-1}. Helium was used as the carrier gas at a flow rate of 1.5 mL·min^{-1}. Calibration curves were calculated by least squares adjustment, with a correlation coefficient value greater than 0.995 for all cases.

Table 7.1. Physico-chemical properties and composition of crude, treated and synthetic glycerol.

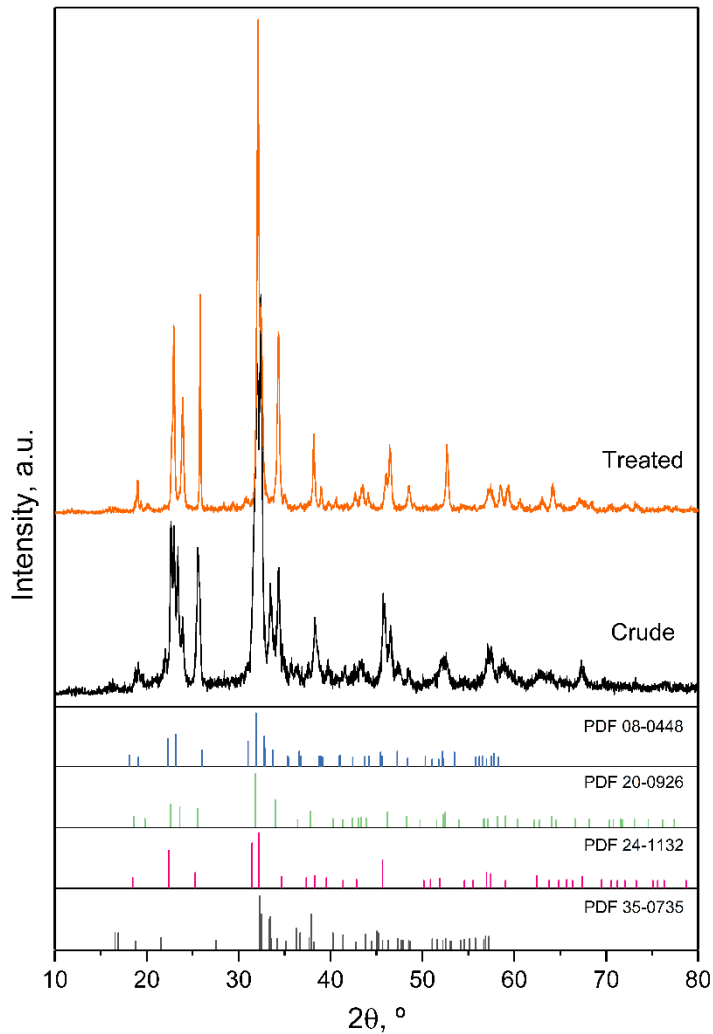|	Crude bioglycerol	Treated bioglycerol	Synthetic glycerol
pH	1.1	7.2	6.6
Density, g·cm^{-3}	1.1112	1.1025	1.0234
Viscosity, mPa·s	1.17	1.15	1.05
TC g·L^{-1}	84.0	55.5	39.9
Composition			
Glycerol, wt.%	13.0	9.7	10.0
Methanol, wt.%	4.8	1.8	0
Acetic acid, wt.%	0	0.6	0
C8:0, ppm	6.4	3.6	3.4
C10:0, ppm	4.3	0.8	0.9
C12:0, ppm	6.9	0.7	0.7
C14:0, ppm	8.7	0.5	0.4
C16:0, ppm	49.5	0.7	1.0
C18:0, ppm	75.6	5.7	6.1
C18:1, ppm	259.8	0.9	BDL
C18:2, ppm	271.0	4.1	BDL
C18:3, ppm	16.0	2.9	1.6
Ash, wt.%	8.84	8.60	0.05

BDL: below detection limit (<0.2 ppm), TC: total carbon, Caprylic acid (C8:0), capric acid (C10:0), lauric acid (C12:0), myristic acid (C14:0), palmitic acid (C16:0), stearic acid (C18:0), oleic acid (C18:1), linoleic acid (C18:2) and linolenic acid (C18:3).

The most relevant physico-chemical properties of the bioglycerols and synthetic glycerol solutions are listed in Table 7.1. Crude bioglycerol solution was unexpectedly acid (pH 1.1), while both the treated and synthetic glycerol solutions were near-neutral. The viscosity of crude bioglycerol solution was slightly higher than the treated one due to the higher content of FAMES, and consequently, both crude and treated were slightly more viscous than synthetic solution. The Total Carbon (TC) content of the crude sample was notably higher than that of both treated and synthetic solutions, due to the presence of fatty acids. The treated solution had more TC than synthetic solution as this was due to the addition of acetic acid for neutralization.

The glycerol content of the treated solution was similar to those commonly used in most studies conducted with synthetic glycerol (10 wt.%) [141,347,348]. Methanol and acetic acid were also present in the treated solutions. Methanol is the most used alcohol in biodiesel production plants, and the crude bioglycerol presented glycerol/methanol ratio of 2.7, much lower than raw glycerol from biodiesel plants (ratio around 20) [349], which indicated that our crude glycerol was a non refined fraction. The presence of both chemical compounds could affect the APR as both are prone to be reformed. By difference, high water content could be inferred in crude bioglycerol, possibly due to washing/rinsing to remove catalyst during biodiesel production. The most notable difference of crude with respect to the treated and synthetic solutions lies in the content of fatty acids, which decreased from 700 ppm (crude solution) to 20 and 15 ppm for the treated and synthetic solutions, respectively. In the as-received crude bioglycerol solution, oleic and linoleic acids clearly predominated among the FAMEs, while stearic and caprylic acids content in the treated and synthetic solutions were notable. The percentage of ash was 8.84 wt.% for crude bioglycerol solution, and it remained similar in the treated solution, both being much higher than that of the synthetic solution (0.05 wt.%).

Ashes from the crude and treated bioglycerol samples were analysed by XRD and WDXRF to determine their composition. XRD pattern of crude bioglycerol ash (Figure 7.1) exhibited attributable peaks of the following crystalline salts: $Na_2CO_3 \cdot H_2O$ (PDF 08-0448), $K_{0.67}Na_{1.33}SO_4$ (PDF 20-0926), Na_2SO_4 (PDF 24-1132) and Na_2HPO_4 (PDF 35-0735). The ashes of the treated sample maintained characteristic peaks of sodium and potassium sulphate. Table 7.2 listed the

results obtained by WDXRF. Confirming XRD analysis, a high presence of Na and S (above 20 wt.% for both) and also considerable content in K were found. The high amount of Na could be attributed to the use of Na-based alkali during the biodiesel processing, while the high S content pointed that the crude bioglycerol solution was acidified with sulphuric acid as part of its purification, which was consistent with the low pH of this sample. The rest of the elements were in a low concentration and were further decreased after treatment.

Figure 7.1. XRD diffractograms of crude and treated bioglycerol ashes.

**Table 7.2.** Comparative ash composition of crude and treated glycerol.

Ash composition, wt.%	Crude bioglycerol	Treated bioglycerol
Al	2.42	0.21
Ca	0.09	-
Cl	0.13	0.12
Fe	0.22	0.15
K	7.11	4.47
Na	21.1	26.9
P	0.76	0.34
S	22.8	22.7
Si	0.17	0.08

7.2   TREATED BIOGLYCEROL APR

Due to the high amount of impurities in the crude bioglycerol solution, its catalytic continuous processing was unfeasible, as the solution clogged the reaction system pipes. After treating crude bioglycerol, several catalytic tests were carried out over 0.625CoAl and 0.3Pt/CoAl catalysts. X_{gly} was calculated based on the glycerol content in the treated bioglycerol overlooking other organic compounds prone to be reformed present in the solution, such as acetic acid [137] and methanol [350].

A first screen was carried out with treated bioglycerol (9.7 wt.% glycerol content) over catalyst 0.625CoAl, at 260 °C/50 bar and WHSV of 0.68 h^{-1}, and the results were compared with the data obtained in previous tests with synthetic glycerol solution (10 wt.%). Figure 7.2 shows total glycerol conversion, carbon conversion to gas, H_2 yield and selectivity to H_2 and CH_4 for both synthetic and treated solutions after 8 h TOS. X_{gly} was barely lower for treated glycerol solution (99.9% for synthetic glycerol vs 98.8% for treated bioglycerol), which was ascribed to the competence for the active sites for glycerol of methanol and acetic acid, especially of the former, because of its higher mole ratio in the feedstream (0.53 mole methanol/mole glycerol and 0.09 mole acetic acid/mole glycerol). Synthetic glycerol, however, clearly presented a carbon conversion to

gas higher than that exhibited by treated bioglycerol. It is consequent, therefore, to have obtained a higher H_2 yield with the synthetic solution. Nevertheless, H_2 yield of treated bioglycerol solution was quite high (Y_{H2} = 50.6%).
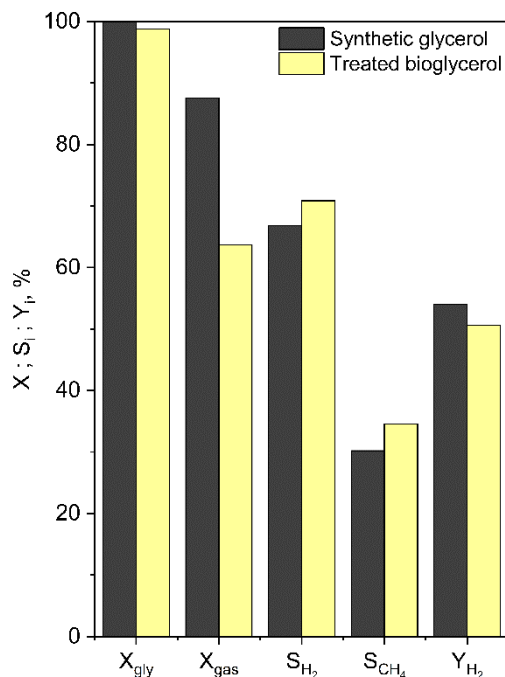
Figure 7.2. Comparison of overall APR catalytic results using synthetic and treated solutions at 8 h TOS over 0.625CoAl. Experimental conditions: 260 °C/50 bar, m_{cat} = 1.80 g, F = 0.02 $cm^3 \cdot min^{-1}$, WHSV = 0.68 h^{-1}).

The simultaneous reforming of the organic impurities and the lower acidity of the treated glycerol could explain the high Y_{H2}. Both impurities in treated glycerol are prone to be reformed. Indeed, Figure 7.3 shows how over 50% of methanol and 35% of acetic acid fed was converted. Methanol and acetic acid potentially give 3 and 4 moles of H_2 per mole, respectively. This performance was also responsible for the higher selectivity to hydrogen and methane obtained by the treated bioglycerol compared to synthetic solution (6% and 14.5% higher, respectively). Methanol has been extensively used as external H-donor in the reductive upgrading of biomass in the so-called catalytic transfer hydrogenation (CTH) systems [351]. Also, acetic acid can act as H-donor [352]. The concurrent increase on S_{H2} and S_{CH4} for the treated glycerol should be

related to the promotion of WGS in a more basic reaction environment [169]. In this regard, the positive effect of basic pH in the hydrogen selectivity is evident.
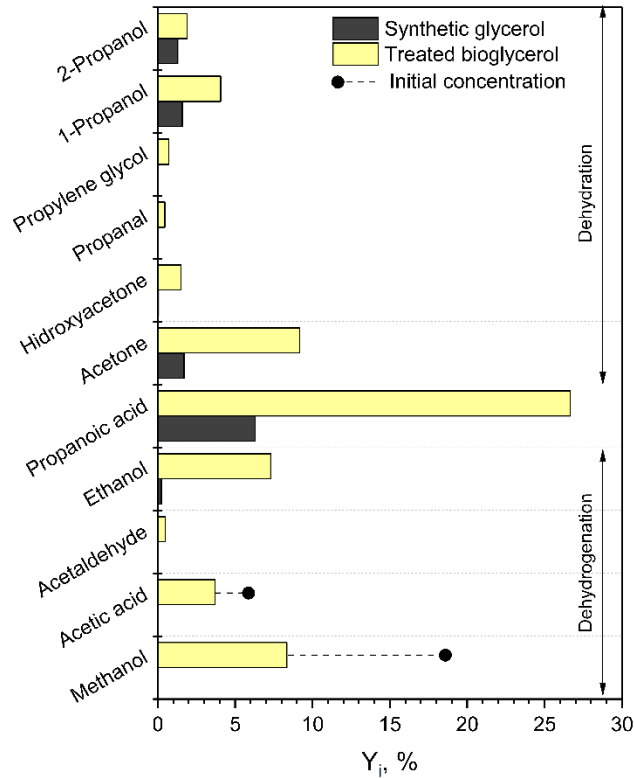
Figure 7.3. Comparison of liquid products yield using synthetic and treated solutions over 0.625CoAl catalyst. Reaction conditions: 260 °C/50 bar, m_{cat} = 1.80 g, F = 0.02 cm³·min⁻¹, WHSV = 0.68 h⁻¹).

The yield of the main liquid products are displayed in Figure 7.3. As a reference, the figure also shows the Y_i that would correspond to the initial concentration (i.e., in the feedstream) of methane and acetic acid. The liquid products obtained with treated glycerol were consistent with the reaction scheme proposed in Chapter 3. Treated bioglycerol presented a much greater diversity and, in general, a higher yield of liquid products (in accordance of its lower X_{gas}). Among the liquid products shown, propanoic acid was, by far, the product with the highest concentration for both synthetic and treated solutions. The presence of methanol and acetic acid in the outlet stream, in lower amount than the feedstream, is a clear sign of the reforming of these compounds simultaneously

with glycerol. There was not clear effect of the impurities on the distribution of the liquid products among dehydration or dehydrogenation paths.
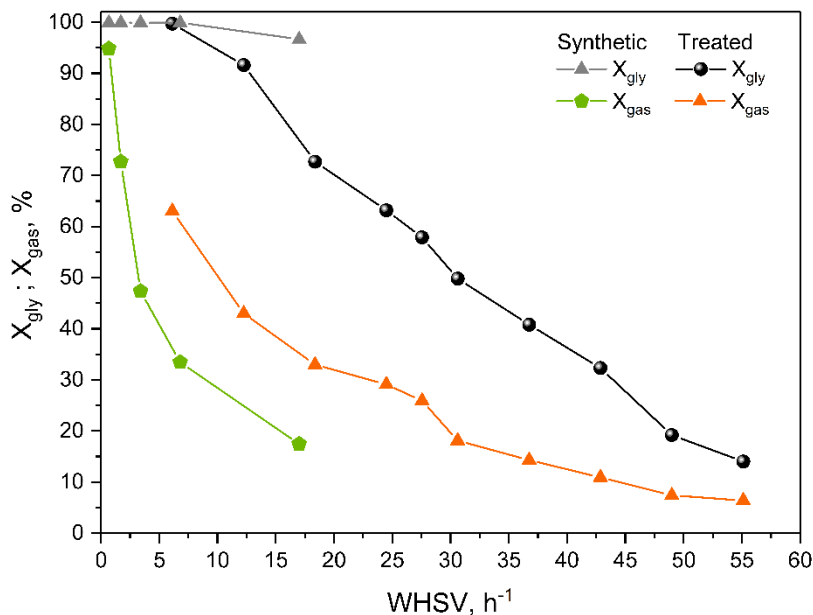
Figure 7.4. Glycerol conversion and carbon conversion to gas, over 0.3Pt/CoAl, as a function of WHSV.

Several APR experiments were performed with treated glycerol over the optimized 0.3Pt/CoAl catalyst, at 260 °C and 50 bar. The catalyst mass was set at 0.5 g and the feedstock flow (9.7 wt.% glycerol content) was varied from 0.05 to 0.45 $cm^3 \cdot min^{-1}$. It must be noted that increasing the feedstock flow while keeping constant the catalyst mass leads to a WHSV variation, which means less contact time. Hence, a sweep of glycerol conversions has been achieved, in the 17-100% range.

The data plotted in Figure 7.4 (corresponding to 1 h TOS), show an expected decrease in both glycerol conversion and carbon conversion to gas with an increase in WHSV. For comparison purposes, the data for synthetic glycerol were also depicted. The same decreasing trend was found when operated with synthetic glycerol, as discussed in Chapter 6. However, despite the much lower WHSV that was used with synthetic glycerol, there are certain differences that are interesting to bring out.

The first difference was related to X_{gly}, which decayed notably faster than that for synthetic glycerol (see Figure 7.4). Such a fast activity decay suggested some catalyst deactivation with the treated glycerol, which could be related to the presence of compounds (salts, fatty acids) that could block the active centres, as reported by other authors [132,353]. Another notable difference was in X_{gas}. If we compare their values for WHSV between 6-7 h^{-1}, in the case of treated glycerol it was much higher than that obtained with synthetic glycerol (33% vs 63%, respectively). A likely explanation was a high conversion of organic impurities to gaseous compounds. The X_{gas} decline for both feedstreams was similar, since at 17 h^{-1}, X_{gas} was approximately 45% lower than that at 5 h^{-1}. The same trend has been seen operating with 0.625CoAl catalyst.
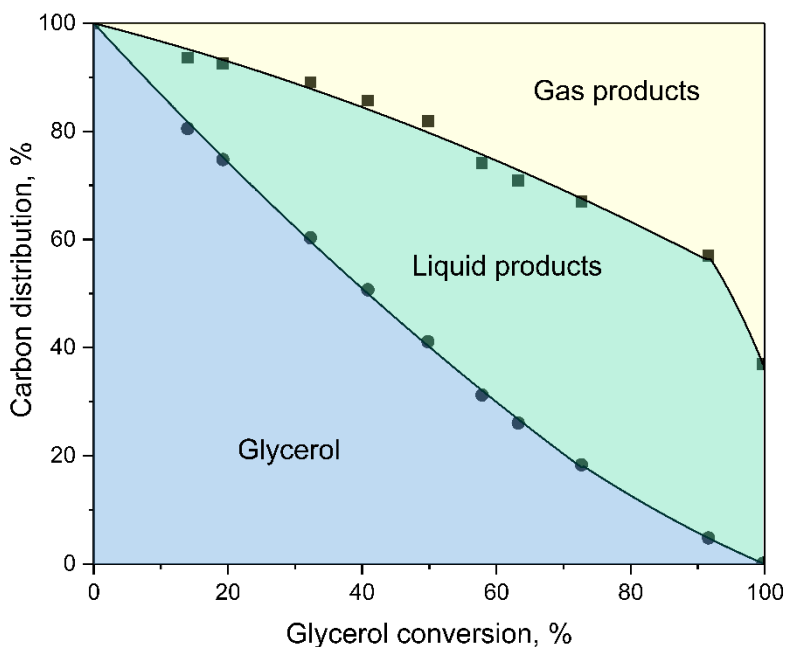
Figure 7.5. Carbon distribution among liquid and gas phases versus bioglycerol conversion for 0.3Pt/CoAl. The following conditions were used: 260 °C/50 bar, 9.7 wt.% glycerol content.

A more interesting approach was the discussion of the data obtained in relation to glycerol conversion. For this, Figure 7.5 displays the carbon distribution between liquid and gas phases versus treated glycerol conversion. The figure shows the molar percentage of carbon that remains as bioglycerol. The

liquid-phase intermediates are represented in the middle part and the upper part reflects carbon in the gas phase products.

Considering the ratio gas products/liquid products (G/L) obtained, the figure revealed three characteristic regions. The first one up to approximately 50% glycerol conversion, where the production of intermediate liquids was more than double than that of the gas phase (G/L varies in 0.38-0.49 range). The high proportion of intermediate liquid products was clearly related to the high feed rates, since at lower contact times the dehydration/dehydrogenation reactions were predominant.

In the X_{gly} range of 50-90%, gas production improved, obtaining a G/L ratio of around 0.65. It seems that above 90% glycerol conversion, yield to gas products boosted. For instance, at 91.6% glycerol conversion a G/L ratio of 0.82 was attained with 42% X_{gas}, and boosted to G/L = 1.71 operating at almost 100% glycerol conversion and 63% carbon conversion to gas. Together with the physico-chemical properties of the catalyst, this fact might serve to tune the reaction pathway.

Figure 7.6.A depicts the most representative parameters of gas phase products (Y_{H2}, S_{H2}, S_{Alk} and S_{CH4}). As might be expected, Y_{H2} increased as the glycerol conversion increased, reaching 45.4% when glycerol conversion was complete. It should be considered that the increase in conversion was achieved by increasing the contact time, which was beneficial to further reform the liquid intermediates to hydrogen product. In terms of selectivity, S_{H2} was superior to 55% even at the lowest X_{gly}. The results obtained in S_{H2} indicated that, even for impurities-containing glycerol, 0.3Pt/CoAl catalyst was very selective to hydrogen, comparable to bimetallic PtCo supported on multiwalled carbon nanotubes [189]. Regarding selectivity of other gas products, interestingly, methane was not the most abundant alkane, except at very high glycerol conversions. S_{CH4} remained almost invariable in the 10-20% in the whole conversion range, while S_{alk} (which accounted for methane, ethane, and propane) presented its highest values (42-51%) at X_{gly} between 40 and 60%. In previous sections we operated with X_{gly} close to 100%, therefore, methane was the main alkane, as occurred in this case (above 75% methane among alkanes for high conversions).
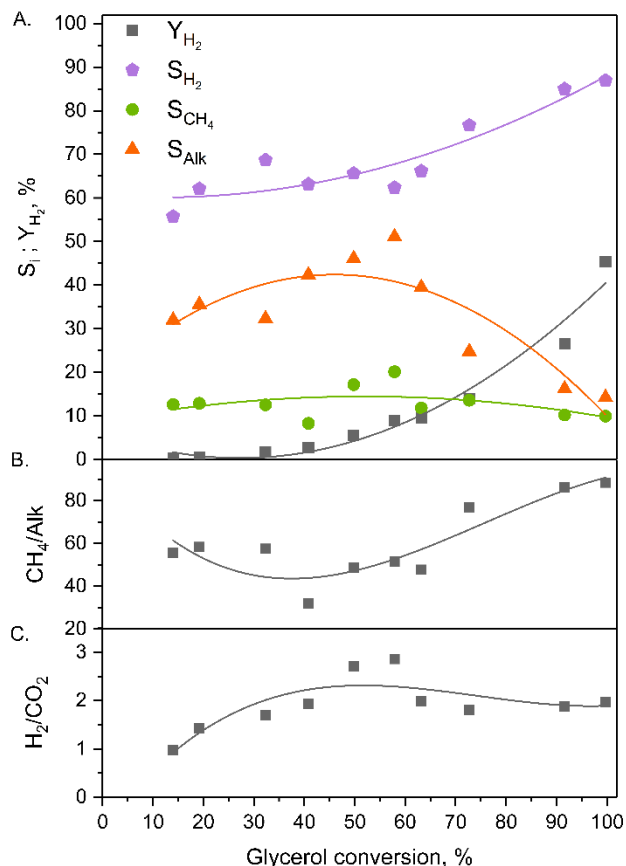
Figure 7.6. (A) Hydrogen yield and selectivities at different conversion levels; (B) methane fraction over all alkanes; and (C) H_2/CO_2 ratio for 0.3Pt/CoAl. Reaction conditions: 260 °C/50 bar, 9.7 wt.% glycerol content.

According to the trend of alkane selectivity towards low glycerol conversions, methane would also be the main alkane. However, when operating at intermediate glycerol conversions (in the 30-70% range), there was a substantial increase in the formation of higher alkanes (see Figure 7.6.B) which was consequently accompanied by the higher H_2/CO_2 ratio (Figure 7.6.C). Methane was formed either by hydrogenation of CO (although less selective than WGS, Chapter 5) or by the dehydration route through decarbonylation. However, the formation of ethane and propane occurred by other routes and required hydrogenation (see the proposed reaction Scheme 3.2). At low glycerol conversions, there was insufficient contact time between H_2 and liquid

intermediates. Moreover, the breaking of the C-C bonds was favoured, leading to the production of methane. At intermediate glycerol conversions, there was a higher probability of producing hydrogenation reactions of intermediates without C-C scission happening. That is, there was sufficient concentration of liquid intermediates that could then be hydrogenated to give alkane precursors (those products that contain C groups not linked to O).

A detailed analysis of the gas phase products is displayed in Figure 7.7. As is reflected in the graph, for the lowest X_{gly} (14%) CO_2 molar concentration was marginally higher than H_2 concentration (43.8% vs. 42.6%), probably driven by the reforming and/or side reactions of the organic impurities present in the treated bioglycerol (e.g. acetic acid can yields CH_4 and CO_2 via simple decomposition) [137]. Nonetheless, H_2 was the foremost gas product in the rest of all the tests performed, with molar concentrations above 60% at high glycerol conversions. Methane and ethane concentrations (and other alkanes grouped as C_{2+}) decreased in favor of H_2 and CO_2 as glycerol conversion increased (longer contact time). Finally, for X_{gly} range between 40-60%, CO was detected at a maximum concentration of 0.3% at intermediate glycerol conversions.
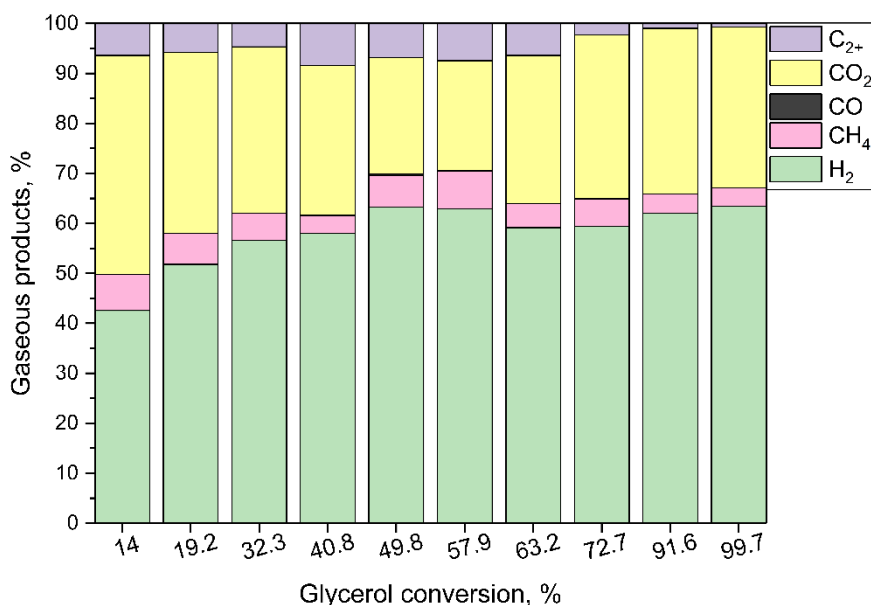
Figure 7.7. Gaseous products distribution at different conversion levels for 0.3Pt/CoAl. Operating conditions: 260 °C/50 bar, 9.7 wt.% glycerol content.

In reference to liquid products, below 40% conversion it was only possible to detect the initial compounds (methanol and acetic acid) and relatively low yields of hydroxyacetone and propylene glycol (maximum 1.9% and 0.8%, respectively). As glycerol conversion increased, other well-known compounds were generated, and four groups of liquid products could be established. On the one hand, the yield of initial organic impurities decreased as the glycerol conversion increased due to the reforming of these compounds themselves. In contrast, hydroxyacetone, propylene glycol (main dehydration compounds) and propanoic acid showed an increase in yield. The latter presented a yield of 17.3% to X_{gly} = 91.6%, much higher than the rest of the compounds. Other relevant liquid compounds were ethanol and ethylene glycol, which exhibited their highest yield in the X_{gly} range of 60-90%. Finally, traces of acetone, 1-propanol and propanal, were detected at high glycerol conversions (X_{gly} > 90%).

Table 7.3. Liquid products yield ranged by glycerol conversion.

Compound	Glycerol conversion, %			
	< 40	40-60	60-90	> 90
Methanol	16.2 - 17.5	9.6 - 13.5	4.2 - 8.8	-
Acetic acid	3.2 - 7.3	0.5	-	-
Ethanol	-	1.6	3.2	0.3
Ethylene glycol	-	0.4	2.9	-
Acetone	-	-	-	0.7
1-Propanol	-	-	-	0.8
Propanal	-	-	-	0.1
Hydroxyacetone	1.9	3.8	5.9	3.9 - 6.7
Propylene glycol	0.8	2.4 - 5.6	10.7 - 11.9	12.2
Propanoic acid	-	4.2 - 6.5	7.2	14.0 - 17.3

7.3   GLOBAL VISION AND SUMMARY

This chapter has addressed the physico-chemical analysis and catalytic testing of bioglycerol (by-product streams from a biodiesel production industry). This crude bioglycerol, in comparison with synthetic solution, had a very low pH, high concentrations of methanol, fatty acids and other organic compounds. Furthermore, inorganic salts and ash were also detected.

Reactor operability was affected due to clogging caused by impurities detected in the bioglycerol. Thus, in order to remove said impurities physico-chemical treatment comprising basification, neutralisation, and filtration, was conducted. Treated bioglycerol presented glycerol content and fatty acid concentrations similar to synthetic glycerol solution. However, the treatment failed to reduce the percentage of ash.

The catalytic assay carried out with 0.625CoAl catalyst, at 260 °C/50 bar and WHSV of 0.68 h^{-1}, showed a high glycerol conversion (98.8%) and considerable carbon conversion to gas (63.7%) after 8 h TOS. Hydrogen formation was favoured by the simultaneous reforming of organic compounds present in bioglycerol. The various catalytic tests performed with 0.3Pt/CoAl at different WHSV allowed a detailed study of the behaviour exhibited at different glycerol conversions. A higher production of gaseous products and a higher hydrogen yield at high conversions were achieved, contrary to the high carbon content in the liquid products obtained at glycerol conversions below 50%.
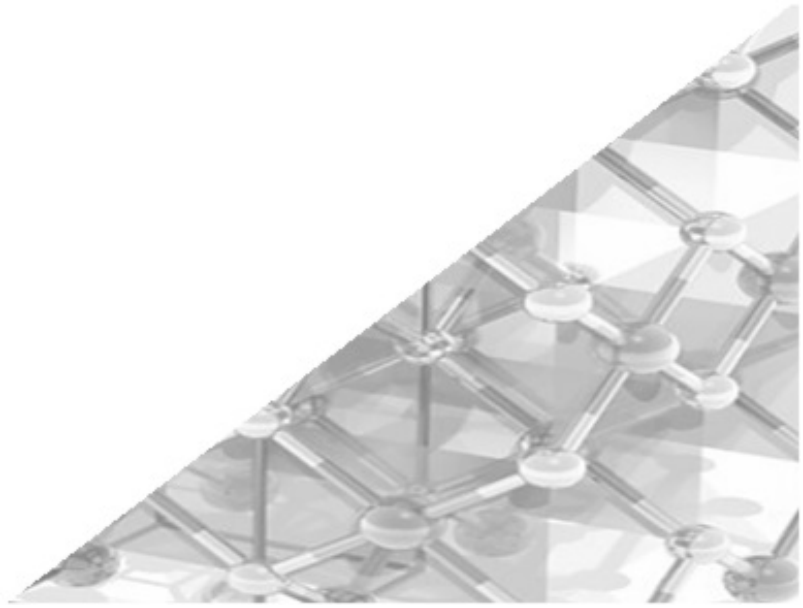
Chapter 8

AQUEOUS-PHASE TRANSFORMATION OF SORBITOL
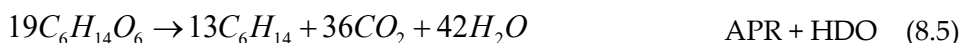
8. AQUEOUS-PHASE TRANSFORMATION OF SORBITOL

Sorbitol, like glycerol, is one of the 12 bio-based value-added chemicals highlighted as valuable starting materials for production of fuels and chemicals, as declared by the United States Department of Energy (DOE) [35]. Sorbitol is a representative sugar alcohol derived from cellulosic fraction of biomass. It is an abundant sugar alcohol that is currently produced by hydrogenation of glucose or directly from cellulose. In recent years, there has been a growing interest in the research of cost-effective catalytic processes for this highly functionalized compound [354].

Liquid-phase processing of sorbitol can be tailored to selectively produce hydrogen (APR process) or heavier alkanes, mainly butane, pentane, and hexane. Sorbitol transformation into biofuels that can be used into gasoline pool and other less oxygenated compounds can be produced by the aqueous-phase hydrodeoxygenation (HDO).

In brief, HDO is a hydrogenolytic reaction that involves the removal of an oxygen atom (deoxygenation) combined with simultaneous or subsequent addition of H_2 (hydrogenation). It was found that the removal of oxygen-containing functionalities can occur through direct hydrogenolysis (C-O bond cleavage with H_2), dehydration (C-O bond cleavage through removal of water), decarbonylation (removal of CO by C-C cleavage), and decarboxylation (removal of CO_2) [355]. The main deoxygenation routes are decarbonylation (on metallic sites) and alcohol dehydration (on acidic sites) [356]. Therefore, HDO requires bifunctional catalysts with a transition metal component on an acidic support [357].

Aqueous-phase sorbitol transformation can be summarised in the following set of equations:

$$C_6H_{14}O_6 \rightarrow 6CO + 7H_2 \hspace{3cm} \text{Decomposition} \quad (8.1)$$

$$CO + H_2O \leftrightarrow CO_2 + H_2 \qquad\qquad\qquad \text{WGS} \quad (8.2)$$

$$C_6H_{14}O_6 + 6H_2O \rightarrow 6CO_2 + 13H_2 \qquad\qquad \text{APR} \quad (8.3)$$

$$C_6H_{14}O_6 + 6H_2 \rightarrow C_6H_{14} + 6H_2O \qquad\qquad \text{HDO} \quad (8.4)$$

$$19C_6H_{14}O_6 \rightarrow 13C_6H_{14} + 36CO_2 + 42H_2O \qquad \text{APR + HDO} \quad (8.5)$$

In the framework of the doctoral stay at the *University of Poitiers*, aqueous-phase transformation of sorbitol was carried out under H_2 or N_2 environment; in the latter case, hydrogen must be generated *in situ* for the HDO. These catalytic tests seek to analyse the versatility of the cobalt-based catalysts when subjected to other operating conditions, to different feedstock and another reactor (CSTR). This chapter details the reaction system and the reaction analysis equipment used, to finally present and compare the most outstanding catalytic results of both processes (under H_2 -HDO- or under N_2 -APR-) for bare Co_3O_4, xCoAl, Ce-doped CoAl and xPt/CoAl catalysts.

8.1   REACTION SYSTEM

Aqueous-phase sorbitol transformation was performed at the laboratories of the research group "*Du Site Actif au Matériau catalytique*" (SAMCat), at the "*Institut de Chimie des milieux et Matériaux*" (IC2MP) located in Poitiers, France. Likewise, the equipment, used to characterize the products (described in section 8.2) corresponds to these laboratories.

8.1.1   Reaction equipment

The process and instrumentation diagram of the experimental reaction setup is shown in Figure 8.1. The reactor (Autoclave Engineers) was made of stainless steel, with a capacity of 300 cm³. The reaction system was suitable for liquid and gas sampling and was equipped with a magnetically driven impeller and temperature control unit. A heating jacket controlled by a Minicor

controller-programmer ensured a correct heating of the reactor. A thermowell containing a descending thermocouple (Ti) measured the temperature of the liquid within the vessel. The system pressure was measured by a pressure transducer (Pi) which can operate up to 100 bar. The experimental device was protected from possible overpressure by a safety valve. The reaction system also includes a stainless steel liquid charging cylinder (D-1) with a capacity of 10 cm^3. A tube plunging into the bottom of that vessel, allowed, by increasing the internal pressure, to expel the liquids towards the autoclave through the opening of the valve V-5. For sampling of gaseous products, the reactor had a gas output line through which non-condensable gas passes after manually activating valves V-9, V-10 and V-11, while sampling of liquids was done by means of the V-7 and V-8 valves.
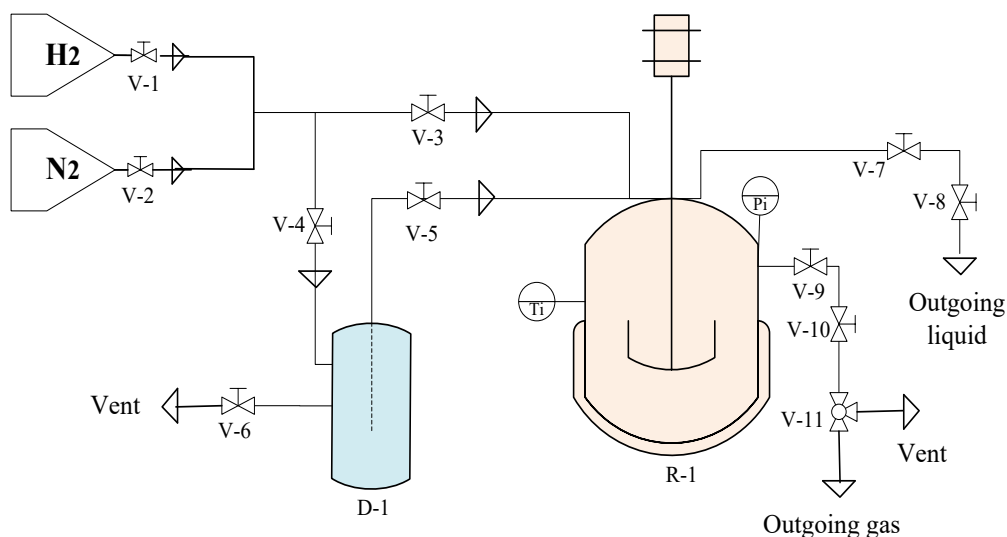
Figure 8.1. Scheme of sorbitol transformation process.

8.1.2   Operating conditions

Aqueous-phase sorbitol transformation over various catalysts was performed at 240 °C and 60 bar, pressurized under H$_2$ (HDO) or N$_2$ (APR). All the tests were carried out in a strictly identical manner, to overcome the diffusion problems of the reagents inherent in the reaction. In addition, the dispersion of the catalyst particles within the reaction mixture was ensured by constant stirring, which

also made it possible to homogenize the solution by limiting the concentration gradients. A stirring speed of 1300 rpm was chosen in order to overcome diffusion phenomena.

Henry´s law was used to estimate the dissolved H_2 or N_2. Due to the high dilution of sorbitol (6.25 wt.% or 0.66 mol %), Henry´s constant for gases in pure water were estimated, once the contribution of water vapour to total pressure was subtracted (using Antoine equation for pure water). At the employed experimental conditions dissolved H_2/sorbitol (HDO) and N_2/sorbitol (APR) molar ratio were 0.37 and 0.10, respectively.

Prior to each experiment, 1 g of catalyst was reduced in an external reactor at 600 °C, in H_2 flow (60 $cm^3 \cdot min^{-1}$, heating rate of 5 °C·min^{-1}) for 0.5 h and then transferred in a glovebox under N_2 atmosphere into the reactor, where previously ultrapure water was deposited. The reactor was, then, loaded with an aqueous solution of sorbitol (6.25 wt.% corresponding to 150 cm^3 of total volume of water in the reactor, with 10 g of sorbitol). After sealing, the autoclave was purged several times and pressurized with H_2 (for HDO) or N_2 (for APR) to the required pressure. Zero time was taken when stirring was switched on once the temperature and pressure reached their set values. During the reaction, at specific intervals, liquid samples were manually collected in vials and analysed offline, while gas product was analysed online. At the end of the test the reactor was cooled, and catalysts were recovered by decantation. The solid was washed with water and then dried overnight at 120 °C.

8.2   PRODUCTS ANALYSIS

The techniques used for the analysis of the products of the sorbitol transformation were the same as formerly explained in Section 2.4. Hence, in this section only that equipment that differs from the equipment at the laboratories of the TQSA research group from UPV/EHU will be described.

8.2.1   Gas chromatography (GC)

Gaseous product, composed by hydrocarbons, H_2, CO_2 and CO, was analysed online with both Varian GC-450 and GC-430 chromatographs equipped with an injection valve and four detection channels (2 TCD and 2 FID).

Table 8.1. GC equipment and analysis conditions in sorbitol transformation.

Chromatograph	Varian 450-GC			Varian 430-GC
Detector	TCD Front	TCD Middle	FID Rear	FID
Detector conditions	Temp.: 175 °C 20.0 $cm^3 \cdot min^{-1}$		Temp.: 175 °C F_{N2}: 15.0 $cm^3 \cdot min^{-1}$	Temp.: 250 °C F_{N2}: 29.0 $cm^3 \cdot min^{-1}$ F_{H2}: 30.0 $cm^3 \cdot min^{-1}$ F_{Air}: 300.0 $cm^3 \cdot min^{-1}$ Makeup Gas: N_2
Carrier gas	N_2	He	He	N_2
Columns	Type Packed	Type WCOT	Type WCOT	
Column flow	0.2 $cm^3 \cdot min^{-1}$			1.0 $cm^3 \cdot min^{-1}$
Oven	50 °C for 10 min, up to 180 °C (8 $°C \cdot min^{-1}$) during 3.75 min.			80 °C for 1 min, up to 220 °C (10 $°C \cdot min^{-1}$) during 15 min.
Loop/Injection volume	10 µL			
Injector		Split 20:1		Split 10:1
Analysis time		30 min		
Products analysed	H_2	CO, CO_2, N_2 & CH_4	Hydrocarbon gases (C_1-C_6)	Hydrocarbon gases (C_5-C_6)
Control system		Galaxie chromatography		

This system allowed the simultaneous analysis of the different gases. The characteristics of the chromatographic system and parameters for the gas analysis are described in Table 8.1.

8.2.2   Liquid chromatography (HPLC)

Liquid products of reaction were manually collected and analysed offline by a HPLC system (Shimadzu Prominence UFLCXR) provided with both refractive index (RI) and ultraviolet (UV) detectors. UV-visible HPLC detector uses light to analyse samples. The analyte was identified by measuring the light absorption of the sample at different wavelengths. UV-visible detectors were used to identify and quantify aromatics, compounds with double bonds with extended conjugation and highly conjugated organic compounds [358]. RI detectors are a simple and effective way to detect analytes that do not absorb UV light.

Table 8.2. HPLC equipment and analysis conditions

Chromatograph	Shimadzu Prominence UFLC$_{XR}$
HPLC pump	LC-20AD$_{XR}$
Auto sampler	SIL-20AC$_{XR}$
Refractive Index Detector	RID-10A
Diode Array Detector	SPD-M20A
Column	Aminex HPX-87 H (30 cm x 7.8 mm)
Column oven	CTO-20AC
Degassing unit	DGU-20A$_{5R}$
Injection volume	20 μL
Mobile phase	Water (4 x 10^{-3} M, Sulfuric acid)
Column	0.5 cm^3·min^{-1}
Column temperature	40 °C
Analysis time	40-120 min
Control system	LabSolutions LC

The analysis was carried out in isocratic mode with a dilute sulphuric acid solution as eluent. After degassing, the eluent was pumped throughout the system at a flow rate of 0.5 cm³.min⁻¹. The autosampler allowed the injection of the sample, which, mixed with the eluent, crosses the column placed in the oven at 40 °C. The compounds separated were detected as a function of their retention time by a UV-visible detector with diode arrays and a differential refractometer (RI) detector. The characteristics of the equipment used and the analysis conditions are summarized in Table 8.2.

8.2.3   Total Organic Carbon (TOC)

The total quantity of carbon in the aqueous-phase was measured by TOC analysis with a Shimadzu apparatus (Carbon-L Series), identical to the one described in section 2.4.3. Before carrying out the analysis, and due to the high carbon concentration in the liquid samples, these samples were diluted to 1/50 in order to reach the standard range between 100 and 1000 $mg_{carbon} \cdot L^{-1}$.

The moles of carbon in the liquid phase obtained from the TOC values were calculated as follows:

$$n_{C,liquid} = \frac{TOC(mg \cdot L^{-1}) \times f_d \times V_{liq}}{M_C \times 1000} \tag{8.6}$$

where, f_d is the sample dilution factor (50); V_{liq} is liquid volume in the reactor and M_C is the molar mass of carbon (12 $g \cdot mol^{-1}$).

8.2.4   Definitions and Calculations

It should be remembered that the concentration for each compound in the sample was calculated from a standard curve of known concentrations established for that compound. The initial concentrations of the gaseous products were expressed as a molar percentage. Therefore, the ideal gas law was used to transform these concentrations into moles (n_i).

$$n_i = 100 \times \frac{\%mol_i \times P \times V_{gas}}{R \times T} \tag{8.7}$$

where, $\%mol_i$ the concentration obtained for a i product; P, T and V_{gas} are total pressure, temperature, and gas volume (150 cm³) in the autoclave, respectively; and R is the constant of ideal gases.

Sorbitol conversion (X_{sorb}) and carbon conversion to gas (X_{gas}) were defined as follows:

$$X_{sorb}(\%) = 100 \times \frac{n_{sorb}^{t=0} - n_{sorb}^{t=t}}{n_{sorb}^{t=0}} \tag{8.8}$$

$n_{sorb}^{t=0}$ and $n_{sorb}^{t=t}$ are the moles of sorbitol initially charged to the reactor (calculated from TOC analysis and considering t = 0 the first 2 min of reaction) and at reaction time t, respectively.

$$X_{gas}(\%) = 100 \times \frac{n_C^{t=0} - n_{C,liquid}^{t=t}}{n_C^{t=0}} \tag{8.9}$$

$n_C^{t=0}$ and $n_{C,liquid}^{t=t}$ are the moles of carbon initially charged and moles of carbon in the liquid phase detected as TOC, respectively.

The product yield (Y_i) was defined on a carbon basis:

$$Y_i(\%) = 100 \times \frac{n_{C,i}^{t=t}}{n_C^{t=0}} \tag{8.10}$$

$n_{C,i}^{t=t}$ is the carbon moles in an specific product i.

For the sake of simplicity, the obtained products were grouped into four categories: light gas (LG), hydrocarbons/heavy gas (HG), monofunctional liquids (MF) and higher oxygenated liquids (HO). The first two (LG and HG) were in the gas phase, while MF and HO were obtained in the liquid phase. Thus, selectivity to each category (S_k), based on C atoms, was defined as follows:

$$S_k = 100 \times \frac{Y_k}{\sum Y_{i,phase}} = 100 \times \frac{\sum Y_{i,k}}{\sum Y_{i,phase}} \qquad (8.11)$$

Y_k is the yield of the products in each category (summation of the yields of the products in category k), and $Y_{i,phase}$ is the yield of the products in all the categories in the same phase.

Meanwhile, hydrogen yield (Y_{H2}) was calculated as the ratio between the moles of H_2 produced and moles of sorbitol fed to the reactor, multiplied by the stoichiometric factor 1/13 (based on equation (8.3):

$$Y_{H_2}(\%) = 100 \times \frac{n_{H_2}^{t=t}}{n_{sorb}^{t=0}} \times \frac{1}{13} \qquad (8.12)$$

The carbon balance fluctuated between 91-112% for sorbitol HDO (Table 8.4) and 82-87% for sorbitol APR (Table 8.4). The difference may lie in the liquid sampling, due to the loss of volatile products and others compounds as insoluble degradation products [343,359]. Despite not achieving an accurate carbon balance of 100%, we consider that the results can be discussed and compared between the different catalysts without incurring major errors.

8.3 RECAP OF CATALYSTS´ PHYSICO-CHEMICAL PROPERTIES

Calcined and freshly reduced catalysts employed in these reactions have been thoroughly discussed in their respective chapters (see Chapters 3, 4 and 5). However, for a better reading and to help the discussion of results in this chapter, the most relevant physico-chemical properties are summarized in Table 8.3.

Table 8.3. Chemical, textural, and structural properties of the freshly reduced catalysts.

Catalyst	S_{BET}, $m^2 \cdot g^{-1}$	Accessible metal, $at._{metal} \cdot g^{-1}$	TOF_{dehyd}, s^{-1}	Surface site density		$A_{isom,0}$, $\mu mol \cdot m^{-2} \cdot h^{-1}$
				Acid, $\mu mol_{NH3} \cdot m^{-2}$	Basic, $\mu mol_{CO2} \cdot m^{-2}$	
Co_3O_4	7.4	$1.22 \cdot 10^{18}$	1.61	0.06	2.01	51.0
0.25CoAl	96.6	$2.28 \cdot 10^{18}$	0.34	0.78	2.20	3.44
0.5CoAl	102.8	$3.92 \cdot 10^{18}$	0.43	0.60	1.95	2.46
0.625CoAl	101.7	$23.0 \cdot 10^{18}$	0.59	0.51	1.90	2.84
0.3CeCoAl	138.3	$14.6 \cdot 10^{18}$	0.84	0.79	1.91	252.4
0.3Pt/CoAl	131.0	$35.6 \cdot 10^{18}$	2.29	0.56	1.16	85.6
1Pt/CoAl	126.1	$46.2 \cdot 10^{18}$	2.20	0.68	1.34	2.10
0.3Pt/Al	138.1	$6.9 \cdot 10^{18}$	0.61	0.34	0.32	165.6

Briefly, the most relevant characteristics were the very low S_{BET} of bare Co_3O_4 and its lower metallic availability compared to the other cobalt spinel catalysts. In this regard, Pt-Co bimetallic catalysts presented the highest metal availability, corroborated by the high intrinsic activity in cyclohexane dehydrogenation reaction. For xCoAl catalysts, the acidity/basicity ratio increased as Co/Al ratio decreased. Ce- and Pt-doped catalysts also showed a higher acid/base sites density ratio than the starting 0.625CoAl catalyst.

8.4   SORBITOL HDO

In this section, the results of the catalytic tests carried out at 240 °C and 60 bar under H_2 atmosphere will be discussed. Both external and internal mass transfer effects were found to be negligible under the conditions used in our experiments (Appendix, Section A).
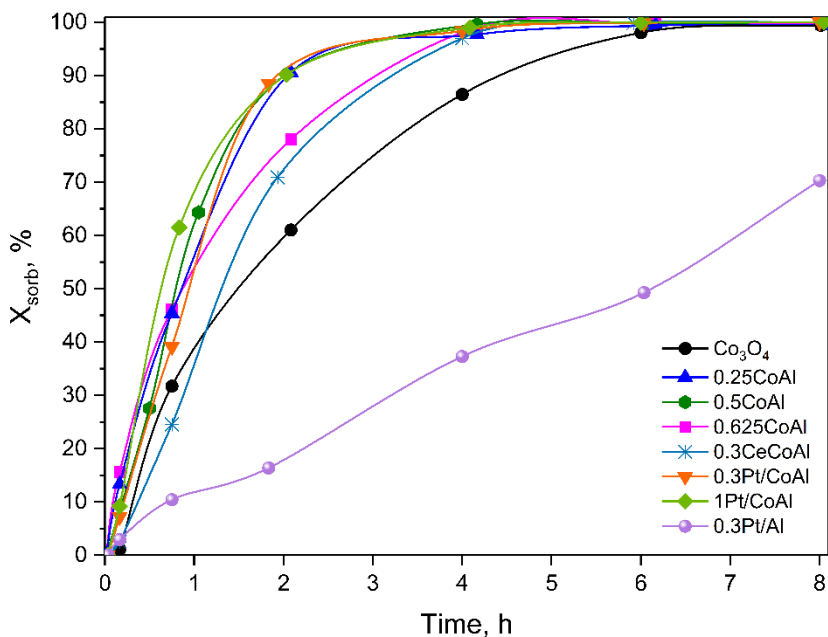
Figure 8.2. Sorbitol conversion as a function of reaction time for all the catalysts. Reaction conditions: 10 g of sorbitol, 150 cm³ of water, 1 g of catalyst, P_{H2} = 60 bar, T = 240 °C.

Sorbitol conversion (X_{sorb}) as a function of reaction time for all the catalysts is displayed in Figure 8.2. These curves allow us to compare the activity of the

various catalysts for a same mass. All the catalysts were effective for converting sorbitol. Without going into detail about the reaction kinetics, a positive reaction order with respect to sorbitol concentration could be deduced, except for 0.3Pt/Al, which showed a typically zero order kinetics (Appendix, Figure C.2).
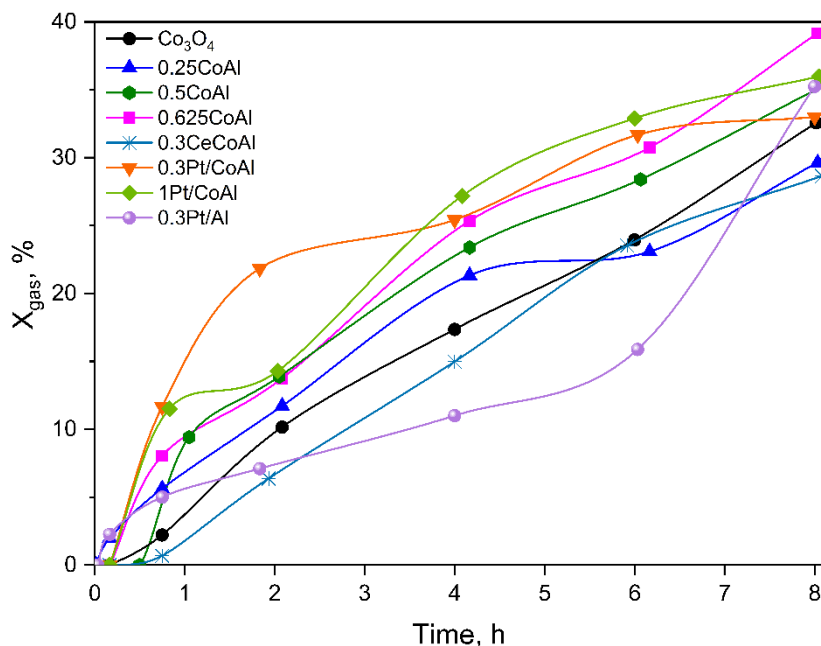
Figure 8.3. Carbon conversion to gas as a function of reaction time for all the catalysts. Reaction conditions: 10 g of sorbitol, 150 cm^3 of water, 1 g of catalyst, P_{H2} = 60 bar, T = 240 °C.

Under the experimental conditions carried out, almost complete conversion of sorbitol was achieved after 4 h of reaction, except for bare Co_3O_4 and 0.3Pt/Al catalysts. Sample Co_3O_4 reached 100% sorbitol conversion after 6 h of reaction. Nonetheless, 0.3Pt/Al sample did not exceed 70% of conversion after 8 h reacting, which could be due to the blockage of Pt active sites by strongly adsorbed species such as H_2 and/or CO formed by decarbonylation [360]. Bare Co_3O_4 was quite active in the first minutes of reaction (32% conversion at 45 min of reaction) but then rapidly deactivated (80% conversion at 4 h). Among monometallic xCoAl catalysts, 0.625CoAl was the most active in the first minutes of reaction, but it deactivated more over time. For example, at 2 h of reaction, 0.625CoAl achieved 77% X_{sorb} while 0.25CoAl and 0.5CoAl catalysts

achieved 90.6% and 90.4%, respectively. It is well known that the formation of Co-Pt alloying minimizes the blockage of the active sites [360].

Moreover, alloying noble metals with transition metals improves the hydrogenation rates [361]. These explained why Pt-containing bimetallic catalysts were the most active among all, 1Pt/CoAl being slightly more active than 0.3Pt/CoAl in the first minutes of reaction. Indeed, 1Pt/CoAl stood out for its high sorbitol conversion at 45 min of reaction (above 60% sorbitol conversion). Ce-doped catalyst, however, did not improve the sorbitol conversion of its counterpart 0.625CoAl catalyst. The effectiveness of Co-based catalysts for sorbitol HDO was also reported by others [343]. During its transformation, sorbitol underwent various types of reactions such as C-O and C-C scissions, resulting in a formation of gas and liquid products. Figure 8.3 shows the carbon conversion to gas for the assayed catalysts. As expected, the carbon conversion to gas products increased with reaction time. Note that the increase of X_{gas} once sorbitol was completely converted (above 4 h for all the catalysts, except for Co_3O_4 and 0.3Pt/Al) indicated the conversion to gas of the liquid intermediates derived from sorbitol.

Pt-containing bimetallic catalysts were the most active in the production of gaseous products, however, a slowdown was observed after 6 h of reaction. The second most active catalysts for gas production were the monometallic xCoAl catalysts. In the first 6 h of reaction, bare Co_3O_4 assay achieved less gas conversion than xCoAl catalysts. Ce-doped catalyst showed low X_{gas} in the whole experiment. For example, at 4 h of reaction, X_{gas} for 0.3Ce/CoAl was 15% while it was 25% for its counterpart 0.625CoAl. In the first hour of reaction, 0.3Pt/Al catalyst was among the most active catalysts for gas production but then X_{gas} increase was smoother, turning this catalyst as the less active for gas production. However, above 6 h of reaction, X_{gas} boosted and converted this catalyst to very active for gas production.
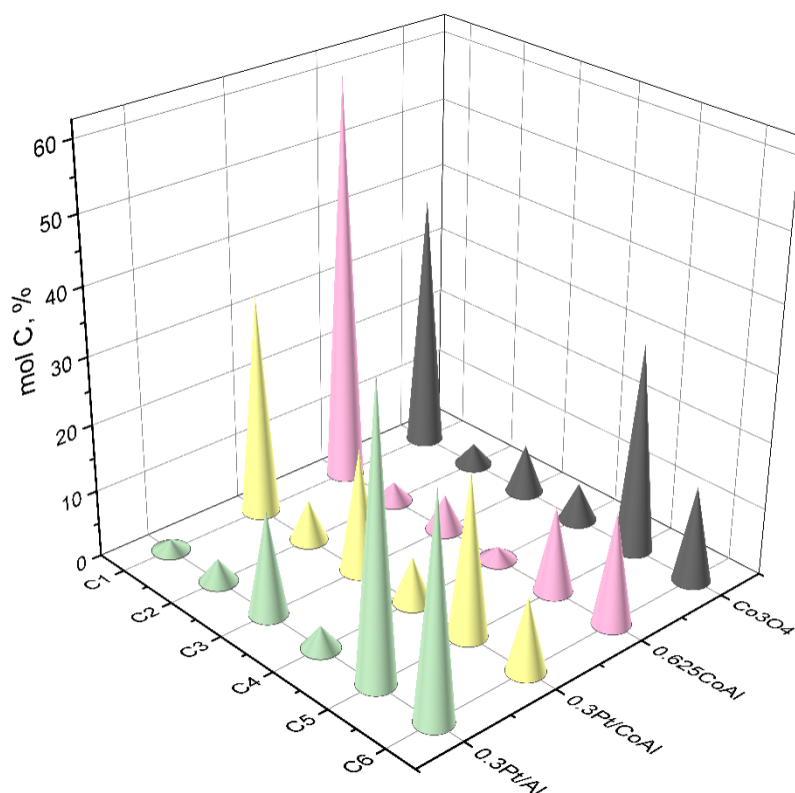
Figure 8.4. Yield of organic compounds as a function of carbon atoms number in the molecules during sorbitol HDO.

For the sake of clarity, the discussion of the products obtained has focused on four distinctive catalysts within each family: Co_3O_4, 0.625CoAl, 0.3Pt/CoAl and 0.3Pt/Al. Figure 8.4 shows the carbon distribution (excluding CO_2) for the selected catalysts. It was deduced that sorbitol HDO involves a sort of reaction of C-C scission at various different positions on the initial substrate chain. Catalysts Co_3O_4 exhibited high yield to C_1 (methane and methanol) and C_5 products (including 2-methyltetrahydrofuran, a potential greener solvent and gasoline blending component). A similar distribution was observed for 0.625CoAl catalyst with an even higher yield towards C_1 compounds. On the other hand, the yield toward C_3 compounds increased for bimetallic 0.3Pt/CoAl. For catalyst 0.3Pt/Al, the yield obtained was: $C_5 > C_6 > C_3 > C_2 \approx C_4 > C_1$. High fragmentation of the molecules was observed, obtaining short-chain compounds

especially in cobalt-containing catalysts, owing to its high capacity for C-C scission [186].
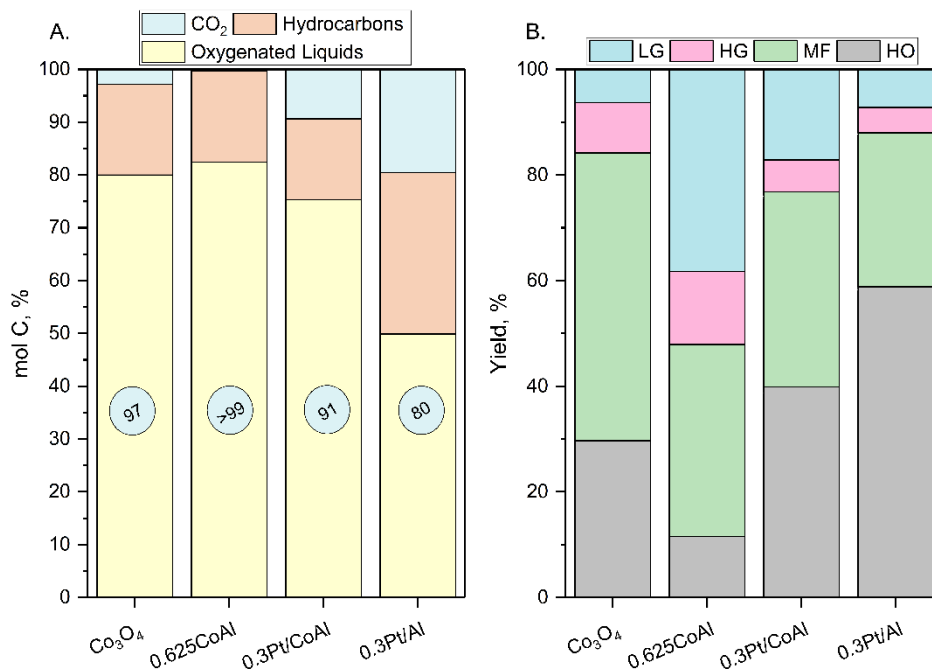
Figure 8.5. Catalytic results obtained at 70–90% of sorbitol conversion under HDO reaction conditions: (A) Carbon global distribution and (B) yield of products by categories.

The global distribution of carbon normalized to 100% obtained at X_{sorb} = 70-90% (which can be considered isoconversion) is presented in Figure 8.5.A for the four catalysts representing each family. These conversion values were obtained at 2 h of reaction for all the catalysts, except for the catalysts Co_3O_4 (4 h) and 0.3 Pt/Al (8 h). In general terms, all catalysts produce a high proportion of liquid products (labelled Oxygenated Liquids, which comprised MF and HO products) and the gas phase is mainly composed of hydrocarbons (LG plus HG after CO_2 subtraction). For all the catalysts, the major part of the products was in liquid phase. Oxygenated liquid compounds represented between 75 and 83% of the output carbon-based molar composition for all catalysts (except for 0.3Pt/Al sample, which corresponded to 50%). On the other hand, the majority of the gas products corresponded to hydrocarbons, which accounted for between 15% and 31%. Regarding hydrocarbons production, it is necessary to highlight sample

0.3Pt/Al, unlike the low results shown by 0.3CeCoAl catalyst (7.5%, not shown in the Figure). The higher CO_2 production shown by xPt/CoAl catalysts (3.5-9.5%) was obviously due to a greater involvement of the catalyst metal part (according to the high metal availability, of high dehydrogenation activity) that promotes C-C bonds cleavage [362]. In this regard, it seemed that 0.3Pt/Al catalyst had high decarbonylating activity, which led to a significant CO_2 production (19.2% of the reacted carbon) [363].

At this point, the high atom economy offered by most of the checked catalysts, above 97% in terms of C-atoms (to give valuable products), must be highlighted. The obtained values are highlighted as circles in Figure 8.5.A. The highest atom economy (above 99%) was achieved by catalyst 0.625CoAl and on the opposite side were catalysts xPt/CoAl (e.g. 0.3Pt/Al sample attained 80.3%).

As stated above, the sorbitol decomposition products were divided into four main categories: Light Gas (LG), composed by CO, CO_2, and C_1-C_4 alkanes; Hydrocarbons/Heavy Gas (HG), composed by C_5-C_6 alkanes; Monofunctionals (MF), involving all species that contain exactly one oxygen functionality (e.g., mono-alcohols, ketones, aldehydes, heterocycles); and Higher Oxygenates (HO), which are all species with two or more oxygens (e.g., polyols, mixed alcohol-carbonyl compounds, hydroxy-heterocycles, carboxylic acids). Figure 8.5.B gathers the carbon distribution among categories and yields for each category for the catalysts more representative of each family. These data can be analysed in conjunction with the carbon selectivity presented in Table 8.4.

Bare Co_3O_4 produced mostly liquid products, leading by MF compounds (54% yield) followed by HO (30% yield) and to a lesser extent gaseous compounds (being HG > LG). Among gases, the high selectivity towards C_{5+} hydrocarbons should be noted (60%, Table 8.4). Monometallic 0.625CoAl was characterized to achieve higher yield to gas than bare Co_3O_4, especially due to the increase on LG yield. A similar trend was obtained in glycerol APR and was ascribed to the fewer metallic sites on the bare Co_3O_4 (see Chapter 3). This increase was done at the expense of HO, which yield decreased from 43.9% to 13.5% when passing from bare Co_3O_4 to 0.625CoAl. The MF yield also decreased considerably for xCoAl catalysts as compared to bare Co_3O_4. A remarkable boost in yield to liquid was observed for bimetallic 0.3Pt/CoAl catalysts if compared to its

counterpart 0.625CoAl. This was held by the HO yield boost after addition of Pt. Thus, HO yield boosted from 11.5% for 0.625CoAl to around 40% for both bimetallic Pt-Co catalysts. The highest number of metallic centres of this catalyst, with high dehydrogenation activity (Table 8.1) could support the above result, as they promote retro-aldol condensation route (Scheme 8.1). For this sample, MF yield, however, remained at the same values than their counterpart. This fact dropped the yield to gas for xPt/CoAl catalysts, especially LG yield. To finish with this first approach, monometallic 0.3Pt/Al catalyst showed the highest yield to liquid (88%), which was sustained on 59% HO and 29% MF. If we dissect these large categories, all Co-containing catalysts presented highest selectivity to C_2-C_4 HO compounds and for MFs, the lightest compounds (C_1-C_4) were also those that presented the highest proportion. Instead, bare 0.3 Pt/Al catalyst exhibited higher yield of C_{5+} liquid compounds (primary dehydration products) because of its higher acid/basic sites density ratio, with moderate activity of Brønsted sites, which are preferred for catalyzing dehydration reactions [364].

Regarding the carbon selectivity for gaseous products, they were divided into three groups (Table 8.4): C_1, C_2-C_4, and C_{5+}. No gaseous products with more than 6 carbon atoms were obtained for any of the catalysts, indicating low C-C coupling activity. Except for bare Co_3O_4 catalyst, for the rest of the catalysts the selectivity decreased as: $S_{C1} \gg S_{C5+} > S_{C2-C4}$. Gas phase C_1 compounds were formed by methane and CO_2, since CO has not been detected. This indicated the high WGS activity of our catalysts, even operating under high P_{H2}. For Co_3O_4, however, $S_{C5+} > S_{C1}$. None of the catalysts achieved selectivity to C_2-C_4 gas products higher than 10%.

To further discuss the results obtained, we will adopt the reaction scheme (

Scheme 8.1. Generalised pathways for aqueous-phase transformation of sorbitol taken from Eagan et al. (2017) [343].

) proposed by Huber et al. for sorbitol HDO [343]. Some authors have found furanic intermediates (2,5-dimethylfuran) for Ru-based catalysts [365]. 2,5-dimethylfuran was not detected for any of our catalysts in the liquid product, which suggested this route was inhibited for our catalysts.

To briefly sum up the sorbitol HDO routes, sorbitol could be dehydrated (via acid catalysis) to form sorbitan by cyclization, isosorbide and other C_{5+} compounds (accounted as HO) and then undergo successive dehydration/hydrogenation reactions to produce C_{5+} MF compounds and subsequently, HG compounds. Retro-aldol condensation route, however, can occur on metallic sites under basic conditions [92] and leads to the formation of lighter HO compounds (glycerol, propylene glycol). These compounds can also undergo further HDO reactions to yield MFs and C_2-C_4 alkanes. Both routes can produce, via decarbonylation or decarboxylation, shorter compounds, and the formation of CO_2 and/or CH_4 either by WGS or by methanation. It is obvious that the products depend on the relative rates of C-C vs. C-O bond cleavage (in metallic and acid sites, respectively). Low C-C cleavage rate and high C-O cleavage rate led to larger alkanes or oxygenates.
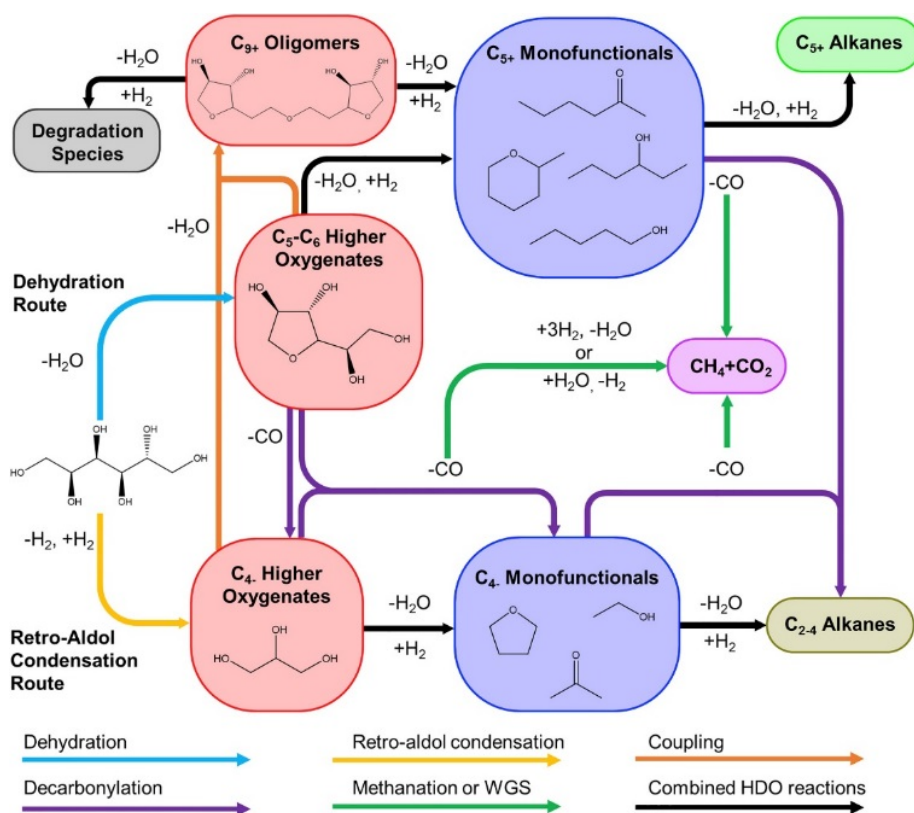

Scheme 8.1. Generalised pathways for aqueous-phase transformation of sorbitol taken from Eagan et al. (2017) [343].

To better elucidate the pathway favoured by each of our catalyst, Figure 8.6.A displays the yields of the early products (sorbitan and isosorbide) and final product (hexane), as key compounds for the dehydration route, whereas Figure 8.6.B presents the yield of C_2-C_3 HO compounds, mainly obtained by retro-aldol condensation route (ethylene glycol, propylene glycol, hydroxyacetone and glycerol). It should be indicated that tetrahydrofuran- and tetrahydropyran-like products were also detected, but for the sake of simplicity, discussion focused on the above mentioned products. It must be noted that retro-aldol condensation plays a critical role in reducing the carbon number of the products. Among the early C_6 intermediate oxygenates, sorbitan was observed only for bare Co_3O_4 (at 4.9% yield) and monometallic 0.3Pt/Al (at 9.0% yield) catalysts. These results were related to the lowest surface acid site density of these catalysts (0.06 and 0.34 $\mu mol_{NH3} \cdot m^{-2}$ for Co_3O_4 and 0.3Pt/Al, respectively, in contrast to averaged 0.65 $\mu mol_{NH3} \cdot m^{-2}$ for the other catalysts) (Table 8.4), which limited the purely acidic-catalysed reaction route. The bimetallic 0.3Pt/CoAl showed a marginal 0.3% yield of sorbitan, showing similar yields of isosorbide than 0.625CoAl. Thus, the ability of 0.3Pt/CoAl to produce sorbitan could be considered as not significant, given the analytical error. Isosorbide, instead, was detected for all catalysts, with a maximum yield of 5.8% for 1Pt/CoAl (not shown). It is interesting to note that the catalysts with which sorbitan was observed had a lower yield of isosorbide. For all catalysts, hexane yield was quite low ($Y_{hexane} < 1\%$), which might be related to the low reactivity of isosorbide, unfavourable for obtaining C_6 alkanes [366].

Among C_2-C_3 HO compounds displayed in Figure 8.6.B, propylene glycol was the most relevant in quantitative terms. Together with glycerol, which yielded between 0.5-5.5%, they were the primary products from retro-aldol route. The highest yield for these products was for 0.3Pt/CoAl catalyst, as this was due to its higher metal content (of high cyclohexane dehydrogenation activity) and lower surface acid/basic sites density ratio. For all catalysts, the higher yield of propylene glycol rather than glycerol is indicative that glycerol underwent into ethylene glycol, hydroxyacetone and, in turn, more propylene glycol. Assuming glycerol was the only precursor for ethylene glycol and hydroxyacetone (other possible precursors were at very low yields), the yields ratio ethylene glycol/hydroxyacetone might be an indicator of C-C/C-O scission activity. In short, due to the predominance of surface basic sites, our Co-containing catalysts

promoted the retro-aldol condensation route for sorbitol HDO. Apart from the above discussed products, other compounds obtained at significant amount in the liquid phase were (in decreasing yield order): methanol, tetrahydrofuran-2-methanol, 2-methyltetrahydrofuran, 1,2-butanediol, tetrahydropyran-2-methanol, xylitol, erythritol, 2-propanol, and 2-butanol.
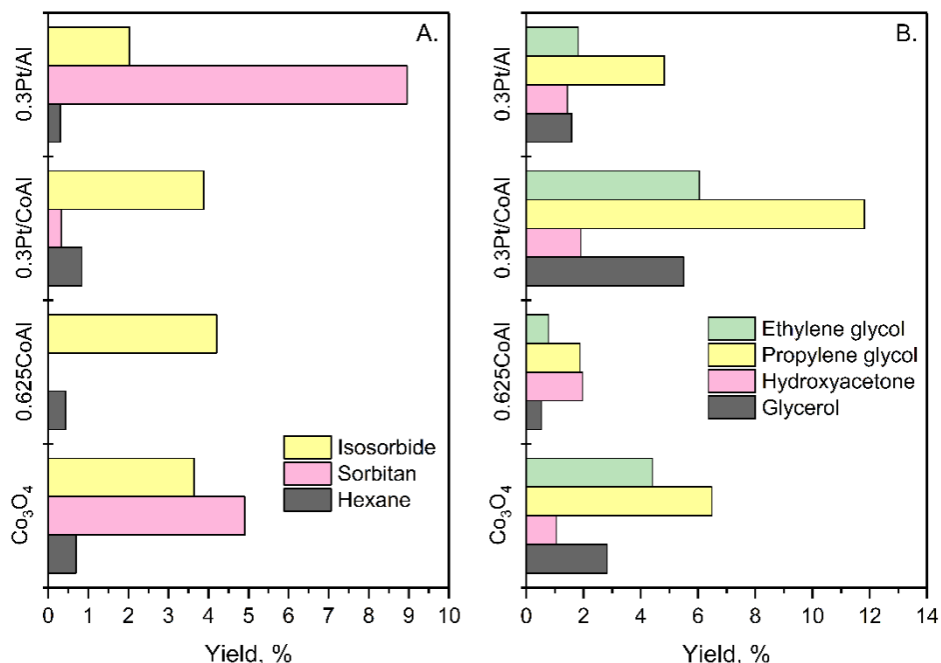
Figure 8.6. Product yield for sorbitol HDO: (A) products of dehydration pathway and (B) main retro-aldol condensation products.

Regarding the carbon selectivity for liquid products (Table 8.4), the high carbon selectivity to C_{5+} of 0.3Pt/Al catalyst (MF+HO: 78%) was noticeable, owing to its higher acid character (acid/basic sites density ratio = 1.06, vs 0.03-0.48 for the other catalyst) with very active Brønsted acid sites, which promoted C-O cleavage [362]. Catalysts 0.625CoAl and 0.3Pt/CoAl, both with a large number of metallic centres, showed the lowest carbon selectivity for C_{5+} liquid products (MF+HO: 33-34%).

Table 8.4. Carbon distribution in the liquid and gas phases at 70-90% (HDO) and at 40-57% (APR) of sorbitol conversion for the assayed catalysts. Reaction conditions: 10 g of sorbitol, 150 cm^3 of water, 1 g of catalyst, 240 °C, 60 bar.

	Sample	Time, h	X_{sorb}, %	X_{gas}, %	Identification ratio[a]	Carbon selectivity for gaseous products			Carbon selectivity for liquid products			
						C_1	C_2-C_4	C_{5+}	C_1-C_4	C_{5+} MF	C_1-C_4 HO	C_{5+} HO
HDO process	Co_3O_4	4	86.4	17.3	0.99	35.6	4.4	60.0	41.4	23.4	16.3	18.9
	0.625CoAl	2	78.0	13.7	1.07	64.2	9.3	26.5	57.5	18.4	10.1	14.0
	0.3Pt/CoAl	2	88.4	21.8	1.09	70.1	3.7	26.2	31.1	17.1	35.0	16.8
	0.3Pt/Al	8	70.3	35.2	1.12	51.8	8.4	39.8	1.1	32.1	21.2	45.6
APR process	Co_3O_4	4	43.2	12.6	0.86	70.3	14.6	15.1	59.6	14.8	5.3	20.3
	0.625CoAl	4	40.9	15.6	0.87	58.3	5.3	36.4	83.9	0.00	11.5	4.6
	0.3Pt/CoAl	2	57.4	18.9	0.87	73.5	4.2	22.3	43.9	27.1	11.3	17.7
	0.3Pt/Al	4	45.3	8.03	0.86	56.5	9.9	33.6	5.0	43.2	9.6	42.2

[a] *identification ratio= Σ(carbon concentration in each identified compound) / $n_C^{t=0}$*

8.5   SORBITOL APR

Sorbitol transformation tests under inert atmosphere were carried out at 240 °C and under 60 bar of N_2. In this case, the hydrogen needed for hydrogenation of the intermediate oxygenates must be produced *in situ*. Under these conditions, in addition to the compounds analysed in the previous section, hydrogen can be obtained in the outlet stream. Regardless of the results sought, given the conditions under which they are carried out (inert atmosphere), these experiments have been called sorbitol APR. In this section, the activity results obtained for a sort of catalysts on sorbitol APR carried out in a batch reactor will be discussed. As in sorbitol HDO, the absence of any mass transfer limitations was confirmed (Appendix, Section A).
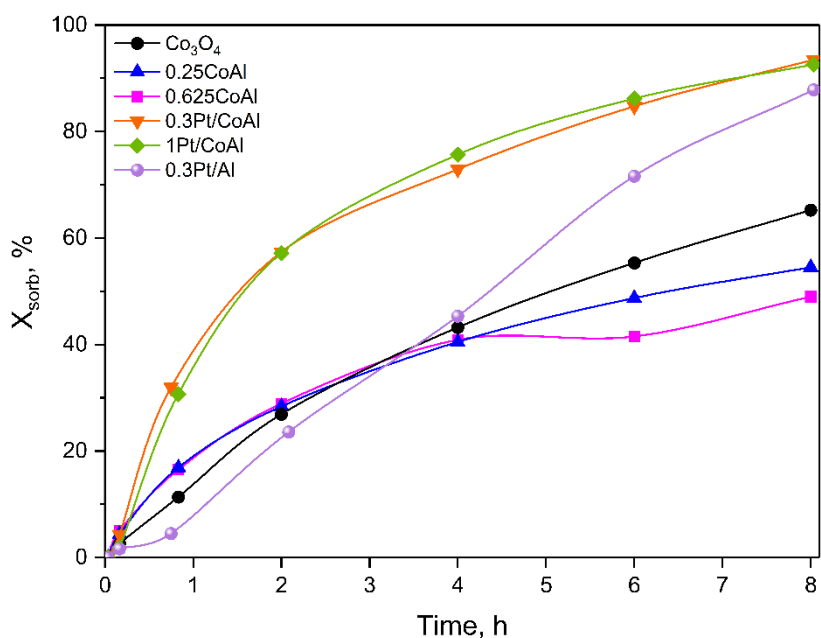
Figure 8.7. Sorbitol conversion as a function of reaction time for all the catalysts. Reaction conditions: 10 g of sorbitol, 150 cm³ of water, 1 g of catalyst, P_{N2} = 60 bar, T = 240 °C.

Figure 8.7 depicts sorbitol conversion as a function of reaction time. Similarly, HDO, 0.3Pt/Al showed zero-order kinetics, and positive reaction order with respect to sorbitol concentration was deduced for the other catalysts. The

apparent kinetic constants calculated by assuming first-order kinetics are given in Figure C.2 from Appendix. For sorbitol transformation, under HDO conditions, apparent kinetic constant values were higher than under APR. Unlike in sorbitol HDO, none of the studied catalyst reached the complete sorbitol conversion in 8 h of reaction. The first conclusion was that catalysts activity in APR was much lower than in HDO, except for catalyst 0.3Pt/Al. For this catalyst, at 8 h reaction, X_{sorb} was 88%, when it was 70% during HDO, ascribed to the lessening of Pt sites blockage by H_2. It is clear that under N_2 pressure (APR), the available H_2 formed by sorbitol reforming was much lower than that under H_2 pressure (HDO), therefore lowering the sorbitol conversion.
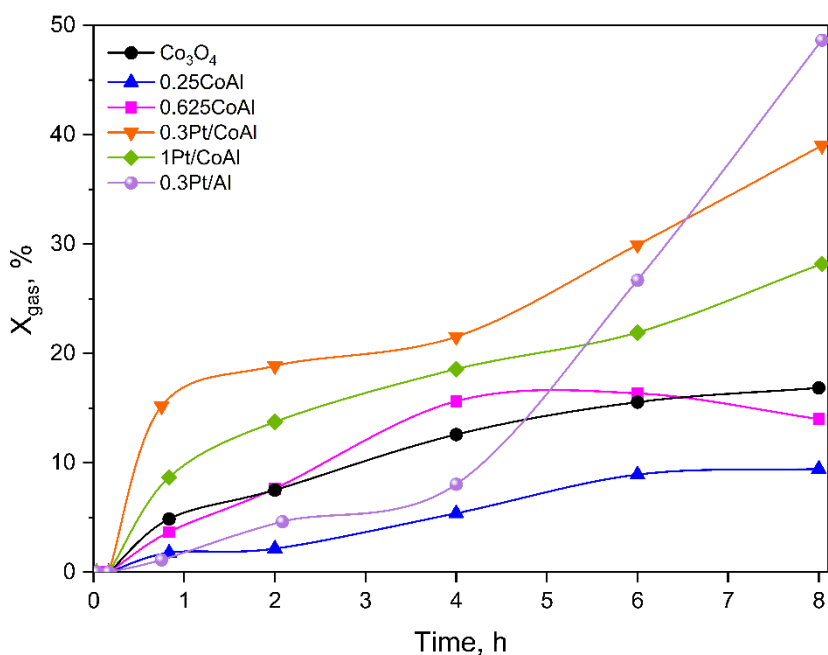
Figure 8.8. Carbon conversion to gas as a function of reaction time for all the catalysts. Reaction conditions: 10 g of sorbitol, 150 cm³ of water, 1 g of catalyst, P_{N2} = 60 bar, T = 240 °C.

Carbon conversion to gas (Figure 8.8) was also lower at APR conditions than that at HDO conditions for the majority of the catalysts. Only 0.3Pt/Al and 0.3Pt/CoAl catalysts improved X_{gas} values, showing the former catalyst the highest value (48.6%) at 8 h reaction. Noteworthy for 0.3Pt/Al catalyst, X_{gas} evolution with reaction time followed a very similar pattern in APR and HDO,

X_{gas} smoothly increasing in the first hours of reaction to boost at 4 h (for APR) and 6 h (for HDO).

By far, bimetallic Pt-Co catalysts (0.3Pt/CoAl and 1Pt/CoAl) were the most active for sorbitol transformation under inert atmosphere (Figure 8.8). Moreover, the sorbitol conversion curves for both catalysts overlapped throughout the reaction time. The maximum conversion achieved was 93.5% for 1Pt/CoAl and 92.6% for 0.3Pt/CoAl at 8 h of reaction. On the contrary, monometallic xCoAl and bare Co_3O_4 were the less active (sorbitol conversions of 65%, 54.5% and 49.0% for Co_3O_4, 0.25CoAl and 0.625CoAl, respectively).
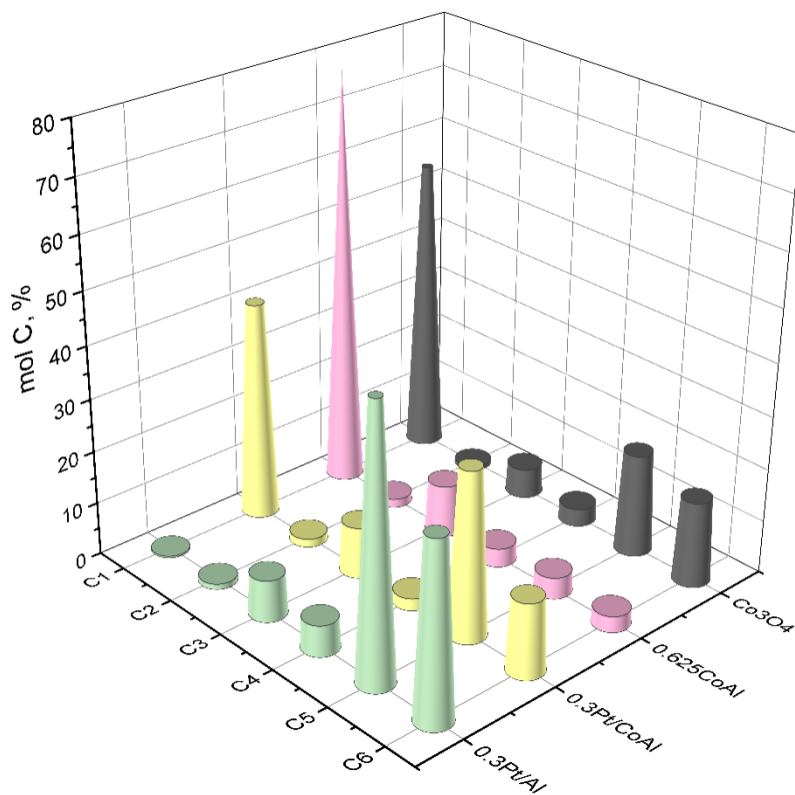
Figure 8.9. Yield of organic compounds as a function of carbon atoms number in the molecules during sorbitol APR.

In line with their higher sorbitol conversion activity, bimetallic 0.3Pt/CoAl and 1Pt/CoAl were those which achieved the highest X_{gas} among the cobalt-

containing catalysts, showing 0.3Pt/CoAl significantly higher X_{gas} (39% vs 28%). As can be seen in Figure 8.8, carbon conversion to gas for monometallic cobalt catalysts was less than 17%.

The yield of organic compounds during sorbitol APR, categorized by number of carbon atoms is shown in Figure 8.9 and exposed slight differences between cobalt-containing catalysts. While bare Co_3O_4 catalyst showed a high yield for the C_1, C_5 and C_6 compounds (55, 19 and 16%, respectively), catalyst 0.625CoAl showed a lower yield towards C_5-C_6 products (3-4%), boosting the production of C_1-C_3 compounds. For its part, bare 0.3Pt/Al showed the highest yield to C_5 products and almost zero yield (0.3%) to C_1 compounds. This low activity of Pt-catalysts for the production of compounds with such a short chain was also noted for 0.3Pt/CoAl catalyst (41%, instead of 78% for its counterpart 0.625CoAl).
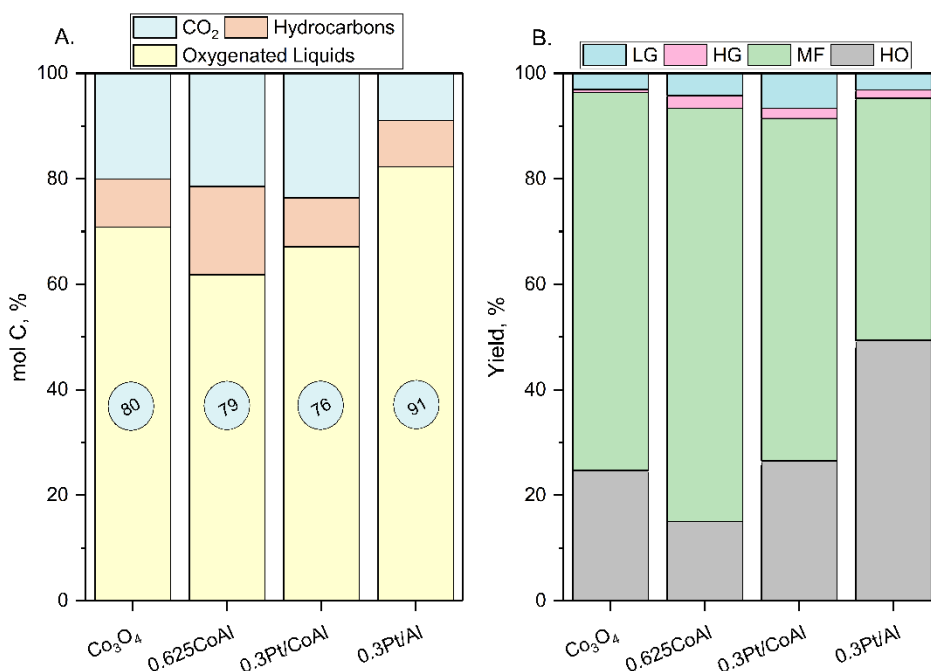
Figure 8.10. Catalytic results showed for sorbitol APR at 40-57% of sorbitol conversion under N_2 atmosphere: (A) Carbon global distribution and (B) yield of products by categories.

The carbon global distribution for each catalysts is shown in Figure 8.10.A for a sorbitol isoconversion (between 40-57%) corresponding to 2 h of reaction for

0.3Pt/CoAl catalyst and 4 h for the rest of the catalysts. Under inert atmosphere, the vast majority of carbon was as Oxygenated liquids, for all the catalysts. At this conversion range, CO_2 (final reforming product) contribution to carbon content in the gas phase predominated over hydrocarbons, except for 0.3Pt/Al catalyst, for which similar carbon was converted to CO_2 and to Hydrocarbon. Catalysts xPt/CoAl were the most active in CO_2 production (0.3Pt/CoAl = 23.6% and 1Pt/CoAl = 17%, as percentage of the converted C) followed by 0.625CoAl (21.5%). As a general trend, higher Oxygenated liquids/Hydrocarbons ratio was obtained in APR conditions (between 1.5 and 3 times higher). Regarding atom economy of carbon, for cobalt-containing catalyst it varied in the 76-91% range, which was notably lower than that obtained at HDO conditions (7-22% lower). The unique exception was 0.3Pt/Al, which had 91% atom economy (15% higher than in HDO).

CO_2 and CH_4 (LG) were the main gases obtained, displaying a joint yield between 3-6%, while HG yield did not exceed 2.5% (Figure 8.10.B). Given carbon selectivity for gaseous products (Table 8.4) it can be asserted that there has been a high C-C bond cleavage activity (C_1 = 56.5-73.5%) for all catalysts. Among liquid compounds, MFs were the most predominant, obtaining an even higher yield than in the reactions carried out under H_2 pressure. Cobalt-containing catalysts were more selective towards C_1-C_4 compounds, which indicates that these catalysts, regardless of the reaction atmosphere, initially favoured retro-aldol reaction route and subsequently, dehydration and hydrogenation reactions took place. It is worth noting that catalysts xPt/CoAl exhibited higher selectivity to C_{5+} HO than C_2-C_4 HO. These results suggest that, under N_2 pressure, dehydration route was more active although it was not dominant.

Figure 8.11 displays the yield of some selected products. Both isosorbide and sorbitan were detected for practically all catalysts (sorbitan was not observed for catalyst 0.625CoAl). Isosorbide yield was very similar for all catalysts (ranging from 1.6% to 2.2% for 0.625CoAl and 0.3Pt/CoAl, respectively). None of the catalysts exhibited good performance for hexane production (Y_{hexane} ranged from 0.2-0.4%). Better results were obtained for H_2 production with catalyst 0.3Pt/CoAl as leader with Y_{H2} = 15%. Catalysts classification based on hydrogen yield would be as follows: 0.3Pt/CoAl $\gg$ 0.3Pt/Al $\approx$ 0.625CoAl $\approx$ Co_3O_4. These

data are consistent with the good performance of these catalysts for obtaining H_2 by glycerol reforming (Chapter 5).
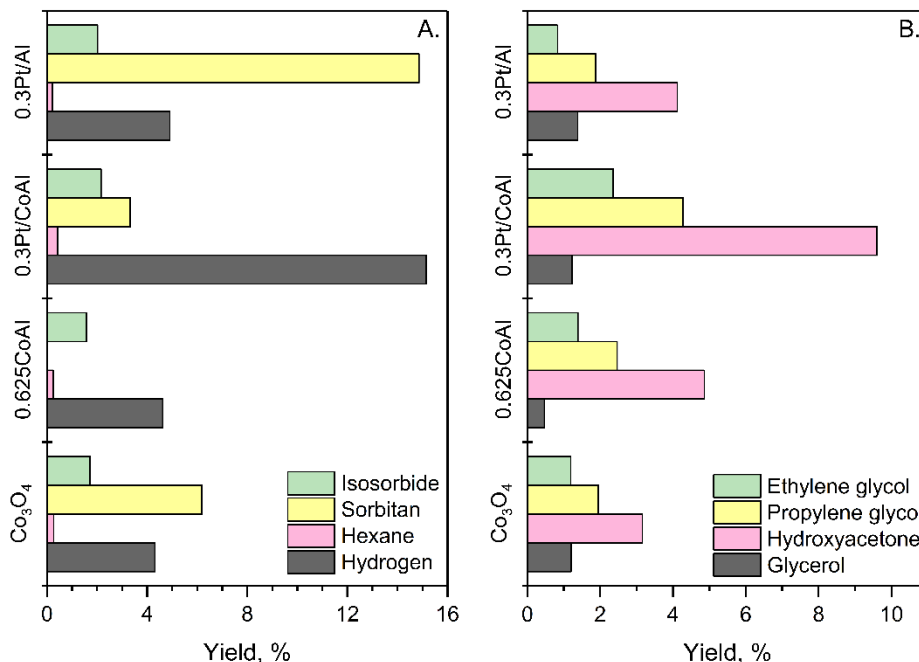
Figure 8.11. Product yield for sorbitol APR: (A) isosorbide, sorbitan, hexane and hydrogen (B) main C_2-C_3 liquid products.

8.6   HDO vs APR OVER 0.3Pt/CoAl CATALYST

The performance of catalyst 0.3Pt/CoAl for sorbitol transformation under H_2 and N_2 atmosphere has been compared at isoconversion conditions. More in detail, the data taken from HDO process has been a 2 h reaction equivalent to X_{sorb} of 88.4% and 21.8% of X_{gas}. Similar conversions (X_{sorb} = 86.7%, X_{gas} = 29.9%) were obtained after 6 h for APR process. Due to the difference of 4 h in the duration of the reaction, catalyst would deactivate at different extent.
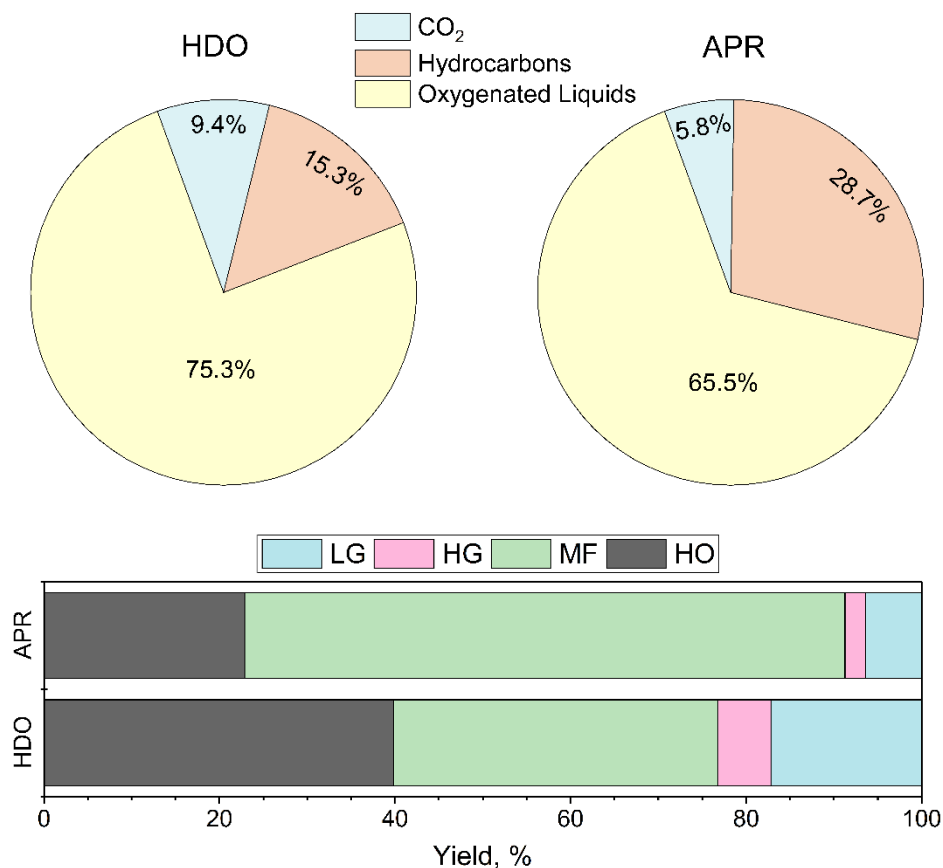
Figure 8.12. Comparative of carbon global distribution (pie chart) and yield of categories of products (stacked bar graph).

As can be seen in Figure 8.12, carrying out the reaction under inert atmosphere (APR) led to a higher proportion of hydrocarbons, thus reducing the conversion to oxygenated liquid products. The variation in CO_2 production was only 3.2%, considered a non-significant dissimilarity. Concerning yield by categories, APR process generated more MF products in contrast to the high HO yield observed in HDO reaction. These manifest differences show that the absence of an external source of hydrogen limits dehydration-hydrogenation reactions. Therefore, in an inert atmosphere and with the high metallic availability of this catalyst, the cleavage of the C-C bond by retro-aldol reaction was favoured.
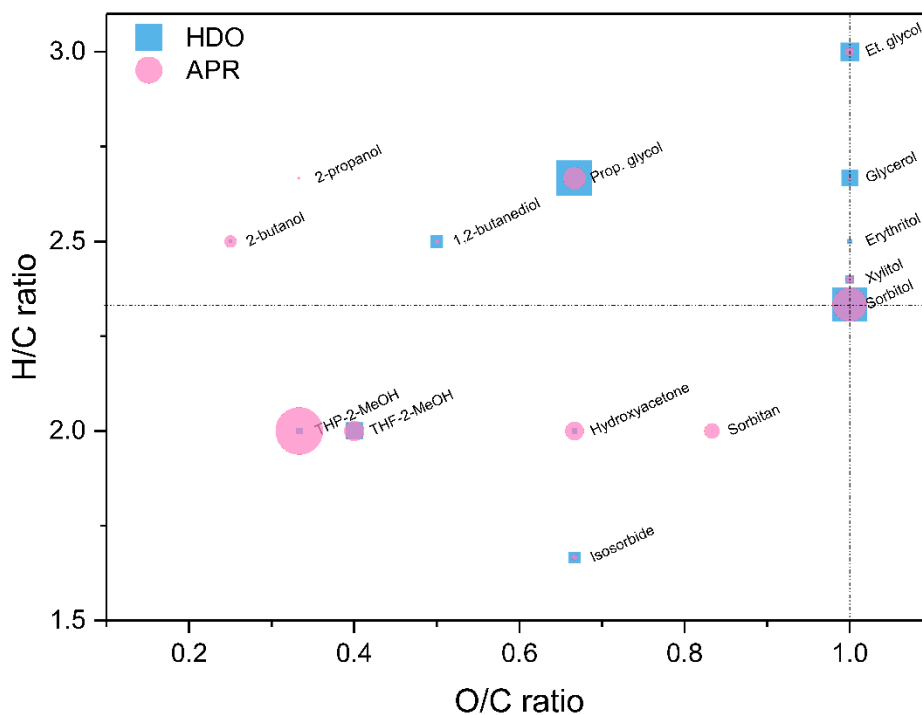
Figure 8.13. Graphical representation (H/C vs. O/C atomic ratio) of liquid products obtained during sorbitol transformation (HDO vs APR) over 0.3Pt/CoAl.

Figure 8.13 displays a graphical representation in the style of the van Krevelen diagram of the liquid products obtained in both processes. Sorbitol HDO over 0.3Pt/CoAl catalyst yielded more hydrogenated liquids (higher H/C ratio) than sorbitol APR, which resulted in a higher yield towards liquids with low H/C and O/C ratio. Other authors, through theoretical studies, have concluded that more hydrogenated intermediates are expected when C-O bond cleavage reactions take place [367]. Instead, the high occurrence of C-C bonds scission in our catalytic system may be associated with decarbonylation, which subsequently produces CO_2 and CH_4, and deoxygenation reactions [343]. Thus, catalytic behaviour observed in sorbitol APR would be explained.

8.7   CHARACTERIZATION OF SPENT CATALYSTS

After catalytic tests, catalysts were characterised by nitrogen adsorption-desorption isotherms, XRD, H_2-TPR and TPH in order to gain

knowledge into the textural and structural modifications and carbon deposition. The results of these characterizations showed similar trends regardless of the type of process performed, so they will be discussed conjointly.
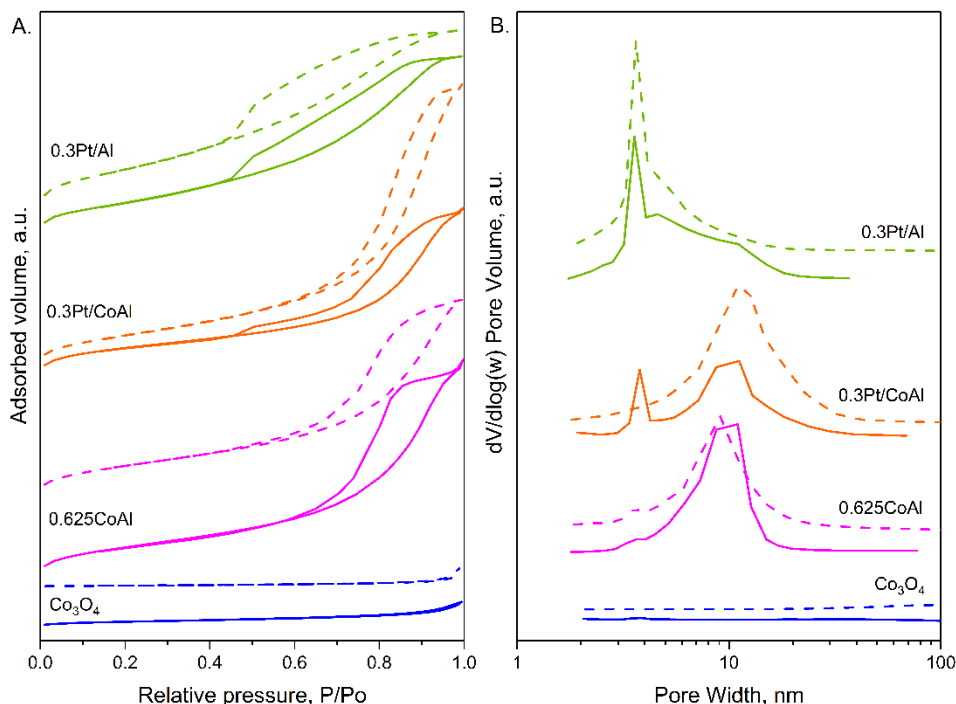
Figure 8.14. Nitrogen adsorption-desorption isotherms (A) and pore size distribution (B) of the samples after sorbitol HDO (solid lines) and APR (dashed lines) reaction.

Figure 8.14 depicts the nitrogen adsorption-desorption isotherms and pore size distribution while Table 8.5 summarises the textural properties of selected spent catalysts. Catalyst Co_3O_4 suffered a strong increase in surface area (from 7.4 to 21.0 $m^2 \cdot g^{-1}$) and a visible decrease in average pore size. For xCoAl catalysts, increase in S_{BET} was less acute as the Co/Al ratio increased. This phenomenon, involving γ-alumina hydration, was previously explained in Chapter 3. Pt-containing catalysts also showed a 10-20% increase in S_{BET}. Conversely, S_{BET} for 0.3CeCoAl decreased from 138.3 to 102.2 $m^2 \cdot g^{-1}$ (Appendix, Table C.2) Average pore size and pore volume decreased for all cobalt aluminate based-catalysts (Pt- and Ce-modified as well). These textural modifications may be due to the increased amount of carbon deposits on the catalyst surface, as will be discussed below.
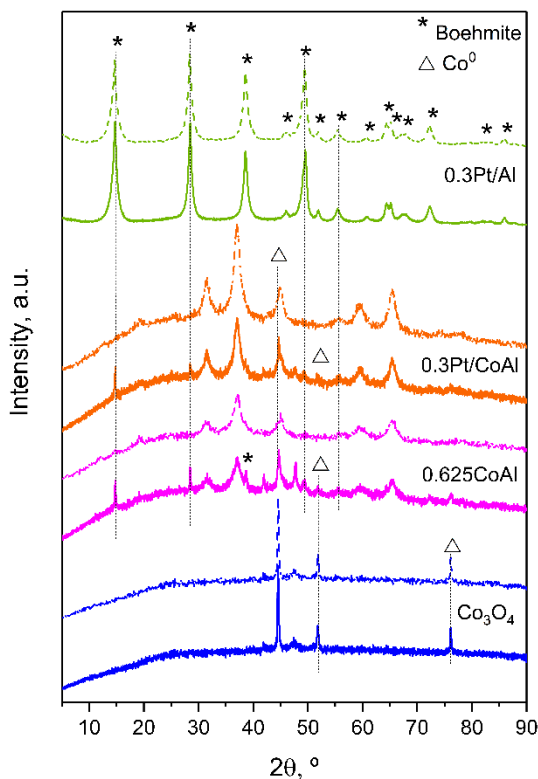
Figure 8.15. XRD patterns of catalysts used in sorbitol HDO (solid lines) and APR (dashed lines).

XRD diffractogram of used catalysts are plotted in Figure 8.15. As could be seen, well-defined metallic cobalt (PDF 015-0806) peaks were still visible in spent catalyst Co_3O_4. Although much weaker, those peaks were also detected in the other cobalt-based catalysts. No peaks of platinum or cerium related species were observed. All samples, whether used in HDO or APR reaction, preserved their characteristic wide peaks from cobalt spinel as in the freshly reduced samples. Sample 0.3Pt/Al exhibited only peaks corresponding to boehmite (PDF 21-1307). Boehmite formation occurred largely for samples with lower cobalt content and for samples 0.625CoAl and 0.3Pt/CoAl, and this phenomenon was more evident after HDO reactions.
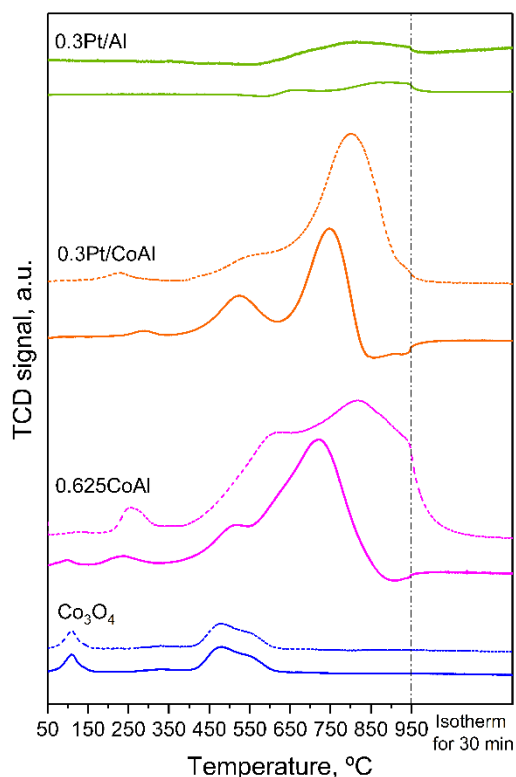
Figure 8.16. H₂-TPR profiles of catalysts after reaction under H₂ atmosphere (solid lines) and N₂ atmosphere (dashed lines).

Figure 8.16 shows the H₂-TPR profiles of the spent catalysts after sorbitol HDO. The reduction profiles clearly showed H₂ consumption at below 600 °C (which was the activation –reduction– temperature of fresh catalysts) for all Co-containing catalysts. However, quantified hydrogen consumption data listed in Table 8.5 were low and very close to the hydrogen required to reduce the cobalt ions as $CoAl_2O_4$ phase (which were not reduced in the activation protocol, as seen in Chapter 3). Furthermore, it must be stressed that a portion of the hydrogen was consumed in the hydrogenation of carbonaceous material. Therefore, the cobalt re-oxidation phenomenon could be considered as insignificant under these conditions. It should be taken into consideration that HDO was carried out under hydrogen gas, which would have been able to preserve the majority of cobalt surface in metallic state.

Carbonaceous deposits measured by TPH (Table 8.5) were quite conclusive, since they presented a relation with the type of catalyst and reaction conditions. The highest carbon deposits, for both HDO and APR reactions, was for Co_3O_4 catalyst, which was characterized by its large Brønsted acidity, favouring dehydration reactions to form coke precursors. 0.3Pt/Al was the catalyst with less coke deposits, and among cobalt-containing catalysts, bimetallic 0.3Pt/CoAl presented slightly less coke than its counterpart 0.625CoAl. This brought out the favourable effect of the noble metal, on which hydrogen dissociated and by spilt over carbon to hydrogenate it [368]. Regarding   reaction conditions, slightly less carbon deposited in HDO. Surprisingly, catalyst 0.3CeCoAl exhibited the highest amount of carbonaceous deposits, with around 97.8 $\mu mol_C \cdot g_{cat}^{-1}$, but a considerably low value in percentage terms (0.12% C). The beneficial effect of cerium against carbon deposits, usually reported for hydrocarbon steam reforming, is related to its high ability to store and release oxygen that could promote the carbon gasification [369]. This required surface ceria in close proximity to carbon deposits, which was not the case for our Ce-containing catalysts, as Ce remained at the lattice. The mild operation temperature, also, attenuated the gasification capacity. In spite of the high hydrogen pressure used (which minimized the carbon deposition) carbon deposits obtained was high, in the range 20.9-97.8 $\mu mol_C \cdot g_{cat}^{-1}$. These values were considerably higher than those obtained in glycerol APR (fixed-bed reactor).

Liquid collected at the end of the reaction showed a slight pink colour, pointing to the presence of dissolved cobalt. Leaching is a phenomenon that constraints cobalt-based catalysts behaviour in liquid-phase reactions. Nevertheless, tests carried out in batch reactors show the peculiarity that the leached species remain in the reaction medium and could continue to be an active part of the process (through homogeneous catalysis) [277]. Thus, quantification of the leached metals does not resolve the uncertainty about the role of this phenomenon in catalytic activity.

Table 8.5. Summary of nitrogen adsorption-desorption, H_2-TPR and TPH results of spent catalysts.

Catalysts	After HDO process					After APR process				
	S_{BET}, $m^2 \cdot g^{-1}$	V_P, $cm^3 \cdot g^{-1}$	d_P, nm	H_2 uptake, $mmol_{H2} \cdot g^{-1}$	$C_{deposits}$, $\mu mol_C \cdot g_{cat}^{-1}$	S_{BET}, $m^2 \cdot g^{-1}$	V_P, $cm^3 \cdot g^{-1}$	d_P, nm	H_2 uptake, $mmol_{H2} \cdot g^{-1}$	$C_{deposits}$, $\mu mol_C \cdot g_{cat}^{-1}$
Co_3O_4	21.0	0.036	7.8	0.26	62.3	22.3	0.047	8.4	0.30	65.4
0.625CoAl	127.2	0.303	8.0	1.78	39.1	132.3	0.289	7.3	3.42	40.4
0.3Pt/CoAl	151.8	0.396	8.5	1.09	29.5	143.8	0.411	9.2	1.88	31.6
0.3Pt/Al	153.7	0.272	5.1	0.24	20.3	199.2	0.287	4.3	0.16	27.1

8.8 GLOBAL VISION AND SUMMARY

Aqueous-phase sorbitol transformation was carried out in a batch reactor, at 240 °C and 60 bar, under H_2 and N_2 atmosphere. Based on their composition, tested catalysts can be arranged into three groups: bare cobalt spinel (0.25CoAl, 0.5CoAl, 0.625CoAl and Co_3O_4), Ce-modified (0.3CeCoAl) and Pt-impregnated (0.3Pt/CoAl, 1Pt/CoAl and 0.3Pt/Al) catalysts.

For sorbitol transformation under H_2 atmosphere, bare cobalt spinel catalysts exhibited a high sorbitol conversion and a moderate carbon conversion to gas. For gaseous products, Co_3O_4 showed greater selectivity to C_{5+} compounds, while xCoAl catalysts favoured CO_2 and CH_4 production. Catalyst 0.3CeCoAl did not show remarkable results, confirming that Ce-modification was not beneficial for obtaining hydrocarbons and did not enhance value-added liquid compounds yield. Meanwhile, Pt-modification improved yield of C_{5+} hydrocarbons (HG).

Overall, sorbitol conversion was lower under N_2 pressurisation. H_2 and CO_2 production acquired relevance. In the absence of H_2 supply, hydrogenation reactions occurred but to a substantially lesser degree. For instance, a lower yield of propylene glycol and ethylene glycol in favour of hydroxyacetone. As was expected, Pt-containing catalysts exhibited the most outstanding results.

In closing, it can be asserted that regardless of the pressurizing gas, the prepared cobalt spinel-based catalysts favoured an initial retro-aldol condensation pathway due to their high metal availability and their predominantly basic sites.

All the catalysts, regardless of the reaction atmosphere, underwent significant textural changes. Regarding phenomena that can lead to deactivation, H_2 consumption calculated from TPR profiles dismissed re-oxidation of any sample. Although carbonaceous material was detected in the samples, its quantification did not exceed 0.12% C. The transformation of γ-alumina to boehmite was corroborated by XRD. This phase change was more pronounced for samples 0.25CoAl and 0.3Pt/Al (higher proportion of aluminium than other metals). It can be concluded that the nature of the atmosphere did not alter the catalysts in a different manner in terms of textural properties, re-oxidation, or coke formation.

Chapter 9

CONCLUSIONS AND SUGGESTIONS

9. CONCLUSIONS AND SUGGESTIONS

9.1 CONCLUSIONS

The development and optimization of processes for the valorisation of biomass-derived compounds plays a pivotal role in the transition towards sustainable energy. From this perspective, this Doctoral Thesis seeks to expand the knowledge about aqueous-phase reforming (APR) process and, at the same time, make a contribution to the circular bioeconomy. In summary and more specifically, the results obtained in this research support the viability of cobalt aluminate based-catalysts for glycerol reforming to produce renewable hydrogen.

To recap, xCoAl catalysts calcined at 500 °C and reduced at 600 °C showed good performance for glycerol APR. Catalytic activity has been related to the considerable surface area, the remarkably small Co^0 particle size and the high metal availability exhibited by these catalysts. Therefore, the best results were obtained with 0.625CoAl sample (higher Co/Al ratio). In long-term reactions, deactivation attributed to sintering and re-oxidation of the active phase and to the leaching of nanoparticles of Co has been noted.

Two main reaction pathways were described: on the one hand, dehydrogenation to glyceraldehyde, promoted by metallic sites, which undergoes C-C scission and subsequently WGS reaction; and on the other hand, dehydration of terminal hydroxyl groups, and succeeding hydrogenation to yield compounds of the carbonyl group (aldehydes and ketones).

Ce-doped by coprecipitation, compared to the starting catalyst 0.625CoAl, subtly improved the selectivity to both hydrogen and alkane. However, it presented inferior results in terms of glycerol conversion, carbon conversion to gas and greater deactivation. The nature of Ce-Co interaction induced the formation of Ce_5Co_{19}-type structure, which could have resulted in lower metal availability, essential for active catalytic activity in glycerol APR. Regarding deactivation, Ce-modification did not reduce re-oxidation phenomenon and the subsequent leaching of the active phase.

Pt-Co bimetallic catalysts demonstrated not only a high activity for glycerol reforming but also proved to be stable during reactions of more than 100 h TOS. Despite the observed increase in methane production when Pt-impregnated 0.625CoAl sample, these catalysts continued to present a high hydrogen yield. Pt-containing catalysts exhibited a lower decrease of metallic surface-active phase and lower amount of carbonaceous material deposits.

Catalytic results of WGS and hydrogenation of CO experiments in liquid phase shed light on methane formation during APR reaction. Since independently of the high availability of hydrogen, Pt-Co bimetallic catalysts were less selective to CO hydrogenation, it can be deduced that methane formation proceeds by decarbonylation.

The effect of the reaction conditions on the behaviour of 0.3Pt/CoAl catalyst for glycerol APR can be summarized as:

- × Glycerol concentration: increasing glycerol content in the feed stream decreased H_2 yield. However, a concentration that provides a balance between high yield of the desired product and that make the process economically viable should be used.

- × Temperature/pressure: at higher temperatures, higher conversions. Furthermore, an increase in reaction temperature favoured the dehydrogenation route and, therefore, H_2 yield is enhanced.

- × Contact time: carbon conversion to gas and H_2 yield are favoured at high contact times (lower WHSV). Short contact times lowered C-C bond cleavage activity and yielded a high amount of liquid products.

- × Type of polyol fed: APR of short-chain compounds is simpler, fewer intermediates and side reactions. Short-chain compounds have a higher hydrogen-producing capacity than long-chain compounds.

Regarding crude bioglycerol processing, its high concentration of fatty acids, inorganic salts and ash could cause reactor clogging and other operational issues. Physico-chemical treatment (basification, neutralisation and filtration)

conducted reduced impurities, which allowed carrying out catalytic tests with said compound.

Catalytic tests showed that organic impurities (mainly methanol and acetic acid) derived from the production and treatment of bioglycerol favour H_2 production, since they are reformable short-chain compounds. In addition, it was found that higher glycerol conversion (longer contact time), improves gas production.

Cobalt-based catalysts showed versatility in aqueous-phase sorbitol transformation. Sorbitol transformation in batch reactor leads to the formation of several high added-value products. Among the catalysts tested, Pt-Co bimetallic samples presented the best performance. Regardless of the reaction atmosphere, our catalytic system favoured retro-aldol condensation reaction pathway, which occurs in metallic/basic sites. However, by not supplying hydrogen, dehydration-hydrogenation reaction was limited. In the same vein, sorbitol conversion was lower under APR conditions (inert atmosphere).

Post-reaction characterization confirmed that our catalysts presented deactivation phenomena similar to those already observed in glycerol APR such as γ-alumina hydration, cobalt re-oxidation and coke formation.

9.2   ISSUES AND CHALLENGES

In view of the results obtained, in this section some aspects to be explored and other topics that have been outside the scope of this work are mentioned.

- × This work has proved the technical feasibility of glycerol reforming as a promising platform compound stemming from biomass for the production of hydrogen. However, economic aspects must be studied.

- × From the same perspective, but analyzing a more technical aspect, the regenerability and recyclability of catalysts should be investigated, since this is a key factor for successful commercialization.

- × In order to further minimized deactivation phenomena other approaches such as strong metal-support interaction could be applied.

×   Regarding Ce-doped catalysts, it is clear that other preparation techniques should be used.

×   It would also be interesting to study the effect of co-feeding through reactor bed of an inert gas that helps to desorb the gas products.

×   A short-term task will be to carry out long-term reactions using treated bioglycerol.

×   Apropos of liquid-phase WGS, further research should focus on a detailed numerical analysis in order to gain further insight into the rate-determining step and the reaction mechanism and elucidate whether gas or liquid phase water molecules are involved in the reaction mechanism. The characterization of spent catalysts is another issue that should be well investigated to shed light on metal state and possible carbon species formation on the sample surface.

Chapter 10

NOMENCLATURE

10. NOMENCLATURE

Abbreviations and Acronyms

33DM1B	3,3-dimethyl-but-1-ene
3-HPA	3-hydroxypropionaldehyde
a.u.	Arbitrary units
AB_2O_4	Spinel general formula
Al_O, Al_T, Al_P	Aluminium in tetrahedral/octahedral/pentahedral coordination, respectively
APR	Aqueous-Phase Reforming
ATR	Autothermal Reforming
BE	Binding Energy
BET	Brunauer-Emmett-Teller
BJH	Barrett-Joyner-Halenda
CCS	Carbon Capture and Storage
$C_{deposits}$	Carbonaceous material deposits
CO-PrOx	Preferential CO Oxidation
CSTR	Continuous Stirred-Tank Reactor
CTH	Catalytic Transfer Hydrogenation Systems
DMFC	Direct Methanol Fuel Cell
DOE	Department of Energy of USA
DR	Dry reforming
ECH	Epichlorohydrin
EDX	Energy Dispersive X-Ray Spectroscopy
EELS	Electron Energy Loss Spectroscopy
EU	European Union

FAMES	Fatty Acid Methyl Ester
fcc	Face-Centered Cubic
FID	Flame Ionization Detector
FTIR	Fourier Transform Infrared Spectroscopy
FWHM	Full Width at Half Maximum
GC	Gas Chromatography
GHG	Greenhouse Gases
HAADF	High-Angle Annular Dark-Field imaging
hcp	Hexagonal Close Packed
HDO	Hydrodeoxygenation
HG	Hydrocarbons/Heavy Gas
HO	Higher Oxygenated liquid compounds
HPLC	High Performance Liquid Chromatography
IC	Inorganic Carbon
IC2MP	Institut de Chimie des Milieux et des Matériaux de l'Université de Poitiers
ICDD	International Centre for Diffraction Data
ICP-OES	Inductively Coupled Plasma Optical Emission Spectroscopy
IEA	International Energy Agency
isom	Isomerization
IUPAC	International Union of Pure and Applied Chemistry
KE	Kinetic Energy
LG	Light Gases
LHV	Lower Heating Value
LNG	Liquefied Natural Gas

MF	Monofunctional liquid compounds
MFC	Microbial Fuel Cell
MS	Mass Spectrometry
NDIR	Non-Dispersive Infrared
NG	Natural Gas
NMR	Nuclear Magnetic Resonance Spectroscopy
NOx	Nitrogen Oxides
O_{ads}	Adsorbed oxygen species
O_h	Octahedral site
O_{latt}	Surface lattice oxygen
PAFC	Phosphoric Acid Fuel Cell
PDF	Powder Diffraction File
PEMFC	Proton Exchange Membrane Fuel Cell
POx	Partial Oxidation
PtOx	Platinum oxide species
RI	Refractive Index detector
SAMCat	Equipe du Site Actif au Matériau Catalytique
SCW	Super Critical Water Reforming
SEM	Scanning Electron Microscopy
SGIker	Servicios Generales de Investigación/ Ikerkuntzarako Zerbitu Orokorrak
SiC	Silicon Carbide
SMR	Steam Reforming of Methane
SR	Steam Reforming
SSNMR	Solid State NMR
STEM	Scanning Transmission Electron Microscopy

TC	Total Carbon
TCD	Thermal Conductivity Detector
T$_d$	Tetrahedral site
TEM	Transmission Electron Microscopy
TGA	Thermogravimetric Analysis
TOC	Total Organic Carbon
TOF	Turnover Frequency
TOS	Time On Stream
TPD	Temperature Programmed Desorption
TPH	Temperature Programmed Hydrogenation
TPR	Temperature Programmed Reduction
TQSA	Tecnologías Químicas para la Sostenibilidad Ambiental
UPV/EHU	Universidad del País Vasco/Euskal Herriko Unibertsitatea
USDA	United States Department of Agriculture
UV-vis-NIR-DRS	Ultraviolet visible Near Infrared Diffuse Reflectance Spectroscopy
WDXRF	Wavelength Dispersive X-Ray Fluorescence
WGS	Water-Gas Shift
WHSV	Weight Hourly Space Velocity
XPS	X-ray Photoelectron Spectroscopy
XRD	X-ray powder Diffraction
μ-GC	Micro Gas Chromatography

Variables and physical constants

A	Proportionality constant (DRS spectroscopy)
a	Lattice parameter
A_{dehyd}	Specific activity of dehydrogenation
A_i	Peak area for each pulse
A_m	Cross sectional area of adsorbate
A_0	Peak area for non-adsorbed pulses
a_{spinel}	Spinel lattice parameter
$C_{G,s}$	Glycerol concentration at the catalyst surface
D	Interplanar spacing
d_{CHEM}	Average metal particle size determined from H_2 chemisorption
d_{Co}	Crystallite size of metallic cobalt
$d_{crystallite}$	Mean diameter of the crystalline domain
D_{G-W}, D_{S-W}	Diffusion coefficients
$D_{G-W,eff}, D_{S-W,eff}$	Effective diffusion coefficients
D_{Me}	Metal dispersion
d_P	Pore diameter
d_{spinel}	Crystallite size of the spinel
$< d_{TEM} >$	Average metal particle size (STEM images)
E_g	Band gap energy
F_{33DM1B}	Reactant flow of 33DM1B
F_C	Carbon molar flow

F_{CO}^{in}, F_{CO}^{out}	Molar flow rate of CO at the reactor inlet and outlet, respectively
F_{cycloh}	Molar flow rate of cyclohexane
f_d	Dilution factor
F_{gas}	Total gas flow rate
F_{gly}^{in}, F_{gly}^{out}	Molar flow rate of glycerol at the reactor inlet and outlet, respectively
F_H^{gas}	Molar flow rate of H atoms in the gas product
$F_{H_2}^{in}$, $F_{H_2}^{out}$	Molar flow rate of hydrogen at the reactor inlet and oulet, respectively
G	Gas flow rate
G′	Gas mass velocity
H	Henry´s law constants
H_{ads}	Adsorbed atomic hydrogen
H^{ref}	Henry's constant at a reference temperature
h,k,l	Miller indices
hv	Photon energy
I_{hkl}	Intensity of the (h k l) diffraction plane
I_D/I_G	Intensity ratio of D/G bands (Raman)
K	Shape factor in Scherrer equation
K_{G-L}, K_{L-S}	Gas-liquid and liquid-solid mass transfer coefficients
L	Liquid flow rate
L′	Liquid mass velocity
m_{cat}	Catalyst mass

M_C, M_{Me}	Molar mass of carbon and metal, respectively
$\dot{m}_f$	Mass flow rate
MR	Mears criterion
m/z	Mass divided by charge number in mass spectroscopy
N	Agitation speed
N	Integer determined by the order given (Bragg´s Law)
N_A	Avogadro's number
n_C	Moles of carbon
n_s, n_{sb}	Number of surface atoms per unit area and per mass of catalyst, respectively
$n_{sorb}^{t=0}$, $n_{sorb}^{t=t}$	Moles of sorbitol initially charged to the reactor and at reaction time t
P, P/Po	Pressure and relative pressure
Q	Metal content of catalyst
R	Universal gas constant
r_{app}	Apparent reaction rate
Re	Particle Reynolds number
r_{obs}	Observed reaction rate
r_P	Catalyst particle radius
RR	Stoichiometric factor
S_{BET}	Specific surface area
Sc	Schmidt number
S_i	Selectivity to prouct i

Sh	Sherwood number
T, T^{ref}	Temperature and reference temperature
t	Time
t_l	Adsorbed layer depth
u_s	Superficial velocity
V_{bulk}	Volume occupied by an atom in bulk metal
V_{gas}	Gas volume
V_{gly}, V_{sorb}	Molar volume of glycerol and sorbitol at boiling point
V_{H2}	Volume of H_2
V_{liq}	Liquid volume in the reactor
V_m	Adsorbate volume for monolayer
V_{mol}	Molar volume of adsorbate
V_P	Pore volume
X_i	Conversion
Y_i	Products yield

Greek symbols

α	Absorption coefficient
β, β_{exp}, β_i	Line broadening due to the crystallite size, experimental width and width correction due to the XRD device, respectively.
ΔE	Spin-orbit separation in XPS
ΔH^0, $\Delta_{sol}H$	Enthalpy
ΔH_2	Net hydrogen variation

δ	Chemical shift
ε_L	Liquid holdup
η	Constant relating to the nature of the electronic transition (DRS spectroscopy)
θ	Contact angle in XRD
λ	Wavelength
μ_w	Water dynamic viscosity
ξ , ξ_{bed}	Catalyst porosity and bed porosity
$\rho , \rho_{bed} , \rho_p$	Mass density, packed bed and catalyst particle density
σ	Surface tension of adsorbate
ς_{G-L}	Gas-liquid mass transfer parameter
ς_{L-S}	Liquid-solid mass transfer parameter
τ	Tortuosity
γ	Inversion parameter (NMR)
ϕ	Work function
Φ_{WP}	Weisz-Prater criterion

Chapter 11

REFERENCES

11. REFERENCES

1. Álvarez, L.J.; Sánchez, I.; Urtasun, A. El efecto de las fluctuaciones del precio del petróleo sobre la inflación española, Boletín económico, 11 May 2017; Banco de España, Ed. 2/2017.

2. Giordano, E. *Las guerras del petróleo: geopolitica, economía y conflicto,* 1st ed. Icaria editorial: pp. 192, ISBN 978-8474266061.

3. Crude Oil Prices - 70 Year Historical Chart. Available online: https://www.macrotrends.net/1369/crude-oil-price-history-chart (Accessed on 13 November 2020).

4. Edenhofer, O.; Pichs-Madruga, R.; Sokona, Y.; Seyboth, K.; Matschoss, P.; Kadner, S.; Zwickel, T.; Eickemeier, P.; Hansen, G.; Schlömer, S.; von Stechow, C. IPCC, 2011: Summary for Policy makers. In: IPCC Special Report on Renewable Energy Sources and Climate Change Mitigation.

5. Transforming Our World: The 2030 Agenda for Sustainable Development A/RES/70/1. United Nations.

6. Allen, M.R.; Dube, O.P.; Solecki, W.; Aragón-Durand, F.; Cramer, W.; Humphreys, S.; Kainuma, M.; Kala, J.; Mahowald, N.; Mulugetta, Y.; Perez, R.; Wairiu, M.; Zickfeld, K. Framing and Context. In: Global Warming of 1.5 °C. An IPCC Special Report on the impacts of global warming of 1.5 °C above pre-industrial levels and related global greenhouse gas emission pathways, in the context of strengthening the global response to the threat of climate change, sustainable development, and efforts to eradicate poverty. 2018.

7. Cherubini, F. The biorefinery concept: Using biomass instead of oil for producing energy and chemicals. *Energy Convers Manag* **2010**, *51*, 1412-1421, doi: 10.1016/j.enconman.2010.01.015.

8. Mathews, A.P. Renewable Energy Technologies: Panacea for World Energy Security and Climate Change? *Procedia Comput Sci* **2014**, *32*, 731-737, doi: 10.1016/j.procs.2014.05.483.

9. Biomass - Energy Explained, Your Guide To Understanding Energy. Available online: https://www.eia.gov/energyexplained/biomass/ (Accessed on 15 October 2019).

10. Jin, W.; Pastor-Pérez, L.; Shen, D.; Sepúlveda-Escribano, A.; Gu, S.; Ramirez Reina, T. Catalytic Upgrading of Biomass Model Compounds: Novel Approaches and Lessons Learnt from Traditional

Hydrodeoxygenation – a Review. *ChemCatChem* **2019**, *11*, 924-960, doi: 10.1002/cctc.201801722.

11.   United States Department of Agriculture. National Institute of Food and Agriculture. Available online: https://nifa.usda.gov/topic/bioenergy (Accessed on 13 November 2020).

12.   IEA (International Energy Agency). Bioenergy Task 42 on biorefineries: co-production of fuels, chemicals, power and materials from biomass, Minutes of the third Task meeting, Copenhagen, Denmark, 25-26 March 2008.

13.   Hingsamer, M.; Jungmeier, G. Chapter Five - Biorefineries. In *The Role of Bioenergy in the Bioeconomy*; Lago, C.; Caldés, N.; Lechón, Y., Eds.; Academic Press: 2019; pp. 179-222.

14.   Williams, C.L.; Dahiya, A.; Porter, P. Chapter 1 - Introduction to Bioenergy. In *Bioenergy*; Dahiya, A., Ed.; Academic Press: Boston, 2015; pp. 5-36.

15.   Parsons, B. Chapter 31 - Economics of Ethanol and Biodiesel. In *Bioenergy*; Dahiya, A., Ed.; Academic Press: Boston, 2015; pp. 523-539.

16.   Ma, F.; Hanna, M.A. Biodiesel production: a review. Journal Series #12109, Agricultural Research Division, Institute of Agriculture and Natural Resources, University of Nebraska–Lincoln. *Bioresour Technol* **1999**, *70*, 1-15, doi: 10.1016/S0960-8524(99)00025-5.

17.   Ciolkosz, D. Chapter 34 - What's So Different about Biodiesel Fuel? In *Bioenergy*; Dahiya, A., Ed.; Academic Press: Boston, 2015; pp. 551-555.

18.   Flach, B.; Lieberz, S.; Bolla, S. Biofuels Annual, E42020-0032. 29 June 2020; Global Agricultural Information Network, USDA.

19.   Directive 2003/30/EC of the European Parliament and of the Council of 8 May 2003 on the promotion of the use of biofuels or other renewable fuels for transport. Available online: https://eur-lex.europa.eu/legal-content/EN/ALL/?uri=CELEX%3A32003L0030 (Accessed on 13 November 2020).

20.   Directive 2009/28/EC of the European Parliament and of the Council of 23 April 2009 on the promotion of the use of energy from renewable sources and amending and subsequently repealing Directives 2001/77/EC and 2003/30/EC (Text with EEA relevance). Available online: https://eur-lex.europa.eu/legal-

content/EN/ALL/?uri=celex%3A32009L0028 (Accessed on 13 November 2020).

21. Directive (EU) 2015/1513 of the European Parliament and of the Council of 9 September 2015 amending Directive 98/70/EC relating to the quality of petrol and diesel fuels and amending Directive 2009/28/EC on the promotion of the use of energy from renewable sources (Text with EEA relevance). Available online: https://eur-lex.europa.eu/legal-content/EN/TXT/?uri=CELEX%3A32015L1513 (Accessed on 13 November 2020).

22. Directive (EU) 2018/2001 of the European Parliament and of the Council of 11 December 2018 on the promotion of the use of energy from renewable sources (Text with EEA relevance.). Available online: https://eur-lex.europa.eu/legal-content/EN/TXT/?uri=uriserv:OJ.L_.2018.328.01.0082.01.ENG&toc=OJ:L:2018:328:TOC (Accessed on 13 November 2020).

23. Commission Implementing Regulation (EU) 2019/1344 of 12 August 2019 imposing a provisional countervailing duty on imports of biodiesel originating in Indonesia. Available online: https://eur-lex.europa.eu/legal-content/EN/TXT/?uri=CELEX%3A32019R1344 (Accessed on 13 November 2020).

24. Commission Implementing Decision (EU) 2019/245 of 11 February 2019 accepting undertaking offers following the imposition of definitive countervailing duties on imports of biodiesel originating in Argentina. Available online: https://eur-lex.europa.eu/legal-content/EN/ALL/?uri=CELEX%3A32019D0245 (Accessed on 16 October 2020).

25. Valin, H.; Peters, D.; van den Berg, M.; Frank, S.; Havlik, P.; Forsell, N.; Hamelinck, C.; Pirker, J.; Mosnier, A.; Balkovic, J.; Schmid, E.; Dürauerand Fulvio di Fulvio, M. The land use change impact of biofuels consumed in the EU Quantification of area and greenhouse gas impacts. *Project number: BIENL13120*, 27 August 2015.

26. Chum, H.; A. Faaij, A.; Moreira, J.; Berndes, G.; Dhamija, P.; Dong, H.; Gabrielle, B.; Goss Eng, A.; Lucht, W.; Mapako, M.; Masera Cerutti, O.; McIntyre, T.; Minowa, T.; Pingoud, K. In IPCC Special Report on Renewable Energy Sources and Climate Change Mitigation. 2011.

27. Jayasinghe, S. Review of U.S. Biodiesel Market: Production, Imports and Profitability. October 2018.

28. Scheinkerman de obschatko, E.; Begenisic, F. *Perspectiva de los biocombustibles en la Argentina y en Brasil,* 1st ed.; Instituto Interamericano de Cooperación para la Agricultura (IICA). Secretaria de Agricultura, Ganadería, Pesca y Alimentación (SAGPYA): Buenos Aires, 2006.

29. Lombana Coy, J.; Vega Jurado, J.; Britton Acevedo, E.; Herrera Velásquez, S. *Análisis del sector biodiesel en Colombia y su cadena de suministro,* Universidad del Norte: Barranquilla, Colombia, 2015.

30. 4th International Conference on Biofuels Standards: Current Issues, Future Trends. Biofuel Developments in Emerging Economies, Gaithersburg, Maryland, USA. National Institute of Standard and technology (NIST), 13-15 November 2012, U.S. Department of Commerce.

31. He, Q.; McNutt, J.; Yang, J. Utilization of the residual glycerol from biodiesel production for renewable energy generation. *Renew Sust Energ Rev* **2017**, *71*, 63-76, doi: 10.1016/j.rser.2016.12.110.

32. Ciriminna, R.; Pina, C.D.; Rossi, M.; Pagliaro, M. Understanding the glycerol market. *Eur J Lipid Sci Technol* **2014**, *116*, 1432-1439, doi: 10.1002/ejlt.201400229.

33. Schwengber, C.A.; Alves, H.J.; Schaffner, R.A.; Da Silva, F.A.; Sequinel, R.; Bach, V.R.; Ferracin, R.J. Overview of glycerol reforming for hydrogen production. *Renew Sust Energ Rev* **2016**, *58*, 259-266, doi: 10.1016/j.rser.2015.12.279.

34. Top Value Added Chemicals from Biomass Volume I- Results of Screening for Potential Candidates from Sugars and Synthesis Gas. Produced by the Staff at Pacific Northwest National Laboratory (PNNL). National Renewable Energy Laboratory (NREL). Office of Biomass Program (EERE). For the Office of the Biomass Program: T. Werpy and G. Petersen, Editors. August 2004. Available online: http://www.osti.gov/bridge.

35. Bozell, J.J.; Petersen, G.R. Technology development for the production of biobased products from biorefinery carbohydrates—the US Department of Energy's "Top 10" revisited. *Green Chem*, 539-554, doi: 10.1039/B922014C.

36. Quispe, C.A.G.; Coronado, C.J.R.; Carvalho Jr., J.A. Glycerol: Production, consumption, prices, characterization and new trends in combustion. *Renew Sust Energ Rev* **2013**, *27*, 475-493, doi: 10.1016/j.rser.2013.06.017.

37. Clark, J.H.; Kraus, G.; Pagliaro, M.; Rossi, M. *The Future of Glycerol,* Royal Society of Chemistry: 2010.

38. Faber, M.d.O.; Ferreira-Leitão, V.S. Optimization of biohydrogen yield produced by bacterial consortia using residual glycerin from biodiesel production. *Bioresour Technol* **2016**, *219*, 365-370, doi: 10.1016/j.biortech.2016.07.141.

39. Lo, Y.; Chen, X.; Huang, C.; Yuan, Y.; Chang, J. Dark fermentative hydrogen production with crude glycerol from biodiesel industry using indigenous hydrogen-producing bacteria. *Int J Hydrog Energy* **2013**, *38*, 15815-15822, doi: 10.1016/j.ijhydene.2013.05.083.

40. Trchounian, K.; Trchounian, A. Escherichia coli hydrogen gas production from glycerol: Effects of external formate. *Renew Energy* **2015**, *83*, 345-351, doi: 10.1016/j.renene.2015.04.052.

41. Fountoulakis, M.S.; Manios, T. Enhanced methane and hydrogen production from municipal solid waste and agro-industrial by-products co-digested with crude glycerol. *Bioresour Technol* **2009**, *100*, 3043-3047, doi: 10.1016/j.biortech.2009.01.016.

42. Bodík, I.; Blšťáková, A.; Sedláček, S.; Hutňan, M. Biodiesel waste as source of organic carbon for municipal WWTP denitrification. *Bioresour Technol* **2009**, *100*, 2452-2456, doi: 10.1016/j.biortech.2008.11.050.

43. Guerrero, J.; Tayà, C.; Guisasola, A.; Baeza, J.A. Glycerol as a sole carbon source for enhanced biological phosphorus removal. *Water Res* **2012**, *46*, 2983-2991, doi: 10.1016/j.watres.2012.02.043.

44. Ezhova, N.N.; Korosteleva, I.G.; Kolesnichenko, N.V.; Kuz'min, E.A.; Khadzhiev, S.N.; Sorokina, E.Y.; Vasil'eva, M.A.; Voronina, Z.D. Glycerol carboxylation to glycerol carbonate in the presence of rhodium complexes with nitrogen-containing macroligands. *Pet Chem* **2012**, *52*, 416-421, doi: 10.1134/S0965544112060060.

45. Phadtare, D.; Kondawar, S.; Athawale, A.; Rode, C. Crystalline LaCoO$_3$ perovskite as a novel catalyst for glycerol transesterification. *Mol Catal* **2019**, *475*, 110496, doi: 10.1016/j.mcat.2019.110496.

46. Talebian-Kiakalaieh, A.; Tarighi, S. Hierarchical faujasite zeolite-supported heteropoly acid catalyst for acetalization of crude-glycerol to fuel additives. *J Ind Eng Chem* **2019**, *79*, 452-464, doi: 10.1016/j.jiec.2019.07.021.

47. Esposito, R.; Raucci, U.; Cucciolito, M.E.; Di Guida, R.; Scamardella, C.; Rega, N.; Ruffo, F. Iron(III) Complexes for Highly Efficient and Sustainable Ketalization of Glycerol: A Combined Experimental and Theoretical Study. *ACS Omega* **2019**, *4*, 688-698, doi: 10.1021/acsomega.8b02546.

48. Okoye, P.U.; Abdullah, A.Z.; Hameed, B.H. A review on recent developments and progress in the kinetics and deactivation of catalytic acetylation of glycerol—A byproduct of biodiesel. *Renew Sust Energ Rev* **2017**, *74*, 387-401, doi: 10.1016/j.rser.2017.02.017.

49. Keogh, J.; Tiwari, M.S.; Manyar, H. Esterification of Glycerol with Acetic Acid Using Nitrogen-Based Brønsted-Acidic Ionic Liquids. *Ind Eng Chem Res* **2019**, *58*, 17235-17243, doi: 10.1021/acs.iecr.9b01223.

50. Barros, F.J.S.; Moreno-Tost, R.; Cecilia, J.A.; Ledesma-Muñoz, A.L.; de Oliveira, L.C.C.; Luna, F.M.T.; Vieira, R.S. Glycerol oligomers production by etherification using calcined eggshell as catalyst. *Mol Catal* **2017**, *433*, 282-290, doi: 10.1016/j.mcat.2017.02.030.

51. Galy, N.; Nguyen, R.; Blach, P.; Sambou, S.; Luart, D.; Len, C. Glycerol oligomerization in continuous flow reactor. *J Ind Eng Chem* **2017**, *51*, 312-318, doi: 10.1016/j.jiec.2017.03.020.

52. Barrault, J.-M.; Clacens, J.; Pouilloux, Y. Selective Oligomerization of Glycerol Over Mesoporous Catalysts. *Top Catal* **2004**, *27*, 137-142, doi: 10.1023/B:TOCA.0000013548.16699.1c.

53. Len, C.; Luque, R. Continuous flow transformations of glycerol to valuable products: an overview. *Sustain Chem Process* **2014**, *2*, 1, doi: 10.1186/2043-7129-2-1.

54. Bagheri, S.; Julkapli, N.M.; Yehye, W.A. Catalytic conversion of biodiesel derived raw glycerol to value added products. *Renew Sust Energ Rev* **2015**, *41*, 113-127, doi: 10.1016/j.rser.2014.08.031.

55. Katryniok, B.; Paul, S.; Bellière-Baca, V.; Rey, P.; Dumeignil, F. Glycerol dehydration to acrolein in the context of new uses of glycerol. *Green Chem*, 2079-2098, doi: 10.1039/C0GC00307G.

56. Santacesaria, E.; Tesser, R.; Di Serio, M.; Casale, L.; Verde, D. New Process for Producing Epichlorohydrin via Glycerol Chlorination. *Ind Eng Chem Res* **2010**, *49*, 964-970, doi: 10.1021/ie900650x.

57. Nakagawa, Y.; Tamura, M.; Tomishige, K. Perspective on catalyst development for glycerol reduction to C3 chemicals with molecular

hydrogen. *Res Chem Intermed* **2018**, *44*, 3879-3903, doi: 10.1007/s11164-018-3481-2.

58.   Yoon, S.J.; Choi, Y.; Son, Y.; Lee, S.; Lee, J. Gasification of biodiesel by-product with air or oxygen to make syngas. *Bioresour Technol* **2010**, *101*, 1227-1232, doi: 10.1016/j.biortech.2009.09.039.

59.   Valliyappan, T.; Ferdous, D.; Bakhshi, N.N.; Dalai, A.K. Production of Hydrogen and Syngas via Steam Gasification of Glycerol in a Fixed-Bed Reactor. *Top Catal* **2008**, *49*, 59-67, doi 10.1007/s11244-008-9062-7.

60.   Xiu, S.; Shahbazi, A.; Wallace, C.W.; Wang, L.; Cheng, D. Enhanced bio-oil production from swine manure co-liquefaction with crude glycerol. *Energy Convers Manag* **2011**, *52*, 1004-1009, doi: 10.1016/j.enconman.2010.08.028.

61.   Ye, Z.; Xiu, S.; Shahbazi, A.; Zhu, S. Co-liquefaction of swine manure and crude glycerol to bio-oil: Model compound studies and reaction pathways. *Bioresour Technol* **2012**, *104*, 783-787, doi: 10.1016/j.biortech.2011.09.126.

62.   Pedersen, T.H.; Jasiūnas, L.; Casamassima, L.; Singh, S.; Jensen, T.; Rosendahl, L.A. Synergetic hydrothermal co-liquefaction of crude glycerol and aspen wood. *Energy Convers Manag* **2015**, *106*, 886-891, doi: 10.1016/j.enconman.2015.10.017.

63.   Dou, B.; Song, Y.; Wang, C.; Chen, H.; Xu, Y. Hydrogen production from catalytic steam reforming of biodiesel byproduct glycerol: Issues and challenges. *Renew Sust Energ Rev* **2014**, *30*, 950-960, doi: 10.1016/j.rser.2013.11.029.

64.   Iriondo, A.; Barrio, V.L.; Cambra, J.F.; Arias, P.L.; Güemez, M.B.; Navarro, R.M.; Sánchez-Sánchez, M.C.; Fierro, J.L.G. Hydrogen Production from Glycerol Over Nickel Catalysts Supported on Al_2O_3 Modified by Mg, Zr, Ce or La. *Top Catal* **2008**, *49*, 46, doi: 10.1007/s11244-008-9060-9.

65.   Chen, D.; Wang, W.; Liu, C. Hydrogen production through glycerol steam reforming over beehive-biomimetic graphene-encapsulated nickel catalysts. *Renew Energy* **2020**, *145*, 2647-2657, doi: 10.1016/j.renene.2019.08.022.

66.   Yus, M.; Soler, J.; Herguido, J.; Menéndez, M. Glycerol steam reforming with low steam/glycerol ratio in a two-zone fluidized bed reactor. *Catal Today* **2018**, *299*, 317-327, doi: 10.1016/j.cattod.2017.08.040.

67. Karthikeyan, D.; Shin, G.S.; Moon, D.J.; Kim, J.H.; Park, N.C.; Kim, Y.C. Aqueous Phase Reforming of Glycerol Over the Pd Loaded Ni/Al$_2$O$_3$ Catalysts. *J Nanosci Nanotechnol* **2011**, *11*, 1443-1446, doi: 10.1166/jnn.2011.3309.

68. El Doukkali, M.; Iriondo, A.; Cambra, J.F.; Jalowiecki-Duhamel, L.; Mamede, A.S.; Dumeignil, F.; Arias, P.L. Pt monometallic and bimetallic catalysts prepared by acid sol–gel method for liquid phase reforming of bioglycerol. *J Mol Catal A Chem* **2013**, *368-369*, 125-136, doi: 10.1016/j.molcata.2012.12.006.

69. Seretis, A.; Tsiakaras, P. Aqueous phase reforming (APR) of glycerol over platinum supported on Al$_2$O$_3$ catalyst. *Renew Energy* **2016**, *85*, 1116-1126, doi: 10.1016/j.renene.2015.07.068.

70. Gutiérrez Ortiz, F.J.; Ollero, P.; Serrera, A.; Sanz, A. Thermodynamic study of the supercritical water reforming of glycerol. *Int J Hydrog Energy* **2011**, *36*, 8994-9013, doi: 10.1016/j.ijhydene.2011.04.095.

71. Byrd, A.J.; Pant, K.K.; Gupta, R.B. Hydrogen production from glycerol by reforming in supercritical water over Ru/Al$_2$O$_3$ catalyst. *Fuel* **2008**, *87*, 2956-2960, doi: 10.1016/j.fuel.2008.04.024.

72. Rennard, D.; Kruger, J.; Schmidt, L. Autothermal Catalytic Partial Oxidation of Glycerol to Syngas and to Non-Equilibrium Products. *ChemSusChem* **2009**, *2*, 89-98, doi: 10.1002/cssc.200800200.

73. Wang, H.; Wang, X.; Li, M.; Li, S.; Wang, S.; Ma, X. Thermodynamic analysis of hydrogen production from glycerol autothermal reforming. *Int J Hydrog Energy* **2009**, *34*, 5683-5690, doi: 10.1016/j.ijhydene.2009.05.118.

74. Pagliaro, M. Chapter 2 - C3-Monomers. In *Glycerol*; Pagliaro, M., Ed.; Elsevier: 2017; pp. 23-57.

75. Pagliaro, M. Chapter 4 - Antifreeze and Multipurpose Cement Aid. In *Glycerol*; Pagliaro, M., Ed.; Elsevier: 2017; pp. 91-107.

76. Pagliaro, M. Chapter 3 - Esters, Ethers, Polyglycerols, and Polyesters. In *Glycerol*; Pagliaro, M., Ed.; Elsevier: 2017; pp. 59-90.

77. Pagliaro, M.; Rossi, M. Chapter 8 - Selective Oxidation. In *The future of glycerol*, 2nd; Ed.; RSC Publishing: 2010; doi: 10.1039/9781849731089-00115.

78. Carrettin, S.; McMorn, P.; Johnston, P.; Griffin, K.; Kiely, C.J.; Attard, G.A.; Hutchings, G.J. Oxidation of Glycerol Using Supported Gold

Catalysts. *Topics in Catalysis* **2004**, *27*, 131-136, doi: 10.1023/B:TOCA.0000013547.35106.0d.

79. Dimitratos, N.; Porta, F.; Prati, L. Au, Pd (mono and bimetallic) catalysts supported on graphite using the immobilisation method: Synthesis and catalytic testing for liquid phase oxidation of glycerol. *Appl Catal A Gen* **2005**, *291*, 210-214, doi: 10.1016/j.apcata.2005.01.044.

80. Demirel-Gülen, S.; Lucas, M.; Claus, P. Liquid phase oxidation of glycerol over carbon supported gold catalysts. *Catal Today* **2005**, *102-103*, 166-172, doi: 10.1016/j.cattod.2005.02.033.

81. Qureshi, B.A.; Lan, X.; Arslan, M.T.; Wang, T. Highly Active and Selective Nano H-ZSM-5 Catalyst with Short Channels along b-Axis for Glycerol Dehydration to Acrolein. *Ind Eng Chem Res* **2019**, *58*, 12611-12622, doi: 10.1021/acs.iecr.9b01882.

82. Mohd, H.M.; Roila Awang; Yunus, W.M.Z.W. A Review of Acetol: Application and Production. *AJAS* **2011**, *8*, doi: 10.3844/ajassp.2011.1135.1139.

83. Basu, S.; Sen, A.K.; Mukherjee, M. Synthesis and performance evaluation of silica-supported copper chromite catalyst for glycerol dehydration to acetol. *J Chem Sci* **2019**, *131*, 82, doi: 10.1007/s12039-019-1662-1.

84. Célerier, S.; Morisset, S.; Batonneau-Gener, I.; Belin, T.; Younes, K.; Batiot-Dupeyrat, C. Glycerol dehydration to hydroxyacetone in gas phase over copper supported on magnesium oxide (hydroxide) fluoride catalysts. *Appl Catal A Gen* **2018**, *557*, 135-144, doi: 10.1016/j.apcata.2018.03.022.

85. Roy, D.; Subramaniam, B.; Chaudhari, R.V. Aqueous phase hydrogenolysis of glycerol to 1,2-propanediol without external hydrogen addition. *Catal Today* **2010**, *156*, 31-37, doi: 10.1016/j.cattod.2010.01.007.

86. Yfanti, V.-L.; Lemonidou, A.A. Mechanistic study of liquid phase glycerol hydrodeoxygenation with in-situ generated hydrogen. *J Catal* **2018**, *368*, 98-111, doi: 10.1016/j.jcat.2018.09.036.

87. Yfanti, V.-L.; Ipsakis, D.; Lemonidou, A.A. Kinetic study of liquid phase glycerol hydrodeoxygenation under inert conditions over a Cu-based catalyst. *React Chem Eng*, 559-571, doi: 10.1039/C8RE00061A.

88. Barbelli, M.L.; Santori, G.F.; Nichio, N.N. Aqueous phase hydrogenolysis of glycerol to bio-propylene glycol over Pt–Sn catalysts. *Bioresour Technol* **2012**, *111*, 500-503, doi: 10.1016/j.biortech.2012.02.053.

89. Nakagawa, Y.; Shinmi, Y.; Koso, S.; Tomishige, K. Direct hydrogenolysis of glycerol into 1,3-propanediol over rhenium-modified iridium catalyst. *J Catal* **2010**, *272*, 191-194, doi: 10.1016/j.jcat.2010.04.009.

90. Amada, Y.; Shinmi, Y.; Koso, S.; Kubota, T.; Nakagawa, Y.; Tomishige, K. Reaction mechanism of the glycerol hydrogenolysis to 1,3-propanediol over Ir–ReO$_x$/SiO$_2$ catalyst. *Appl Catal B Environ* **2011**, *105*, 117-127, doi: 10.1016/j.apcatb.2011.04.001.

91. Shinmi, Y.; Koso, S.; Kubota, T.; Nakagawa, Y.; Tomishige, K. Modification of Rh/SiO$_2$ catalyst for the hydrogenolysis of glycerol in water. *Appl Catal B Environ* **2010**, *94*, 318-326, doi: 10.1016/j.apcatb.2009.11.021.

92. Vilcocq, L.; Cabiac, A.; Especel, C.; Guillon, E.; Duprez, D. Transformation of Sorbitol to Biofuels by Heterogeneous Catalysis: Chemical and Industrial Considerations. *Oil Gas Sci.Technol.– Rev.IFP Energies nouvelles* **2013**, *68*, 841-860, doi: 10.2516/ogst/2012073.

93. Mota, C.J.A.; Peres Pinto, B.; de Lima, A.L. Thermochemical Routes of Glycerol Transformation to Commodity Chemicals. In *Glycerol: A Versatile Renewable Feedstock for the Chemical Industry*; Mota, C.J.A.; Peres Pinto, B.; de Lima, A.L., Eds.; Springer International Publishing: Cham, 2017; pp. 39-57.

94. Lin, Y. Catalytic valorization of glycerol to hydrogen and syngas. *Int J Hydrog Energy* **2013**, *38*, 2678-2700, doi: 10.1016/j.ijhydene.2012.12.079.

95. Wang, W. Thermodynamic analysis of glycerol partial oxidation for hydrogen production. *Fuel Process Technol* **2010**, *91*, 1401-1408, doi: 10.1016/j.fuproc.2010.05.013.

96. Wang, X.; Li, M.; Wang, M.; Wang, H.; Li, S.; Wang, S.; Ma, X. Thermodynamic analysis of glycerol dry reforming for hydrogen and synthesis gas production. *Fuel* **2009**, *88*, 2148-2153, doi: 10.1016/j.fuel.2009.01.015.

97. Markočič, E.; Kramberger, B.; van Bennekom, J.G.; Jan Heeres, H.; Vos, J.; Knez, Ž Glycerol reforming in supercritical water; a short review. *Renew Sust Energ Rev* **2013**, *23*, 40-48, doi: 10.1016/j.rser.2013.02.046.

98. Cortright, R.D.; Davda, R.R.; Dumesic, J.A. Hydrogen from catalytic reforming of biomass-derived hydrocarbons in liquid water. *Nature* **2002**, *418*, 964-967, doi: 10.1038/nature01009.

99. Kumar, S. Role of Hydrogen in the Energy Sector. In *Clean Hydrogen Production Methods*; Kumar, S., Ed.; Springer International Publishing: Cham, 2015; pp. 1-9.

100. IEA for the G20. The Future of Hydrogen: Seizing today's opportunitie. June 2019.

101. Viswanathan, B. Chapter 9 - Hydrogen as an Energy Carrier. In *Energy Sources*; Viswanathan, B., Ed.; Elsevier: Amsterdam, 2017; pp. 161-183.

102. Nehrir, M.H.; Wang, C. 6 - Fuel cells. In *Electric Renewable Energy Systems*; Rashid, M.H., Ed.; Academic Press: Boston, 2016; pp. 92-113.

103. Hydrogen council. Hydrogenscaling up: A sustainable pathway for the global energy transition. November 2017. Available online: www.hydrogencouncil.com.

104. Nassaralla, C.L. Iron Production. In *Encyclopedia of Materials: Science and Technology*; Buschow, K.H.J.; Cahn, R.W.; Flemings, M.C.; Ilschner, B.; Kramer, E.J.; Mahajan, S.; Veyssière, P., Eds.; Elsevier: Oxford, 2001; pp. 4296-4301.

105. Sharma, S.; Ghoshal, S.K. Hydrogen the future transportation fuel: From production to applications. *Renew Sust Energ Rev* **2015**, *43*, 1151-1158, doi: 10.1016/j.rser.2014.11.093.

106. Huang, Z.; Lu, L.; Jiang, D.; Xing, D.; Ren, Z.J. Electrochemical hythane production for renewable energy storage and biogas upgrading. *Appl Energy* **2017**, *187*, 595-600, doi: 10.1016/j.apenergy.2016.11.099.

107. Edwards, P.P.; Kuznetsov, V.L.; David, W.I.F.; Brandon, N.P. Hydrogen and fuel cells: Towards a sustainable energy future. *Energy Policy* **2008**, *36*, 4356-4362, doi: 10.1016/j.enpol.2008.09.036.

108. Haszeldine, R.S. Carbon Capture and Storage: How Green Can Black Be? *Science* **2009**, *325*, 1647-1652, doi : 10.1126/science.1172246.

109. Coutanceau, C.; Baranton, S.; Audichon, T. Chapter 3 - Hydrogen Production From Water Electrolysis. In *Hydrogen Electrochemical Production*; Coutanceau, C.; Baranton, S.; Audichon, T., Eds.; Academic Press: 2018; pp. 17-62.

110. Roeb, M.; Agrafiotis, C.; Sattler, C. 11 - Hydrogen production via thermochemical water splitting. In *Compendium of Hydrogen Energy*; Subramani, V.; Basile, A.; Veziroğlu, T.N., Eds.; Woodhead Publishing: Oxford, 2015; pp. 319-347.

111. Nikolaidis, P.; Poullikkas, A. A comparative overview of hydrogen production processes. *Renew Sust Energ Rev* **2017**, *67*, 597-611, doi: 10.1016/j.rser.2016.09.044.

112. Vargas, S.R.; Santos, P.V.d.; Giraldi, L.A.; Zaiat, M.; Calijuri, M.d.C. Anaerobic phototrophic processes of hydrogen production by different strains of microalgae Chlamydomonas sp. *FEMS Microbiol Lett* **2018**, *365*, doi 10.1093/femsle/fny073.

113. Hassan, A.H.S.; Mietzel, T.; Brunstermann, R.; Schmuck, S.; Schoth, J.; Küppers, M.; Widmann, R. Fermentative hydrogen production from low-value substrates. *World J Microbiol Biotechnol* **2018**, *34*, 176, doi: 10.1007/s11274-018-2558-9.

114. Hallenbeck, P.C.; Benemann, J.R. Biological hydrogen production; fundamentals and limiting processes. *Int J Hydrog Energy* **2002**, *27*, 1185-1193, doi: 10.1016/S0360-3199(02)00131-3.

115. Das, D.; Veziroglu, T.N. Advances in biological hydrogen production processes. *Int J Hydrog Energy* **2008**, *33*, 6046-6057, doi: 10.1016/j.ijhydene.2008.07.098.

116. Neira d'Angelo, MF. *Aqueous phase reforming of bio-carbohydrates: reactor engineering and catalysis*. PhD Thesis: Technische Universiteit Eindhoven, 2014; pp. 181, doi: 10.6100/IR780924.

117. Valenzuela, M.B.; Jones, C.W.; Agrawal, P.K. Batch Aqueous-Phase Reforming of Woody Biomass. *Energy Fuels* **2006**, *20*, 1744-1752, doi: 10.1021/ef060113p.

118. Wen, G.; Xu, Y.; Xu, Z.; Tian, Z. Direct conversion of cellulose into hydrogen by aqueous-phase reforming process. *Catal Commun* **2010**, *11*, 522-526, doi: 10.1016/j.catcom.2009.12.008.

119. Coronado, I.; Pitínová, M.; Karinen, R.; Reinikainen, M.; Puurunen, R.L.; Lehtonen, J. Aqueous-phase reforming of Fischer-Tropsch alcohols over nickel-based catalysts to produce hydrogen: Product distribution and reaction pathways. *Appl Catal A Gen* **2018**, *567*, 112-121, doi: 10.1016/j.apcata.2018.09.013.

120. Remón, J.; García, L.; Arauzo, J. Cheese whey management by catalytic steam reforming and aqueous phase reforming. *Fuel Process Technol* **2016**, *154*, 66-81, doi: 10.1016/j.fuproc.2016.08.012.

121. Oliveira, A.S.; Baeza, J.A.; Calvo, L.; Alonso-Morales, N.; Heras, F.; Lemus, J.; Rodriguez, J.J.; Gilarranz, M.A. Exploration of the treatment of fish-canning industry effluents by aqueous-phase reforming using Pt/C catalysts. *Environ Sci: Water Res Technol* **2018**, *4*, 1979-1987, doi: 10.1039/C8EW00414E.

122. Oliveira, A.S.; Baeza, J.A.; Calvo, L.; Alonso-Morales, N.; Heras, F.; Rodriguez, J.J.; Gilarranz, M.A. Production of hydrogen from brewery wastewater by aqueous phase reforming with Pt/C catalysts. *Appl Catal B Environ* **2019**, *245*, 367-375, doi: 10.1016/j.apcatb.2018.12.061.

123. Chheda, J.; Huber, G.; Dumesic, J. Liquid-Phase Catalytic Processing of Biomass-Derived Oxygenated Hydrocarbons to Fuels and Chemicals. *Angew Chem Int Edit* **2007**, *46*, 7164-7183, doi: 10.1002/anie.200604274.

124. Davda, R.R.; Shabaker, J.W.; Huber, G.W.; Cortright, R.D.; Dumesic, J.A. A review of catalytic issues and process conditions for renewable hydrogen and alkanes by aqueous-phase reforming of oxygenated hydrocarbons over supported metal catalysts. *Appl Catal B Environ* **2005**, *56*, 171-186, doi: 10.1016/j.apcatb.2004.04.027.

125. Kunkes, E.L.; Soares, R.R.; Simonetti, D.A.; Dumesic, J.A. An integrated catalytic approach for the production of hydrogen by glycerol reforming coupled with water-gas shift. *Appl Catal B Environ* **2009**, *90*, 693-698, doi: 10.1016/j.apcatb.2009.04.032.

126. Ripken, R.M.; Meuldijk, J.; Gardeniers, J.G.E.; Le Gac, S. Influence of the Water Phase State on the Thermodynamics of Aqueous-Phase Reforming for Hydrogen Production. *ChemSusChem* **2017**, *10*, 4909-4913, doi: 10.1002/cssc.201700189.

127. Gokhale, A.A.; Dumesic, J.A.; Mavrikakis, M. On the Mechanism of Low-Temperature Water Gas Shift Reaction on Copper. *J Am Chem Soc* **2008**, *130*, 1402-1414, doi: 10.1021/ja0768237.

128. Tuza, P.V.; Manfro, R.L.; Ribeiro, N.F.P.; Souza, M.M.V.M. Production of renewable hydrogen by aqueous-phase reforming of glycerol over Ni-Cu catalysts derived from hydrotalcite precursors. *Renew Energy* **2013**, *50*, 408-414, doi: 10.1016/j.renene.2012.07.006.

129. Huber, G.W.; Dumesic, J.A. An overview of aqueous-phase catalytic processes for production of hydrogen and alkanes in a biorefinery. *Catal Today* **2006**, *111*, 119-132, doi: 10.1016/j.cattod.2005.10.010.

130. Chen, G.; Li, W.; Chen, H.; Yan, B. Progress in the aqueous-phase reforming of different biomass-derived alcohols for hydrogen production. *J Zhejiang Univ. sci. A* **2015**, *16*, 491-506, doi: 10.1631/jzus.A1500023.

131. Shabaker, J.W.; Huber, G.W.; Davda, R.R.; Cortright, R.D.; Dumesic, J.A. Aqueous-Phase Reforming of Ethylene Glycol Over Supported Platinum Catalysts. *Catal Letters* **2003**, *88*, 1-8, doi: 10.1023/A:1023538917186.

132. Lehnert, K.; Claus, P. Influence of Pt particle size and support type on the aqueous-phase reforming of glycerol. *Catal Commun* **2008**, *9*, 2543-2546, doi: 10.1016/j.catcom.2008.07.002.

133. Luo, N.; Fu, X.; Cao, F.; Xiao, T.; Edwards, P.P. Glycerol aqueous phase reforming for hydrogen generation over Pt catalyst - Effect of catalyst composition and reaction conditions. *Fuel* **2008**, *87*, 3483-3489, doi: 10.1016/j.fuel.2008.06.021.

134. Sakamoto, T.; Miyao, T.; Yoshida, A.; Naito, S. Effect of Re and Mo addition upon liquid phase methanol reforming with water over SiO_2, ZrO_2 and TiO_2 supported Ir catalysts. *Int J Hydrog Energy* **2010**, *35*, 6203-6209, doi: 10.1016/j.ijhydene.2010.03.113.

135. Espinosa-Moreno, F.; Balla, P.; Shen, W.; Chavarria-Hernandez, J.; Ruiz-Gómez, M.; Tlecuitl-Beristain, S. Ir-Based Bimetallic Catalysts for Hydrogen Production through Glycerol Aqueous-Phase Reforming. *Catalysts* **2018**, *8*, doi: 10.3390/catal8120613.

136. Nozawa, T.; Yoshida, A.; Hikichi, S.; Naito, S. Effects of Re addition upon aqueous phase reforming of ethanol over TiO_2 supported Rh and Ir catalysts. *Int J Hydrog Energy* **2015**, *40*, 4129-4140, doi: 10.1016/j.ijhydene.2015.01.152.

137. Nozawa, T.; Mizukoshi, Y.; Yoshida, A.; Naito, S. Aqueous phase reforming of ethanol and acetic acid over TiO_2 supported Ru catalysts. *Appl Catal B Environ* **2014**, *146*, 221-226, doi: 10.1016/j.apcatb.2013.06.017.

138. Guo, Y.; Liu, X.; Azmat, M.U.; Xu, W.; Ren, J.; Wang, Y.; Lu, G. Hydrogen production by aqueous-phase reforming of glycerol over Ni-B catalysts. *Int J Hydrog Energy* **2012**, *37*, 227-234, doi: 10.1016/j.ijhydene.2011.09.111.

139. Wen, G.; Xu, Y.; Xu, Z.; Tian, Z. Characterization and Catalytic Properties of the Ni/Al$_2$O$_3$ Catalysts for Aqueous-phase Reforming of Glucose. *Catal Letters* **2009**, *129*, 250-257, doi: 10.1007/s10562-008-9810-0.

140. Zhu, L.; Guo, P.; Chu, X.; Yan, S.; Qiao, M.; Fan, K.; Zhang, X.; Zong, B. An environmentally benign and catalytically efficient non-pyrophoric Ni catalyst for aqueous-phase reforming of ethylene glycol. *Green Chem*, 1323, doi: 10.1039/B808190E.

141. Wen, G.; Xu, Y.; Ma, H.; Xu, Z.; Tian, Z. Production of hydrogen by aqueous-phase reforming of glycerol. *Int J Hydrog Energy* **2008**, *33*, 6657-6666, doi: 10.1016/j.ijhydene.2008.07.072.

142. Yun, Y.S.; Park, D.S.; Yi, J. Effect of nickel on catalytic behaviour of bimetallic Cu–Ni catalyst supported on mesoporous alumina for the hydrogenolysis of glycerol to 1,2-propanediol. *Catal Sci Technol*, 3191, doi: 10.1039/C4CY00320A.

143. Wei, Z.; Sun, J.; Li, Y.; Datye, A.K.; Wang, Y. Bimetallic catalysts for hydrogen generation. *Chem Soc Rev* **2012**, *41*, 7994-8008, doi: 10.1039/C2CS35201J.

144. Iriondo, A.; Cambra, J.F.; Barrio, V.L.; Guemez, M.B.; Arias, P.L.; Sanchez-Sanchez, M.C.; Navarro, R.M.; Fierro, J.L.G. Glycerol liquid phase conversion over monometallic and bimetallic catalysts: Effect of metal, support type and reaction temperatures. *Appl Catal B Environ* **2011**, *106*, 83-93, doi: 10.1016/j.apcatb.2011.05.009.

145. Coronado, I.; Stekrova, M.; García Moreno, L.; Reinikainen, M.; Simell, P.; Karinen, R.; Lehtonen, J. Aqueous-phase reforming of methanol over nickel-based catalysts for hydrogen production. *Biomass Bioenergy* **2017**, *106*, 29-37, doi: 10.1016/j.biombioe.2017.08.018.

146. Shabaker, J.W.; Huber, G.W.; Dumesic, J.A. Aqueous-phase reforming of oxygenated hydrocarbons over Sn-modified Ni catalysts. *J Catal* **2004**, *222*, 180-191, doi: 10.1016/j.jcat.2003.10.022.

147. Huber, G.W.; Shabaker, J.W.; Evans, S.T.; Dumesic, J.A. Aqueous-phase reforming of ethylene glycol over supported Pt and Pd bimetallic catalysts. *Appl Catal B Environ* **2006**, *62*, 226-235, doi: 10.1016/j.apcatb.2005.07.010.

148. El Doukkali, M.; Iriondo, A.; Cambra, J.F.; Arias, P.L. Recent improvement on H$_2$ production by liquid phase reforming of glycerol: Catalytic properties and performance, and deactivation studies. *Top Catal* **2014**, *57*, 1066-1077, doi: 10.1007/s11244-014-0271-y.

149. van Haasterecht, T.; Ludding, C.C.I.; de Jong, K.P.; Bitter, J.H. Stability and activity of carbon nanofiber-supported catalysts in the aqueous phase reforming of ethylene glycol. *J Energy Chem* **2013**, *22*, 257-269, doi: 10.1016/S2095-4956(13)60032-7.

150. van Haasterecht, T.; Ludding, C.C.I.; de Jong, K.P.; Bitter, J.H. Toward stable nickel catalysts for aqueous phase reforming of biomass-derived feedstock under reducing and alkaline conditions. *J Catal* **2014**, *319*, 27-35, doi: 10.1016/j.jcat.2014.07.014.

151. Cobalt Institute promoting the sustainable and responsible production and use of cobalt in all forms. Available online: https://www.cobaltinstitute.org/production-and-supply.html (Accessed on 18 November 2020).

152. Mucha, L.; Sadof, K.D.; Frankel, T.C. Perspective - The hidden costs of cobalt mining. *Washington Post.* ISSN 0190-8286. 28 February 2018. Available online: https://www.washingtonpost.com/news/in-sight/wp/2018/02/28/the-cost-of-cobalt/ (Accessed on 07 November 2020).

153. Ayala, L.; Rondón, A. Efectos del trabajo infantil en la salud del menor trabajador. *Rev Salud Publica* **2004**, *6*, 270-288.

154. Disegi, J.A.; Kennedy, R.L.; Pilliar, R. *Cobalt-base Alloys for Biomedical Applications*, ASTM International: 1999; pp. 225.

155. Ostadi, M.; Rytter, E.; Hillestad, M. Evaluation of kinetic models for Fischer–Tropsch cobalt catalysts in a plug flow reactor. *Chem Eng Res Design* **2016**, *114*, 236-246, doi: 10.1016/j.cherd.2016.08.026.

156. Ohtsuka, Y.; Arai, T.; Takasaki, S.; Tsubouchi, N. Fischer–Tropsch Synthesis with Cobalt Catalysts Supported on Mesoporous Silica for Efficient Production of Diesel Fuel Fraction. *Energy Fuels* **2003**, *17*, 804-809, doi: 10.1021/ef020235r.

157. Javadli, R.; de Klerk, A. Desulfurization of heavy oil. *Appl Petrochem Res* **2012**, *1*, 3-19, doi: 10.1007/s13203-012-0006-6.

158. Orchin, M.; Rupilius, W. On the Mechanism of the Oxo Reaction. *Catal Rev Sci Eng* **1972**, *6*, 85-131, doi: 10.1080/01614947208078692.

159. Xie, X.; Yin, H.; Dou, B.; Huo, J. Characterization of a potassium-promoted cobalt–molybdenum/alumina water-gas shift catalyst. *Appl Catal* **1991**, *77*, 187-198, doi: 10.1016/0166-9834(91)80064-4.

160. Nagai, M.; Matsuda, K. Low-temperature water–gas shift reaction over cobalt–molybdenum carbide catalyst. *J Catal* **2006**, *238*, 489-496, doi: 10.1016/j.jcat.2006.01.003.

161. Taguchi, M.; Nakane, T.; Hashi, K.; Ohki, S.; Shimizu, T.; Sakka, Y.; Matsushita, A.; Abe, H.; Funazukuri, T.; Naka, T. Reaction temperature variations on the crystallographic state of spinel cobalt aluminate. *Dalton Trans* **2013**, *42*, 7167-7176, doi: 10.1039/C3DT32828G

162. Peymannia, M.; Soleimani-Gorgani, A.; Ghahari, M.; Jalili, M. The effect of different dispersants on the physical properties of nano $CoAl_2O_4$ ceramic ink-jet ink. *Ceram Int* **2015**, *41*, 9115-9121, doi: 10.1016/j.ceramint.2015.03.311.

163. Gaudon, M.; Robertson, L.C.; Lataste, E.; Duttine, M.; Ménétrier, M.; Demourgues, A. Cobalt and nickel aluminate spinels: Blue and cyan pigments. *Ceram Int* **2014**, *40*, 5201-5207, doi: 10.1016/j.ceramint.2013.10.081.

164. Granone, L.I.; Ulpe, A.C.; Robben, L.; Klimke, S.; Jahns, M.; Renz, F.; Gesing, T.M.; Bredow, T.; Dillert, R.; Bahnemann, D.W. Effect of the degree of inversion on optical properties of spinel ZnFe2O4. *Phys Chem Chem Phys* **2018**, *20*, 28267-28278, doi: 10.1039/C8CP05061A.

165. Liu, Y.; Jia, L.; Hou, B.; Sun, D.; Li, D. Cobalt aluminate-modified alumina as a carrier for cobalt in Fischer–Tropsch synthesis. *Appl Catal A Gen* **2017**, *530*, 30-36, doi: 10.1016/j.apcata.2016.11.014.

166. Zawadzki, M.; Walerczyk, W.; López-Suárez, F.E.; Illán-Gómez, M.J.; Bueno-López, A. $CoAl_2O_4$ spinel catalyst for soot combustion with NO_x/O_2. *Catal Commun* **2011**, *12*, 1238-1241, doi: 10.1016/j.catcom.2011.04.021.

167. Wong, Y.J.; Koh, M.K.; Khavarian, M.; Mohamed, A.R. Investigation on cobalt aluminate as an oxygen carrier catalyst for dry reforming of methane. *Int J Hydrog Energy* **2017**, *42*, 28363-28376, doi: 10.1016/j.ijhydene.2017.09.151.

168. Manfro, R.L.; Da Costa, A.F.; Ribeiro, N.F.P.; Souza, M.M.V.M. Hydrogen production by aqueous-phase reforming of glycerol over nickel catalysts supported on CeO_2. *Fuel Process Technol* **2011**, *92*, 330-335, doi: 10.1016/j.fuproc.2010.09.024.

169. Guo, Y.; Azmat, M.U.; Liu, X.; Wang, Y.; Lu, G. Effect of support's basic properties on hydrogen production in aqueous-phase reforming of

glycerol and correlation between WGS and APR. *Appl Energy* **2012**, *92*, 218-223, doi: 10.1016/j.apenergy.2011.10.020.

170. Matolín, V.; Cabala, M.; Matolínová, I.; Škoda, M.; Václavů, M.; Prince, K.C.; Skála, T.; Mori, T.; Yoshikawa, H.; Yamashita, Y.; Ueda, S.; Kobayashi, K. Pt and Sn Doped Sputtered CeO_2 Electrodes for Fuel Cell Applications. *Fuel Cells* **2010**, *10*, 139-144, doi: 10.1002/fuce.200900036.

171. Murray, E.P.; Tsai, T.; Barnett, S.A. A direct-methane fuel cell with a ceria-based anode. *Nature* **1999**, *400*, 649-651, doi: 10.1038/23220.

172. Sato, S.; Takahashi, R.; Sodesawa, T.; Honda, N.; Shimizu, H. Selective dehydration of diols to allylic alcohols catalyzed by ceria. *Catal Commun* **2003**, *4*, 77-81, doi: 10.1016/S1566-7367(02)00260-1.

173. Cutrufello, M.G.; Ferino, I.; Rombi, E.; Solinas, V.; Colón, G.; Navío, J.A. Catalytic activity of a ceria-lanthana system for 4-methylpentan-2-ol dehydration. *Reaction Kinetics and Catal Letters* **2003**, *79*, 93-99, doi: 10.1023/A:1024111801980.

174. Gliński, M.; Kijeński, J.; Jakubowski, A. Ketones from monocarboxylic acids: Catalytic ketonization over oxide systems. *Appl Catal A Gen* **1995**, *128*, 209-217, doi: 10.1016/0926-860X(95)00082-8.

175. Gliński, M.; Szudybill, J. Catalytic ketonization over oxide catalysts, Part VI.a Cross-ketonization of aliphatic and aromatic esters. *React Kinet Catal L* **2002**, *77*, 335-340, doi: 10.1023/A:1020844204146.

176. Plint, N.D.; Coville, N.J.; Lack, D.; Nattrass, G.L.; Vallay, T. The catalysed synthesis of symmetrical ketones from alcohols. *J Mol Catal A Chem* **2001**, *165*, 275-281, doi: 10.1016/S1381-1169(00)00445-3.

177. Vivier, L.; Duprez, D. Ceria-Based Solid Catalysts for Organic Chemistry. *ChemSusChem* **2010**, *3*, 654-678, doi: 10.1002/cssc.201000054.

178. Wang, Q.; Yeung, K.L.; Bañares, M.A. Ceria and its related materials for VOC catalytic combustion: A review. *Catal Today* **2020**, *356*, 141-154, doi: 10.1016/j.cattod.2019.05.016.

179. Shen, Q.; Lu, G.; Du, C.; Guo, Y.; Wang, Y.; Guo, Y.; Gong, X. Role and reduction of NOx in the catalytic combustion of soot over iron–ceria mixed oxide catalyst. *Chem Eng J* **2013**, *218*, 164-172, doi: 10.1016/j.cej.2012.12.010.

180. Gamboa-Rosales, N.K.; Ayastuy, J.L.; Gutiérrez-Ortiz, M.A. Effect of Au in Au–Co_3O_4/CeO_2 catalyst during oxygen-enhanced water gas shift. *Int*

J Hydrog Energy **2016**, *41*, 19408-19417, doi: 10.1016/j.ijhydene.2016.05.237.

181. Trimm, D.L. Coke formation and minimisation during steam reforming reactions. *Catal Today* **1997**, *37*, 233-238, doi: 10.1016/S0920-5861(97)00014-X.

182. Roy, B.; Leclerc, C.A. Study of preparation method and oxidization/reduction effect on the performance of nickel-cerium oxide catalysts for aqueous-phase reforming of ethanol. *J Power Sources* **2015**, *299*, 114-124, doi: 10.1016/j.jpowsour.2015.08.069.

183. Yu, W.; Porosoff, M.D.; Chen, J.G. Review of Pt-Based Bimetallic Catalysis: From Model Surfaces to Supported Catalysts. *Chem Rev* **2012**, *112*, 5780-5817, doi: 10.1021/cr300096b.

184. Morozan, A.; Jousselme, B.; Palacin, S. Low-platinum and platinum-free catalysts for the oxygen reduction reaction at fuel cell cathodes. *Energy Environ Sci* **2011**, *4*, 1238-1254, doi: 10.1039/C0EE00601G.

185. Guha, A.; Lu, W.; Zawodzinski, T.A.; Schiraldi, D.A. Surface-modified carbons as platinum catalyst support for PEM fuel cells. *Carbon* **2007**, *45*, 1506-1517, doi: 10.1016/j.carbon.2007.03.023.

186. Davda, R.R.; Shabaker, J.W.; Huber, G.W.; Cortright, R.D.; Dumesic, J.A. Aqueous-phase reforming of ethylene glycol on silica-supported metal catalysts. *Appl Catal B Environ* **2003**, *43*, 13-26, doi: 10.1016/S0926-3373(02)00277-1.

187. King, D.L.; Zhang, L.; Xia, G.; Karim, A.M.; Heldebrant, D.J.; Wang, X.; Peterson, T.; Wang, Y. Aqueous phase reforming of glycerol for hydrogen production over Pt-Re supported on carbon. *Appl Catal B Environ* **2010**, *99*, 206-213, doi: 10.1016/j.apcatb.2010.06.021.

188. He, C.; Zheng, J.; Wang, K.; Lin, H.; Wang, J.; Yang, Y. Sorption enhanced aqueous phase reforming of glycerol for hydrogen production over Pt-Ni supported on multi-walled carbon nanotubes. *Appl Catal B Environ* **2015**, *162*, 401-411, doi: 10.1016/j.apcatb.2014.07.012.

189. Dietrich, P.J.; Akatay, M.C.; Sollberger, F.G.; Stach, E.A.; Miller, J.T.; Delgass, W.N.; Ribeiro, F.H. Effect of Co Loading on the Activity and Selectivity of PtCo Aqueous Phase Reforming Catalysts. *ACS Catal* **2014**, *4*, 480-491, doi: 10.1021/cs4008705.

190. Aguirre, M.A.; Hidalgo, M.; Canals, A. *Análisis elemental con técnicas basadas en plasma: ICP-OES/MS y LIBS: Avances en la preparación de*

muestras líquidas: nebulización múltiple y microextracción en gota, Publicia: 2017.

191. Madinabeitia, S.G.d.; Lorda, M.E.S.; Ibarguchi, J.I.G. Simultaneous determination of major to ultratrace elements in geological samples by fusion-dissolution and inductively coupled plasma mass spectrometry techniques. *Anal Chim Acta* **2008**, *625*, 117-130, doi: 10.1016/j.aca.2008.07.024.

192. Condon, J.B. *Surface Area and Porosity Determinations by Physisorption: Measurements and Theory*, Elsevier Science: 2006.

193. Brunauer, S.; Emmett, P.H.; Teller, E. Adsorption of Gases in Multimolecular Layers. *J Am Chem Soc* **1938**, *60*, 309-319, doi: 10.1021/ja01269a023.

194. Matthias, T.; Katsumi, K.; Neimark, A.V.; Olivier, J.P.; Rodriguez-Reinoso Francisco; Jean, R.; Sing, K.S. Physisorption of gases, with special reference to the evaluation of surface area and pore size distribution (IUPAC Technical Report). *Pure Appl Chem* **2015**, *87*, 1051, doi 10.1515/pac-2014-1117.

195. Shih, K. *X-Ray Diffraction: Structure, Principles and Applications*, Nova Science Publishers, Incorporated: 2013.

196. Robinson, I.K.; Tweet, D.J. Surface X-ray diffraction. *Rep Prog Phys* **1992**, *55*, 599-651, doi: 10.1088/0034-4885/55/5/002.

197. Fadoni, M.; Lucarelli, L. Temperature programmed desorption, reduction, oxidation and flow chemisorption for the characterisation of heterogeneous catalysts. Theoretical aspects, instrumentation and applications. *Stud Surf Sci Catal* **1999**, *120 A*, 177-225.

198. Gorte, R.J. Temperature-programmed desorption for the characterization of oxide catalysts. *Catal Today* **1996**, *28*, 405-414, doi: 10.1016/S0920-5861(96)00249-0.

199. Christmann, K. Some general aspects of hydrogen chemisorption on metal surfaces. *Prog in Surf Sci* **1995**, *48*, 15-26, doi: 10.1016/0079-6816(95)93412-Z.

200. Reuel, R.C.; Bartholomew, C.H. The stoichiometries of H_2 and CO adsorptions on cobalt: Effects of support and preparation. *J Catal* **1984**, *85*, 63-77, doi: 10.1016/0021-9517(84)90110-6.

201. Jongsomjit, B.; Goodwin, J.G. Co-support compound formation in Co/Al$_2$O$_3$ catalysts: effect of reduction gas containing CO. *Catal Today* **2002**, *77*, 191-204, doi: 10.1016/S0920-5861(02)00245-6.

202. Coats, A.W.; Redfern, J.P. Thermogravimetric analysis. A review. *Analyst* **1963,** *88*, 906-924, doi: 10.1039/AN9638800906.

203. Weyland, M. Electron Tomography of Catalysts. *Top Catal* **2002**, *21*, 175-183, doi: 10.1023/A:1021385427655.

204. Makuła, P.; Pacia, M.; Macyk, W. How To Correctly Determine the Band Gap Energy of Modified Semiconductor Photocatalysts Based on UV–Vis Spectra. *J Phys Chem Lett* **2018**, *9*, 6814-6817, doi: 10.1021/acs.jpclett.8b02892.

205. Chen, F. Basic Principles and Applications of Solid-State NMR in Catalysis. *J Thermodyn Cataly* **2014**, *5*, 1-2, doi: 10.4172/2157-7544.1000e127.

206. Walls, J.M. *Methods of Surface Analysis: Techniques and Applications*, Cambridge University Press: 1990.

207. Wachs, I.E. In situ Raman spectroscopy studies of catalysts. *Top Catal* **1999**, *8*, 57-63, doi: 10.1023/A:1019100925300.

208. Martin, D.; Duprez, D. Evaluation of the acid-base surface properties of several oxides and supported metal catalysts by means of model reactions. *J Mol Catal A Chem* **1997**, *118*, 113-128, doi: 10.1016/S1381-1169(96)00371-8.

209. Karmal, S.; Perot, G.; Duprez, D. Role of the support in the skeletal isomerization of 3,3-dimethyl-1-butene on oxided and sulfided CoMo/Al$_2$O$_3$ catalysts. *J Catal* **1991**, *130*, 212-219, doi: 10.1016/0021-9517(91)90105-D.

210. Boudart, M. Catalysis by Supported Metals. *Adv Catal* **1969**, *20*, 153-166, doi: 10.1016/S0360-0564(08)60271-0.

211. Blakely, D.W.; Somorjai, G.A. The dehydrogenation and hydrogenolysis of cyclohexane and cyclohexene on stepped (high miller index) platinum surfaces. *J Catal* **1976**, *42*, 181-196, doi: 10.1016/0021-9517(76)90252-9.

212. González-Marcos, M.P.; Iñarra, B.; Guil, J.M.; Gutiérrez-Ortiz, M.A. Use of test reactions for the characterisation of bimetallic Pt-Sn/Al$_2$O$_3$ catalysts. *Appl Catal A Gen* **2004**, *273*, 259-268, doi: 10.1016/j.apcata.2004.06.041.

213. Pairojpiriyakul, T.; Croiset, E.; Kiatkittipong, W.; Kiatkittipong, K.; Arpornwichanop, A.; Assabumrungrat, S. Hydrogen production from catalytic supercritical water reforming of glycerol with cobalt-based catalysts. *Int J Hydrog Energy* **2013**, *38*, 4368-4379, doi: 10.1016/j.ijhydene.2013.01.169.

214. Grenoble, D.C.; Estadt, M.M.; Ollis, D.F. The chemistry and catalysis of the water gas shift reaction: 1. The kinetics over supported metal catalysts. *J Catal* **1981**, *67*, 90-102, doi: 10.1016/0021-9517(81)90263-3.

215. Llorca, J.; Homs, N.; Sales, J.; de la Piscina, P.R. Efficient Production of Hydrogen over Supported Cobalt Catalysts from Ethanol Steam Reforming. *J Catal* **2002**, *209*, 306-317, doi: 10.1006/jcat.2002.3643.

216. Banach, B.; Machocki, A.; Rybak, P.; Denis, A.; Grzegorczyk, W.; Gac, W. Selective production of hydrogen by steam reforming of bio-ethanol. *Catal Today* **2011**, *176*, 28-35, doi: 10.1016/j.cattod.2011.06.006.

217. Davidson, S.D.; Sun, J.; Hong, Y.; Karim, A.M.; Datye, A.K.; Wang, Y. The effect of ZnO addition on Co/C catalyst for vapor and aqueous phase reforming of ethanol. *Catal Today* **2014**, *233*, 38-45, doi: 10.1016/j.cattod.2013.12.044.

218. Skoufa, Z.; Xantri, G.; Heracleous, E.; Lemonidou, A.A. A study of Ni–Al–O mixed oxides as catalysts for the oxidative conversion of ethane to ethylene. *Appl Catal A Gen* **2014**, *471*, 107-117, doi: 10.1016/j.apcata.2013.11.042.

219. Savova, B.; Loridant, S.; Filkova, D.; Millet, J.M.M. Ni–Nb–O catalysts for ethane oxidative dehydrogenation. *Appl Catal A Gen* **2010**, *390*, 148-157, doi: 10.1016/j.apcata.2010.10.004.

220. Solsona, B.; Concepción, P.; Demicol, B.; Hernández, S.; Delgado, J.J.; Calvino, J.J.; López Nieto, J.M. Selective oxidative dehydrogenation of ethane over SnO_2-promoted NiO catalysts. *J Catal* **2012**, *295*, 104-114, doi: 10.1016/j.jcat.2012.07.028.

221. Zhu, H.; Ould-Chikh, S.; Anjum, D.H.; Sun, M.; Biausque, G.; Basset, J.; Caps, V. Nb effect in the nickel oxide-catalyzed low-temperature oxidative dehydrogenation of ethane. *J Catal* **2012**, *285*, 292-303, doi: 10.1016/j.jcat.2011.10.005.

222. Li, G.; Hu, L.; Hill, J.M. Comparison of reducibility and stability of alumina-supported Ni catalysts prepared by impregnation and co-precipitation. *Appl Catal A Gen* **2006**, *301*, 16-24, doi: 10.1016/j.apcata.2005.11.013.

223. Bartholomew, C.H. Mechanisms of catalyst deactivation. *Appl Catal A Gen* **2001**, *212*, 17-60, doi: 10.1016/S0926-860X(00)00843-7.

224. Ji, Y.; Zhao, Z.; Duan, A.; Jiang, G.; Liu, J. Comparative Study on the Formation and Reduction of Bulk and Al_2O_3-Supported Cobalt Oxides by H_2-TPR Technique. *J Phys Chem C* **2009**, *113*, 7186-7199, doi: 10.1021/jp8107057.

225. Musolino, M.G.; Busacca, C.; Mauriello, F.; Pietropaolo, R. Aliphatic carbonyl reduction promoted by palladium catalysts under mild conditions. *Appl Catal A Gen* **2010**, *379*, 77-86, doi: 10.1016/j.apcata.2010.03.008.

226. Kung, H.H. Catalytic behavior of a cation in a solid solution—An electrostatic potential approach. *J Catal* **1982**, *73*, 387-395, doi: 10.1016/0021-9517(82)90111-7.

227. Jongsomjit, B.; Panpranot, J.; Goodwin Jr., J.G. Co-support compound formation in alumina-supported cobalt catalysts. *J Catal* **2001**, *204*, 98-109, doi: 10.1006/jcat.2001.3387.

228. Srisawad, N.; Chaitree, W.; Mekasuwandumrong, O.; Praserthdam, P.; Panpranot, J. Formation of $CoAl_2O_4$ Nanoparticles via Low-Temperature Solid-State Reaction of Fine Gibbsite and Cobalt Precursor. *J Nanomater* **2012**, *2012*, 108369, doi: 10.1155/2012/108369.

229. Kannan, S.; Swamy, C.S. Catalytic decomposition of nitrous oxide over calcined cobalt aluminum hydrotalcites. *Catal Today* **1999**, *53*, 725-737.

230. Hemeda, O.M.; Amer, M.A.; Aboul-Enein, S.; Ahmed, M.A. Effect of sintering on X-Ray and IR spectral behaviour of the $MnAl_xFe_{2-x}O_4$ ferrite system. *phys stat sol (a)* **1996**, *156*, 29-38, doi: 10.1002/pssa.2211560105.

231. Ray, A.E.; Smith, S.R.; Scofield, J.D. Study of the phase transformation of cobalt. *J Phase Equilib* **1991**, *12*, 644-647, doi: 10.1007/BF02645161.

232. Yang, X.; Sun, Z.; Wang, D.; Forsling, W. Surface acid–base properties and hydration/dehydration mechanisms of aluminum (hydr)oxides. *J Colloid Interface Sci* **2007**, *308*, 395-404, doi: 10.1016/j.jcis.2006.12.023.

233. Liu, Y.; Chen, Z.; Hu, S.; Yu, G.; Peng, Y. The influence of silicon atom doping phagraphene nanoribbons on the electronic and magnetic properties. *Mater Sci Eng B Solid State Adv Technol* **2017**, *220*, 30-36, doi: 10.1016/j.mseb.2017.03.002.

234. Choojun, K.; Worathanaseth, A.; Kuhatasanadeekul, S.; Kurato, T.; Ketaniruj, S.; Phichitsurathaworn, P.; Promchana, P.; Prakobtham, K.;

Numwong, N.; Poo-arporn, Y.; Sooknoi, T. Effect of cobalt complex precursors on reactivity of cationic cobalt catalysts: Cyclohexane dehydrogenation. *Catal Commun* **2019**, *125*, 108-113, doi: 10.1016/j.catcom.2019.04.005.

235. Drault, F. *Développement de catalyseurs à base de métaux de transitionnon nobles en remplacement du platine pour des réactionsd'hydrogénation*. PhD Thesis: Université de Poitiers, 2018; pp. 251. Available online: http://theses.univ-poitiers.fr

236. Ai, L.; Jiang, J. Rapid synthesis of nanocrystalline Co_3O_4 by a microwave-assisted combustion method. *Powder Technol* **2009**, *195*, 11-14, doi: 10.1016/j.powtec.2009.05.006.

237. Tang, C.; Wang, C.; Chien, S. Characterization of cobalt oxides studied by FT-IR, Raman, TPR and TG-MS. *Thermochim Acta* **2008**, *473*, 68-73, doi: 10.1016/j.tca.2008.04.015.

238. Mindru, I.; Marinescu, G.; Gingasu, D.; Patron, L.; Ghica, C.; Giurginca, M. Blue $CoAl_2O_4$ spinel via complexation method. *Mater Chem Phys* **2010**, *122*, 491-497, doi: 10.1016/j.matchemphys.2010.03.032.

239. Alex, T.C.; Kumar, R.; Roy, S.K.; Mehrotra, S.P. Mechanically induced reactivity of gibbsite: Part 2. Attrition milling. *Powder Technol* **2014**, *264*, 229-235, doi: 0.1016/j.powtec.2014.05.029.

240. Brik, Y.; Kacimi, M.; Ziyad, M.; Bozon-Verduraz, F. Titania-Supported Cobalt and Cobalt–Phosphorus Catalysts: Characterization and Performances in Ethane Oxidative Dehydrogenation. *J Catal* **2001**, *202*, 118-128, doi: 10.1006/jcat.2001.3262.

241. Vakros, J.; Kordulis, C.; Lycourghiotis, A. Cobalt Oxide Supported γ-Alumina Catalyst with Very High Active Surface Area Prepared by Equilibrium Deposition Filtration. *Langmuir* **2002**, *18*, 417-422, doi: 10.1021/la010040w.

242. Wood, D.L.; Remeika, J.P. Optical Absorption of Tetrahedral Co^{3+} and Co^{2+} in Garnets. *J Chem Phys* **1967**, *46*, 3595-3602, doi: 10.1063/1.1841263.

243. Sarellas, A.; Niakolas, D.; Bourikas, K.; Vakros, J.; Kordulis, C. The influence of the preparation method and the Co loading on the structure and activity of cobalt oxide/γ-alumina catalysts for NO reduction by propene. *J Colloid Interface Sci* **2006**, *295*, 165-172, doi: 10.1016/j.jcis.2005.08.020.

244. Olusola, O.J.; Sudip, M. Temperature programme reduction (TPR) studies of cobalt phases in γ-alumina supported cobalt catalysts. *J. Pet. Technol. Altern. Fuels* **2016**, *7(1)*, 1-12, doi: 10.5897/JPTAF2015.0122

245. Šepelák, V.; Indris, S.; Bergmann, I.; Feldhoff, A.; Becker, K.D.; Heitjans, P. Nonequilibrium cation distribution in nanocrystalline $MgAl_2O_4$ spinel studied by ^{27}Al magic-angle spinning NMR. *Solid State Ion* **2006**, *177*, 2487-2490, doi: 10.1016/j.ssi.2006.04.014.

246. Šepelák, V.; Bergmann, I.; Indris, S.; Feldhoff, A.; Hahn, H.; Becker, K.D.; Grey, C.P.; Heitjans, P. High-resolution ^{27}Al MAS NMR spectroscopic studies of the response of spinel aluminates to mechanical action. *J Mater Chem* **2011**, *21*, 8332-8337, doi: 10.1039/C0JM03721D.

247. Voß, M.; Borgmann, D.; Wedler, G. Characterization of Alumina, Silica, and Titania Supported Cobalt Catalysts. *J Catal* **2002**, *212*, 10-21, doi: 10.1006/jcat.2002.3739.

248. Gazzoli, D.; Occhiuzzi, M.; Cimino, A.; Cordischi, D.; Minelli, G.; Pinzari, F. XPS and EPR study of high and low surface area CoO–MgO solid solutions: surface composition and Co^{2+} ion dispersion. *J Chem Soc, Faraday Trans* **1996**, *92*, 4567-4574, doi: 10.1039/FT9969204567.

249. Chen, Z.; Shi, E.; Li, W.; Zheng, Y.; Zhuang, J.; Xiao, B.; Tang, L. Preparation of nanosized cobalt aluminate powders by a hydrothermal method. *Mater Sci Eng B Solid State Adv Technol* **2004**, *107*, 217-223, doi: 10.1016/j.mseb.2003.11.013.

250. Biesinger, M.C.; Payne, B.P.; Grosvenor, A.P.; Lau, L.W.M.; Gerson, A.R.; Smart, R.S.C. Resolving surface chemical states in XPS analysis of first row transition metals, oxides and hydroxides: Cr, Mn, Fe, Co and Ni. *Appl Surf Sci* **2011**, *257*, 2717-2730, doi: 10.1016/j.apsusc.2010.10.051.

251. Pawlak, D.A.; Woźniak, K.; Frukacz, Z.; Barr, T.L.; Fiorentino, D.; Seal, S. ESCA Studies of Yttrium Aluminum Garnets. *J. Phys. Chem. B* **1999**, *103*, 1454-1461.

252. Hu, B.; Kim, W.; Sulmonetti, T.P.; Sarazen, M.L.; Tan, S.; So, J.; Liu, Y.; Dixit, R.S.; Nair, S.; Jones, C.W. A Mesoporous Cobalt Aluminate Spinel Catalyst for Nonoxidative Propane Dehydrogenation. *ChemCatChem* **2017**, *9*, 3330-3337, doi: 10.1002/cctc.201700647.

253. Azer, C.; Ramadan, A.R.; Ghaly, G.; Ragai, J. Preparation and Characterization of Cobalt Aluminate Spinels $CoAl_2O_4$ Doped with Magnesium Oxide. *Adsorp Sci Technol* **2012**, *30*, 399-407, doi: 10.1260/0263-6174.30.5.399.

254. Hegde, S.; Tharpa, K.; Akuri, S.R.; K., R.; Kumar, A.; Deshpande, R.; Nair, S.A. In situ spectroscopic studies on vapor phase catalytic decomposition of dimethyl oxalate. *Phys Chem Chem Phys* **2017**, *19*, 8034-8045, doi: 10.1039/C6CP07769B.

255. Di Cosimo, J.I.; Díez, V.K.; Xu, M.; Iglesia, E.; Apesteguía, C.R. Structure and Surface and Catalytic Properties of Mg-Al Basic Oxides. *J Catal* **1998**, *178*, 499-510, doi: 10.1006/jcat.1998.2161.

256. Pala Rosas, I.; Contreras, J.L.; Salmones, J.; Tapia, C.; Zeifert, B.; Navarrete, J.; Vázquez, T.; García, D.C. Catalytic Dehydration of Glycerol to Acrolein over a Catalyst of Pd/LaY Zeolite and Comparison with the Chemical Equilibrium. *Catalysts* **2017**, *7*, doi: 10.3390/catal7030073.

257. Gandarias, I.; Arias, P.L.; Requies, J.; Güemez, M.B.; Fierro, J.L.G. Hydrogenolysis of glycerol to propanediols over a Pt/ASA catalyst: The role of acid and metal sites on product selectivity and the reaction mechanism. *Appl Catal B Environ* **2010**, *97*, 248-256, doi: 10.1016/j.apcatb.2010.04.008.

258. Guo, X.; Li, Y.; Song, W.; Shen, W. Glycerol Hydrogenolysis over Co Catalysts Derived from a Layered Double Hydroxide Precursor. *Catal Letters* **2011**, *141*, 1458, doi: 10.1007/s10562-011-0642-y.

259. Li, Y.; Liu, H.; Ma, L.; He, D. Glycerol hydrogenolysis to propanediols over supported Pd–Re catalysts. *RSC Adv* **2014**, *4*, 5503-5512, doi: 10.1039/C3RA46134C.

260. Kurajica, S.; Popović, J.; Tkalčec, E.; Gržeta, B.; Mandić, V. The effect of annealing temperature on the structure and optical properties of sol–gel derived nanocrystalline cobalt aluminate spinel. *Mater Chem Phys* **2012**, *135*, 587-593, doi: 10.1016/j.matchemphys.2012.05.030.

261. Remón, J.; Giménez, J.R.; Valiente, A.; García, L.; Arauzo, J. Production of gaseous and liquid chemicals by aqueous phase reforming of crude glycerol: Influence of operating conditions on the process. *Energy Convers Manag* **2016**, *110*, 90-112, doi: 10.1016/j.enconman.2015.11.070.

262. El Doukkali, M.; Iriondo, A.; Arias, P.L.; Requies, J.; Gandarías, I.; Jalowiecki-Duhamel, L.; Dumeignil, F. A comparison of sol–gel and impregnated Pt or/and Ni based γ-alumina catalysts for bioglycerol aqueous phase reforming. *Appl Catal B Environ* **2012**, *125*, 516-529, doi: 10.1016/j.apcatb.2012.06.024.

263. Vannice, M.A. The catalytic synthesis of hydrocarbons from H_2:CO mixtures over the group VIII metals: I. The specific activities and product distributions of supported metals. *J Catal* **1975**, *37*, 449-461, doi: 10.1016/0021-9517(75)90181-5.

264. Stangeland, K.; Kalai, D.; Li, H.; Yu, Z. CO_2 Methanation: The Effect of Catalysts and Reaction Conditions. *Energy Procedia* **2017**, *105*, 2022-2027, doi: 10.1016/j.egypro.2017.03.577.

265. Kirilin, A.; Tokarev, A.; Murzina, E.; Kustov, L.; Mikkola, J.; Murzin, D. Reaction Products and Transformations of Intermediates in the Aqueous-Phase Reforming of Sorbitol. *ChemSusChem* **2010**, *3*, 708-718, doi: 10.1002/cssc.200900254.

266. Sanchez-Escribano, V.; Larrubia Vargas, M.A.; Finocchio, E.; Busca, G. On the mechanisms and the selectivity determining steps in syngas conversion over supported metal catalysts: An IR study. *Appl Catal A Gen* **2007**, *316*, 68-74, doi: 10.1016/j.apcata.2006.09.020.

267. Alhanash, A.; Kozhevnikova, E.F.; Kozhevnikov, I.V. Gas-phase dehydration of glycerol to acrolein catalysed by caesium heteropoly salt. *Appl Catal A Gen* **2010**, *378*, 11-18, doi: 10.1016/j.apcata.2010.01.043.

268. Maris, E.P.; Davis, R.J. Hydrogenolysis of glycerol over carbon-supported Ru and Pt catalysts. *J Catal* **2007**, *249*, 328-337, doi: 10.1016/j.jcat.2007.05.008.

269. de Vlieger, D.J.M.; Mojet, B.L.; Lefferts, L.; Seshan, K. Aqueous Phase Reforming of ethylene glycol – Role of intermediates in catalyst performance. *J Catal* **2012**, *292*, 239-245, doi: 10.1016/j.jcat.2012.05.019.

270. Sun, D.; Yamada, Y.; Sato, S.; Ueda, W. Glycerol hydrogenolysis into useful C3 chemicals. *Appl Catal B Environ* **2016**, *193*, 75-92, doi: 10.1016/j.apcatb.2016.04.013.

271. Lefèvre, G.; Duc, M.; Lepeut, P.; Caplain, R.; Fédoroff, M. Hydration of γ-Alumina in Water and Its Effects on Surface Reactivity. *Langmuir* **2002**, *18*, 7530-7537, doi: 10.1021/la025651i.

272. Tran, N.H.; Kannangara, G.S.K. Conversion of glycerol to hydrogen rich gas. *Chem Soc Rev* **2013**, *42*, 9454-9479, doi: 10.1039/C3CS60227C.

273. Kitakami, O.; Sato, H.; Shimada, Y.; Sato, F.; Tanaka, M. Size effect on the crystal phase of cobalt fine particles. *Phys Rev B* **1997**, *56*, 13849-13854, doi: 10.1103/PhysRevB.56.13849.

274. Ketchie, W.C.; Maris, E.P.; Davis, R.J. In-situ X-ray Absorption Spectroscopy of Supported Ru Catalysts in the Aqueous Phase. *Chem Mater* **2007**, *19*, 3406-3411, doi: 10.1021/cm0702868.

275. van Berge, P.J.; van de Loosdrecht, J.; Barradas, S.; van der Kraan, A.M. Oxidation of cobalt based Fischer–Tropsch catalysts as a deactivation mechanism. *Catal Today* **2000**, *58*, 321-334, doi: 10.1016/S0920-5861(00)00265-0.

276. Kirilin, A.V.; Tokarev, A.V.; Kustov, L.M.; Salmi, T.; Mikkola, J.; Murzin, D.Y. Aqueous phase reforming of xylitol and sorbitol: Comparison and influence of substrate structure. *Appl Catal A Gen* **2012**, *435-436*, 172-180, doi: 10.1016/j.apcata.2012.05.050.

277. Sievers, C.; Noda, Y.; Qi, L.; Albuquerque, E.M.; Rioux, R.M.; Scott, S.L. Phenomena Affecting Catalytic Reactions at Solid–Liquid Interfaces. *ACS Catal* **2016**, *6*, 8286-8307, doi: 10.1021/acscatal.6b02532.

278. de Sousa, F.F.; de Sousa, H.S.A.; Oliveira, A.C.; Junior, M.C.C.; Ayala, A.P.; Barros, E.B.; Viana, B.C.; Filho, J.M.; Oliveira, A.C. Nanostructured Ni-containing spinel oxides for the dry reforming of methane: Effect of the presence of cobalt and nickel on the deactivation behaviour of catalysts. *Int J Hydrog Energy* **2012**, *37*, 3201-3212, doi: 10.1016/j.ijhydene.2011.11.072.

279. Miranda, B.C.; Chimentão, R.J.; Santos, J.B.O.; Gispert-Guirado, F.; Llorca, J.; Medina, F.; Bonillo, F.L.; Sueiras, J.E. Conversion of glycerol over 10%Ni/γ-Al$_2$O$_3$ catalyst. *Appl Catal B Environ* **2014**, *147*, 464-480, doi: 10.1016/j.apcatb.2013.09.026.

280. Phung, T.K.; Pham, T.L.M.; Nguyen, A.T.; Vu, K.B.; Giang, H.N.; Nguyen, T.; Huynh, T.C.; Pham, H.D. Effect of Supports and Promoters on the Performance of Ni-Based Catalysts in Ethanol Steam Reforming. *Chem Eng Technol* **2020**, *43*, 672-688, doi: 10.1002/ceat.201900445.

281. Sádaba, I.; López Granados, M.; Riisager, A.; Taarning, E. Deactivation of solid catalysts in liquid media: the case of leaching of active sites in biomass conversion reactions. *Green Chem* **2015**, *17*, 4133-4145, doi: 10.1039/C5GC00804B.

282. Barbelli, M.L.; Pompeo, F.; Santori, G.F.; Nichio, N.N. Pt catalyst supported on α-Al$_2$O$_3$ modified with CeO$_2$ and ZrO$_2$ for aqueous-phase-reforming of glycerol. *Catal Today* **2013**, *213*, 58-64, doi: 10.1016/j.cattod.2013.02.023.

283. Rahman, M.M.; Church, T.L.; Minett, A.I.; Harris, A.T. Effect of CeO_2 Addition to Al_2O_3 Supports for Pt Catalysts on the Aqueous-Phase Reforming of Glycerol. *ChemSusChem* **2013**, *6*, 1006-1013, doi: https://doi.org/10.1002/cssc.201200797.

284. Chen, A.; Guo, H.; Song, Y.; Chen, P.; Lou, H. Recyclable CeO_2–ZrO_2 and CeO_2–TiO_2 mixed oxides based Pt catalyst for aqueous-phase reforming of the low-boiling fraction of bio-oil. *Int J Hydrog Energy* **2017**, *42*, 9577-9588, doi: 10.1016/j.ijhydene.2017.03.092.

285. Ayastuy, J.L.; Gurbani, A.; González-Marcos, M.P.; Gutiérrez-Ortiz, M.A. Selective CO oxidation in H_2 streams on $CuO/Ce_xZr_{1-x}O_2$ catalysts: Correlation between activity and low temperature reducibility. *Int J Hydrog Energy* **2012**, *37*, 1993-2006, doi: 10.1016/j.ijhydene.2011.04.178.

286. Li, P.; Chen, X.; Ma, L.; Bhat, A.; Li, Y.; Schwank, J.W. Effect of Ce and La dopants in Co_3O_4 nanorods on the catalytic activity of CO and C_3H_6 oxidation. *Catal Sci Technol* **2019**, *9*, 1165-1177, doi: 10.1039/C8CY02460J.

287. Babitha, K.K.; Sreedevi, A.; Priyanka, K.P.; Sabu, B.; Varghese, T. Structural characterization and optical studies of CeO_2 nanoparticles synthesized by chemical precipitation. *Indian J. Pure Appl. Phys* **2015**, *53(9)*, 596-603.

288. Ranga Rao, G.; Sahu, H.R. XRD and UV-Vis diffuse reflectance analysis of CeO_2-ZrO_2 solid solutions synthesized by combustion method. *J Chem Sci* **2001**, *113*, 651-658, doi: 10.1007/BF02708797.

289. Regulska, E.; Breczko, J.; Basa, A.; Dubis, A.T. Rare-Earth Metals-Doped Nickel Aluminate Spinels for Photocatalytic Degradation of Organic Pollutants. *Catalysts* **2020**, *10*, doi: 10.3390/catal10091003.

290. Bêche, E.; Charvin, P.; Perarnau, D.; Abanades, S.; Flamant, G. Ce 3d XPS investigation of cerium oxides and mixed cerium oxide ($Ce_xTi_yO_z$). *Surf Interface Anal* **2008**, *40*, 264-267, doi: 10.1002/sia.2686.

291. Kuo, Y.; Lee, C.; Chen, Y.; Liang, H. Gadolinia-doped ceria films deposited by RF reactive magnetron sputtering. *Solid State Ion* **2009**, *180*, 1421-1428, doi: 10.1016/j.ssi.2009.08.016.

292. Teterin, Y.A.; Teterin, A.Y.; Lebedev, A.M.; Utkin, I.O. The XPS spectra of cerium compounds containing oxygen. *J Electron Spectros Relat Phenomena* **1998**, *88-91*, 275-279, doi: 10.1016/S0368-2048(97)00139-4.

293. Achamma, G.; Qureshi, M.S.; Malik, M.M. X-Ray Photoelectron Spectroscopy and Raman Studies of ZnO:Ce Nanocrystals. *J Appl Spectrosc* **2019**, *86*, 831-835, doi: 10.1007/s10812-019-00902-5.

294. Liu, Y.; Dai, H.; Deng, J.; Xie, S.; Yang, H.; Tan, W.; Han, W.; Jiang, Y.; Guo, G. Mesoporous Co3O4-supported gold nanocatalysts: Highly active for the oxidation of carbon monoxide, benzene, toluene, and o-xylene. *J Catal* **2014**, *309*, 408-418, doi: 10.1016/j.jcat.2013.10.019.

295. Sun, M.; Li, W.; Zhang, B.; Cheng, G.; Lan, B.; Ye, F.; Zheng, Y.; Cheng, X.; Yu, L. Enhanced catalytic performance by oxygen vacancy and active interface originated from facile reduction of OMS-2. *Chem Eng J* **2018**, *331*, 626-635, doi: 10.1016/j.cej.2017.09.028.

296. Kong, M.; Li, Y.; Chen, X.; Tian, T.; Fang, P.; Zheng, F.; Zhao, X. Tuning the Relative Concentration Ratio of Bulk Defects to Surface Defects in TiO$_2$ Nanocrystals Leads to High Photocatalytic Efficiency. *J Am Chem Soc* **2011**, *133*, 16414-16417, doi: 10.1021/ja207826q.

297. Morterra, C.; Magnacca, G. Surface characterization of modified aluminas. Part 5.—Surface acidity and basicity of CeO$_2$–Al$_2$O$_3$ systems. *J Chem Soc, Faraday Trans* **1996**, *92*, 5111-5116, doi: 10.1039/FT9969205111.

298. Sahu, S.K., *Studies on liquid liquid extraction of Ce iii using some commercial extractants and their binary mixtures*. PhD Thesis: Department of Chemistry, Shiksha o Anusandhan University, 2017.

299. Ayastuy, J.L.; Iglesias-González, A.; Gutiérrez-Ortiz, M.A. Synthesis and characterization of low amount tin-doped ceria (Ce$_x$Sn$_{1-x}$O$_{2-\delta}$) for catalytic CO oxidation. *Chem Eng J* **2014**, *244*, 372-381, doi: 10.1016/j.cej.2014.01.077.

300. Beckers, J.; Rothenberg, G. Redox properties of doped and supported copper–ceria catalysts. *Dalton Trans* **2008**, 6573-6578, doi: 10.1039/B809769K.

301. Ochoa, A.; Arregi, A.; Amutio, M.; Gayubo, A.G.; Olazar, M.; Bilbao, J.; Castaño, P. Coking and sintering progress of a Ni supported catalyst in the steam reforming of biomass pyrolysis volatiles. *Appl Catal B Environ* **2018**, *233*, 289-300, doi: 10.1016/j.apcatb.2018.04.002.

302. Burton, J.C.; Sun, L.; Long, F.H.; Feng, Z.C.; Ferguson, I.T. First- and second-order Raman scattering from semi-insulating 4H–SiC. *Phys Rev B* **1999**, *59*, 7282-7284, doi: 10.1103/PhysRevB.59.7282.

303. Naumenko, A.P.; Korniyenko, N.E.; Yashchuk, V.M.; Singamaneni, S.; Bliznyuk Valery N.; Raman Spectroscopy of Carbon Nanostructures: Nonlinear Effects and Anharmonicity. In *Raman Spectroscopy for Nanomaterials Characterization*; Challa S.S.R. Kumar, Ed.; SpringerMaterials: 2012, doi: 10.1007/978-3-642-20620-7_7.

304. Kirilin, A.V.; Tokarev, A.V.; Manyar, H.; Hardacre, C.; Salmi, T.; Mikkola, J.; Murzin, D.Y. Aqueous phase reforming of xylitol over Pt-Re bimetallic catalyst: Effect of the Re addition. *Catal Today* **2014**, *223*, 97-107, doi: 10.1016/j.cattod.2013.09.020.

305. Jabłońska, M. TPR study and catalytic performance of noble metals modified Al_2O_3, TiO_2 and ZrO_2 for low-temperature NH_3-SCO. *Catal Commun* **2015**, *70*, 66-71, doi: 10.1016/j.catcom.2015.07.012.

306. Benvenutti, E.V.; Franken, L.; Moro, C.C.; Davanzo, C.U. FTIR Study of Hydrogen and Carbon Monoxide Adsorption on Pt/TiO_2, Pt/ZrO_2, and Pt/Al_2O_3. *Langmuir* **1999**, *15*, 8140-8146, doi: 10.1021/la990195s.

307. Fedyna, M.; Żak, A.; Jaroszewska, K.; Mokrzycki, J.; Trawczyński, J. Composite of Pt/AlSBA-15+zeolite catalyst for the hydroisomerization of n-hexadecane: The effect of platinum precursor. *Microporous Mesoporous Mater* **2020**, *305*, 110366, doi: 10.1016/j.micromeso.2020.110366.

308. Kwak, J.H.; Hu, J.Z.; Kim, D.H.; Szanyi, J.; Peden, C.H.F. Penta-coordinated Al^{3+} ions as preferential nucleation sites for BaO on γ-Al_2O_3: An ultra-high-magnetic field ^{27}Al MAS NMR study. *J Catal* **2007**, *251*, 189-194, doi: 10.1016/j.jcat.2007.06.029.

309. Zhang, J.; Sun, S.; Li, Y.; Zhang, X.; Zhang, P.; Fan, Y. A strategy in deep eutectic solvents for carbon nanotube-supported PtCo nanocatalysts with enhanced performance toward methanol electrooxidation. *Int J Hydrog Energy* **2017**, *42*, 26744-26751, doi: 10.1016/j.ijhydene.2017.09.090.

310. Khassin, A.A.; Yurieva, T.M.; Kaichev, V.V.; Bukhtiyarov, V.I.; Budneva, A.A.; Paukshtis, E.A.; Parmon, V.N. Metal–support interactions in cobalt-aluminum co-precipitated catalysts: XPS and CO adsorption studies. *J Mol Catal A Chem* **2001**, *175*, 189-204, doi: 10.1016/S1381-1169(01)00216-3.

311. Shyu, J.Z.; Otto, K. Identification of platinum phases on γ-alumina by XPS. *Appl Surf Sci* **1988**, *32*, 246-252, doi: 10.1016/0169-4332(88)90085-2.

312. Bergman, S.L.; Granestrand, J.; Tang, Y.; París, R.S.; Nilsson, M.; Tao, F.F.; Tang, C.; Pennycook, S.J.; Pettersson, L.J.; Bernasek, S.L. In-situ characterization by Near-Ambient Pressure XPS of the catalytically

active phase of Pt/Al$_2$O$_3$ during NO and CO oxidation. *Appl Catal B Environ* **2018**, *220*, 506-511, doi: 10.1016/j.apcatb.2017.08.047.

313. Coronado, I.; Stekrova, M.; Reinikainen, M.; Simell, P.; Lefferts, L.; Lehtonen, J. A review of catalytic aqueous-phase reforming of oxygenated hydrocarbons derived from biorefinery water fractions. *Int J Hydrog Energy* **2016**, *41*, 11003-11032, doi: 10.1016/j.ijhydene.2016.05.032.

314. Tsubaki, N.; Sun, S.; Fujimoto, K. Different Functions of the Noble Metals Added to Cobalt Catalysts for Fischer–Tropsch Synthesis. *J Catal* **2001**, *199*, 236-246, doi: 10.1006/jcat.2001.3163.

315. Wawrzetz, A.; Peng, B.; Hrabar, A.; Jentys, A.; Lemonidou, A.A.; Lercher, J.A. Towards understanding the bifunctional hydrodeoxygenation and aqueous phase reforming of glycerol. *J Catal* **2010**, *269*, 411-420, doi: 10.1016/j.jcat.2009.11.027.

316. Ravenelle, R.M.; Copeland, J.R.; Kim, W.; Crittenden, J.C.; Sievers, C. Structural Changes of γ-Al$_2$O$_3$-Supported Catalysts in Hot Liquid Water. *ACS Catal* **2011**, *1*, 552-561, doi: 10.1021/cs1001515.

317. Dietrich, P.J.; Sollberger, F.G.; Akatay, M.C.; Stach, E.A.; Delgass, W.N.; Miller, J.T.; Ribeiro, F.H. Structural and catalytic differences in the effect of Co and Mo as promoters for Pt-based aqueous phase reforming catalysts. *Appl Catal B Environ* **2014**, *156-157*, 236-248, doi: 10.1016/j.apcatb.2014.03.016.

318. Chen, W.; Kimpel, T.F.; Song, Y.; Chiang, F.; Zijlstra, B.; Pestman, R.; Wang, P.; Hensen, E.J.M. Influence of Carbon Deposits on the Cobalt-Catalyzed Fischer–Tropsch Reaction: Evidence of a Two-Site Reaction Model. *ACS Catal* **2018**, *8*, 1580-1590, doi: 10.1021/acscatal.7b03639.

319. Klouz, V.; Fierro, V.; Denton, P.; Katz, H.; Lisse, J.P.; Bouvot-Mauduit, S.; Mirodatos, C. Ethanol reforming for hydrogen production in a hybrid electric vehicle: process optimisation. *J Power Sources* **2002**, *105*, 26-34, doi: 10.1016/S0378-7753(01)00922-3.

320. Miao, B.; Ma, S.S.K.; Wang, X.; Su, H.; Chan, S.H. Catalysis mechanisms of CO$_2$ and CO methanation. *Catal Sci Technol* **2016**, *6*, 4048-4058, doi: 10.1039/C6CY00478D.

321. García-Serna, J.; Gallina, G.; Biasi, P.; Salmi, T. Liquid Holdup by Gravimetric Recirculation Continuous Measurement Method. Application to Trickle Bed Reactors under Pressure at Laboratory Scale. *Ind Eng Chem Res* **2017**, *56*, 13294-13300, doi: 10.1021/acs.iecr.7b01810.

322. Knobloch, C.; Güttel, R.; Turek, T. Holdup and Pressure Drop in Micro Packed-Bed Reactors for Fischer-Tropsch Synthesis. *Chem Ing Tech* **2013**, *85*, 455-460, doi: 10.1002/cite.201200202.

323. Sander, R. Compilation of Henry's law constants (version 4.0) for water as solvent. *Atmospheric Chem Phys* **2015**, *15*, 4399-4981, doi: 10.5194/acp-15-4399-2015.

324. Duarte de Farias, A.M.; Barandas, A.P.M.G.; Perez, R.F.; Fraga, M.A. Water-gas shift reaction over magnesia-modified Pt/CeO_2 catalysts. *J Power Sources* **2007**, *165*, 854-860, doi: 10.1016/j.jpowsour.2006.12.054.

325. Chen, W.; Pestman, R.; Zijlstra, B.; Filot, I.A.W.; Hensen, E.J.M. Mechanism of Cobalt-Catalyzed CO Hydrogenation: 1. Methanation. *ACS Catal* **2017**, *7*, 8050-8060, doi: 10.1021/acscatal.7b02757.

326. Liu, Q.; Bian, B.; Fan, J.; Yang, J. Cobalt doped Ni based ordered mesoporous catalysts for CO_2 methanation with enhanced catalytic performance. *Int J Hydrog Energy* **2018**, *43*, 4893-4901, doi: 10.1016/j.ijhydene.2018.01.132.

327. Jahangiri, H.; Bennett, J.; Mahjoubi, P.; Wilson, K.; Gu, S. A review of advanced catalyst development for Fischer–Tropsch synthesis of hydrocarbons from biomass derived syn-gas. *Catal Sci Technol* **2014**, *4*, 2210-2229, doi: 10.1039/C4CY00327F.

328. Herranz, T.; Deng, X.; Cabot, A.; Guo, J.; Salmeron, M. Influence of the Cobalt Particle Size in the CO Hydrogenation Reaction Studied by In Situ X-Ray Absorption Spectroscopy. *J Phys Chem B* **2009**, *113*, 10721-10727, doi: 10.1021/jp901602s.

329. Xiang, Y.; Kovarik, L.; Kruse, N. Rate and selectivity hysteresis during the carbon monoxide hydrogenation over promoted Co/MnO_x catalysts. *Nat Commun* **2019**, *10*, 3953, doi: 10.1038/s41467-019-11836-z.

330. Shabaker, J.W.; Davda, R.R.; Huber, G.W.; Cortright, R.D.; Dumesic, J.A. Aqueous-phase reforming of methanol and ethylene glycol over alumina-supported platinum catalysts. *J Catal* **2003**, *215*, 344-352, doi: 10.1016/S0021-9517(03)00032-0.

331. Catti, M.; Ghaani, M.R.; Pinus, I. Overpressure Role in Isothermal Kinetics of H_2 Desorption–Absorption: the $2LiBH_4$–Mg_2FeH_6 System. *J Phys Chem C* **2013**, *117*, 26460-26465, doi: 10.1021/jp409009n.

332. Razali, N.; Abdullah, A.Z. Production of lactic acid from glycerol via chemical conversion using solid catalyst: A review. *Appl Catal A Gen* **2017**, *543*, 234-246, doi: 10.1016/j.apcata.2017.07.002.

333. Papageridis, K.N.; Siakavelas, G.; Charisiou, N.D.; Avraam, D.G.; Tzounis, L.; Kousi, K.; Goula, M.A. Comparative study of Ni, Co, Cu supported on γ-alumina catalysts for hydrogen production via the glycerol steam reforming reaction. *Fuel Process Technol* **2016**, *152*, 156-175, doi: 10.1016/j.fuproc.2016.06.024.

334. Aman, D.; Radwan, D.; Ebaid, M.; Mikhail, S.; van Steen, E. Comparing nickel and cobalt perovskites for steam reforming of glycerol. *Mol Catal* **2018**, *452*, 60-67, doi: 10.1016/j.mcat.2018.03.022.

335. García, B.; Moreno, J.; Iglesias, J.; Melero, J.A.; Morales, G. Transformation of Glucose into Sorbitol on Raney Nickel Catalysts in the Absence of Molecular Hydrogen: Sugar Disproportionation vs Catalytic Hydrogen Transfer. *Top Catal* **2019**, *62*, 570-578, doi: 10.1007/s11244-019-01156-3.

336. Pérez, R.; Souza, M.; Tapanes, N.; Diaz, G.; Aranda, D. Production of Hydrogen from Aqueous Phase Reforming of Glycerol: Economic Evaluation. *Engineering* **2014**, *6*, 12-18.

337. Sladkovskiy, D.A.; Godina, L.I.; Semikin, K.V.; Sladkovskaya, E.V.; Smirnova, D.A.; Murzin, D.Y. Process design and techno-economical analysis of hydrogen production by aqueous phase reforming of sorbitol. *Chem Eng Res Design* **2018**, *134*, 104-116, doi: 10.1016/j.cherd.2018.03.041.

338. Faheem, M.; Saleheen, M.; Lu, J.; Heyden, A. Ethylene glycol reforming on Pt(111): first-principles microkinetic modeling in vapor and aqueous phases. *Catal Sci Technol* **2016**, *6*, 8242-8256, doi: 10.1039/C6CY02111E.

339. Pipitone, G.; Zoppi, G.; Bocchini, S.; Rizzo, A.M.; Chiaramonti, D.; Pirone, R.; Bensaid, S. Aqueous phase reforming of the residual waters derived from lignin-rich hydrothermal liquefaction: investigation of representative organic compounds and actual biorefinery streams. *Catal Today* **2020**, *345*, 237-250, doi: 10.1016/j.cattod.2019.09.040.

340. Duarte, H.A.; Sad, M.E.; Apesteguía, C.R. Bio-hydrogen production by APR of C_2-C_6 polyols on Pt/Al_2O_3: Dependence of H_2 productivity on metal content. *Catal Today* **2017**, *296*, 59-65, doi: 10.1016/j.cattod.2017.04.067.

341. Tokarev, A.V.; Kirilin, A.V.; Murzina, E.V.; Eränen, K.; Kustov, L.M.; Murzin, D.Y.; Mikkola, J.-. The role of bio-ethanol in aqueous phase reforming to sustainable hydrogen. *Int J Hydrog Energy* **2010**, *35*, 12642-12649, doi: 10.1016/j.ijhydene.2010.07.118.

342. Clarke, M.L. Hydroformylation. Fundamentals, Processes, and Applications in Organic Synthesis. By Armin Börner and Robert Franke. *Angew Chem Int Ed* **2016**, *55*, 13377-13377, doi: 10.1002/anie.201607967.

343. Eagan, N.M.; Chada, J.P.; Wittrig, A.M.; Buchanan, J.S.; Dumesic, J.A.; Huber, G.W. Hydrodeoxygenation of Sorbitol to Monofunctional Fuel Precursors over Co/TiO$_2$. *Joule* **2017**, *1*, 178-199, doi: 10.1016/j.joule.2017.07.004.

344. Tan, H.W.; Abdul Aziz, A.R.; Aroua, M.K. Glycerol production and its applications as a raw material: A review. *Renew Sust Energ Rev* **2013**, *27*, 118-127, doi: 10.1016/j.rser.2013.06.035.

345. Yang, F.; Hanna, M.A.; Sun, R. Value-added uses for crude glycerol-a byproduct of biodiesel production. *Biotechnol Biofuels* **2012**, *5*, 13, doi: 10.1186/1754-6834-5-13.

346. ISO 2098:1972 Glycerols for industrial use - Determination of ash - Gravimetric method. 1972.

347. Callison, J.; Subramanian, N.D.; Rogers, S.M.; Chutia, A.; Gianolio, D.; Catlow, C.R.A.; Wells, P.P.; Dimitratos, N. Directed aqueous-phase reforming of glycerol through tailored platinum nanoparticles. *App Catal B Environ* **2018**, *238*, 618-628, doi: 10.1016/j.apcatb.2018.07.008.

348. Bastan, F.; Kazemeini, M.; Larimi, A.S. Aqueous-phase reforming of glycerol for production of alkanes over Ni/Ce$_x$Zr$_{1-x}$O$_2$ nano-catalyst: Effects of the support's composition. *Renew Energy* **2017**, *108*, 417-424, doi: 10.1016/j.renene.2017.02.076.

349. Hájek, M.; Skopal, F. Treatment of glycerol phase formed by biodiesel production. *Bioresour Technol* **2010**, *101*, 3242-3245, doi: 10.1016/j.biortech.2009.12.094.

350. Li, D.; Li, Y.; Liu, X.; Guo, Y.; Pao, C.; Chen, J.; Hu, Y.; Wang, Y. NiAl$_2$O$_4$ Spinel Supported Pt Catalyst: High Performance and Origin in Aqueous-Phase Reforming of Methanol. *ACS Catal* **2019**, *9*, 9671-9682, doi: 10.1021/acscatal.9b02243.

351. Zhang, J.; Chen, J. Selective Transfer Hydrogenation of Biomass-Based Furfural and 5-Hydroxymethylfurfural over Hydrotalcite-Derived

Copper Catalysts Using Methanol as a Hydrogen Donor. *ACS Sustainable Chem Eng* **2017**, *5*, 5982-5993, doi: 10.1021/acssuschemeng.7b00778.

352. Mayorga, M.A.; Cadavid, J.; Lopez, C.; Suarez, O.; Bonilla, J.; Vargas, J.; Narvaez, P.; Rodriguez, L.I. Selection of Hydrogen Donors for the Production of Renewable Diesel by in Situ Catalytic Deoxygenation of Palm Oil. *Chem Eng Trans* **2020**, *80*, 61-66, doi: 10.3303/CET2080011.

353. Boga, D.A.; Liu, F.; Bruijnincx, P.C.A.; Weckhuysen, B.M. Aqueous-phase reforming of crude glycerol: effect of impurities on hydrogen production. *Catal Sci Technol* **2016**, *6*, 134-143, doi: 10.1039/C4CY01711K.

354. Zada, B.; Chen, M.; Chen, C.; Yan, L.; Xu, Q.; Li, W.; Guo, Q.; Fu, Y. Recent advances in catalytic production of sugar alcohols and their applications. *Sci China Chem* **2017**, *60*, 853-869, doi: 10.1007/s11426-017-9067-1.

355. He, Z.; Wang, X. Hydrodeoxygenation of model compounds and catalytic systems for pyrolysis bio-oils upgrading. *Catal Sustain Energy* **2012**, *1*, 28-52, doi: 10.2478/cse-2012-0004.

356. Moreno, B.M.; Li, N.; Lee, J.; Huber, G.W.; Klein, M.T. Modeling aqueous-phase hydrodeoxygenation of sorbitol over $Pt/SiO_2–Al_2O_3$. *RSC Adv* **2013**, *3*, 23769-23784, doi: 10.1039/C3RA45179H.

357. Vilcocq, L.; Koerin, R.; Cabiac, A.; Especel, C.; Lacombe, S.; Duprez, D. New bifunctional catalytic systems for sorbitol transformation into biofuels. *Appl Catal B Environ* **2014**, *148-149*, 499-508, doi: 10.1016/j.apcatb.2013.11.016.

358. Nakahara, M. The Science of Color. 2002, pp. 108.

359. Maris, E.P.; Ketchie, W.C.; Murayama, M.; Davis, R.J. Glycerol hydrogenolysis on carbon-supported PtRu and AuRu bimetallic catalysts. *J Catal* **2007**, *251*, 281-294, doi: 10.1016/j.jcat.2007.08.007.

360. Zhang, C.; Lai, Q.; Holles, J.H. Influence of adsorption strength in aqueous phase glycerol hydrodeoxygenation over Ni@Pt and Co@Pt overlayer catalysts. *Catal Sci Technol* **2016**, *6*, 4632-4643, doi: 10.1039/C6CY00097E.

361. Do, P.T.M.; Foster, A.J.; Chen, J.; Lobo, R.F. Bimetallic effects in the hydrodeoxygenation of meta-cresol on γ-Al_2O_3 supported Pt–Ni and Pt–Co catalysts. *Green Chem* **2012**, *14*, 1388-1397, doi: 10.1039/C2GC16544A.

362. Kim, S.; Kwon, E.E.; Kim, Y.T.; Jung, S.; Kim, H.J.; Huber, G.W.; Lee, J. Recent advances in hydrodeoxygenation of biomass-derived oxygenates over heterogeneous catalysts. *Green Chem* **2019**, *21*, 3715-3743, doi: 10.1039/C9GC01210A.

363. Vilcocq, L.; Cabiac, A.; Especel, C.; Lacombe, S.; Duprez, D. Sorbitol transformation in aqueous medium: Influence of metal/acid balance on reaction selectivity. *Catal Today* **2012**, *189*, 117-122, doi: 10.1016/j.cattod.2012.03.051.

364. Messou, D.; Vivier, L.; Canaff, C.; Especel, C. Biofuel Synthesis from Sorbitol by Aqueous Phase Hydrodeoxygenation over Bifunctional Catalysts: In-depth Study of the Ru–Pt/SiO_2–Al_2O_3 Catalytic System. *Catalysts* **2019**, *9*, doi: 10.3390/catal9020146.

365. Op de Beeck, B.; Dusselier, M.; Geboers, J.; Holsbeek, J.; Morré, E.; Oswald, S.; Giebeler, L.; Sels, B.F. Direct catalytic conversion of cellulose to liquid straight-chain alkanes. *Energy Environ Sci* **2015**, *8*, 230-240, doi: 10.1039/C4EE01523A.

366. Messou, D.; Vivier, L.; Especel, C. Sorbitol transformation over bimetallic Ru-Pt/SiO_2-Al_2O_3 catalysts: Effect of the preparation method. *Energy Convers Manag* **2016**, *127*, 55-65, doi: 10.1016/j.enconman.2016.08.095.

367. West, R.M.; Kunkes, E.L.; Simonetti, D.A.; Dumesic, J.A. Catalytic conversion of biomass-derived carbohydrates to fuels and chemicals by formation and upgrading of mono-functional hydrocarbon intermediates. *Catal Today* **2009**, *147*, 115-125, doi: 10.1016/j.cattod.2009.02.004.

368. Prins, R. Hydrogen Spillover. Facts and Fiction. *Chem Rev* **2012**, *112*, 2714-2738, doi: 10.1021/cr200346z.

369. Demsash, H.D.; Mohan, R. Steam reforming of glycerol to hydrogen over ceria promoted nickel–alumina catalysts. *Int J Hydrog Energy* **2016**, *41*, 22732-22742, doi: 10.1016/j.ijhydene.2016.10.082.

370. Godina, L.I.; Kirilin, A.V.; Tokarev, A.V.; Simakova, I.L.; Murzin, D.Y. Sibunit-Supported Mono- and Bimetallic Catalysts Used in Aqueous-Phase Reforming of Xylitol. *Ind Eng Chem Res* **2018**, *57*, 2050-2067, doi: 10.1021/acs.iecr.7b04937.

371. Siddiqi, M.A.; Lucas, K. Correlations for prediction of diffusion in liquids. *Can J Chem Eng* **1986**, *64*, 839-843, doi: 10.1002/cjce.5450640519.

372. Maloney, J.O. *Perry's Chemical Engineers' Handbook,* 8th ed.; McGraw-Hill Professional: 2008.

373. Ramachandran, P.A.; Chaudhari, R.V. *Three-phase Catalytic Reactors,* Gordon and Breach Science Publishers: 1983.

374. Chaudhari, R.V.; Gholap, R.V.; Emig, G.; Hofmann, H. Gas-liquid mass transfer in "dead-end" autoclave reactors. *Can J Chem Eng* **1987**, *65*, 744-751, doi: 10.1002/cjce.5450650506.

375. Crezee, E.; Hoffer, B.W.; Berger, R.J.; Makkee, M.; Kapteijn, F.; Moulijn, J.A. Three-phase hydrogenation of d-glucose over a carbon supported ruthenium catalyst—mass transfer and kinetics. *Appl Catal A Gen* **2003**, *251*, 1-17, doi: 10.1016/S0926-860X(03)00587-8.

376. 375. Wilke, C.R.; Chang, P. Correlation of diffusion coefficients in dilute solutions. *AIChE J* **1955**, *1*, 264-270, doi: 10.1002/aic.690010222.

Chapter 12

APPENDIX

A.   MASS TRANSFER LIMITATIONS

A.1   MASS TRANSFER LIMITATIONS ON FIXED-BED RACTOR

The existence of internal mass transfer limitations was checked by Weisz-Prater criterion:

$$\Phi_{WP} = \frac{(r_{obs}) \cdot \rho_p \cdot r_P^2}{D_{G-W,eff} \cdot C_{G,S}} \tag{A.1}$$

where (r_{obs}) is the observed reaction rate measured at the beginning of the reaction (mol·(s·kg$_{cat}$)$^{-1}$); ρ_{cat} is the catalyst density (4400 kg·m^{-3}); r_P is the catalyst particle radius (8·10^{-5} m, for the largest particle size); $D_{G-W,eff}$ is the effective diffusion coefficient of glycerol in water (m^2·s^{-1}); and $C_{G,s}$ is the glycerol concentration at the catalyst surface that was assumed the same as the bulk, namely 1108.5 mol·m^{-3}. This model assumes molecular diffusion of glycerol in pores filled with water solvent, and does not take into account the effect of the formation of gas bubbles (H$_2$, CO, CH$_4$, C$_{2+}$.) durig the reaction.

The effective diffusion coefficient was defined as:

$$D_{G-W,eff} = D_{G-W} \frac{\xi}{\tau} \tag{A.2}$$

where the ratio between ξ (porosity) and τ (tortuosity) was assumed to be 0.1 [370] and D_{G-W} was calculated using Siddiqi-Lucas correlation [371] for glycerol in water solutions:

$$D_{G-W} = 2.98 \cdot 10^{-7} \cdot V_{gly}^{-0.5473} \cdot \mu_w^{-1.026} \cdot T \tag{A.3}$$

where, V_{gly} is the molar volume of glycerol at boiling point (75.6 cm³·mol⁻¹); μ_w is water dynamic viscosity (estimated to be 0.111 mPa·s); and T is the absolute temperature.

Typical values that ensure the absence of internal mass diffusion limitations are as follows: $\Phi_{WP} < 6$ for a zero-order reaction; $\Phi_{WP} < 0.6$ for a first-order reaction; and $\Phi_{WP} < 0.3$ for a second-order reaction.

Table A.1 reports the values calculated to determine the mass transfer limitations. For all the experiments shown in this Thesis, the calculated value of Φ_{WP} fulfilled this condition.

Mears criterion was used to confirm the absence of external mass transfer limitations:

$$\frac{MR}{n} = \frac{\left(r_{obs}\right) \cdot \rho_{bed} \cdot r_P}{K_{L-S} \cdot C_{G,s}} < 0.15 \tag{A.4}$$

where n is the reaction order; ρ_{bed} is the packed bed density (kg·m⁻³); and K_{L-S} is the mass transfer coefficient (m·s⁻¹) that was estimated using the Chilton-Colburn analogy and Wilson-Geankoplis correlation for liquid mass transfer at very low Reynolds numbers (0.0015 < Re < 55) [372].

$$Sh = \frac{1.09}{\xi_{bed}} \cdot \mathrm{Re}^{1/3} \cdot Sc^{1/3} \tag{A.5}$$

$$\mathrm{Re} = \frac{2 \cdot r_P \cdot u_s \cdot \rho}{\mu_w} \tag{A.6}$$

$$Sc = \frac{\mu_w}{\rho \cdot D_{G-W}} \tag{A.7}$$

Table A.1. Weisz-Prater and Mears criterion values for glycerol APR reactions.

Chapter	Reaction conditions, °C/bar	catalyst mass, g	feedstream flow, cm^3·min^{-1}	WHSV, h^{-1}	Reaction rate, mol·(s·kg$_{cat}$)$^{-1}$	Φ_{WP}	MR/n
3-4	235/35	0.5	0.2	24.5	$7.39\cdot10^{-3}$	$1.39\cdot10^{-1}$	$7.00\cdot10^{-2}$
	260/50	0.5	0.2	24.5	$7.39\cdot10^{-3}$	$1.32\cdot10^{-1}$	$6.78\cdot10^{-2}$
5	260/50	1.8	0.02	0.68	$2.05\cdot10^{-4}$	$3.67\cdot10^{-3}$	$4.06\cdot10^{-3}$
6	260/50	0.9	0.1	6.80	$2.05\cdot10^{-3}$	$3.67\cdot10^{-2}$	$2.37\cdot10^{-2}$
	260/50	1.8	0.5	17.0	$5.13\cdot10^{-3}$	$9.18\cdot10^{-2}$	$3.47\cdot10^{-2}$
7	260/50	0.5	0.05	6.12	$1.85\cdot10^{-3}$	$3.30\cdot10^{-2}$	$2.69\cdot10^{-2}$
	260/50	0.5	0.45	55.1	$1.66\cdot10^{-2}$	$2.97\cdot10^{-1}$	$1.16\cdot10^{-1}$

$$K_{L-S} = \frac{Sh \cdot D_{G-W}}{2 \cdot r_P}$$ (A.8)

where Sh is the Sherwood number; ρ is the fluid density; Re is the particle Reynolds number; Sc is the Schmidt number; ξ_{bed} is bed porosity (typically 0.5); and u_s is the superficial velocity (m·s^{-1}).

Under the least favourable conditions, the obtained MR/n (Table A.1) confirm that external diffusion is negligible in the experiments performed for this work.

A.2   MASS TRANSFER LIMITATIONS FOR SORBITOL TRANSFORMATION

For sorbitol reactions (Chapter 8), the significance of gas-liquid, liquid-solid and internal mass transfer resistances were calculated from the correlations proposed by Ramachandran and Chaudhari [373].

   ×   <u>Gas-liquid mass transfer</u>

Gas-liquid mass transfer resistance is considered negligible if:

$$\varsigma_{G-L} = \frac{\left(r_{obs}\right)}{K_{G-L} \cdot a_b \cdot C_{gas}} < 0.1$$ (A.9)

where K_{G-L} is the gas-liquid mass transfer coefficient, which depends on agitation speed, impeller diameter, gas to liquid volume ratio, position of the impeller and reactor size [374], as follows:

$$K_{G-L} \cdot a_b = 1.48 \times 10^{-3} \left(N\right)^{2.18} \left(\frac{V_{gas}}{V_{liq}}\right)^{1.88} \left(\frac{d_i}{d_t}\right)^{2.16} \left(\frac{h_1}{h_2}\right)^{1.16}$$ (A.10)

The calculated values were determined to be in the range of $1.53 \cdot 10^{-7}$-$1.25 \cdot 10^{-2}$, which indicates that gas-liquid mass transfer limitation was insignificant in all experiments.

× Liquid-solid mass transfer

Liquid-solid mass transfer does not affect the reaction rate if:

$$\varsigma_{L-S} = \frac{(r_{obs}) \cdot r_P \cdot \rho_P}{3 \cdot w \cdot K_{L-S} \cdot C_{sorb}} < 0.1 \tag{A.11}$$

Where K_{L-S} is the liquid-solid mass transfer coefficient, estimated by means of the dimensionless Sherwood number (A.8) and the following equations [375]:

$$Sh = 2 + 0.4 \, \text{Re}^{3/4} \, Sc^{1/3} \tag{A.12}$$

$$\text{Re} = \left(\frac{16 \cdot N_P d_i^5 N^3 r_P^4 \rho_w^3}{\mu_w^3 \cdot V_{liq}} \right)^{1/3} \tag{A.13}$$

$$Sc = \frac{\mu_w}{\rho_w \cdot D_{S-W}} \tag{A.14}$$

The diffusion coefficient of sorbitol in water was calculated using the Wilke-Chang equation [376]:

$$D_{S-W} = \frac{7.4 \cdot 10^{-8} \left(\varphi \cdot M_w \right)^{1/2} T}{\mu_w \cdot V_{sorb}^{0.6}} \tag{A.15}$$

where φ is the association parameter of water (assumed 2.6); Mw is the molecular weight of water; and the molar volume of sorbitol at boiling point (V_{sorb}) is 122.15 cm³·mol⁻¹.

The highest calculated value for parameter ς_{L-S} was 1.42·10⁻², which ensures the absence of liquid-solid mass transfer limitation to the conditions studied.

   ×   <u>Internal mass transfer</u>

No pore diffusion limitations occur if

$$\Phi = \frac{d_p}{6} \left(\frac{(n+1) \cdot \rho_p \cdot r_{obs}}{2 \cdot D_{S-W,eff} \cdot w \cdot C_{sorb}} \right) < 0.2 \qquad\qquad \text{(A.16)}$$

At low sorbitol conversions, the calculated values reflected that it was on the boundaries for internal mass transfer effect (1.91·10⁻¹, in the worst scenario).

B.   PEARSON CORRELATION MATRIX OF GLYCEROL APR PRODUCTS FROM xCoAl CATALYSTS.

		H_2	CH_4	CO	CO_2	Ethylene	Ethane	Propane	Propylene	C_{4+}	Ethylene glycol	Propylene glycol	Hydroxyacetone	Ethanol
CH_4	r	-0.913**												
	p value	0.000												
CO	r	0.946**	-0.914**											
	p value	0.000	0.000											
CO_2	r	-0.988**	0.934**	-0.975**										
	p value	0.000	0.000	0.000										
Ethylene	r	0.967**	-0.948**	0.944**	-0.974**									
	p value	0.000	0.000	0.000	0.000									
Ethane	r	0.862**	-0.951**	0.924**	-0.907**	0.925**								
	p value	0.000	0.000	0.000	0.000	0.000								
Propane	r	0.546*	-0.751**	0.690**	-0.626*	0.675**	0.889**							
	p value	0.035	0.001	0.004	0.013	0.006	0.000							
Propylene	r	0.833**	-0.906**	0.891**	-0.896**	0.904**	0.924**	0.846**						
	p value	0.001	0.000	0.000	0.000	0.000	0.000	0.001						
C_{4+}	r	0.836**	-0.922**	0.901**	-0.891**	0.893**	0.983**	0.886**	0.873**					
	p value	0.000	0.000	0.000	0.000	0.000	0.000	0.000	0.000					
Ethylene glycol	r	-0.903**	0.956**	-0.947**	0.933**	-0.930**	-0.917**	-0.835**	-0.845**	-0.843**				
	p value	0.000	0.000	0.000	0.000	0.000	0.000	0.001	0.001	0.001				
1,2-Propylene glycol	r	0.255	-0.223	0.133	-0.141	0.241	0.020	-0.111	0.010	-0.127	-0.368			
	p value	0.423	0.486	0.681	0.661	0.451	0.950	0.731	0.976	0.695	0.239			
Hydroxyacetone	r	0.431	-0.451	0.417	-0.368	0.448	0.326	0.256	0.220	0.190	-.592*	.877**		
	p value	0.162	0.141	0.177	0.240	0.144	0.301	0.423	0.491	0.554	0.043	0.000		
Ethanol	r	-0.941**	0.972**	-0.975**	0.971**	-0.975**	-0.954**	-0.864**	-0.900**	-0.895**	0.984**	-0.274	-0.495	
	p value	0.000	0.000	0.000	0.000	0.000	0.000	0.000	0.000	0.000	0.000	0.389	0.102	
Acetone	r	-0.883**	0.952**	-0.969**	0.943**	-0.955**	-0.962**	-0.892**	-0.940**	-0.905**	0.954**	-0.197	-0.449	0.978**
	p value	0.000	0.000	0.000	0.000	0.000	0.000	0.000	0.000	0.000	0.000	0.540	0.143	0.000

**   Significant at $p < 0.01$ (two-tailed)

*   Significant at $p < 0.05$ (two-tailed)

C. EXTENSION OF SORBITOL TRANSFORMATION RESULTS

Table C.1. Carbon distribution in the liquid and gas phases for the rest of catalysts tested in sorbitol transformation. Reaction conditions: 10 g of sorbitol, 150 cm^3 of water, 1 g of catalyst, 240 °C and 60 bar.

Sample	Time, h	X_{sorb}, %	X_{gas}, %	Identification ratio[c]	Carbon selectivity for gaseous products			Carbon selectivity for liquid products			
					C_1	C_2-C_4	C_{5+}	C_1-C_4 MF	C_{5+} MF	C_1-C_4 HO	C_{5+} HO
0.25CoAl[a]	2	90.5	11.7	0.92	61.7	7.2	31.1	32.5	13.2	44.8	9.5
0.5CoAl[a]	2	90.4	13.9	1.08	63.8	7.3	28.9	38.8	21.9	14.9	24.4
0.3CeCoAl[a]	2	70.9	6.37	0.91	70.6	6.7	22.7	17.0	19.4	46.2	17.4
1Pt/CoAl[a]	2	90.2	14.3	0.93	59.7	4.2	36.1	36.9	10.8	39.6	12.6
0.25CoAl[b]	4	40.5	5.38	0.82	72.6	5.3	22.1	43.2	34.8	8.2	13.8
1Pt/CoAl[b]	2	57.2	13.7	0.87	74.0	3.6	22.4	44.8	25.4	10.5	19.3

[a] *Sorbitol HDO reaction at 70-90% of sorbitol conversion.*

[b] *sorbitol APR reaction at 40-57% of sorbitol conversion*

[c] *identification ratio= Σ(carbon concentration in each identified compound)/ $n_C^{t=0}$*

Table C.2. Summary of nitrogen adsorption-desorption, H_2-TPR and TPH results of used catalysts after sorbitol transformation.

	After HDO process				
Catalysts	S_{BET}, $m^2 \cdot g^{-1}$	V_P, $cm^3 \cdot g^{-1}$	d_P, nm	H_2 uptake, $mmol_{H2} \cdot g^{-1}$	$C_{deposits}$, $\mu mol_C \cdot g_{cat}^{-1}$
0.25CoAl	167.6	0.253	5.1	2.14	20.9
0.5CoAl	147.3	0.340	7.2	2.49	43.6
0.3CeCoAl	102.2	0.275	7.8	1.26	97.8
1Pt/CoAl	152.8	0.395	8.3	0.65	74.6
	After APR process				
Catalysts	S_{BET}, $m^2 \cdot g^{-1}$	V_P, $cm^3 \cdot g^{-1}$	d_P, nm	H_2 uptake, $mmol_{H2} \cdot g^{-1}$	$C_{deposits}$, $\mu mol_C \cdot g_{cat}^{-1}$
0.25CoAl	205.9	0.343	5.5	1.31	27.7
1Pt/CoAl	169.5	0.461	9.1	0.96	76.9
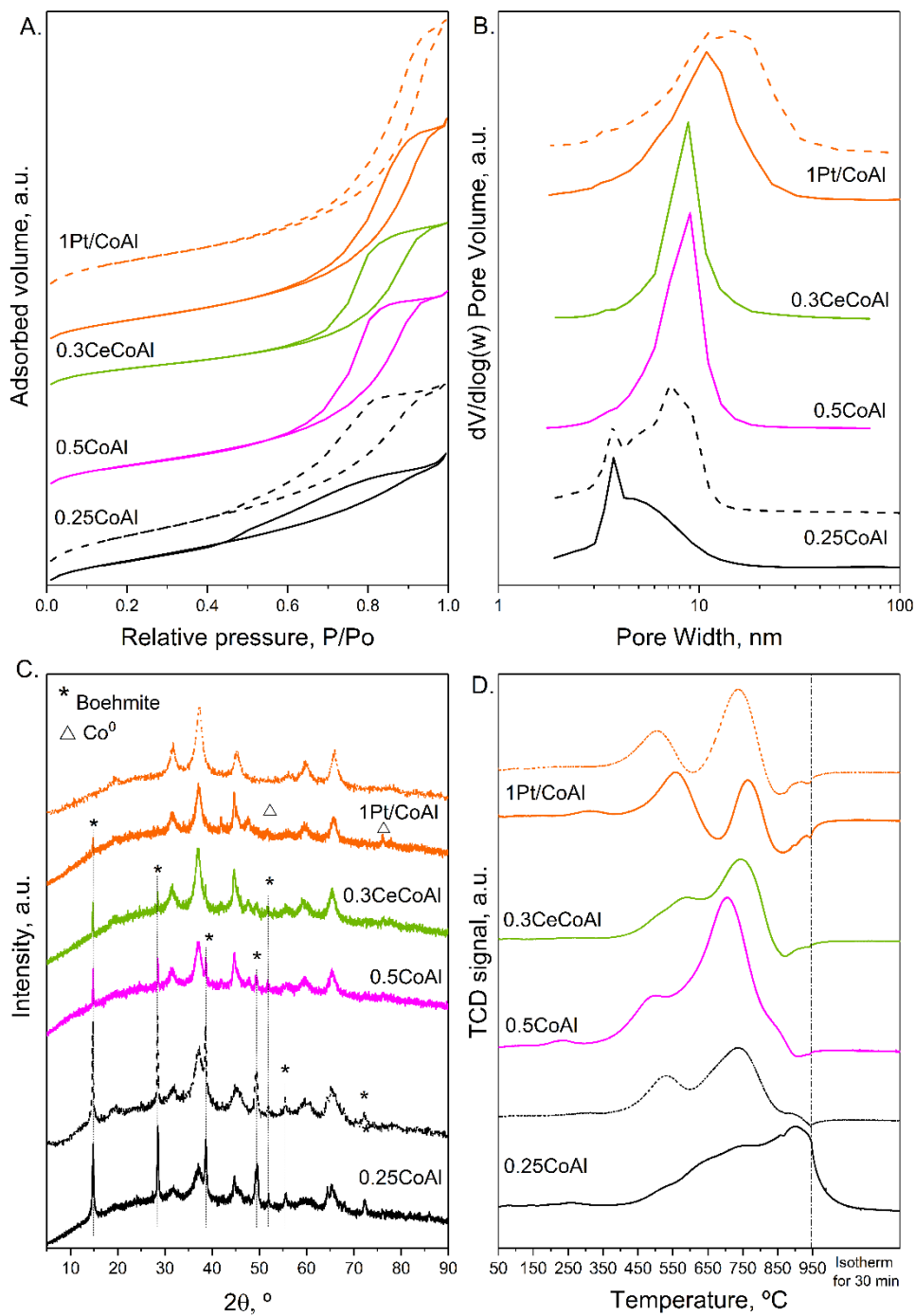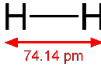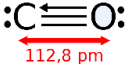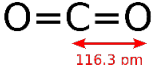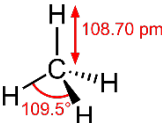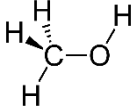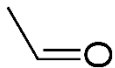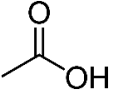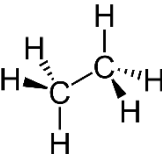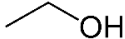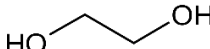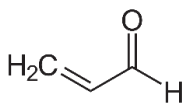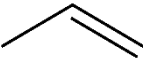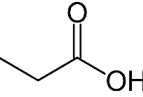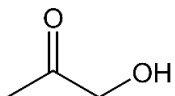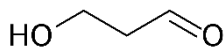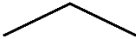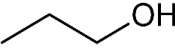
Figure C.1. N$_2$ physisorption isotherms (A), pore size distribution (B), XRD (C) and H$_2$-TPR (D) of spent catalysts after sorbitol HDO (solid lines) and APR (dashed lines).
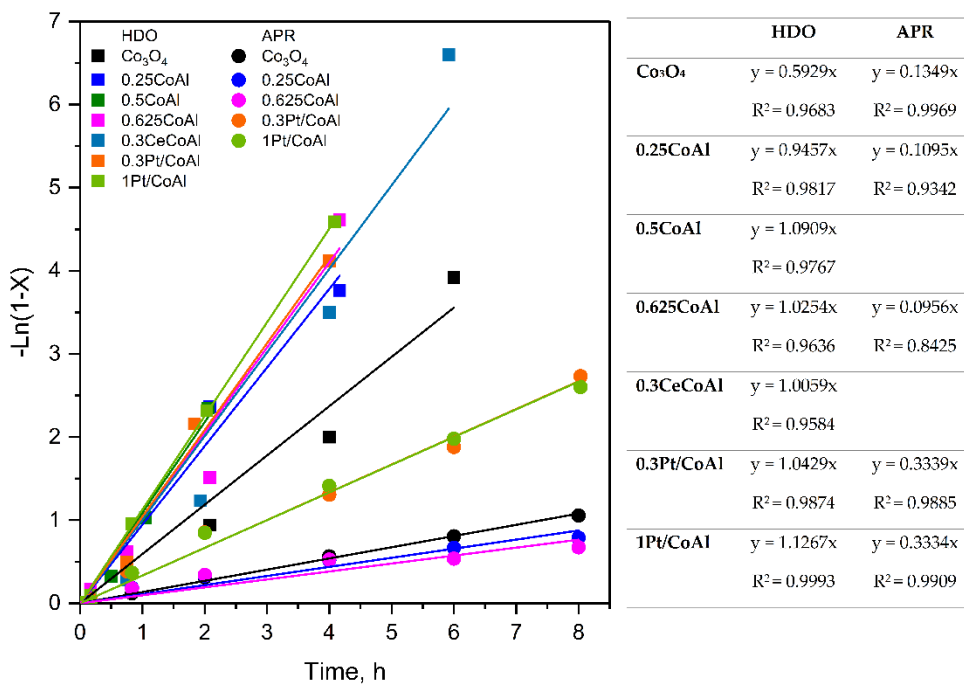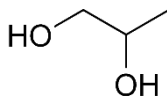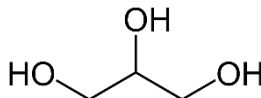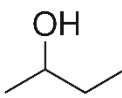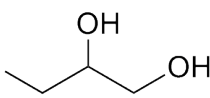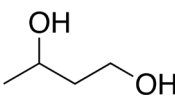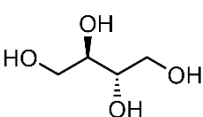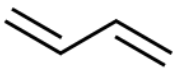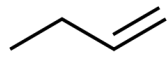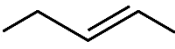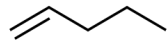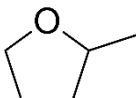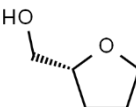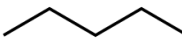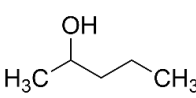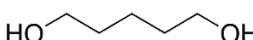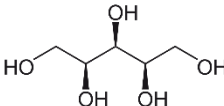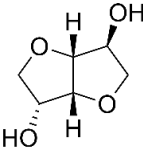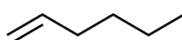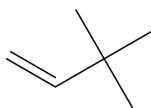
Figure C.2. First order rate plot of −ln(1−X$_{sorb}$) vs. time for sorbitol transformation under H$_2$ (HDO) and N$_2$ (APR) atmosphere.
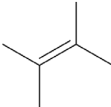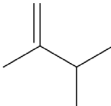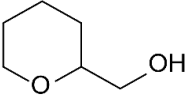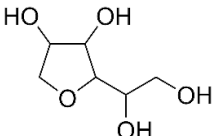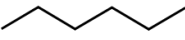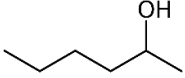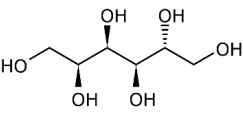
D. RELEVANT CHEMICAL COMPOUNDS IN THIS WORK

Name	Chemical formula	Molar mass (g.mol⁻¹)
Hydrogen	H_2	2.02
Carbon monoxide Flue gas	CO	28.01
Carbon dioxide Carbonic acid gas	CO_2	44.01
Methane Marsh gas Natural gas Hydrogen carbide	CH_4	16.04
Methanol Methyl alcohol Wood alcohol	CH_4O	32.04
Acetaldehyde Ethanal Acetic aldehyde	C_2H_4O	44.05
Acetic acid Ethanoic acic	$C_2H_4O_2$	60.05
Ethane	C_2H_6	30.07
Ethanol Ethylic alcohol Grain alcohol	C_2H_6O	46.07

Ethane-1,2-diol Ethylene glycol	$C_2H_6O_2$	HO⌒OH	62.07
2-Propenal Acrolein Acrylaldehyde	C_3H_4O	H_2C⌒CHO	56.06
Propene	C_3H_6		42.08
Propan-2-one Propanone Acetone Dimethyl ketone	C_3H_6O		58.08
Propanoic acid Propionic acid	$C_3H_6O_2$		74.08
1-Hydroxypropan-2-one Hydroxyacetone Acetol	$C_3H_6O_2$		74.08
3-HPA 3-Hydroxypropanal Reuterin	$C_3H_6O_2$	HO⌒O	74.08
Propane	C_3H_8		44.10
Propan-1-ol 1-Propanol n-propyl alcohol	C_3H_8O	OH	60.096
Propan-2-ol 2-Propanol Isopropanol	C_3H_8O	OH	60.096

Propane-1,2-diol Propylene glycol Methyl ethyl glycol	$C_3H_8O_2$		76.095
Propane-1,2,3-triol Glycerol Glycerin	$C_3H_8O_3$		92.094
Butane Butyl hydride	C_4H_{10}		58.12
Butan-2-ol 2-butanol sec-Butyl alcohol	$C_4H_{10}O$		74.123
Butane-1,2-diol 1,2-butanediol	$C_4H_{10}O_2$		90.121
Butane-1,3-diol 1,3 butanediol 1,3-butylene glycol	$C_4H_{10}O_2$		90.122
(2R,3S)-Butane-1,2,3,4-tetrol Erythritol	$C_4H_{10}O_4$		122.120
Butadiene Buta-1,3-diene Biethylene	C_4H_6		54.09
1-Butene Ethylethylene	C_4H_8		56.11
2-Butene	C_4H_8		56.11
1-Pentene	C_5H_{10}		70.13

2-methylTHF	$C_5H_{10}O$		86.134
(R)-Tetrahydrofuran-2-methanol THF-2-MeOH 2R)-Tetrahydro-2-furanylmethanol	$C_5H_{10}O_2$		102.13
Pentane	C_5H_{12}		72.15
Pentan-2-ol 2-pentanol Sec-amyl alcohol	$C_5H_{12}O$		88.148
pentane-1,5-diol 1,5-pentanediol Pentamethylene glycol	$C_5H_{12}O_2$		104.147
(2R,3R,4S)-Pentane-1,2,3,4,5-pentol Xylitol	$C_5H_{12}O_5$		152.146
Benzene Cyclohexa-1,3,5-triene	C_6H_6		78.11
1,4-Dianhydrosorbitol D-isosorbide	$C_6H_{10}O_4$		146.142
1-Hexene Hexylene Butyl ethylene	C_6H_{12}		84.16
3,3-Dimethylbut-1-ene 33DM1B	C_6H_{12}		84.16

2,3-Dimethylbut-2-ene 23DM2B	C_6H_{12}		84.16
2,3-Dimethylbut-1-ene 23DM1B	C_6H_{12}		84.16
Cyclohexane	C_6H_{12}		84.16
Tetrahydropyran-2-methanol THP-2-MeOH 2-Tetrahydropyranyl methanol	$C_6H_{12}O_2$		116.16
(3S)-2-(1,2-Dihydroxyethyl) tetrahydrofuran-3,4-diol 1,4-anhydrosorbitol Sorbitan	$C_6H_{12}O_5$		164.16
Hexane	C_6H_{14}		86.18
2-Hexanol	$C_6H_{14}O$		102.174
(2S,3R,4R,5R)-Hexane-1,2,3,4,5,6-hexol D-Sorbitol D-glucitol	$C_6H_{14}O_6$		182.17

E.   DISSEMINATION OF RESULTS

### E.1   ARTICLES DERIVED FROM THE DOCTORAL THESIS
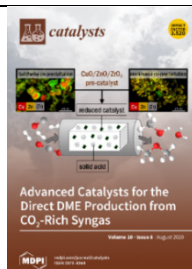
Bimetallic Pt-Co Catalysts for the Liquid-Phase WGS. A.J. Reynoso, J.L. Ayastuy, U. Iriarte-Velasco, M.A. Gutiérrez-Ortiz.

Catalysts, 10(8), 830. doi: 10.3390/catal10080830

Highly stable Pt/CoAl$_2$O$_4$ catalysts in Aqueous-Phase Reforming of glycerol. A.J. Reynoso, U. Iriarte-Velasco, M.A. Gutiérrez-Ortiz, J.L. Ayastuy.
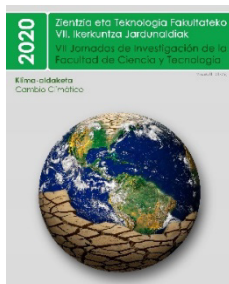
Catalysis Today, (2020). doi: 10.1016/j.cattod.2020.03.039
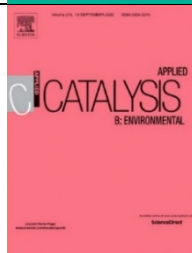
Cobalt aluminate spinel-derived catalysts for glycerol aqueous phase reforming. A.J. Reynoso, J.L. Ayastuy, U. Iriarte-Velasco, M.A. Gutiérrez-Ortiz.

Applied Catalysis B: Environmental, 239 (2018) 86-101. doi:10.1016/j.apcatb.2018.08.001

E.2   CONTRIBUTIONS TO CONFERENCES

Valorisation of biomass-derived compounds over transition metal catalysts. A.J. Reynoso, A. Morales-Marín, A. Choya, A. Sanz, N. Vera-Hincapie, A. Gil, Z. Boukha, B. De Rivas, U. Iriarte-Velasco, J.L. Ayastuy, R. López-Fonseca, J.I. Gutiérrez-Ortiz and M.A. Gutiérrez-Ortiz.

VII Research Conference of the Faculty of Science and Technology, Leioa (Spain), 28-30 sept 2020 (oral)

Highly stable Pt/CoAl$_2$O$_4$ catalysts for the Aqueous Phase Reforming of glycerol. A.J. Reynoso, J.L. Ayastuy, U. Iriarte-Velasco, M.A. Gutiérrez-Ortiz.

5th International Congress on Catalysis for Biorefineries (CatBior V), Turku/Abo (Finland), 23-27 sept 2019 (oral).

Reformado en fase líquida de derivados de la biomasa con Pt/CoAl2O4: Influencia de las variables de operación en la producción de hidrógeno. A.J. Reynoso, J.L. Ayastuy, A. Morales-Marín, U. Iriarte-Velasco, M.A. Gutiérrez-Ortiz.

Reunión de la Sociedad española de Catálisis (SECAT19), Córdoba (Spain), 24-26 jun 2019 (oral).

Cobalt aluminate catalysts for aqueous phase reforming: Glycerol to Hydrogen. A.J. Reynoso, J.L. Ayastuy, U. Iriarte-Velasco, M.A. Gutiérrez-Ortiz.

Seminaire SAMCat, Poitiers (France), 7 feb 2019 (oral).

Efecto de la adición de Ce sobre el rendimiento en el reformado acuoso de glicerol de catalizadores de Ni y Co obtenidos a partir de sus aluminatos. A. Morales-Marín, A.J. Reynoso, B. Molinuevo, J.L. Ayastuy, U. Iriarte, M.A. Gutiérrez-Ortiz.

XXVI Congreso Ibero-Americano de Catálise, Coimbra (Portugal), 9-14 sept 2018 (poster).

Catalizadores de Co a partir de CoAl$_2$O$_4$ modificado con cerio para la obtencion de H$_2$ por APR de glicerol. A. J. Reynoso, J.L. Ayastuy, A. Morales-Marín, U. Iriarte, M.A. Gutiérrez-Ortiz.

III Encuentro de Jóvenes Investigadores de la SECAT, Valencia (Spain), 25-27 jun 2018 (poster).

Effect of the Co/Al ratio on the selectivity towards hydrogen during glycerol dehydration/dehydrogenation reactions in TPD experiments. J.L. Ayastuy, A.J. Reynoso, U. Iriarte-Velasco, M.A. Gutiérrez-Ortiz.

10th World Congress of Chemical Engineering (WCCE10), Barcelona (Spain), 1-5 oct 2017 (poster).

Cobalt aluminate nanoparticles catalysts: Impact of hard-template removal method. A.J. Reynoso, J.L. Ayastuy, A. Morales-Marín, M.A. Gutiérrez-Ortiz.

Glycerol-TPD on cobalt aluminate spinel catalysts. A.J. Reynoso, U. Iriarte-Velasco, M.A. Gutiérrez-Ortiz, J.L. Ayastuy.

13th European Congress on Catalysis (EuropaCat2017), Florence (Italy), 27-31 ago 2017 (poster).

Hydrogen production by aqueous phase reforming of glycerol on cobalt aluminate catalysts. A.J. Reynoso, J.L. Ayastuy, A. Morales-Marín, M.A. Gutiérrez-Ortiz, U. Iriarte-Velasco.

Reunión de la Sociedad española de Catálisis (SECAT17), Oviedo (Spain), 26-28 jun 2017 (oral).

Cobalt aluminate nanoparticles synthesized by nanocasting: Effect of Co/Al ratio on glycerol APR. A.J. Reynoso, A. Morales-Marín, J.L. Ayastuy, M.A. Gutiérrez-Ortiz.

1st Trans Pyrenean Meeting in Catalysis, Toulouse (France), 13-14 oct 2016 (poster).

Characterization of spinel-derived cobalt catalysts for glycerol aqueous phase reforming. A.J. Reynoso, J.L. Ayastuy, M.A. Gutiérrez-Ortiz, A. Morales-Marín.

3rd International Symposium on Catalysis for Clean Energy and Sustainable Chemistry, Madrid (Spain), 7-9 sept 2016 (poster).

In the current context regarding the increase in energy demand and the need to decarbonize the global energy system to avoid even further deterioration of the on-going climate change crisis, hydrogen is a promising energy alternative. The use of hydrogen, produced from biomass, would drastically reduce CO_2 emissions, contribute to reducing the current dependence on fossil fuels and, due to its greater availability, would improve the economic situation of many countries that are still plagued by energy poverty. Aqueous-phase reforming (APR) is a suitable and energy-efficient alternative process for hydrogen and other high value-added chemical production.

This Doctoral Thesis aims to contribute to a development of new cobalt aluminate-based catalysts for glycerol valorisation through H_2 production by APR establishing a structure-activity relationship. This research provides further insight into the aqueous-phase reforming of biomass-derived oxygenated compounds, the effect of operating conditions, the correlation with liquid-phase WGS reaction and the feasibility of crude bioglycerol as a feedstock.